TO MY PARENTS

SURFACE SEGREGATION IN CuNi AND AgPd ALLOYS

A THESIS SUBMITTED FOR THE DEGREE OF DOCTOR OF PHILOSOPHY OF THE UNIVERSITY OF LONDON AND FOR THE DIPLOMA OF IMPERIAL COLLEGE

BY

CARLOS EDUARDO ROJAS

PHYSICS DEPARTMENT

IMPERIAL COLLEGE OF SCIENCE AND TECHNOLOGY

LONDON.

JUNE 1983

ABSTRACT

Surface segregation studies on CuNi and AgPd alloys have been carried out using AES and LEED.

Current theoretical models for predicting the segregating component and determining the equilibrium surface composition of binary alloys are reviewed. The segregation energy of Ag to the low index surfaces of a AgPd alloy is calculated using an electronic model of surface segregation based on a multiple scattering formalism. These calculations predict a larger Ag enrichment on the more "open" surfaces of AgPd.

Quantification of AES spectra is discussed and a computing programme is developed for the calculation of the surface composition of binary alloys.

$Cu_{0.05}$ $Ni_{0.95}$ (100), (110), (111) and $Cu_{0.5}$ $Ni_{0.5}$ (111) faces were analysed. Extensive Cu enrichment was observed using the LMM and M_1VV Cu and Ni Auger transitions. By combining these measurements with X-ray photoemission data obtained from the same samples, two kinds of possible composition profiles after heat treatment at 873K were determined: a) a monotonic decreasing profile with $\sim$ 90% Cu in the topmost layer and a sharp decrease to bulk composition levels, or b) an oscillatory profile with the same high Cu composition in the topmost layer and a minimum in composition in the third and fourth layers.

AES determination of the surface composition was also carried out on $Ag_{0.01}$ $Pd_{0.99}$ (100), (110), (111), poly-crystalline $Ag_{0.05}$ $Pd_{0.95}$ and $Ag_{0.95}$ $Pd_{0.05}$ and S contaminated $Ag_{0.07}$ $Pd_{0.93}$ (111) - (012) samples. Data on the kinetics of segregation in the 673K - 973K is presented.

Face specificity of Ag enrichment was observed; the equilibrium Ag composition of the close-packed (111) surface being lower than in the more open (100) and (110) surfaces.

S segregation was observed to cause reversible Ag desegregation.

Thermal desorption spectra of CO on $Ag_{0.01}$ $Pd_{0.99}$ (100) with different surface composition show that the effect of Ag is to dilute the CO-Pd adsorption sites.

LIST OF CONTENTS

		Page
	Introduction	18
	CHAPTER 1	
	Bulk properties of CuNi and AgPd alloys	21
Section	Title	
1.1	Thermodynamic properties of solid metal solutions.	23
1.1.1	Ideal solutions.	23
1.1.2	Regular solutions.	24
1.1.3	Quasichemical approach.	26
1.1.4	Non regular solutions.	29
1.1.5	First and second nearest neighbours	30
1.1.6	Thermodynamic properties of CuNi and AgPd.	30
1.2	Electronic structure of CuNi and AgPd alloys.	34
1.2.1	Band structure of Ni, Cu, Pd and Ag.	34
1.2.2	Band structure of CuNi and AgPd.	38
	References.	42

CHAPTER 2

Theory of surface segregation 43

Section	Title	
2.1	Thermodynamic approach.	43
2.2	Strain effects.	49
2.3	Broken bond model.	51
2.4	Calculation of surface energies.	56
2.5	Miedema's semiempirical scheme.	58
2.6	Chemisorption induced surface segregation.	61
2.7	Model of Mezey and Giber.	62
	References.	68

CHAPTER 3

Electronic theory of surface segregation 69

Section	Title	
3.1	One-electron model of surface segregation.	69
3.2	Formalism.	72
3.2.1	Scattering from a single muffin-tin centre.	73
3.2.2	Multiple scattering.	77
3.2.3	Calculation of $\eta(E)$.	81
3.3	Results of the calculations for AgPd.	86
3.4	Surface core level energy shifts.	99
	References.	104

CHAPTER 4

Quantitative Auger Spectroscopy. 105

Section	Title	
4.1	Auger Electron Spectroscopy.	105
4.2	Quasiatomic versus band-like Auger spectra.	109
4.3	Quantitative Auger electron spectroscopy of binary alloys.	112
4.3.1	The attenuation function.	113
4.3.2	Electron inelastic mean free paths.	115
4.3.3	The Backscattering factor.	118
4.3.4	Homogeneous binary alloys.	120
4.3.5	Enrichment restricted to the first monolayer.	126
	References.	129
	Appendix	231

CHAPTER 5

Experimental equipment and sample preparation 130

Section	Title	
5.1	Ultra high vacuum system and ancillary equipment.	130
5.2	Sample preparation.	133
5.3	Sample holder.	135
5.4	Temperature controller.	137
5.5	LEED experimental arrangement.	140
5.6	AES experimental arrangement.	142
5.7	XPS system.	145
	References.	146

CHAPTER 6

Surface segregation in CuNi. Experimental results. 147

Section	Title	
6.1	Experimental procedure.	147
6.2	AES evidence for Cu surface segregation	148
6.2.1	High energy Auger transitions.	148
6.2.2	Low energy (M_1VV) Auger transitions.	151
6.3	Quantitative analysis of the surface composition using the M_1VV Auger signals.	154
6.4	Approach to equilibrium.	156
6.5	Determination of the composition profile.	161
6.6	Composition profile of $Cu_{0.05}$ $Ni_{0.95}$ at T = 873K.	164
6.7	Composition profile of $Cu_{0.5}$ $Ni_{0.5}$ (111) at T = 873K.	169
6.8	Diffraction patterns.	172
6.9	Discussion.	172
6.10	Conclusions.	175
	References.	177

CHAPTER 7

Surface Segregation in AgPd. Experimental Results 178

Section	Title	
7.1	Experimental procedure.	178
7.2	AES evidence for Ag surface enrichment.	179
7.3	XPS evidence for Ag surface enrichment.	183
7.4	Calibration of the sulphur Auger signal.	186
7.5	Ag segregation in $Ag_{0.01}$ $Pd_{0.99}$ (100) (110)(111) at 773K.	193
7.6	Effect of temperature on Ag segregation.	195
7.7	Ag-S cosegregation in S contaminated $Ag_{0.07}$ $Pd_{0.93}$.	199
7.8	Annealing of AgPd alloys in the presence of CO.	213
7.9	Thermal desorption of CO from $Ag_{0.01}$ $Pd_{0.99}$ (100).	214
7.10	Discussion.	221
7.11	Conclusions.	228
	References.	230

LIST OF FIGURES AND TABLES

Number	Caption	Page
Chapter 1		
Fig. 1.1	Phase diagrams for the CuNi and AgPd systems.	22
Fig. 1.2	Lattice parameter of CuNi and AgPd.	25
Fig. 1.3	Schematic illustration of the different kinds of "bonds" in a random alloy AB.	27
Fig. 1.4	ΔS_m, ΔH_m, and ΔG_m for CuNi and AgPd.	31
Fig. 1.5	Regular solution test for CuNi and AgPd.	33
Fig. 1.6	Band structure and density of states for Ni and Cu.	36
Fig. 1.7	Band structure and density of states for Pd and Ag.	37
Fig. 1.8	Schematic representation of the "effective medium" in CPA.	39
Fig. 1.9	Complex energy bands for CuNi.	39
Table 1.1	Bond enthalpies in CuNi and AgPd alloys.	34
Chapter 2		
Fig. 2.1	Schematic representation of surface enrichment in a substitutional alloy AB.	44
Fig. 2.2	Gibbs' dividing surface.	44
Table 2.1	Atomic radii and bulk and shear moduli of Ni, Cu, Pd and Ag.	51
Table 2.2	Values of the surface energy at zero temperature γ_o^s and the temperature derivative $d\gamma/dT$ for Ni, Cu, Pd and Ag.	58

number	Caption	Page
Chapter 2 cont.		
Table 2.3	Miedema's model parameters for Ni, Cu, Pd and Ag.	60
Table 2.4	Top layer composition of $Ag_{0.01}$ $Pd_{0.99}$ at T = 773K predicted by different models.	66
Chapter 3		
Fig. 3.1	Cohesive energy for metals along the 3d and 4d transition series.	70
Fig. 3.2	Phase shifts $\delta_\ell(E)$ for the muffin--tin potential of Cu.	78
Fig. 3.3	Change in the density of states caused by the $\ell = 2$ resonance of figure 3.2.	78
Fig. 3.4	Impurity MT in bulk site.	82
Fig. 3.5	Impurity MT at surface site.	82
Fig. 3.6	Hard ball models of muffin-tin clusters.	87
Fig. 3.7	Phase shifts for a Ag(Pd) MT and for Ag(Pd) MT interacting with vacuum MTs.	88
Fig. 3.8	Phase shifts for a Ag impurity in bulk Pd and at the (100) Pd surface.	90-92
Fig. 3.9	Phase shifts for Pd in bulk Pd and at the (100) Pd surface.	93-95
Chapter 4		
Fig. 4.1	Schematic diagram of an experimental arrangement for AES and of a "j k ℓ" Auger transition.	107
Fig. 4.2	Geometrical configuration sample--analyser used for calculating the attenuation function.	116

number	Caption	Page
Chapter 4 cont.		
Fig. 4.3	Electron inelastic mean free path in pure elements.	117
Fig. 4.4	Backscattering factor as a function of atomic number.	118
Fig. 4.5	Backscattering factor as a function of primary beam incidence angle for Mg and Al.	121
Chapter 5		
Fig. 5.1	Schematic diagram of the ultra high vacuum system.	131
Fig. 5.2	Sample holders.	136
Fig. 5.3	Diagram of the temperature controller and heating curve T(t).	139
Fig. 5.4	Experimental arrangement used for LEED.	141
Fig. 5.5	Experimental arrangement used for AES.	141
Chapter 6		
Fig. 6.1	Auger spectra of contaminated and clean $Cu_{0.05}$ $Ni_{0.95}$ sample.	149
Fig. 6.2	High energy Auger spectra of Ni and Cu.	150
Fig. 6.3	Evidence for Cu surface segregation. High energy spectra.	152
Fig. 6.4	Evidence for Cu surface segregation. Low energy spectra.	153
Fig. 6.5	Simulated CuNi (M_1VV) Auger spectra.	155
Fig. 6.6	Comparison of experimental and simulated Auger spectra.	157
Fig. 6.7	Calibration curve for CuNi(M_1VV) Auger spectra.	158

number	Caption	Page
Chapter 6 cont.		
Fig. 6.8	Cu "effective surface composition" as a function of time for $Cu_{0.05}$ $Ni_{0.95}$ (100) at T = 800K.	159
Fig. 6.9	Schematic representation of an arbitrary composition profile and of the function $C^{A}_{eff}(d)$.	163
Fig. 6.10	Surface composition of $Cu_{0.05}$ $Ni_{0.95}$ (100) as a function of electron escape depth .	167
Fig. 6.11	Composition profiles for $Cu_{0.05}$ $Ni_{0.95}$ (100) at T = 873K used to fit data in fig. 6.10.	168
Fig. 6.12	Surface composition of $Cu_{0.5}$ $Ni_{0.5}$ (111) as a function of electron escape depth.	170
Fig. 6.13	Possible composition profiles for $Cu_{0.5}$ $Ni_{0.5}$ (111) at T = 873K.	171
Fig. 6.14	Comparison of LEED patterns of Cu, Ni and CuNi.	173
Table 6.1	Calculated electron escape depths.	165
Chapter 7		
Fig. 7.1	Auger spectra of contaminated and clean AgPd sample.	180
Fig. 7.2	$M_{4,5}VV$ Auger signals of pure Pd and Ag.	181
Fig. 7.3	Auger evidence for Ag surface enrichment.	182
Fig. 7.4	3d XPS spectra of $Ag_{0.01}$ $Pd_{0.99}$ (111) at normal and grazing emission	184
Fig. 7.5	Conduction band XPS spectrum of $Ag_{0.01}$ $Pd_{0.99}$ (111) at normal and grazing emission.	185
Fig. 7.6	Auger spectrum of PdS.	188

number	Caption	Page
Chapter 7 cont.		
Fig. 7.7	Calibration curve for S on AgPd obtained using PdS Auger spectrum.	189
Fig. 7.8	S/AgPd(111) LEED patterns used for the calibration of the Auger sulphur signal.	191
Fig. 7.9	Calibration curve for S on AgPd (111) obtained from the combination of LEED and AES data.	192
Fig. 7.10	Segregation curve for $Ag_{0.01}$ $Pd_{0.99}$ (100) at 773K.	194
Fig. 7.11	Segregation curve for $Ag_{0.01}$ $Pd_{0.99}$ (111) at 773K.	195
Fig. 7.12	Segregation curve for $Ag_{0.01}$ $Pd_{0.99}$ (110) at 773K.	196
Fig. 7.13	Segregation curve for $Ag_{0.01}$ $Pd_{0.99}$ (110) at 873K.	198
Fig. 7.14	Segregation curve for $Ag_{0.01}$ $Pd_{0.99}$ (110) at 973K.	199
Fig. 7.15	Segregation curves for $Ag_{0.07}$ $Pd_{0.93}$ (012) and (111) at 823K.	201
Fig. 7.16	Ag surface composition as a function of S fractional monolayer for $Ag_{0.07}$ $Pd_{0.93}$ (012) and (111) surfaces.	203
Fig. 7.17	LEED patterns of sulphur segregating to the $Ag_{0.07}$ $Pd_{0.93}$ (012) surface.	204
Fig. 7.18	LEED patterns of sulphur segregating to the $Ag_{0.07}$ $Pd_{0.93}$ (111) surface.	205
Fig. 7.19	Auger S line shape for different segregation levels on $Ag_{0.07}$ $Pd_{0.93}$ (012).	206

number	Caption	Page
Chapter 7 cont.		
Fig. 7.20	Auger S line shape variation on $Ag_{0.07}$ $Pd_{0.93}$ (111) due to increasing segregation levels.	208
Fig. 7.21	Comparison of Auger S line shapes.	210
Fig. 7.22	Palladium 3d XPS spectra in AgPd and PdS.	211
Fig. 7.23	Sulphur 2p XPS spectra of S on AgPd and S in PdS.	212
Fig. 7.24	Segregation curve for polycrystalline $Ag_{0.05}$ $Pd_{0.95}$ at 673K.	215
Fig. 7.25	Segregation curve for polycrystalline $Ag_{0.05}$ $Pd_{0.95}$ at 773K.	216
Fig. 7.26	Thermal desorption spectra of CO on $Ag_{0.01}$ $Pd_{0.99}$ (100) after argon bombardment.	218
Fig. 7.27	Thermal desorption spectra for 1 L CO on $Ag_{0.01}$ $Pd_{0.99}$ (100) with different Ag effective surface compositions.	219
Fig. 7.28	Heats of sulphur adsorption versus heats of bulk sulphide formation.	223
Fig. 7.29	Approximate energy diagram for the adsorption and solution of S in Ag and Pd.	225

INTRODUCTION

The equilibrium composition of an alloy at the surface is, in general, different from its composition in the bulk. In the equilibration process one of the components of the alloy can segregate from the bulk producing as a result a surface enriched in that component.

This phenomenon, known as surface segregation, is of great interest in surface science. A theoretical description has been available since the times of J.W. Gibbs, but it has been only with the development of ultra-high-vacuum techniques and surface sensitive probes that experiments under well defined conditions could be performed and a clearer picture has begun to emerge.

It has been, however, the central role played by surface segregation in fields of technological importance like metallurgy and heterogeneous catalysis which has driven the interest in its study in recent years.

In metallurgy it has been observed that segregation of certain impurities to the grain boundaries of commercial materials is associated with embrittlement and fracture under service conditions.

In the field of heterogeneous catalysis we find that many bimetallic alloys are used as catalysts; their activity and selectivity being often quite different from those of their pure components. It is now widely accepted that it is

the local environment of the atoms taking part in a given catalytic reaction that determines their chemical behaviour. It is therefore the surface composition of an alloy which basically determines its catalytic properties.

At present, surface segregation studies in alloys are restricted to relatively simple binary systems. Existing theoretical models, using macroscopic parameters, have identified "driving forces" for segregation and are able to predict with fair accuracy which of the components of a binary alloy will enrich the surface region.

A number of these models provide quantitative predictions about the equilibrium composition profile that await experimental confirmation.

It is necessary to develop and test "first principles" electronic models of surface segregation in order to include this phenomenon within the present framework of solid state physics.

Most experimental works have been done on polycrystalline materials. For a more complete characterization, experimental data on well defined single crystal samples must be obtained.

The influence of impurities and of gaseous environments must also be investigated.

The kinetics of segregation have received little at-

tention from the experimental point of view. More data on this aspect is clearly needed.

It is the purpose of this thesis to contribute to the understanding and characterization of surface segregation in alloys through the study of copper-nickel and silver--palladium as model systems.

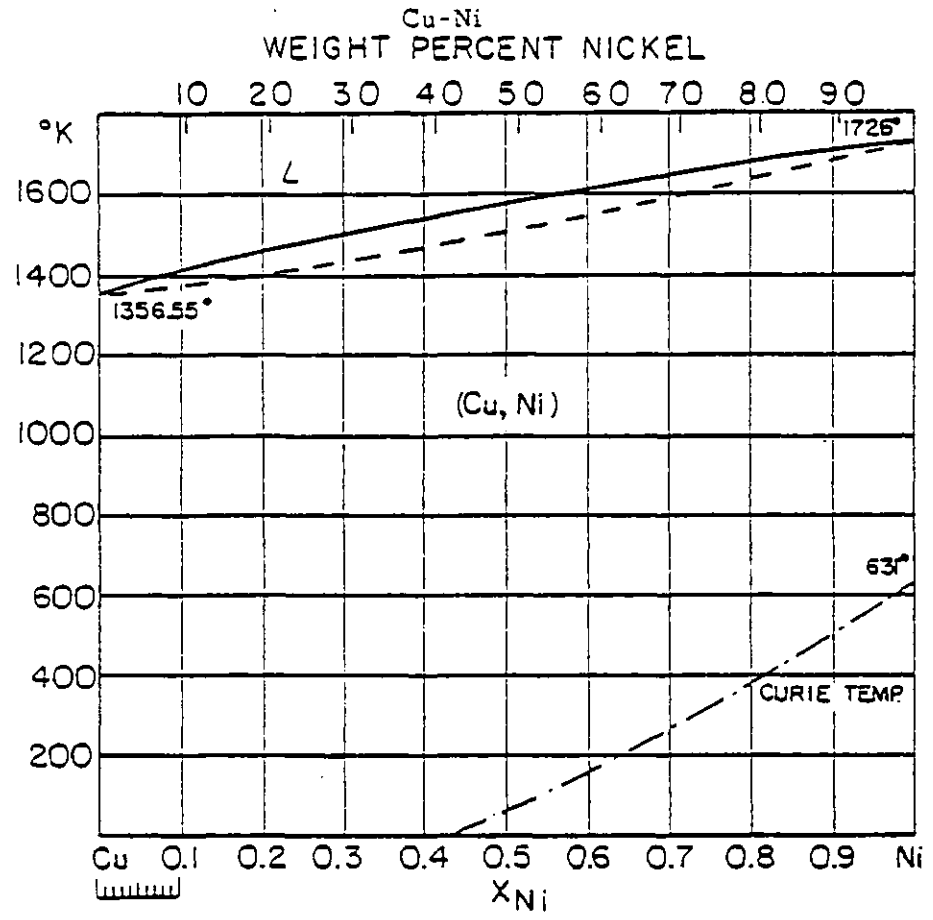
CHAPTER 1

BULK PROPERTIES OF CuNi AND AgPd ALLOYS

The description of the surface segregation in alloys rests on the knowledge of the bulk properties of the alloy and its components. Before tackling the problem of surface segregation in CuNi and AgPd it is instructive to consider the bulk properties of these alloys.

Both CuNi and AgPd are substitutional alloys and, like their components, have a f.c.c. crystalline structure. Figure 1.1 shows the respective phase diagrams. As can be seen, these phase diagrams are very simple, displaying complete miscibility over the entire range of compositions. This simplicity is one of the main factors in choosing these two alloys as model systems in many studies of surface segregation; possible complications due to phase changes upon variation in composition or temperature are avoided. In reality a miscibility gap is expected for the CuNi system at a critical temperature below which it will tend to form clusters of Cu and Ni. This critical temperature could be in the range of 150 - 200°C[1], low enough as to neglect this effect in surface segregation experiments.

The CuNi and AgPd systems can then be characterized as solid solutions. In order to introduce some useful concepts, the thermodynamic properties of such systems are considered next.



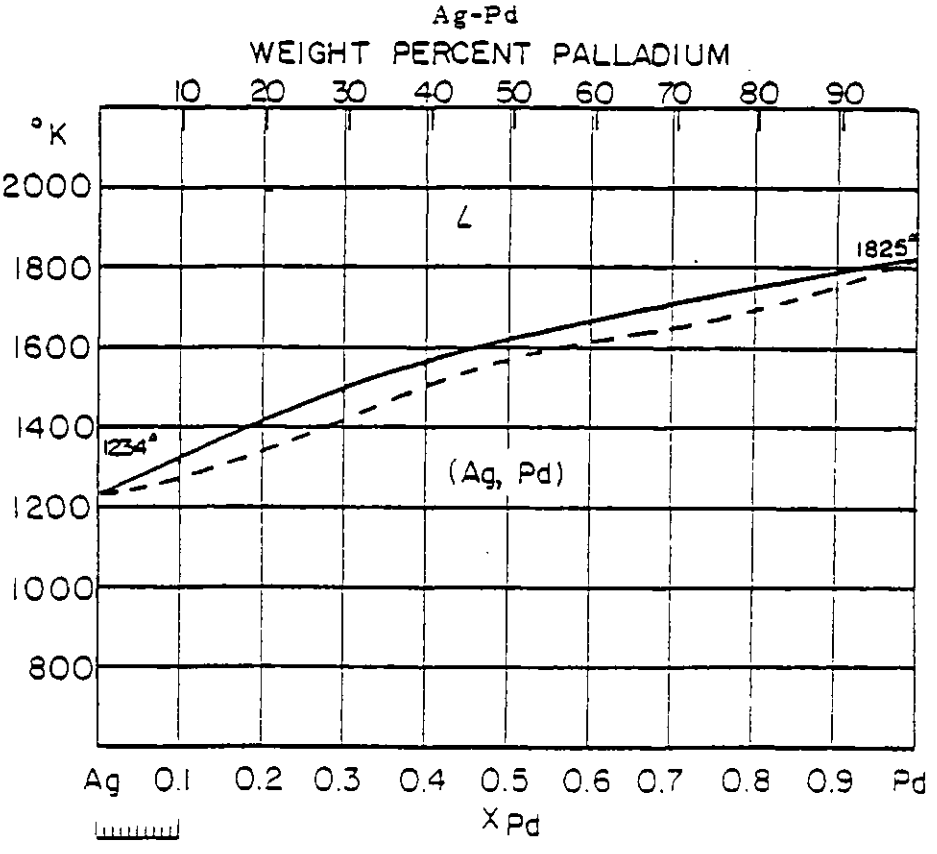


Figure 1.1 Phase diagrams for the CuNi and AgPd systems. (After Hultgren et.al.[6]).

1.1 Thermodynamic properties of solid metal solutions.

The thermodynamical description will be done in terms of the changes in the Gibbs free energy

$$G = H - TS \qquad 1.1$$

where H is the enthalpy, S the entropy and T the absolute temperature.

Assume we form a binary solution AB of atom fraction X_A, X_B from their pure components A and B in a given standard state. Associated with this process there is a free energy change ΔG_m known as the free energy of mixing. At constant temperature

$$\Delta G_m = \Delta H_m - T\Delta S_m \qquad 1.2$$

where ΔH_m is the enthalpy or heat of mixing and ΔS_m the entropy of mixing.

1.1.1 Ideal solutions.

A solution is termed ideal if no heat is absorbed or released upon its formation and if the distribution of atoms A and B is completely random. In this case the mixing enthalpy

$$\Delta H_m = 0 \qquad 1.3$$

and the entropy of mixing is only configurational. For a large number of atoms Stirling's formula can be used, giving

$$\Delta S_m = - k_B(X_A \ln X_A + X_B \ln X_B) \qquad 1.4$$

where k_B is the Boltzmann's constant and

$$X_B = 1 - X_A \qquad 1.5$$

It can be seen that ΔS_m is always positive and symmetric about $X_A = X_B = 0.5$.

For an ideal solution Vegard's law holds over the entire composition range i.e. the lattice parameter "a" of the solution is given by

$$a = X_A a_A + X_B a_B \qquad 1.6$$

where a_A and a_B are the lattice parameters of the pure components A and B.

For CuNi and AgPd a small variation from Vegard's law is observed. See figure 1.2.

Of course, most solutions do not behave in this ideal fashion but the concept of ideal solution is useful as a reference for real solutions.

1.1.2 Regular solutions.

As the next step towards the characterization of real solutions let us consider the so called regular solutions. In the formation of this kind of solution there is a net absorption or release of heat so the enthalpy of mixing is different from zero

$$\Delta H_m \neq 0 \qquad 1.7$$

but the atoms are still randomly distributed, so the entropy of mixing is configurational as given by equation 1.4.

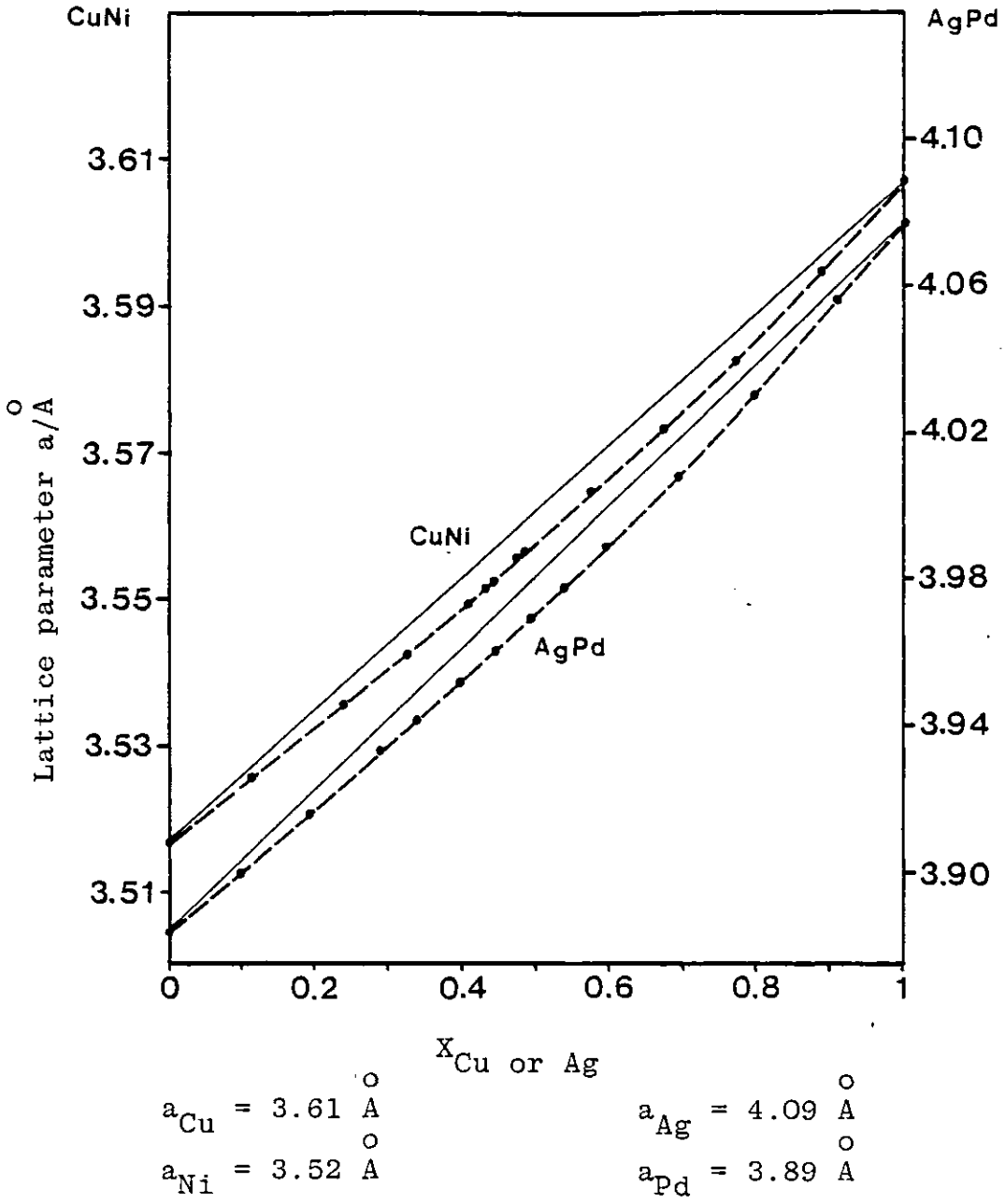


Figure 1.2 Lattice parameter of CuNi at 18°C and AgPd at 22°C. Solid line: Vegard's law. (After Coles[2]).

1.1.3 Quasichemical approach

A simple model for handling the energetics of solid solutions that has proved very valuable in understanding various phenomena is the quasichemical approach.

In this model the total cohesive energy of the solid solution is approximated by a summation of nearest neighbours pair interactions. It is assumed that between each pair of atoms there is a chemical bond with a certain energy, the nature of which is unspecified. Only nearest neighbours are considered and size effects are not taken into account.

The energies or enthalpies of formation of the alloy crystals are then calculated by forming or breaking bonds of different energies. The energy of each "bond" is assumed to be independent of the other bonds formed by the atom, i.e. it is independent of composition.

In the case of a binary alloy AB there will be three kinds of bonds, A-A, A-B and B-B as shown schematically in figure 1.3; each of them with an associated enthalpy H_{AA}, H_{AB} and H_{BB} respectively.

The enthalpy of the solution is then given by

$$H = n_{AA}H_{AA} + n_{AB}H_{AB} + n_{BB}H_{BB} \qquad 1.8$$

where n_{AA}, n_{AB}, n_{BB} are the number of nearest neighbours bonds of each kind. The number of bonds are determined in a statistical calculation on a lattice frame of reference

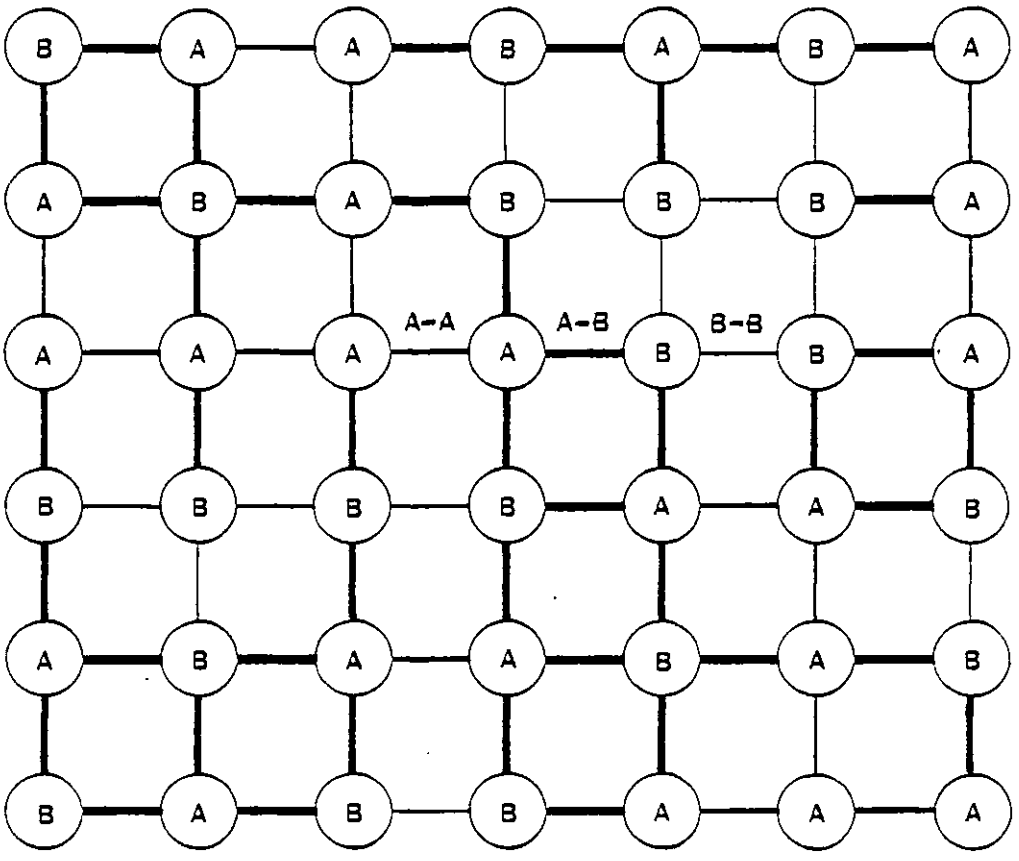


Figure 1.3 Schematic illustration of the different kinds of "bonds" in a random alloy AB.

with coordination number Z. The bonding enthalpies H_{AA} and H_{BB} for the pure elements can be obtained from experimental values of heats of sublimation ΔH_v. For instance, if we consider the sublimation of one mole of A atoms, we have

$$- \Delta H_v = \frac{1}{2} Z N_o H_{AA} \qquad 1.9$$

where N_o is Avogadro's number.

A direct comparison of the strength of the A-B bond with the average strength of the A-A and B-B bonds is made through the regular solution parameter ω defined as

$$\omega = H_{AB} - \frac{1}{2}(H_{AA} + H_{BB}) \qquad 1.10$$

Note that ω is independent of the alloy composition.

Considering that the coordination number Z is the same for the alloy and for the pure components, in a regular solution ω is related to the molar enthalpy of mixing by the expression

$$\Delta H_m = N_o Z X_A X_B \omega \qquad 1.11$$

so ω can be determined from the experimental values of ΔH_m. Equation 1.11 shows that within this model, the enthalpy of mixing in a regular solution is a parabolic function of composition, symmetric about $X_A = X_B = 0.5$.

For an ideal solution the heat of mixing is zero so $\omega = 0$ and

$$H_{AB} = \frac{1}{2}(H_{AA} + H_{BB}) \qquad 1.12$$

A negative value of ω indicates that the A-B bond is more stable than the A-A or B-B bonds; the formation of the alloy from the pure components will be exothermic and at low

temperatures there will be a preference for mixing of unlike atoms.

A positive value of ω indicates that bonding between like atoms is more stable than between unlike atoms, the alloy formation will be endothermic and at low temperatures there will be a tendency to clustering of like atoms.

1.1.4 Non regular solutions

We have seen that for non zero values of ω there will be a departure from random mixing and hence the regular solution approximation will be valid only if ω is sufficiently small compared with $k_B T$.

The departure from random mixing occurring in non regular solutions with its corresponding loss of entropy has been considered in higher order approximations within the quasichemical approach. In this case the molar enthalpy of mixing is given by[4]

$$\Delta H_m = X_A X_B Z N_o \omega \left[1-X_A X_B(e^{-2\omega/k_B T} -1)\right] \qquad 1.13$$

For moderate values of ω this equation reduces to

$$\Delta H_m = X_A X_B Z N_o \omega (1+X_A X_B 2\omega/k_B T) \qquad 1.14$$

and the molar entropy and free energy of mixing reduce to

$$\Delta S_m = -k_B N_o(X_A \ln X_A + X_B \ln X_B) - X_A^2 X_B^2 Z N_o \omega^2/k_B T^2 \qquad 1.15$$

and

$$\Delta G_m = X_A X_B N_o Z \omega (1+\bar{3} X_A X_B \omega/k_B T) + T N_o k_B (X_A \ln X_A + X_B \ln X_B) \qquad 1.16$$

1.1.5 First and second nearest neighbours.

Thermodynamic values calculated using the quasichemical approach can be estimated more accurately if first and second nearest neighbour pairwise bonds are considered. The enthalpy of the second nearest neighbour bonds can be approximated by a fraction of the enthalpy of the first nearest neighbour bonds.

For the pure metal A,

$$H_{AA}(2^{nd}\text{n.n.}) = H_{AA}(1^{st}\text{n.n.})e^{-q(d_2-d_1)} \qquad 1.17$$

where d_1 and d_2 are the first and second nearest neighbour bond lengths and q is a constant.

An effective coordination number Z_{eff} can then be defined as

$$Z_{eff} = Z_1 + e^{-q(d_2-d_1)} Z_2 \qquad 1.18$$

where Z_1 and Z_2 are the number of first and second nearest neighbours respectively and $e^{-q(d_2-d_1)}$ takes the approximate value of 0.3 in the case of f.c.c. crystals and 0.6 in the case of b.c.c. crystals[5].

1.1.6 Thermodynamic properties of CuNi and AgPd.

Experimental values of the mixing enthalpy, entropy and free energy as a function of composition for CuNi and AgPd are shown in figure 1.4.

As can be observed these solutions are far from being

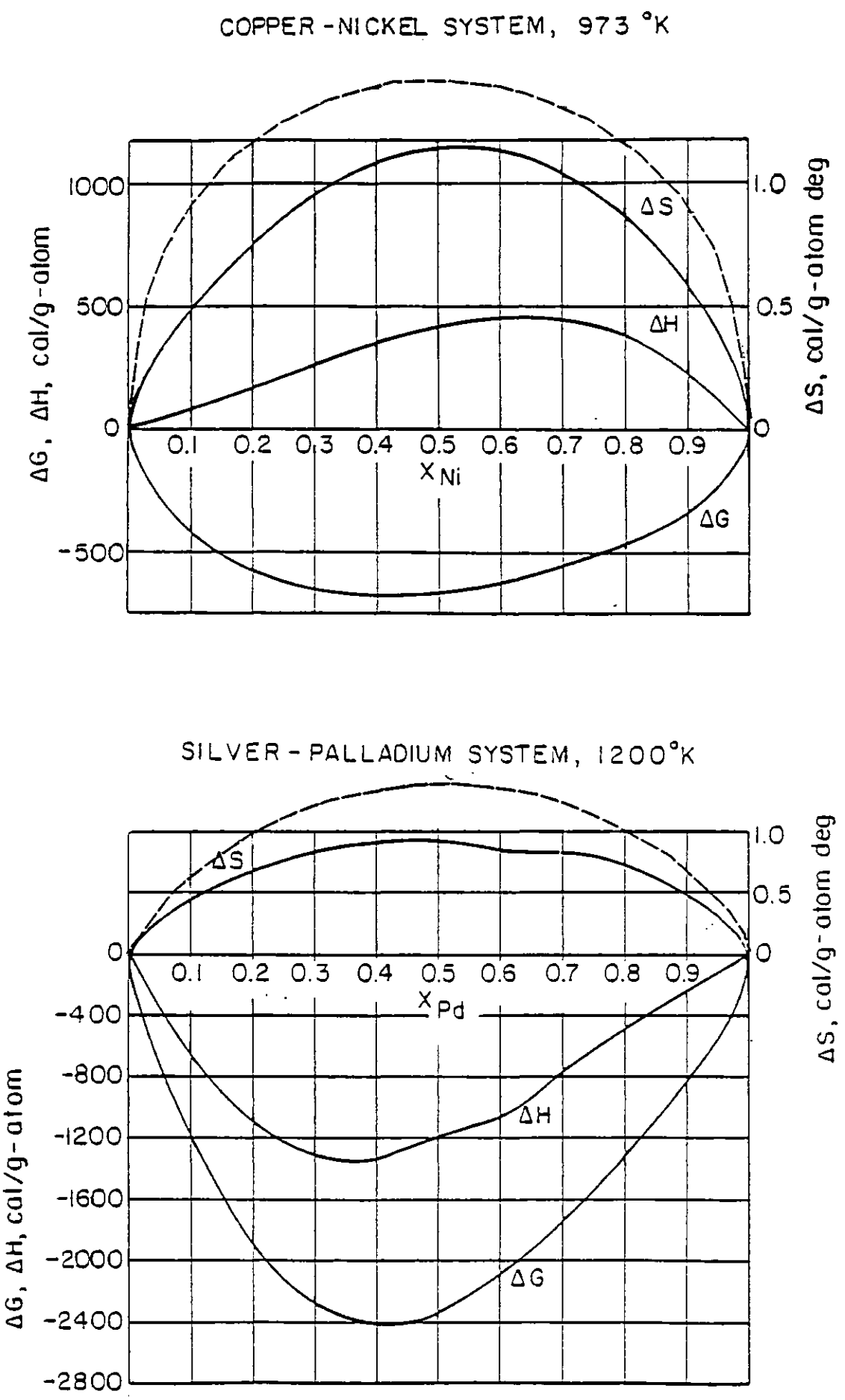


Figure 1.4 ΔS_m, ΔH_m and ΔG_m for CuNi and AgPd. (After Hultgren et.al.[6]).

ideal. The enthalpy of mixing for CuNi is positive while for AgPd is negative; a tendency to clustering exists in CuNi and a tendency to short range ordering in AgPd. The broken line in fig. 1.4 represents the configurational entropy (eq. 1.4). The experimental values of ΔS_m are smaller than the ideal value for all compositions, this difference can not be accounted for by using equation 1.14 instead of equation 1.11, so it depends on other contributions (thermal, electronic, etc.)

Values of the regular solution parameter ω can be calculated from the values of ΔH_m or from the activity coefficients f_A, f_B corresponding to the reactions $A_{pure} = A_{in\ alloy}$ and $B_{pure} = B_{in\ alloy}$, according to the relations[7]

$$\ln f_A = (X_B^2\ Z/RT)\omega \qquad 1.19$$

$$\ln f_B = (X_A^2\ Z/RT)\omega$$

where R is the gas constant.

Equations 1.19 show that in a regular solution $\ln f_A$ is a linear function of X_B^2 and the quantity ω may be evaluated from the slope of the $\ln f_A$ vs X_B^2 line. This relation is often used as a test for a regular solution, and is given in figure 1.5 for CuNi and AgPd. As can be seen both alloys, and specially AgPd, depart from the regular behaviour. The regular solution parameter ω has been, however calculated for this alloy by making a least squares fitting of the data points with a straight line.

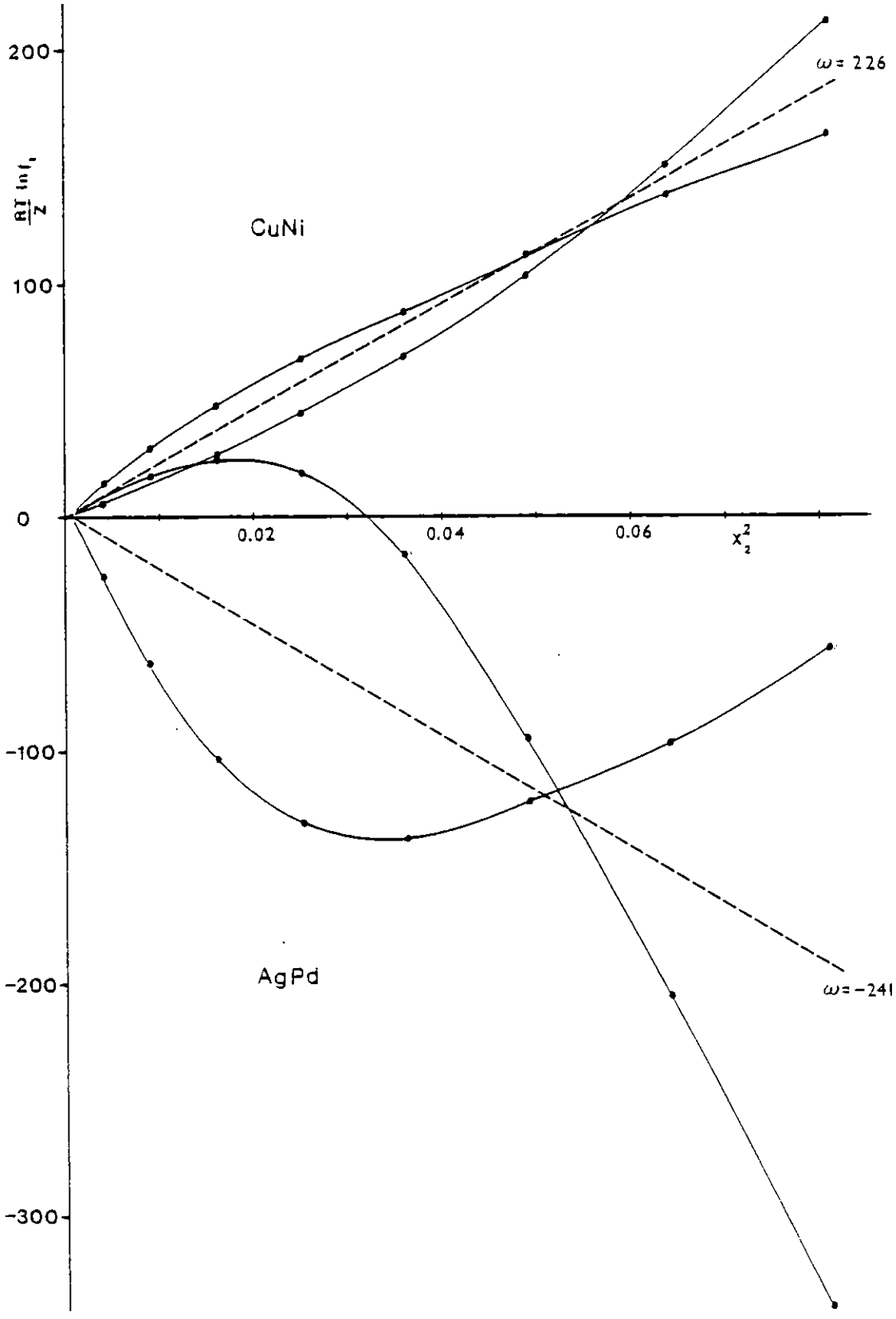


Figure 1.5 Regular solution test for CuNi and AgPd; data from ref. 6. Dashed line: least squares fit.

Table 1.1 collects the estimated values of the different bond enthalpies in CuNi and AgPd and the thermodynamic quantities used for their calculation.

Table 1.1 Bond enthalpies in CuNi and AgPd alloys.

	$\Delta H_{v,298}$ / (cal / mole)	H_{AA}/eV
Ni	102800	- 0.743
Cu	80500	- 0.582
Pd	90000	- 0.650
Ag	67900	- 0.491

	ω / (cal / mole)	H_{AB}/eV
CuNi (973K)	+ 226	- 0.652
AgPd (1200K)	- 241	- 0.581

1.2 Electronic Structure of CuNi and AgPd alloys

1.2.1 Band Structure of Ni, Cu, Pd and Ag.

A very succesful account of the electronic structure and ground state properties of ordered solids is given by the band theory. The original many-body problem is replaced by an effective one-electron Schroedinger equation in which the potential has the spatial periodicity of the crystalline array; the Bloch functions and the band structure $E(\vec{k})$ constitute the solution of this equation. Various numerical methods have been developed in order to obtain this solution; the Korringa-Kohn-Rostoker (KKR) method being one of the

more effective, particularly for the description of transition and noble metals. The KKR is a very general, multiple scattering approach in which the energy bands are given by the secular equation

$$|| \; t^{-1}(E) - B(\vec{k},E) \; || = 0 \qquad 1.20$$

where the t - matrix describes the scattering by the atomic potentials and the matrix B $(\vec{k},E)$ contains the KKR structure constants, determined by the crystal lattice [8].

The band structure of Ni, Cu, Pd and Ag, calculated using the KKR method[9] are given in figures 1.6 and 1.7.

Comparison of the essential features in the band structures of Ni and Cu reveals that the s-p bands are very similar and that the main difference is in the location of the d bands relative to the Fermi level; Ni presenting a high density of states near the Fermi energy and Cu at about 2 eV. below. The respective bandwidths w are

$$w_{Ni} = 4.8 \text{ eV} \quad \text{and} \quad w_{Cu} = 3.2 \text{ eV}.$$

Comparison of the band structures of Pd and Ag follows approximately the same pattern. Pd has a rather broad band, with high density of states at the Fermi level; the corresponding feature in Ag is at about 3.3 eV below E_F. The bandwidths are

$$w_{Pd} = 5.6 \text{ eV} \quad \text{and} \quad w_{Ag} = 3.1 \text{ eV}$$

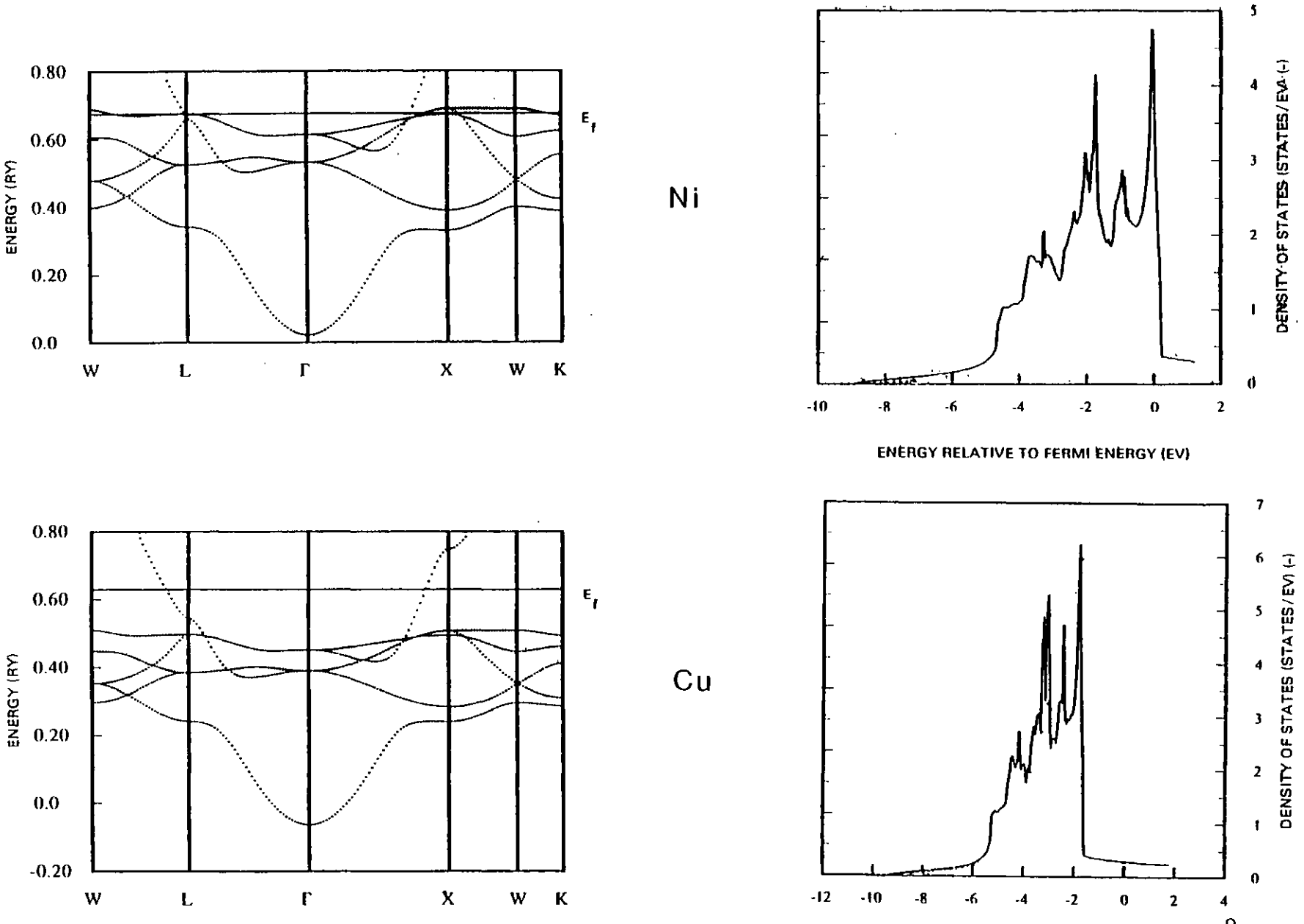


Figure 1.6 Band structure and density of states of Ni and Cu. (After Moruzzi et.al.[9]).

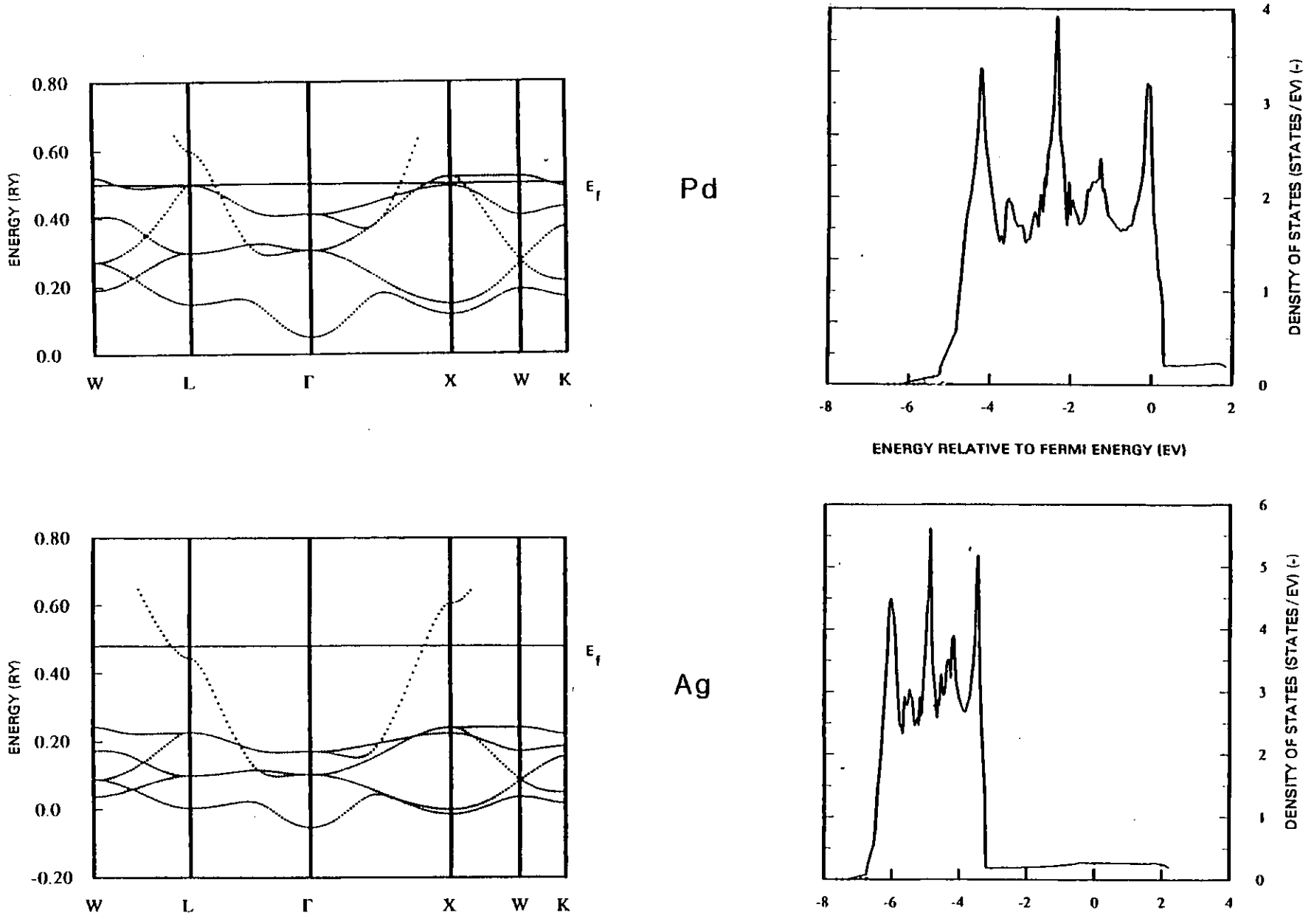


Figure 1.7 Band structure and density of states of Pd and Ag. (After Moruzzi et.al.[9]).

1.2.2 Band structure of CuNi and AgPd.

The band theory rests on the existence of translational symmetry in the solid. In a random alloy this symmetry is lost, so one might expect a complete collapse of the band theory description. In a substitutional alloy, however, some degree of order remains, since the different atoms are located on the sites of a periodical lattice. As far as the average electronic properties of the alloy is concerned substantial progress can be made by replacing the disordered system by an ordered one of appropriately chosen effective atoms; see figure 1.8.

Various schemes have been proposed to choose this effective medium; the coherent potential approximation (CPA) being generally recognized as the more satisfactory. In this scheme the condition is imposed that the average scattering from A and B atoms placed in the effective CPA medium be equal to zero,

$$X_A t_A^{eff} + (1 - X_A) t_B^{eff} = 0 \qquad 1.21$$

where t_A^{eff} and t_B^{eff} denote the t - matrices of A and B atoms placed in the effective medium. Equation 1.21 is then solved for the unknown t_{eff} that describes the CPA medium in the form of an ordered lattice of scatterers. The KKR method can then be applied to this effective crystal, giving the secular equation

$$|| \; t_{eff}^{-1}(E) - B(\vec{k},E) \; || = 0 \qquad 1.22$$

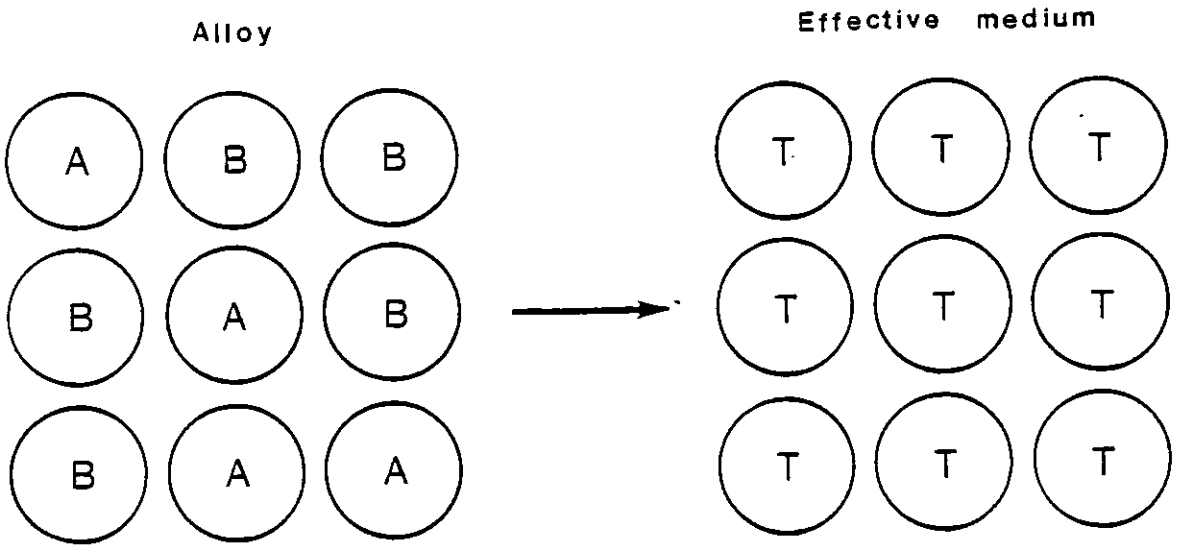


Figure 1.8 Schematic representation of the "effective medium" replacing a disordered alloy for discussing its average properties.

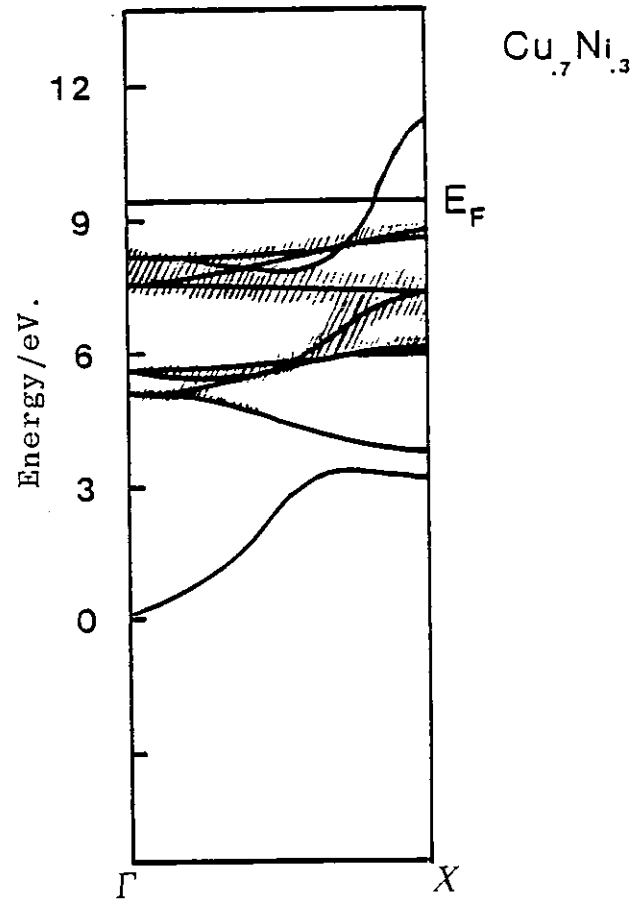


Figure 1.9 Complex energy bands for CuNi (After Bansil and Pessa[10]).

equivalent to equation 1.20, from which the electronic structure of the random alloy is calculated. This electronic structure is best discussed in terms of the configurationally averaged Bloch spectral function $A_B(\vec{k}, E)$ readily calculable within the KKR-CPA. For a pure metal, $A_B(\vec{k}, E)$ consists of a superposition of δ - functions, the position of which define the usual $E(\vec{k})$ relation of band theory. In an alloy, these δ - functions spread out into finite peaks. If one wants to keep the terminology of the band theory, and solves equation 1.22 for a fixed $\vec{k}$, the solutions obtained are complex numbers, the imaginary part representing the dissorder smearing of states in an alloy, that have a finite lifetime.

One can conclude therefore, that in a random substitutional alloy, the energy bands is still a meaningful concept. Figure 1.9 shows a complex energy band for a CuNi alloy[10].

These band structure calculations have given satisfactory agreement with angle-resolved-photoemission-spectroscopy (ARPES) experiments for both CuNi and AgPd alloys. The density of states in these alloys consists of two parts, each of which can be identified with one of the components.

In Cu rich CuNi alloys a Ni d impurity state is present. With increasing Ni concentration this feature becomes better defined and there is a progressive smearing of the Cu d states. In Ni rich CuNi alloys there is little

Cu related structure.

In AgPd there are separate Ag and Pd bands at each concentration. Pd features are somewhat broader in Pd Ag than in pure Pd; this effect is less pronounced in Ni from CuNi alloys.[11]

References (Chapter 1)

1. P.E.C. Franken and V. Ponec, J. Catal., 42 (1976) 398

2. B.R. Coles, J. Inst. Metals 84 (1955-56) 346

3. R. Hultgren, P. Desai, D. Hawkins, M. Gleiser, K. Kelley, D. Wagman, "Selected values of the Thermodynamic Properties of the Elements", American Society for Metals, Metals Park, Ohio (1973).

4. R.A. Swalin, "Thermodynamics of Solids", John Wiley & Sons, Inc. New York, London (1962)

5. D. Tomanek, V. Kumar, S. Holloway, K.H. Bennemann, Solid St. Comm. 41 (1982) 273.

6. R. Hultgren, P. Desai, D. Hawkins, M. Gleiser, K. Kelley, "Selected Values of the Thermodynamic Properties of Binary Alloys", American Society for Metals, Metal Park, Ohio (1973).

7. B.L. Averbach, in "Energetics in Metallurgical Phenomena", edited by W.M. Mueller (Gordon and Breach, N.Y. 1965) Vol. II.

8. J.M. Ziman, "Solid State Physics" (1971) Ed. H. Ehrenreich, F. Seitz and D. Turnbull (Academic Press).

9. V.L. Moruzzi, J.F. Janak and A.R. Williams, "Calculated Electronic Properties of Metals", (1978) Pergamon Press Inc.

10. A Bansil and M. Pessa - Nordic Conference on Surface Science (1982)

11. M. Pessa, H. Asonen, M. Lindroos, A.J. Pindor, B.L. Giorffy and W. Temmerman, J. Phys F: Metal Phys. 11 (1981) 233.

CHAPTER 2

THEORY OF SURFACE SEGREGATION

It is now well established that at equilibrium, the surface region of an alloy presents a composition different from that in the bulk. The extent of the "surface region" is not always well defined and in many respects depends on the experimental probe used to detect this phenomenon. When a more detailed description is required one often refers to the composition profile. Figure 2.1 shows schematically the surface enrichment of component A in a substitutional alloy AB.

The theoretical description of surface segregation aims to identify its causes and to quantify its extent. In what follows the main existing theoretical approaches are discussed.

2.1 Thermodynamic approach

The equilibrium thermodynamic approach to the description of surface segregation was given by J.W. Gibbs. His treatment compares an actual system, formed by two bulk phases α and β, separated by an interface region, with an hypothetical system in which there is a "dividing surface" separating both bulk phases, without any transitional region. The parameters of the two phases change discontinuosly at the dividing surface from the values characteristic of α to the values characteristic of β. See figure 2.2. For our

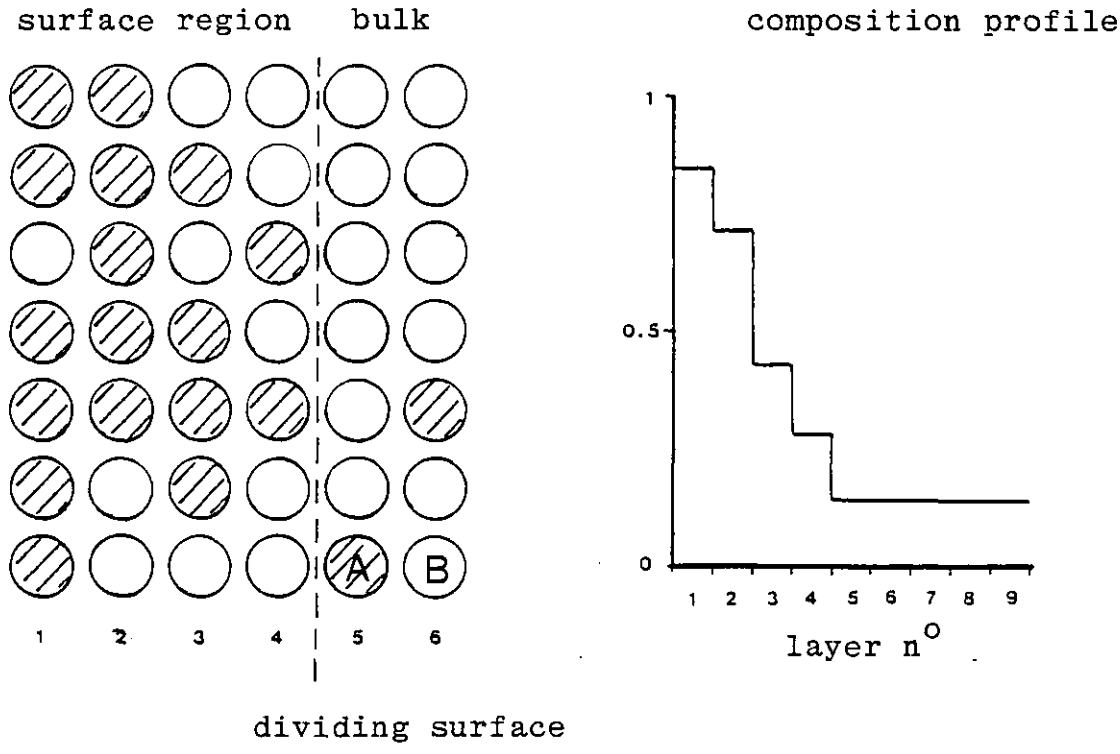


Figure 2.1 Schematic representation of surface enrichment in a substitutional alloy AB.

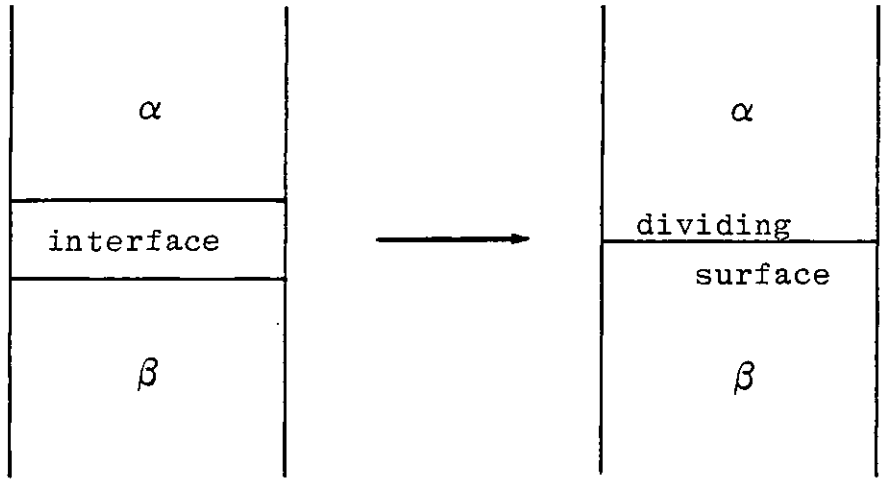


Figure 2.2 Gibbs' dividing surface.

purposes the phase α could correspond to the alloy and the phase β to the vapour (or vacuum) in contact with it.

Any macroscopic extensive property x^s, associated with an area A of the surface is defined with reference to a plane, the dividing surface, paralell to the real surface by

$$x^s = x^{tot} - x^\alpha - x^\beta \qquad 2.1$$

x^{tot} is the value of that property in the entire real system and x^α (x^β) is its value for the α (β) phase if it retained all its bulk properties up to the dividing surface. x^s is referred to as the surface excess of the considered property and corresponds to the amount by which that quantity in a real system exceeds the quantities in the uniform bulk phases of the hypothetical system.

The amount of any component N_i^s associated with an interface of area A is then given by

$$N_i^s = A\Gamma_i = N_i^{tot} - N_i^\alpha - N_i^\beta \qquad 2.2$$

Γ_i is the specific surface excess number of atoms of component i; it can be negative, zero or positive. The surface excess quantities depend on the location of the dividing surface. In a solution the most common convention is to fix it in such a position that the surface excess of the solvent is zero; see figure 2.1. The surface excess Γ_i

is simply the surface concentration in a real system if the segregation is restricted to the first layer.

At equilibrium the temperature T and the chemical potentials μ_i are uniform through the system and for a planar surface the pressure P is uniform too. Therefore, the increase in energy dE of the actual system in any reversible change is given by

$$dE^{tot} = TdS^{tot} - P^{\alpha}dV^{\alpha} - P^{\beta}dV^{\beta} + \gamma dA + \Sigma_i \mu_i dN_i^{tot} \qquad 2.3$$

where γ is the surface tension or surface energy of the interface. It may be defined as the reversible work of formation of a unit area of the interface at constant V,T and μ_i. The increase in energy of each phase of the hypothetical system is given by

$$dE^{\alpha} = TdS^{\alpha} - P^{\alpha}dV^{\alpha} + \Sigma_i \mu_i dN_i^{\alpha} \qquad 2.4$$

$$dE^{\beta} = TdS^{\beta} - P^{\beta}dV^{\beta} + \Sigma_i \mu_i dN_i^{\beta} \qquad 2.5$$

Subtracting 2.4 and 2.5 from 2.3 one gets

$$dE^{S} = TdS^{S} + \gamma dA + \Sigma \mu_i dN_i^{S} \qquad 2.6$$

Since 2.6 corresponds to an homogeneous equation of first degree, it may be integrated, using the Euler, theorem to

$$E^{S} = TS^{S} + \gamma A + \Sigma_i \mu_i N_i^{S} \qquad 2.7$$

Differentiating eq. 2.7 one gets

$$dE^S = TdS^S + S^S dT + \gamma dA + Ad\gamma + \sum_i \mu_i dN_i^S + \sum_i N_i^S d\mu_i \qquad 2.8$$

and comparing 2.6 and 2.8 one obtains

$$Ad\gamma = -S^S dT - \Sigma_i N_i^S d\mu_i \qquad 2.9$$

the so called Gibbs adsorption equation, that in the case of constant temperature gives the Gibbs adsorption isotherm

$$\Gamma_i = -(d\gamma/d\mu_i)_{T,\mu_j} \qquad j \neq i \qquad 2.10$$

This isotherm expresses the surface excess of one of the components in terms of the dependence of the surface tension on the chemical potential of that component.

Equation 2.10 predicts that the surface will be enriched in that component which lowers the surface tension.

So far the discussion has been based on general thermodynamics. If one wants to obtain numerical values for Γ_i in a particular system it is necessary to know the exact relation between γ and μ_i. Not much is known experimentally about such relations; some insight, however, can be gained in theoretical treatments of some simple systems.

Let us consider, for instance, an ideal substitutional binary alloy AB. In this case

$$\gamma = \gamma_i + \frac{RT}{A} \ln \left(\frac{X_i^s}{1-X_i^s} \right) \qquad 2.11$$

where γ_i is the surface energy of the pure component i; X_i^s, X_i^b are respectively the surface and bulk compositions of component i, and A is the molar surface area.

From equation 2.11 the following expression can be obtained

$$\frac{X_A^s}{(1-X_A^s)} = \frac{X_A^b}{(1-X_A^b)} e^{-(\gamma_A - \gamma_B) A/RT} \qquad 2.12$$

Equation 2.12 relates the surface composition X_A^s to the bulk composition X_A^b and predicts that at equilibrium the surface will be enriched in that component which has the smaller surface energy in its pure state.

For a regular substitutional solution, assuming that the enrichment occurs only on the first layer, equation 2.12 is replaced by [1]

$$\frac{X_A^s}{(1-X_A^s)} = \frac{X_A^b}{(1-X_A^b)} e^{-\Delta H_s/RT} \qquad 2.13$$

where the molar heat or enthalpy of segregation ΔH_s has been introduced. ΔH_s is the "driving force" for segregation and corresponds to the enthalpy change when an atom A in the bulk exchange positions with an atom B at the surface. According to this expression the surface composition of A will be larger than in the bulk if ΔH_s is negative. The

extent of enrichment also depends on the temperature, being less at high temperatures.

A number of theoretical and phenomenological models for estimating ΔH_s have been proposed in order to predict or quantify surface enrichment in binary alloys. A brief description of the most common ones is given next.

2.2 Strain effects.

The two types of atoms present in a binary alloy have, in general, different sizes. When the solute atom is incorporated into the solvent bulk matrix, a strain field is produced around it with its associated strain energy. Some authors[1,2] postulate that this strain energy is totally eliminated by exchanging the odd-sized bulk solute atom with a surface solvent atom.

The strain energy E_{el} can be calculated using linear elasticity theory in the limit of infinite dilution.

Two commonly used expressions for E_{el}[1,2] are

$$E_{el} = 24\pi\ B\ G\ r_1\ r_2\ (r_2 - r_1)^2 / (3Br_2 + 4Gr_1) \qquad 2.14$$

and

$$E_{el} = \frac{16}{3}\ \pi\ G\ r_1^3\ \left(\frac{r_2}{r_1} - 1\right)^2 \qquad 2.15$$

where B and G are the bulk and shear moduli of solute and solvent respectively and r_1, r_2 are the atomic radii for solvent and solute in their pure states respectively.

In this model the enthalpy of segregation is simply given by

$$\Delta H_s = -E_{el} \qquad 2.16$$

and since E_{el} is always positive ΔH_s will be always negative, what implies that solute segregation will always occur and that it will be so for both oversized and undersized solute atoms. It is now accepted, however, that oversized solute atoms cause a much larger strain that undersized atoms; for the latter the elastic energy driving force is too small to produce surface segregation.

Cu atoms have larger size than Ni atoms so we can expect on the basis of this strain effect that Cu solute atoms enrich the surface of CuNi alloys. An equivalent situation is expected for Ag solute atoms in AgPd alloys.

Using the values given in table 2.1 in equation 2.14 one obtains for Cu in Ni

$$E_{el} = 193 \text{ cal/mol}$$

and for Ag in Pd

$$E_{el} = 836 \text{ cal/mol.}$$

These values of E_{el} are too small to give an account of the

surface enrichment observed in CuNi and AgPd alloys. It has been suggested[3] that the strain effects are important for surface segregation in binary alloys only when

$$| 1 - r_1/r_2 | > 0.1 \qquad 2.17$$

Table 2.1

Atomic radii and Bulk and Shear moduli of Ni, Cu, Pd and Ag.[15]

	Atomic radius /Å	Bulk modulus /(N/m^2)	Shear modulus /(N/m^2)
Ni	1.38	1.86×10^{11}	0.750×10^{11}
Cu	1.41	1.308×10^{11}	0.451×10^{11}
Pd	1.52	1.807×10^{11}	0.511×10^{11}
Ag	1.59	1.006×10^{11}	0.286×10^{11}

2.3 Broken bond model

The broken bond model is based on the quasichemical approach to solutions summarized in chapter 1. This model has proven very useful in identifying the different factors affecting surface segregation. The basic idea is that the atoms at the surface have unsaturated or missing "bonds" as compared with the atoms in the bulk. Assuming that the atom A forms "weak" bonds and the atom B "strong" ones, the energy of the whole system can be minimized by increasing the number of "strong" bonds, what is achieved if atoms B

preferentially occupy bulk sites and atoms A enrich the surface.

Values of ΔH_s can easily be calculated in this model. In order to achieve this it is convenient to express the coordination number Z as

$$Z = Z_l + 2\ Z_v \qquad 2.18$$

where Z_l is the number of lateral bonds made by an atom within its plane an Z_v is the number of bonds made by an atom to each of the two adjacent planes of atoms. Atoms at the surface have the reduced coordination $Z_l + Z_v$.

The enthalpy of segregation can then be computed carrying out the exchange of A and B atoms according to the following stages:

a) Remove one atom B from the surface to infinity.

b) Remove one atom A from the bulk to infinity.

c) Replace atom B in the bulk.

d) Replace atom A at the surface.

The value of ΔH_s obtained is

$$\Delta H_s = \frac{1}{2} Z_v (H_{BB} - H_{AA}) + Z\omega \left[Z_l (X_A^b - X_A^s) + Z_v (X_A^b - \frac{1}{2}) \right] \qquad 2.19$$

where H_{AA}, H_{BB} are the bond enthalpies of the A-A and B-B bonds, ω is the regular solution parameter (eq. 1.10) and X_A^s, X_A^b are the surface and bulk atom fractions of component A.

Numerical evaluation of 2.19 can proceed in several ways. H_{AA} and H_{BB} can be evaluated from the enthalpies of sublimation according to equation 1.9. They can also be evaluated from the values of the surface energy according to[1]

$$\gamma_i = -\frac{1}{2} Z_v H_{ii} \qquad 2.20$$

ω can be obtained from the experimental values of the enthalpy of mixing (eq. 1.11) or from the activity coefficients of alloying (eq. 1.19).

Equation 2.19 then results in

$$\Delta H_s = (\gamma_A - \gamma_B) A + \omega \left[Z_1 (X_A^b - X_A^s) + Z_v (X_A^b - \tfrac{1}{2}) \right] \qquad 2.21a$$

or

$$\Delta H_s = \frac{Z_v}{Z} (\Delta H_v^A - \Delta H_v^B) + \omega \left[Z_1 (X_A^b - X_A^s) + Z_v (X_A^b - \tfrac{1}{2}) \right] \qquad 2.21b$$

the use of surface energy data instead of heats of sublimation is usually preferred. A number of important factors affecting surface segregation can be deduced from equations 2.21 and 2.13.

a) from the first term of 2.21 it is seen that the surface will tend to be enriched in component A if the surface energy of pure A is smaller than the surface energy of pure B; or if the heat of sublimation of pure A is smaller than the heat of sublimation of pure B.

b) from the same term in 2.21b it is seen that the extent

of enrichment is also determined by the ratio Z_v/Z. This factor characterizes the atomic roughness of the surface; when Z_v/Z is small, a smooth surface, the enrichment is minimized. For a f.c.c. crystal the values of Z_v/Z are 0.25, 0.33, and 0.42 for the (111), (100) and (110) faces respectively so the enrichment is expected to increase in this sequence. Inclusion of second nearest neighbours interactions through the use of effective coordination numbers reduces the difference between the various faces.

c) The effect of the first term in eq. 2.21 can be enhanced or reduced by the influence of the second term, depending on the sign of the regular solution parameter ω. For clustering alloys (Eg. CuNi), $\omega > 0$, enrichment is favoured and for ordering alloys (Eg. AgPd), $\omega < 0$ enrichment is diminished.

d) This second term also shows that the heat of segregation depends on the surface composition.

A number of improvements have been carried out on this model. Several authors [4,5,6] consider segregation to different atomic layers. By minimizing the total free energy they obtain a system of equations that can be solved numerically to give the composition profile. Usually about 5 or 6 layers are enough to describe this profile. The most interesting prediction is that for $\omega < 0$, the preference for A-B bonds is such that when the surface layer is enriched

in component A, the second layer is enriched in component B producing a sort of damped oscillation in the composition profile. For $\omega > 0$ a monotonic decreasing composition profile is predicted. It is important to note that these details depend on the value of the regular solution parameter ω, and for many alloys this value is not well defined.

Formulations for non regular solutions[5,7] have also been developed but, in general, it has been found that these models do not give results very different from the regular solutions models.

Another factor that has been taken into account is the relaxation of the surface bonds[4,5,7]. The bonds formed by atoms at the surface are expected to be perturbed and for them a relaxation parameter δ is defined by

$$H_{ij}^{r} = H_{ij} (1 + \delta) \qquad 2.22$$

where H_{ij}^{r} is the relaxed enthalpy of the i-j bond. δ is considered to be positive and its influence is to reduce the amount of surface enrichment. There is a discrepancy about the value of δ ; figures between $\sim$ 0.1 and 0.2 have been found to produce reasonable agreement with experiments[5,6], but these values are considered to be too high.

Equation 2.13 implicitly assumes that the only contribution to the entropy is configurational, but entropy

contributions due to electrons and thermal vibrations must also be included, so equation 2.13 is modified[8] to

$$\frac{X_A^s}{1-X_A^s} = \frac{X_A^b}{1-X_A^b} e^{-\Delta H_s/RT} e^{\Delta S/R} \qquad 2.23$$

An expression for ΔS is difficult to estimate but it is in general relatively small and it is usually used as an adjustable parameter.

2.4 Calculation of surface energies.

Experimental values of surface energies are much more accurate for liquid metals than for solid metals. In addition most of the existing experimental data has been obtained for liquids, while there are many solids for which there is no experimental information at all.

For liquids, the experimental value at temperature T, γ^l, is related to the value at T = 0, γ_o^l by

$$(\gamma V_m^{2/3})_T^l = (\gamma V_m^{2/3})_o^l - bT \qquad 2.24$$

where V_m is the molar volume and the constant b has the value

$$b = 1.17 \times 10^{-8} \text{ cal/K}$$

For solids, the equivalent expression is

$$(\gamma V_m^{2/3})_T^s = (\gamma V_m^{2/3})_o^s - bT \qquad 2.25$$

with the same value of b .

By comparing $(\gamma V_m^{2/3})_o^s$ and $(V_m^{2/3})_o^l$ for those metals for which experimental data is available, it has been found[9] that these values are related by

$$(\gamma V_m^{2/3})_o^s = 1.13\ (\gamma V_m^{2/3})_o^l \qquad 2.26$$

so in order to obtain values of surface energy in solids from the experimental values in liquids, it is recommended that the expression below should be used

$$(\gamma V_m^{2/3})_T^s = 1.13\ (\gamma V_m^{2/3})_o^l - bT \qquad 2.27$$

The molar volume V_m can be obtained from the density and the atomic weight M according to

$$V_m = M/\rho \qquad 2.28$$

The molar area A is related to the molar volume according to

$$A = fN_o^{1/3}\ V_m \qquad 2.29$$

where f is a structure factor; its value for melts of f.c.c. solids[10] is 1.09. The molar surface area can also be calculated directly from the structure of the particular face under study.

Values of γ_o^s and the temperature derivative $d\gamma/dT$ for Ni, Cu, Pd and Ag are given in table 2.2.

Table 2.2 .

Values of the surface energy at zero temperature γ_o^s and the temperature derivative d γ/dT for Ni, Cu, Pd and Ag.

	γ_o^s /(cal/m^2)	dγ/dT /(cal/m^2 K)
Ni	0.586	-4.8×10^{-5}
Cu	0.442	-4.5×10^{-5}
Pd	0.502	-3.8×10^{-5}
Ag	0.299	-3.6×10^{-5}

2.5 Miedema's semiempirical scheme

A.R. Miedema and coworkers [11] have developed a phenomenological model for calculating the heats of solution ΔH_{sol} of binary alloys. They use the "macroscopic atom model," based on the assumption that atoms can be treated as macroscopic pieces of metal and the alloy is formed by bringing together Wigner-Seitz (WS) atomic cells from the pure metals.

The change in boundary conditions when transfering atoms from the pure metals A and B to the alloy AB produces two different energy effects:

a) The first is that charge flows across the interface between the atoms in order to equilibrate the electronic chemical potentials. This effect is determined by the difference in the chemical potentials for electrons, $\Delta\phi$ leading to an attractive

contribution to ΔH_{sol}.

b) The second effect is due to a discontinuity in the electron density n_{WS} across the interface of the WS cells. Removing this discontinuity leads to a repulsive contribution to ΔH_{sol}.

The enthalpy of solution (per mol of solute transition metal A in a transition metal B is given by

$$\Delta H_{sol}{}^{A \text{ in } B} = \frac{2PV_A^{2/3}}{(n_{WS}{}^{A})^{-1/3} + (n_{WS}{}^{B})^{-1/3}} \left[-(\Delta\phi^*)^2 + (Q/P)(\Delta n_{WS}{}^{1/3})^2 \right] \qquad 2.30$$

where P and Q are constants and the experimental values of Φ have been adjusted to the new values ϕ^* in order to predict correctly the sign of ΔH_{sol} in a great number of alloys. This model has been very succesful in accounting for the heats of solution of transition and noble metal alloys.

Expressing ϕ^* in volts, n_{WS} in the arbitrary units of reference 11, V_A in cm^3 and enthalpies in Kj/mole, the constant P and Q are given by

$$P = 14.1 \qquad\qquad Q/P = 9.4$$

In reference 11 are tabulated the necessary values for evaluating ΔH_{sol} for a number of metals. The values corresponding to Ni, Cu, Pd and Ag are quoted in table 2.3.

Table 2.3

Model parameters for Ni, Cu, Pd, and Ag.

	ϕ^*/V	$n_{WS}^{1/3}$	$V^{2/3}/cm^2$
Ni	5.20	1.75	3.5
Cu	4.55	1.47	3.7
Pd	5.45	1.67	4.3
Ag	4.45	1.39	4.7

For dilute alloys, the enthalpy of segregation of the solute A to an average surface of the alloy AB is given[12] by

$$\Delta H_s = \frac{1}{3}\left[g(\gamma_A - \gamma_B)V_A^{2/3} - f\,\Delta H_{sol}^{A \text{ in } B} \right] \qquad 2.31$$

Here, g is a constant equal to 4×10^8, f is a surface relaxation factor that has been given the value 0.71 and V_A is the molar volume of the solute.

The terms of equation 2.31 parallel those in equation 2.21a. One important difference is that in a dilute alloy the average surface area that appears in 2.21a is basically determined by the solvent but in 2.31 only the surface area of the solute is present, taking into account in this way size effects in surface segregation. No regular solution parameter appears in 2.31 but, being dilute, the solutions can be considered as regular.

2.6 Chemisorption induced surface segregation

So far, the models that have been presented apply to segregation at clean surfaces but one may expect important differences in the alloy surface composition when a chemisorbed species is present. Chemisorption can constitute a driving force to enrich the surface with the alloy component forming the strongest adsorption bond. Consider, for instance an alloy AB that under clean conditions shows A surface enrichment. If a species C chemisorbs on the alloy surface forming strong bonds with component B and weak bonds with component A, then the equilibrium surface somposition could show enrichment in component B.

Denoting by E_{CA} and E_{CB} the chemisorption energies (negative values) of the adsorbate C on A and B respectively, and assuming that these energies are independent of the alloy composition and coverage θ, the effect of chemisorption induced surface segregation can be easily included[13] in the models considered substituting ΔH_s in equation 2.13 by

$$\Delta H_s^{chem} = \Delta H_s + (E_{CA} - E_{CB})\,\theta \qquad 2.32$$

It is important to note that this equation refers to the equilibrium state, that will be achieved after a given time depending on the temperature and the segregation kinetics of the alloy. In many experimental situations

the temperatures used in order to observe segregation in a reasonable time can be too high to have a chemisorbed species present.

2.7 Model of Mezey and Giber

A more formal treatment of the surface segregation problem has been recently published by L.Z. Mezey and J. Giber[14]. They give a thermodynamical description valid for a system with any number of components. Here, their treatment is resumed for the case of a binary alloy.

The system is characterized by a bulk phase b and a surface region formed by m homogeneous surface layers k = 1,2.....m. The mole number of each component n_A^c, n_B^c are assumed to be constant,

$$\begin{aligned} n_A^c &= n_A^b + \sum_{k=1}^{m} n_A^k \\ n_B^c &= n_B^b + \sum_{k=1}^{m} n_B^k \end{aligned} \qquad 2.33$$

and on each layer the n_A^k, n_B^k mole numbers are subjected to the constraint

$$\phi^k = \phi_A^k n_A^k + \phi_B^k n_B^k = \phi_o \text{ (constant)} \qquad 2.34$$

where ϕ_i^k is the partial molar surface area of component i in layer k.

The free energy of the system is given by

$$g^c = \left[\mu_A^b n_A^b + \sum_{k=1}^{m} \mu_A^k n_A^k\right] + \left[\mu_B^b n_B^b + \sum_{k=1}^{m} \mu_B^b n_B^k\right] \qquad 2.35$$

where μ_i is the chemical potential of component i.

g^c can be expressed as

$$g^c = (\mu_A{}^b n_A{}^b + \mu_B{}^b n_B{}^c) + \Delta g^c \qquad 2.36$$

with

$$\Delta g^c = \sum_{k=1}^{m} (\mu_A{}^k - \mu_A{}^b) n_A{}^k + \sum_{k=1}^{m} (\mu_B{}^k - \mu_B{}^b) n_B{}^k \equiv \gamma \phi_o \qquad 2.37$$

Δg^c corresponds to the excess free energy in Gibbs treatment and γ is defined by 2.37 as the "generalized free energy" of the system.

The constraints 2.34 are included through the Lagrange multipliers and the stationary values of g^c given as

$$\begin{aligned} \bar{\mu}_A{}^k - \mu_A{}^b + \lambda^k \bar{\phi}_A{}^k &= 0 \\ \bar{\mu}_B{}^k - \mu_B{}^b + \lambda^k \bar{\phi}_B{}^k &= 0 \end{aligned} \qquad 2.38$$

The equilibrium value of the generalized surface free energy; $\bar{\gamma}$ is found to consist of layer contributions, each one equal to $-\lambda^k$

$$\bar{\gamma} = \sum_{k=1}^{m} \bar{\gamma}^k = \sum_{k=1}^{m} (-\lambda^k) \qquad 2.39$$

and the equibibrium composition of the different layers is given by

$$\bar{X}_i{}^k = X_i{}^b \, e^{(\bar{\gamma}^k \phi_i{}^k)/RT} \, e^{(\mu_i{}^{e,b} - \bar{\mu}_i{}^{e,k})/RT} \qquad (i = A,B) \qquad 2.40$$

where X_i is the mole fration of i and $\mu_i{}^e$ is the excess

chemical potential defined respect to the bulk phase of pure i.

The functions $\mu_i^{e,k}$ are given by

$$\mu_i^{e,1} = \gamma_i^{o} \phi_i^{o} + (1-2\alpha)\mu^{e,b}(X^k) + \alpha\mu_i^{e,b}(X^{k+1})$$

$$\mu_i^{k} = \alpha\mu_i^{e,b}(X^{k-1}) + (1-2\alpha)\mu^{e,b}(X^{k+1}) \qquad (i=A,B) \qquad 2.41$$

Here, γ_i^{o} is the surface free energy of the component i; the value of α is obtained from $\alpha = (\alpha_A^{o} + \alpha_B^{o})/2$ where

$$\alpha_i^{o} = \gamma_i^{o}\ \phi_i^{o} / G_i^{o} \qquad (i = A,B) \qquad 2.42$$

and G_i^{o} is the free energy of sublimation minus the isothermal work of expansion to the volume of a perfect gas.

Mezey and Giber[16] have calculated the equilibrium composition of the first seven layers of an "average" low index face of $Ag_{0.01}\ Pd_{0.99}$ at T = 773K . Experimental values for single crystal surfaces of this alloy at the same temperature are presented in chapter 7 of this thesis.

The calculated Ag composition is shown below

layer N^{o}	1	2	3	4	5-7
X_{Ag}	0.6893	0.0081	0.01	0.10101	0.01

A strong Ag enrichment is predicted in the first layer and some Pd enrichment in the second. This

oscillating behaviour in the composition profile appears because of the ordering tendency of AgPd alloys. Bulk composition is regained after the fourth layer. The accuracy of the values given is, however, too high to be compared with realistic experimental data and rounding these values off to two decimal places gives $X_{Ag} = 0.69$ in the first layer and bulk composition in the rest.

Table 2.4 compares this value with the values obtained using the various monolayer models described before.

All these models predict Ag surface enrichment. Miedema's model gives the largest value and the strain effects model the smallest one. As mentioned earlier the effects of size difference between Ag and Pd are small and can be neglected in comparison with other effects.

The rigorous method of Mezey and Giber predicts a surface composition very similar to the one predicted by the simple ideal solution model, implying that the difference of surface energies (or heats of sublimation) of the pure components is the main factor determining surface segregation in this alloy. This factor is slightly countered by the real mixture effects in the bulk and at the surface which ammount to $\sim$ 11% of the main factor.

The regular solution model based on heat of sublimation data predicts a marked difference in composition in the three low index faces. This difference is basically determined by

Table 2.4

Top layer composition of a $Ag_{0.01}$ $Pd_{0.99}$ alloy at T = 773K predicted by different models.

Model	face	X_{Ag}	ΔH_s/(cal/mol)
1 Mezey and Giber (eq.2,40)	average	0.69	-
2 Strain effects (eq. 2.14)	average	0.02	-836
3 Miedema (eq. 2.31)	average	0.93	-11100
4 Ideal solution (eq. 2.12)	average	0.71	-8405
5 Regular solution (eq. 2.21a)	(100)	0.56	-7407
6 Regular solution (eq. 2.21b)	(100)	0.41	-6479
7 "	(111)	0.20	-4880
8 "	(110)	0.69	-8255

Parameters used in the calculations:

T = 773K

ω_{AgPd} = -241 cal/mol

γ_{Pd} = 0.472 cal/m^2

γ_{Ag} = 0.271 cal/m^2

ΔH_v(Pd) = 86889 cal/mol

ΔH_v(Ag) = 64879 cal/mol

A_{Pd} = 39470 m^2/mol

A_{Ag} = 44160 m^2/mol

the ratio z_v/z in equation 2.21b and might be exaggerated by the assumption of only nearest neighbours interaction.

Another model of surface segregation, based in the electronic properties of the alloy is presented in the next chapter.

References (Chapter 2)

1. P. Wynblatt and R.C. Ku, Surf. Sci. 65 (1977) 511.

2. F.F. Abraham and C.R. Brundle, J. Vac. Sci. Technol. 18 (1981) 506.

3. D.F. Ollis, J. Catal. 59 (1979) 430.

4. F.L. Williams and D. Nason, Surf. Sci. 45 (1974) 377.

5. V.Kumar, Phys. Rev. B 23 (1981) 3756.

6. A. Crucq, L. Degols, G. Lienard and A. Frenet Surf. Sci. 80 (1979) 78.

7. H.H. Brongersma and M.J.Spaarnay, Surf. Sci. 71 (1978) 657.

8. V. Kumar, Surf. Sci. 84 (1979) L231

9. A.R. Miedema, Z. Metallk, 69 (1978) 287.

10. S.H. Overbury P.A. Bertrand and G.A. Somorjai. Chem. Rev. 75 (1975) 547.

11. A.R. Miedema and P.F. Chatel, "A semiempirical approach to the heat of formation problem". Simposium: "Theory of alloy phase formation". American Metallurgical Society Meeting 1979 (New Orleans).

12. A.R. Miedema, Z. Metallk 69 (1978) 455.

13. D. Tomanek, S. Mukherjee, V. Kumar and K.H. Bennemann, Surf. Sci. 114 (1982) 11.

14. L.Z. Mezey and J. Giber, Surf. Sci. 117 (1982) 220.

15. K.A. Gschneidner, in: Solid State Physics, vol. 16, Eds. F. Seitz and D. Turnbull (Academic Press, N.Y. 1964) p. 275.

16. L.Z. Mezey and J. Giber (private communication).

CHAPTER 3

ELECTRONIC THEORY OF SURFACE SEGREGATION

The surface segregation models considered in chapter 2 rely on the supply of experimental data about certain macroscopic quantities like surface energies, sublimation and mixing enthalpies and elastic moduli . In order to understand the phenomenon of surface segregation on a more fundamental level, a first principles approach is necessary. In this chapter a one-electron model is used to study surface segregation in the AgPd system.

3.1 One-electron model of surface segregation

The cohesive energy of transition metals changes in a very simple fashion across the transition series, as shown in figure 3.1.

The metallic cohesion of these metals is essentially due to the broadening of d levels into an unfilled d band.[1] Band structure calculations have given a good account of the regularity displayed in this figure.

The d electrons are also thought to play an important role in the mechanisms responsible for the surface segregation in transition and noble metal alloys. This electronic driving force for segregation of component A to the surface of a binary alloy AB is given by the change ΔE in the

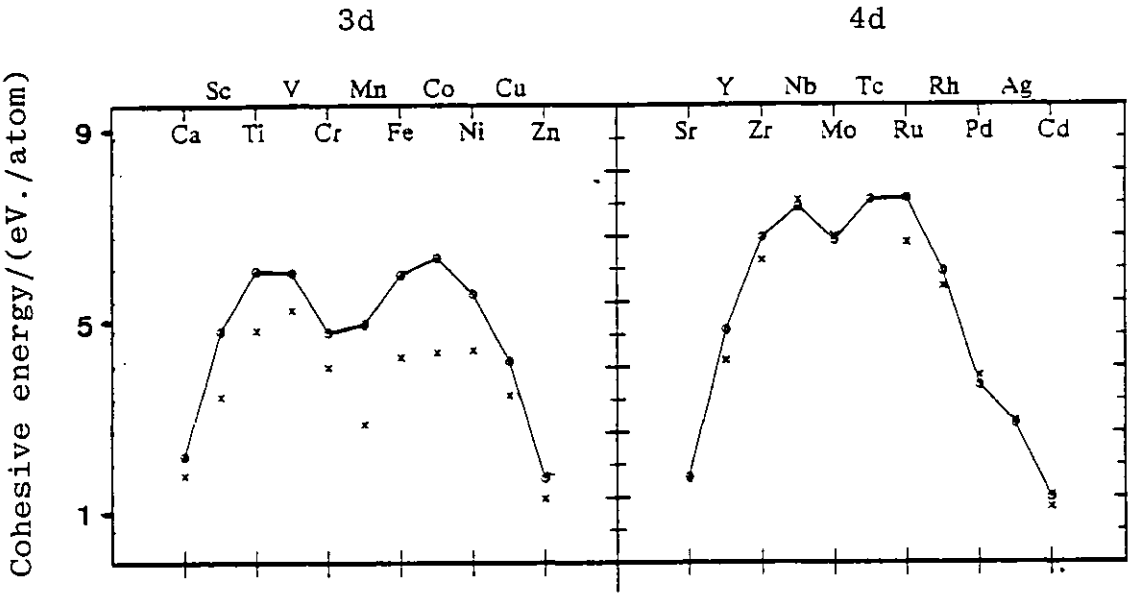


Figure 3.1. Cohesive energy for metals along the 3d and 4d transition series. (After Moruzzi et.al.[6]).

internal energy when an atom A located in the bulk exchanges position with an atom B at the surface. ΔE can be written[2] as the difference of the surface energies per atom of A and B

$$\Delta E_s = (E_A^s + E_B^b) - (E_A^b + E_B^s)$$

$$= (E_A^s - E_A^b) - (E_B^s - E_B^b) \qquad 3.1$$

$$= \sigma_A - \sigma_B$$

where the superscripts s,b denote surface and bulk respectively.

Neglecting charge transfer and taking into account only the d contribution to the energy at O K, each term in equation 3.1 is given in the Hartree approximation as

$$\sigma_x = \int_0^{E_F} n_x^s(E)EdE - \int_0^{E_F} n_x^b(E)EdE \qquad 3.2$$

where $n_i^b(E)$ and $n_i^s(E)$ are the partial densities of d states of an atom i in the bulk and at the surface respectively.

A negative value of ΔE_s in equation 3.1 corresponds to the segregation of A to the surface.

Ph. Lambin and J.P. Gaspard have calculated ΔE_s in CuNi using the electronic bulk and surface densities of states, computed in the tight-binding approximation using

the moments method[2]. They consider cluster sizes of about 1000 atoms arranged in about 50-100 inequivalent configurations.

The calculation procedure adopted in this work follows a model developed by J.P. Muscat[3]. In this model, information about the possibility of segregation towards the surface in an alloy AB is obtained in the limit of a single impurity interacting with a cluster of host atoms. A multiple scattering formalism is used, in which a cluster of "muffin-tin" potentials are embedded at the surface or in the bulk of a free electron gas, and the value ΔE_s arising from the exchange of positions of a bulk impurity atom with a surface host atom is calculated.

3.2 Formalism

This approach is based on the KKR formalism, and depends on considering the potential within the muffin-tin approximation, i.e.: an array of non-overlapping, spherically symmetric potential wells separated by a region of constant potential. The radius of the well is referred to as the muffin-tin radius r_{MT}.

In the embedded cluster model a continuum of electrons represents the conduction band; a cluster of MTs is then included and the scattering properties of this system considered. One calculates the change in density of states of the continuum of electrons due to the presence of a

single MT (the impurity atom) that is in interaction with the others.

In order to introduce some concepts, it is useful to treat first the case of scattering by a single MT.

Atomic energies are used: $e = \hbar = m = 1$. The unit of energy is the Hartree, given by

$$1 \text{ Hartree} = e^2/a_o$$

where a_o, the Bohr radius, is the unit of length.

In this system of units the kinetic energy of an electron is given by

$$H_o = -\frac{\nabla^2}{2}$$

the bottom of the conduction band is taken as the origin of the energy scale, hence the energy band is at positive energies.

3.2.1 Scattering from a single MT centre.

Consider the scattering of an electron by a single MT potential located at the origin r = O. Since the potential is spherically symmetric, angular momentum is conserved during the scattering and the solution to the Schrodinger equation

$$\left[-\frac{\nabla^2}{2} + v(r) \right] \psi(\vec{r}) = E\,\psi(\vec{r}) \qquad 3.3$$

can be written in the form

$$\Psi(r,E) = \sum_{L} a_L(E)\, R_l(r,E)\, Y_L(\hat{r}) \qquad 3.4$$

where the quantum numbers l,m are denoted by the compound symbol L = (l,m)

$$\sum_{L} = \sum_{l=0}^{\infty} \sum_{n=-l}^{+l}$$

$Y_L(\hat{r})$ is the spherical harmonic

$$Y_L(\hat{r}) = Y_l^m(\theta,\Phi)$$

and R_l is the solution of the radial Schrodinger equation

$$\left[\frac{1}{r^2}\frac{d}{dr^2}r + \frac{l(l+1)}{r^2} + v(r)\right] R_l(r,E) = E\, R_l(r,E) \qquad 3.5$$

Outside the MT sphere, for $r > r_{MT}$ $(v(r) = 0)$ equation 3.5 becomes the radial Schrodinger equation for free electrons, whose two linearly independent solutions are the spherical Bessel and Neumann functions $j_l(\sqrt{2E}\, r)$ and $n_l(\sqrt{2E}\, r)$ respectively.

Without loss of generality this linear combination can be written as

$$R_l(r,E) = \cos\delta_l\, j_l(\sqrt{2E}\, r) - \sin\delta_l\, n_l(\sqrt{2E}\, r) \qquad 3.6$$

where the constants δ_l are called the phase shifts. Note

that the asymptotic limit of R_l is given by

$$\lim_{r\to\infty} R_l(r,E) = \frac{1}{\sqrt{2E}\ r} \sin\left[\sqrt{2E}\ r - l\pi/2 + \delta_l(E)\right] \qquad 3.7$$

Had there been no MT, the solution would have been $j_l\ (\sqrt{2E}\ r)$ which is regular at the origin, and the asymptotic behaviour would have been

$$\lim_{r\to\infty} j\ (\sqrt{2E}\ r) = \frac{1}{\sqrt{2E}\ r} \sin\left[\sqrt{2E}\ r - l\pi/2\right] \qquad 3.8$$

so the introduction of the MT simply creates a phase shift $\delta_l(E)$ in the asymptotic limit $r \to \infty$. This is why $\delta_l\ (E)$ is referred to as the phase shift. The phase shift depends not only on the scattering potential, but also on the energy of the incident electron. It must be noted that equation 3.6 defines the phase shift to within an integral multiple of π.

The effect of the potential within the MT on the wavefunction outside this region is completely determined by the phase shifts. If the solution to the radial Schrodinger equation is known inside the MT sphere, then the phase shifts can be evaluated from the condition of continuity of the logarithmic derivative of R_l at the MT boundary.

For $r \leq r_{MT}$, equation 3.5 can be solved numerically, and its logarithmic derivative at $r = r_{MT}$

$$\gamma_l(E) \equiv R_l^{-1}\ (dR_l/dr)\Big|_{r = r_{MT}} \qquad 3.9$$

must be equal to the logarithmic derivative of the radial wavefunction outside the MT sphere.

In this way one obtains the relation

$$\delta_l(E) = \cot^{-1}\left[\frac{n_l(\sqrt{2E}\, r_{MT})\, \gamma_l - \sqrt{2E}\, n_l'(\sqrt{2E}\, r_{MT})}{j_l(\sqrt{2E}\, r_{MT})\, \gamma_l - \sqrt{2E}\, j_l'(\sqrt{2E}\, r_{MT})}\right] \qquad 3.10$$

from which one can evaluate the phase shifts once the $\gamma_l\ (r_{MT})$ are known.

The phase shift is related to the scattering amplitude $f(k^2, \theta)$ in scattering theory,

$$\psi_k(\vec{r}) = e^{i\vec{k},r} + f^2(k^2,\phi)\, e^{ikr}/(kr) \qquad 3.11$$

according to

$$f_l(E) = \sin \delta_l(E)\, e^{i\delta_l(E)} \qquad 3.12$$

and to the total scattering cross section according to

$$\sigma = (4\pi/E) \sum_l (2l+1) \sin^2 \delta_l(E) \qquad 3.13$$

Thus a phase shift near $\pi/2$ means very strong scattering, while δ_l near 0 or π means weak scattering.

A phase shift rising from 0 to π within a small energy interval about E_r where it is equal to $\pi/2$ is called a scattering resonance.

The MT potential of all transition metals produce a l = 2 resonance. Except for f-band metals, δ_l (E) is practically zero for l>2 in the energy range of the conduction band.

The phase shifts for the MT potential of Cu is shown in figure 3.2.

The difference between the density of states of the system with the scatterer, n(E) and without the scatterer $n_o(E)$ is given by the Friedel sum

$$\Delta n(E) = n(E) - n_o(E) = \left(\frac{2}{\pi}\right) \sum_l (2l + 1) \frac{d\delta_l}{dE} \qquad 3.14$$

This expression shows that a phase shift varying rapidly with energy gives rise to a large density of states near the resonance energy.

Figure 3.3 displays the function Δn(E) which corresponds to the l = 2 phase shift of figure 3.2.

3.2.2 Multiple scattering.

Let us consider now the scattering of an electron by a cluster of MT scatterers. In this case the Schrodinger equation is solved within the framework of the multiple scattering theory. The solution to this multiple scattering centre problem can be constructed from the solution to the individual scattering centre problem.

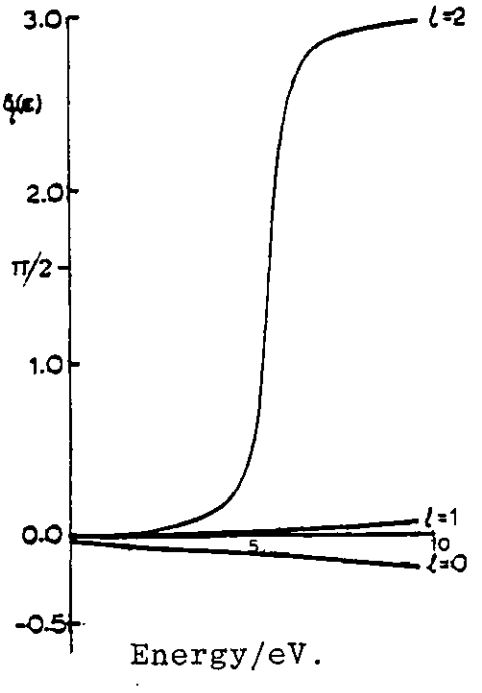


Figure 3.2 Phase shifts $\delta_\ell(E)$ for the muffin-tin potential of Cu.

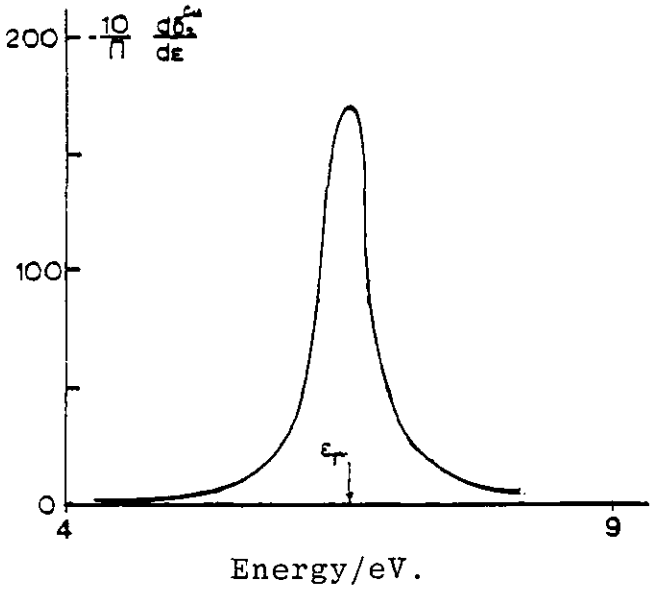


Figure 3.3. Change in the density of states caused by the ℓ = 2 resonance of figure 3.2.

The Lloyd formula expresses the change in density of states in the free electron gas caused by the inclussion of the cluster of MT scatterers as a derivative with respect to energy of a phase shift[4]

$$\Delta n(E) = (2/\pi)\ (d\ \delta_T\ (E)/dE) \qquad 3.15$$

where δ_T is the phase shift coming from all the MTs in the cluster.

δ_T can be expressed as the argument of the determinant of a matrix M

$$\delta_T\ (E) = Im\ \{\ ln\ [\ det\ M(E)]\ \} \qquad 3.16$$

The matrix elements of M(E) are given by

$$M_{ilm,jl'm'} = (i e^{i\delta_l}/\sin\ \delta_l)\ \delta_{ij}\ \delta_{ll'}\ \delta_{mm'} + + 4\pi \sum_{l_1, m_1} i^{l-l'-l_1} I(L_1,L,L')h_{l_1}(kR_{ij})\ Y^*_{lm}\ (R_{ij}) \qquad 3.17$$

In this expression, the subscripts i and j refer to the MT sites, located at $\vec{R}_i$ and $\vec{R}_j$, l and m are angular momentum quantum numbers, $\vec{R}_{ij} = \vec{R}_j - \vec{R}_i$, δ_l is a single scatterer phase shift, given by equation 3.10; h_l is the spherical Hankel function ($h_l = j_l + i\ n_l$) and I (L_1, L, L') is the Gaunt number, which is an integral

$$(L,L',L'') = \int Y^*_L\ (\Omega)Y_{L'}(\Omega)Y_{L''}(\Omega)\ d\Omega \qquad 3.18$$

of triple products of spherical harmonics.

Let us now assume that the cluster consists of a central MT or impurity atom surrounded by other MTs. Equation 3.16 enables one to calculate the phase shift due to the whole cluster; what is required, however, in order to obtain the partial density of states, is the phase shift coming from a single MT (the impurity) when it is interacting with the others. In order to obtain this it is necessary to substract from δ_T the phase shifts which originate in all the MTs except the central one.

Labelling the central MT as "o", the total matrix M can be expressed as

$$M = \begin{bmatrix} M_{oo} & M_{os} \\ M_{so} & M_{ss} \end{bmatrix} \qquad 3.19$$

where M_{oo} is the matrix corresponding to the isolated MT impurity, M_{os} corresponds to the coupling between "o" and the rest of the MTs, M_{so} is its reciprocal and M_{ss} corresponds to all the MTs except the central one.

The determinant of M is then given by

$$\det M = \det M_{ss} \times \det (M_{oo} - M_{os} M_{ss}^{-1} M_{so}) \qquad 3.20$$

and

$$\log \det M = \log \det M_{ss} + \log \det (M_{oo} - M_{os} M_{ss}^{-1} M_{so}) \qquad 3.21$$

Comparing equations 3.21 and 3.16, it can be seen that in this way one has separated that part of the total phase shift which originates from all the MTs surrounding the central one. Thus, the perturbed phase shift $\eta(E)$ in which one is interested may be simply written as

$$\eta = \frac{2}{\pi} \log \det \left(M_{oo} - M_{os}\, M_{ss}^{-1}\, M_{so}\right) \qquad 3.22$$

The matrix elements of M_{oo}, M_{os}, M_{so} and M_{ss} are given be equation 3.17.

The values of η are calculated numerically using a programme developed by J.P. Muscat[5].

In the following section is is explained how this calculation is carried out.

3.2.3 Calculation of η (E).

At this point it is necessary to specify the system further. The impurity atom will be located either in a bulk site or at a surface site.

In the case of a bulk site, a cluster of host MTs is located on concentric shells around the central impurity MT. For interaction only with nearest neighbours one single shell is considered. See figure 3.4.

The distance between the impurity atom and the host

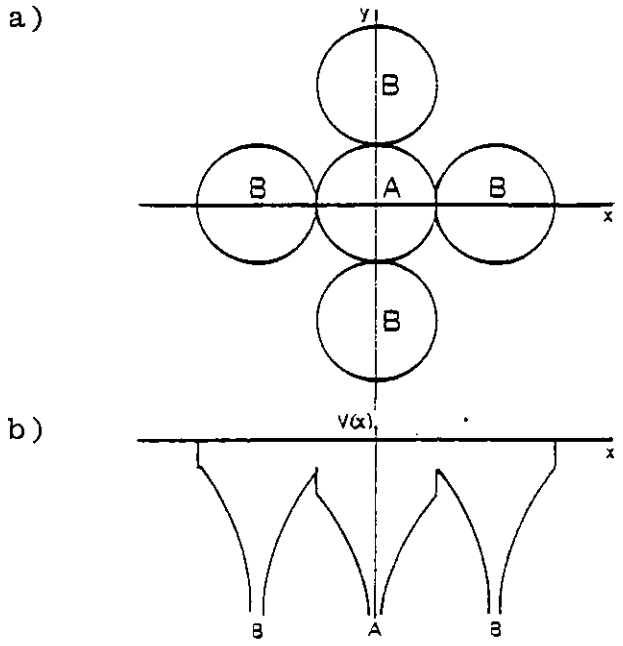


Figure 3.4. a) Impurity MT in bulk site

b) Potential along x direction in (a).

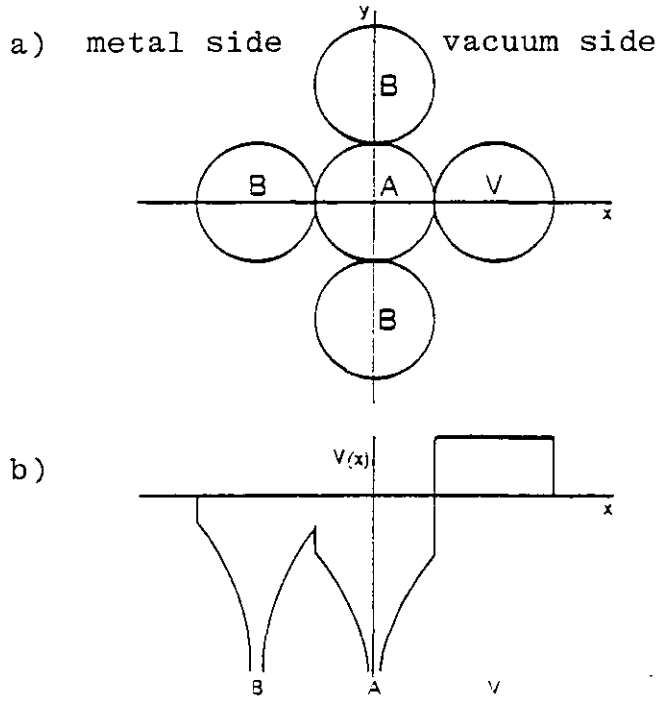


Figure 3.5. a) Impurity MT at surface site.

b) Potential along x direction in (a).

nearest neighbour atom is taken as half the sum of the nearest neighbours distance for the alloy constituents A and B in the corresponding pure metals. The potentials inside both the host and the impurity MTs are taken from published self-consistent band structure calculations[6].

In the case of the impurity located at a surface site, the cluster is again constructed in terms of shells of MTs around the surface impurity. These shells are now made up of two kinds of MTs: On the metal side of the surface the MTs enclose a potential characteristic of the host atoms, and on the vacuum side of the surface, the MTs enclose a repulsive potential barrier, equal to the sum of the host metal work function and its Fermi energy. This MT is called a vacuum MT,V. See figure 3.5.

In either case the whole cluster is embedded in a free electron gas.

The necessary data to determine the matrix elements of equation 3.17 consist of (i) the phase shifts δ_l and (ii) the position of the MTs.

(i) The phase shifts δ_l

In order to determine the single scatterer phase shifts δ_l, the logarithmic derivatives and the MT radii are needed. For the metal MTs only the case l = 2 is considered. For the vacuum MTs, l values from 0 to l_{max} are included;

in the present case $l_{max} = 2$ was chosen. The values of γ_2 depend on the potential selected. The MT radii and the potentials for the impurity Ag and the host Pd were obtained from reference 6. The impurity potential is shifted in order to align its Fermi energy with that of the host atom. Once the phase shifts δ_l are obtained the diagonal elements of M (eq. 3.17) can be worked out.

(ii) The position of the MTs.

The position of the MTs is determined by the crystalline structure of the alloy. Their coordinates are expressed in terms of the lattice parameter a, taken as

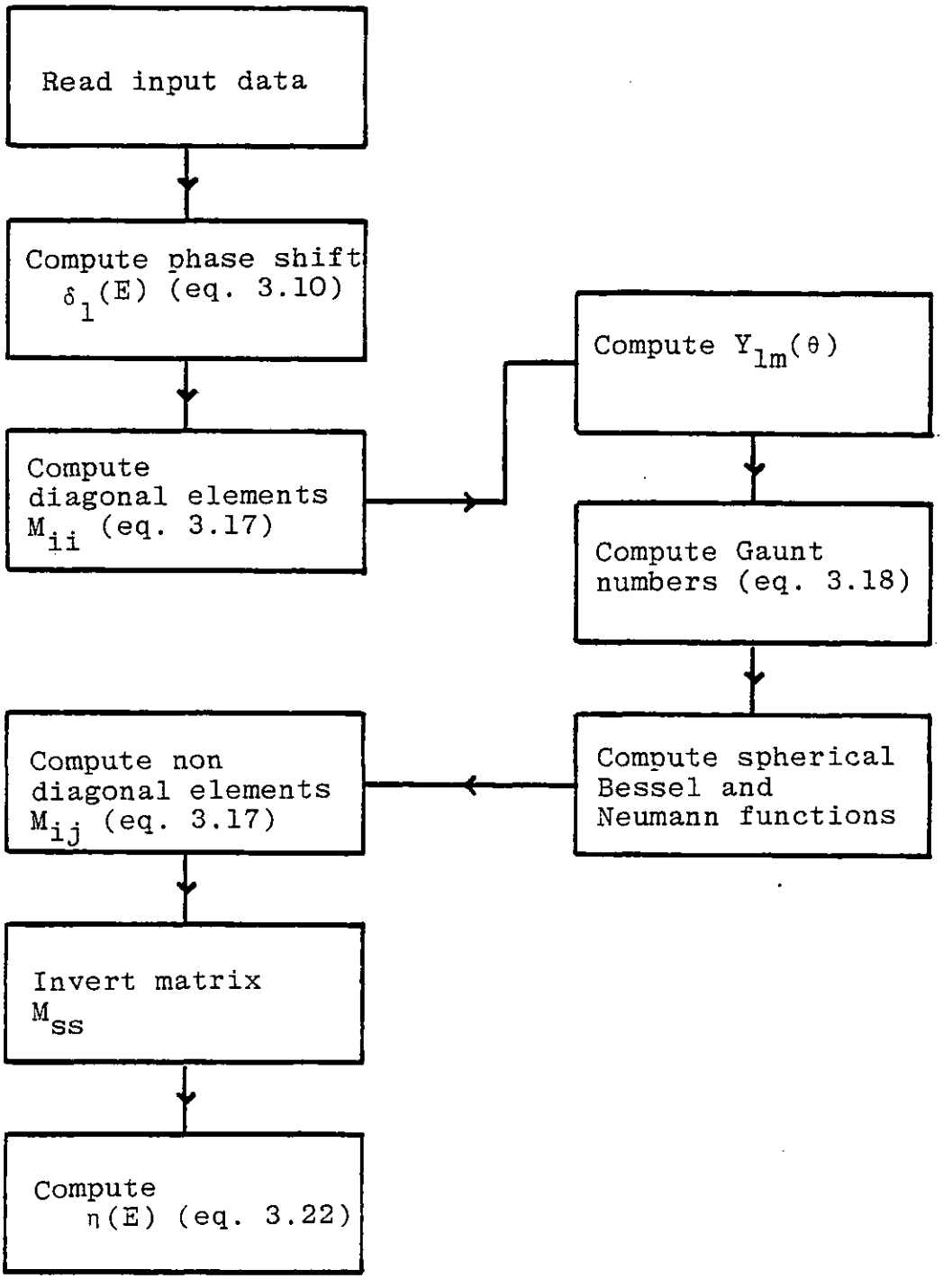
$$a = \tfrac{1}{2} (a_{host} + a_{impurity}) \qquad 3.23$$

Given the MT coordinates the quantities $\vec{R}_{ij}$ are determined along with the non diagonal matrix elements of M. The programme gives also the possibility of relaxing the positions of the vacuum MTs.

The calculations performed by the programme are reduced by taking into account the symmetry of the cluster of MTs, so the order of the axis of symmetry of the central site is also needed.

The programme calculates the phase shifts as a function of energy so the energy values at which η is calculated must be specified.

The following diagram summarizes the different stages in which the programme computes $\eta(E)$.



3.3 Results of the calculations for AgPd

This electronic model of surface segregation has been applied to the case of a Ag impurity in a Pd host, using clusters of 13 MTs. Results corresponding to the segregation of Ag to the (100) face of a AgPd alloy are presented next.

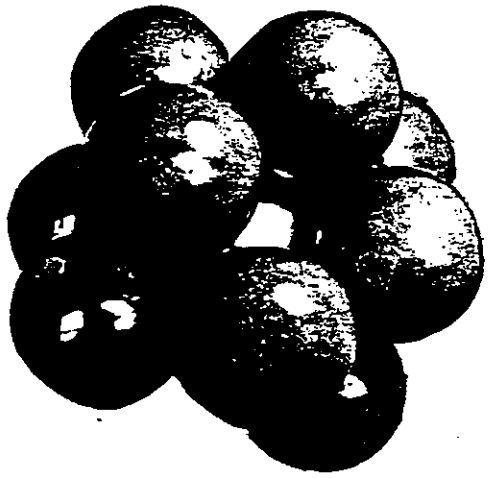
A shell of 12 Pd MTs around the central impurity was used for the bulk case, while a cluster of 8 Pd MTs and four vacuum MTs was taken to represent the (100) surface; see figure 3.6.

a) Phase shifts.

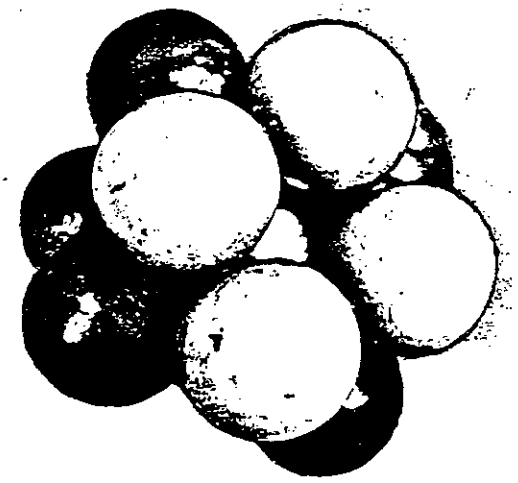
By making use of the symmetry of the impurity site, the phase shift η can be written as the sum of different contributions which can be calculated independently. In the case of the bulk and (100) clusters the phase shifts can be separated in contributions corresponding to $m = 0$, $m = \pm 1$ and $m = \pm 2$.

The solid line in figure 3.7a shows the $m = 0$ phase shift for a single Ag impurity in a bulk free electron gas of density corresponding to the sp band of Pd. It consists, as expected, of a single d resonance. The solid line of figure 3.7b corresponds to the phase shift of a Pd impurity in the same electron gas. The Pd resonance occurs at higher energies and is much broader than the Ag resonance. In a band structure calculation this gives rise to the broad d

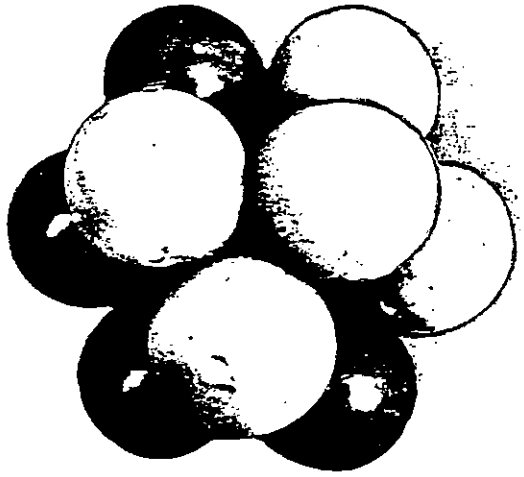
Bulk



(100) surface



(110) surface



(111) surface

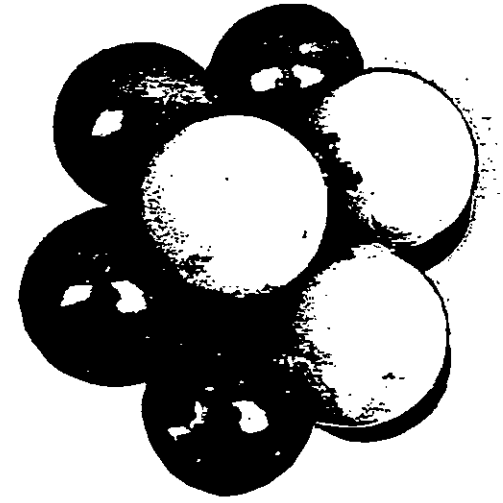


Figure 3.6 Hard ball models of the muffin-tin clusters used in the calculation. The white spheres represent the vacuum muffin-tins.

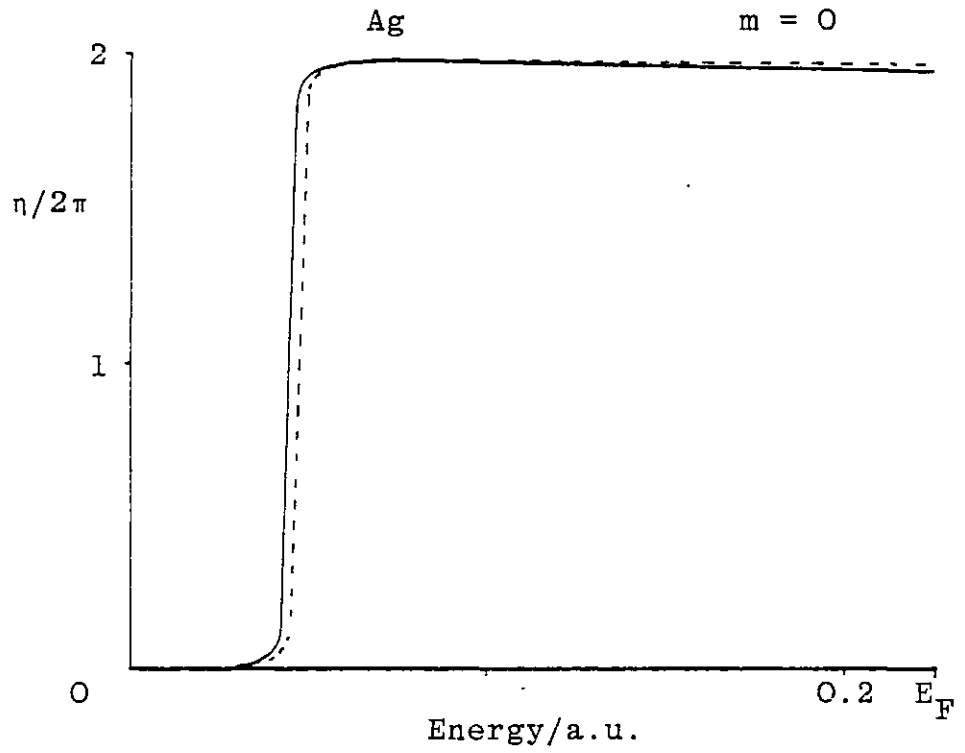


Figure 3.7a) Phase shift for a single Ag MT (solid curve) and for a Ag MT interacting with vacuum MTs (dashed curve).

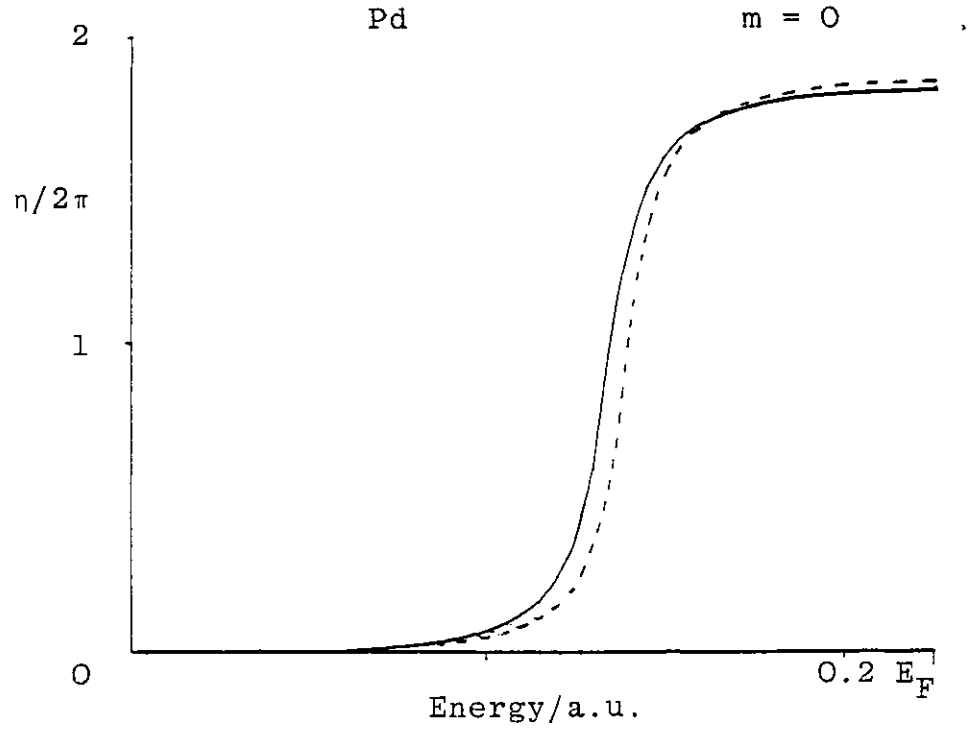


Figure 3.7b) Phase shift for a single Pd MT (solid curve) and for a Pd MT interacting with vacuum MTs (dashed curve).

Pd band and the narrow d Ag band shown in figure 1.7.

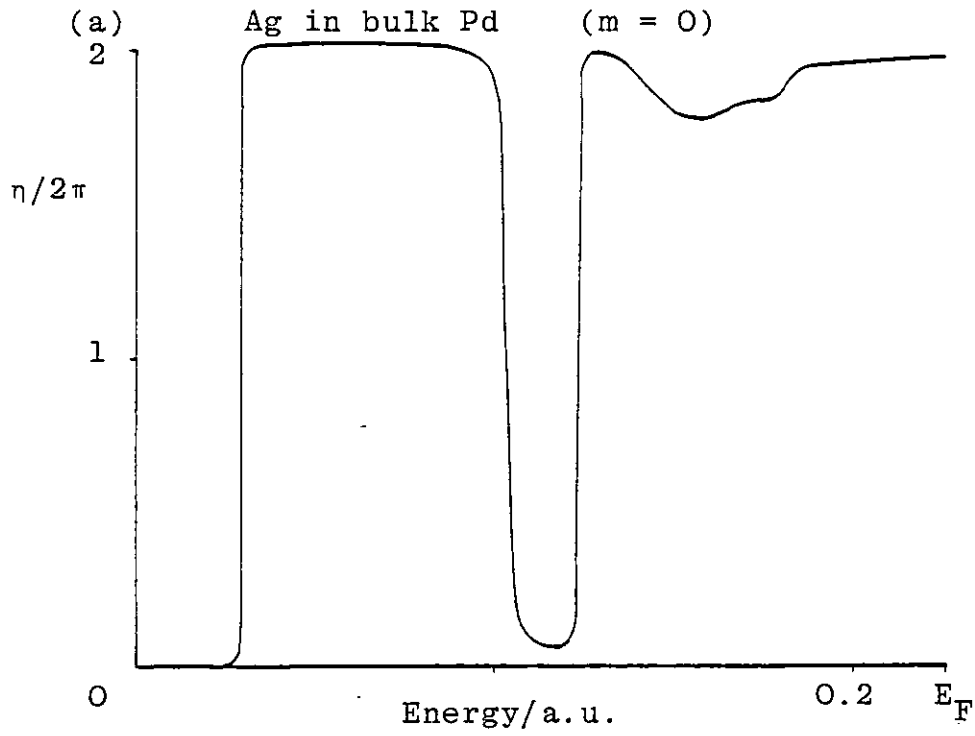
The dashed lines in these figures correspond to the same impurities interacting only with the four vacuum MTs or "surface". As can be seen, the interaction with the vacuum MTs produces a shift of the resonance towards higher energies.

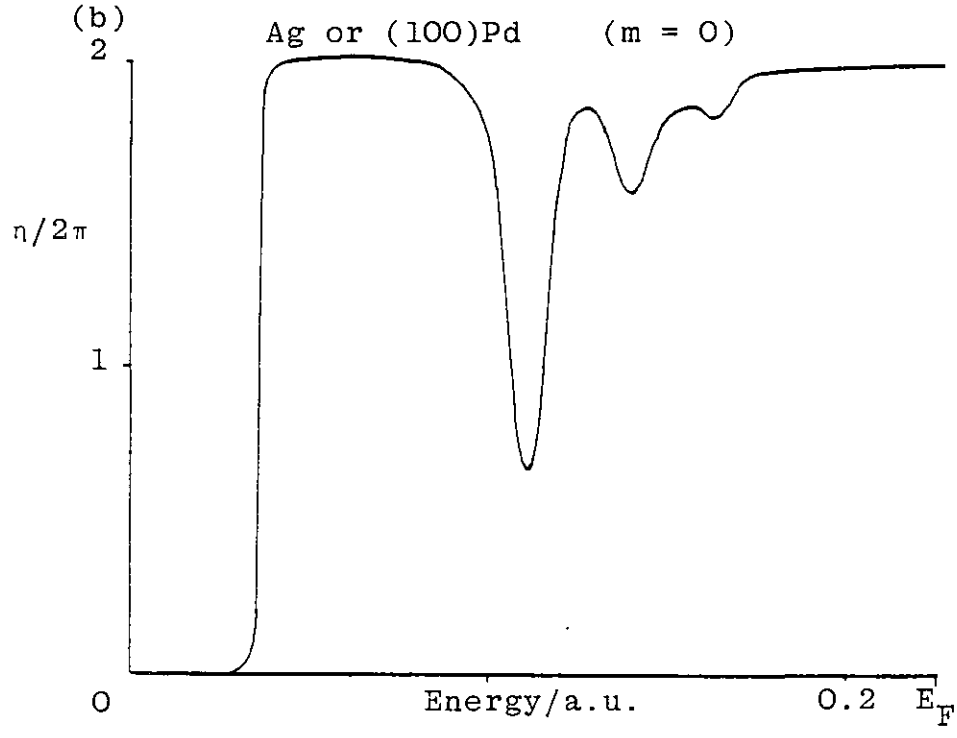
Figure 3.8a shows the m = 0 phase shift for a Ag impurity in bulk Pd and figure 3.8b for a Ag impurity on the (100) face of Pd. Comparing figures 3.7a and 3.8a one observes that due to the presence of the twelve Pd host atoms, the Ag single resonance has been split into a pair of bonding-antibonding resonances.

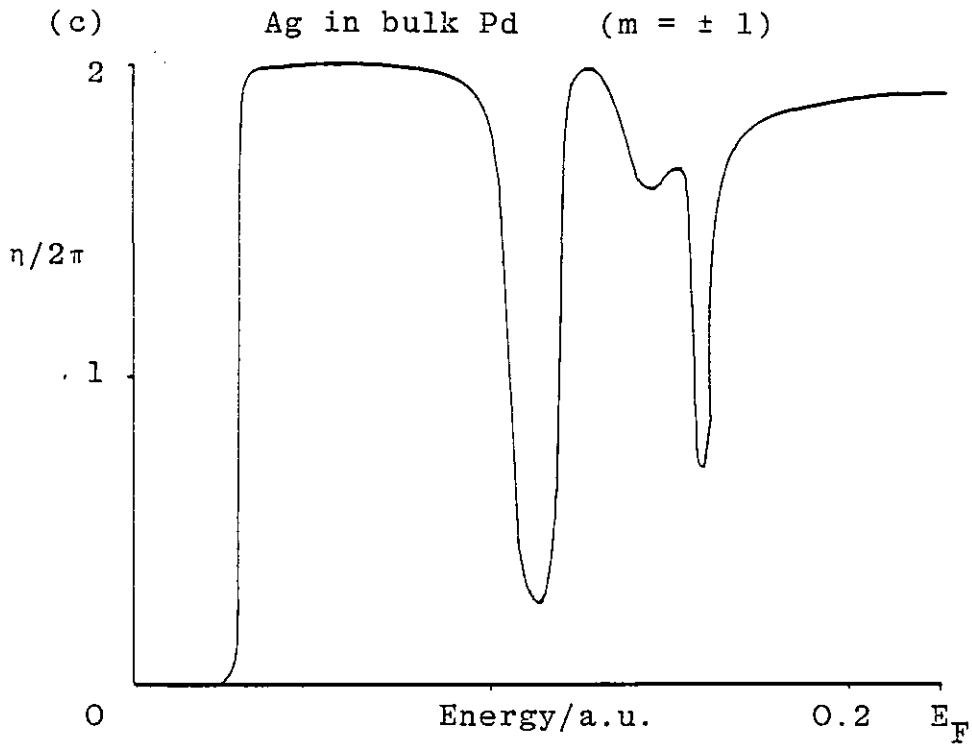
Comparing figures 3.8a and 3.8b one can see that in the case of the Ag impurity on the Pd(100) face the splitting is still present but the second resonance is less pronounced, due to the smaller number of Pd atoms neighbouring the Ag impurity.

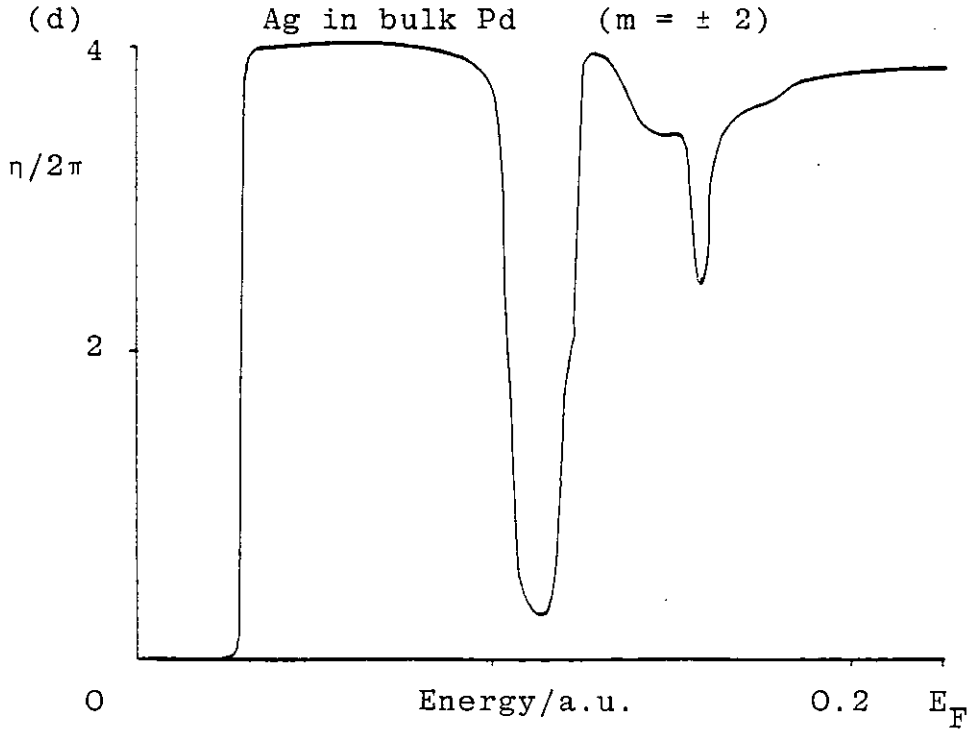
Figures 3.8c - 3.8f show the m = ± 1 and m = ± 2 contribution to the phase shifts of the Ag impurity. Although more structure is present, the trend followed is the same as for the m = 0 contribution.

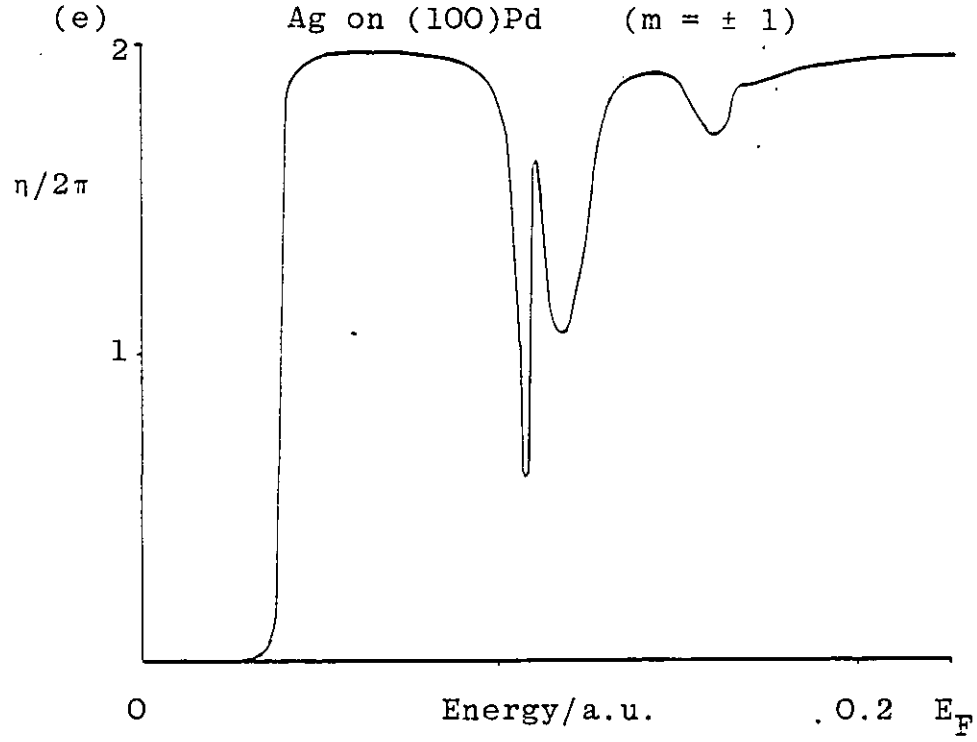
Finally, figures 3.9a - 3.9f display the phase shifts corresponding to a Pd impurity in the bulk and on the (100) surface of Pd. A behaviour similar to the one described for


(a)
Ag in bulk Pd
(m = 0)
2
η/2π
1
0
Energy/a.u.
0.2
E_F


(b)
Ag or (100)Pd
(m = 0)
2
η/2π
1
0
Energy/a.u.
0.2
E_F


(c)
Ag in bulk Pd
(m = ± 1)
2
η/2π
1
0
Energy/a.u.
0.2
E_F


(d)
Ag in bulk Pd
(m = ± 2)
4
η/2π
2
0
Energy/a.u.
0.2
E_F



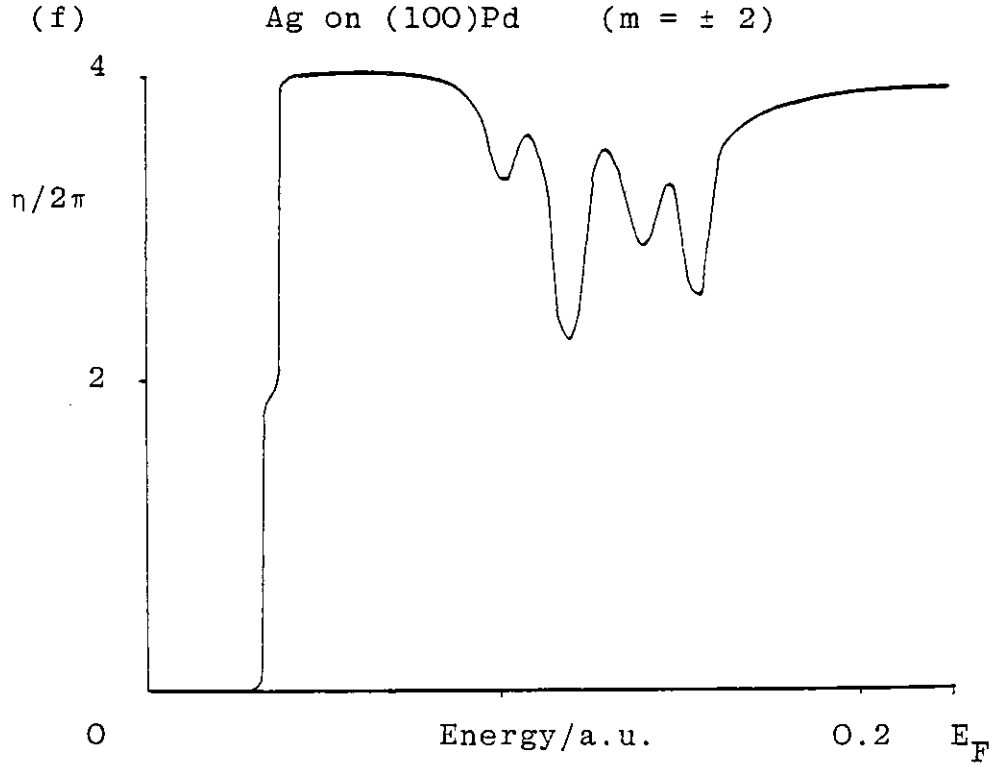
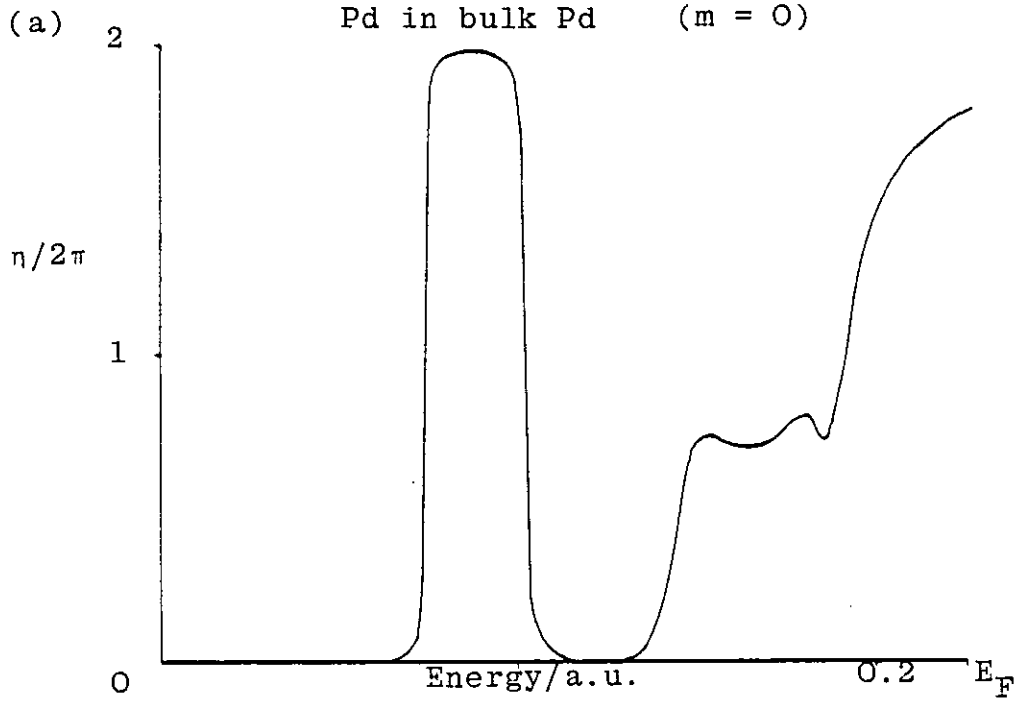
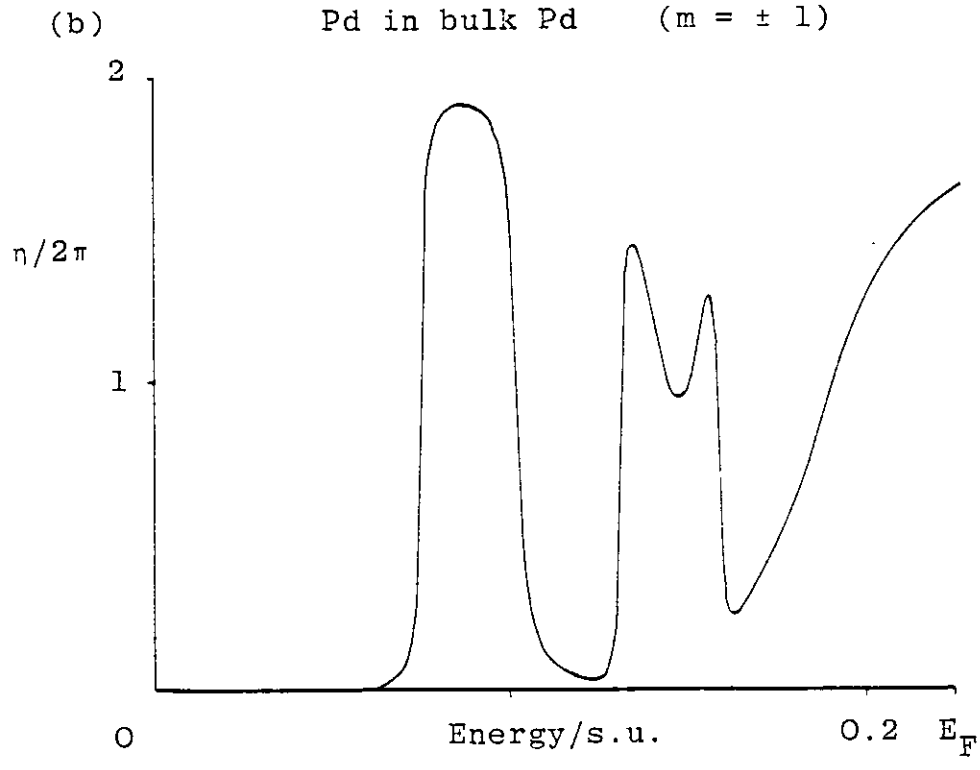
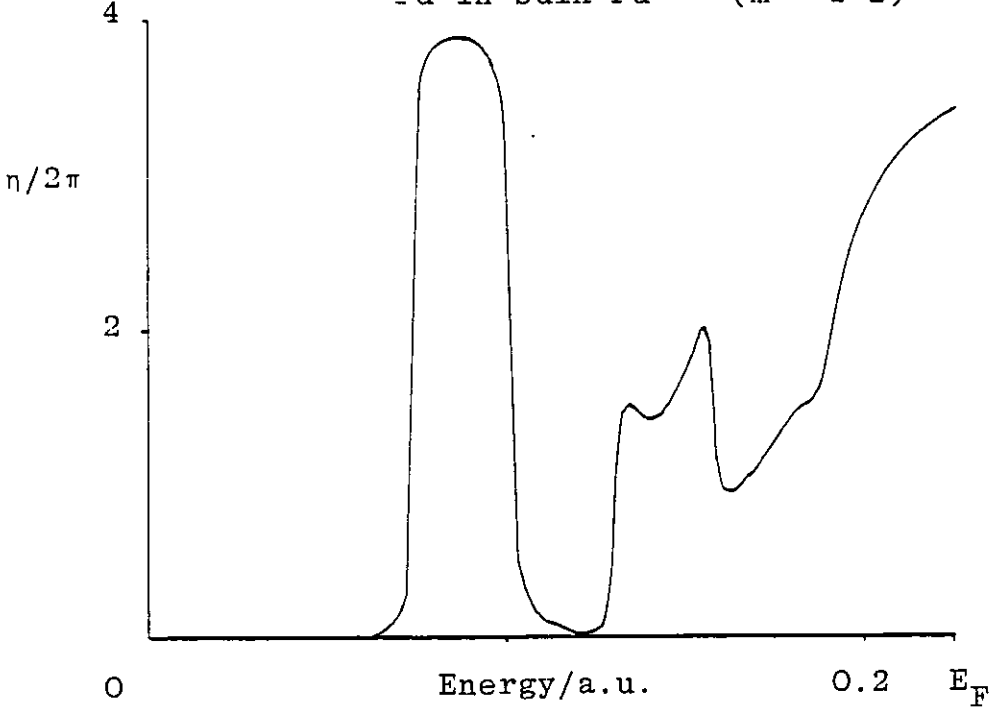


Figure 3.8 phase shifts for a Ag impurity in bulk Pd and at the (100) Pd surface.

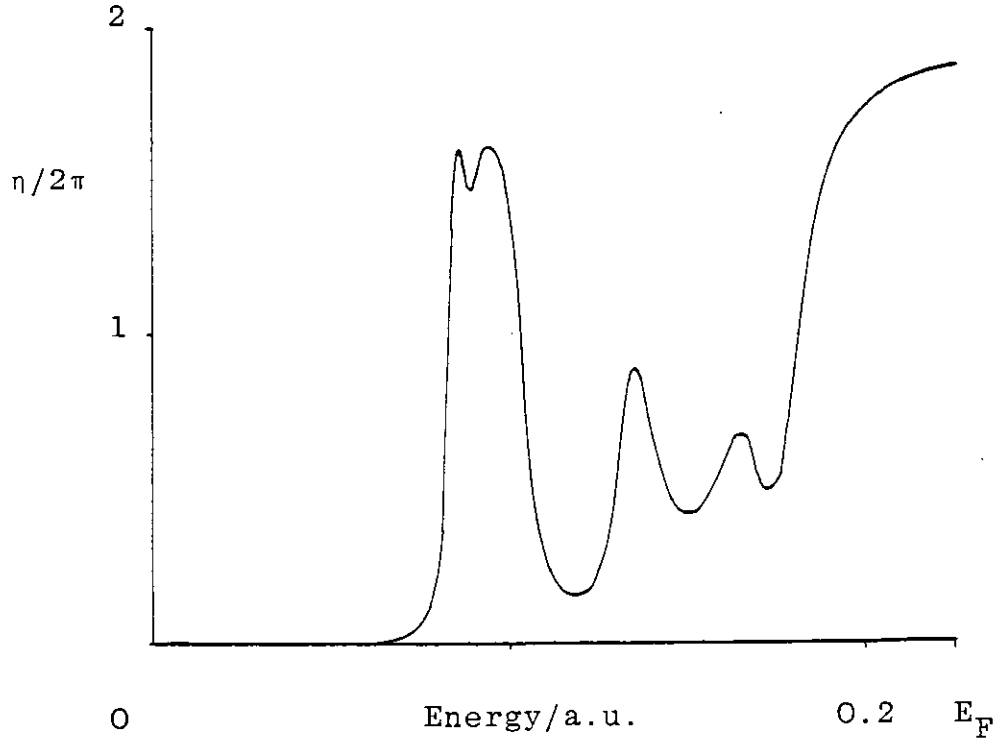

(a)
Pd in bulk Pd (m = O)
2
η/2π
1
O
Energy/a.u.
0.2
E_F

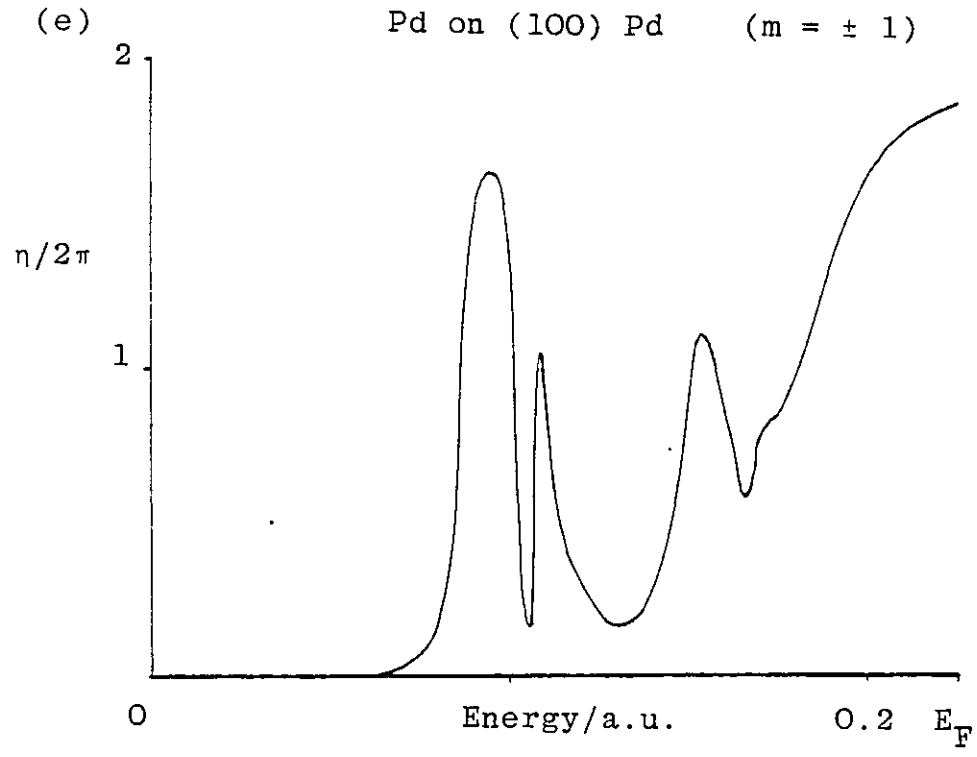

(b)
Pd in bulk Pd (m = ± 1)
2
η/2π
1
O
Energy/s.u.
0.2
E_F

(c) Pd in bulk Pd (m = ± 2)



(d) Pd on (100) Pd (m = 0)





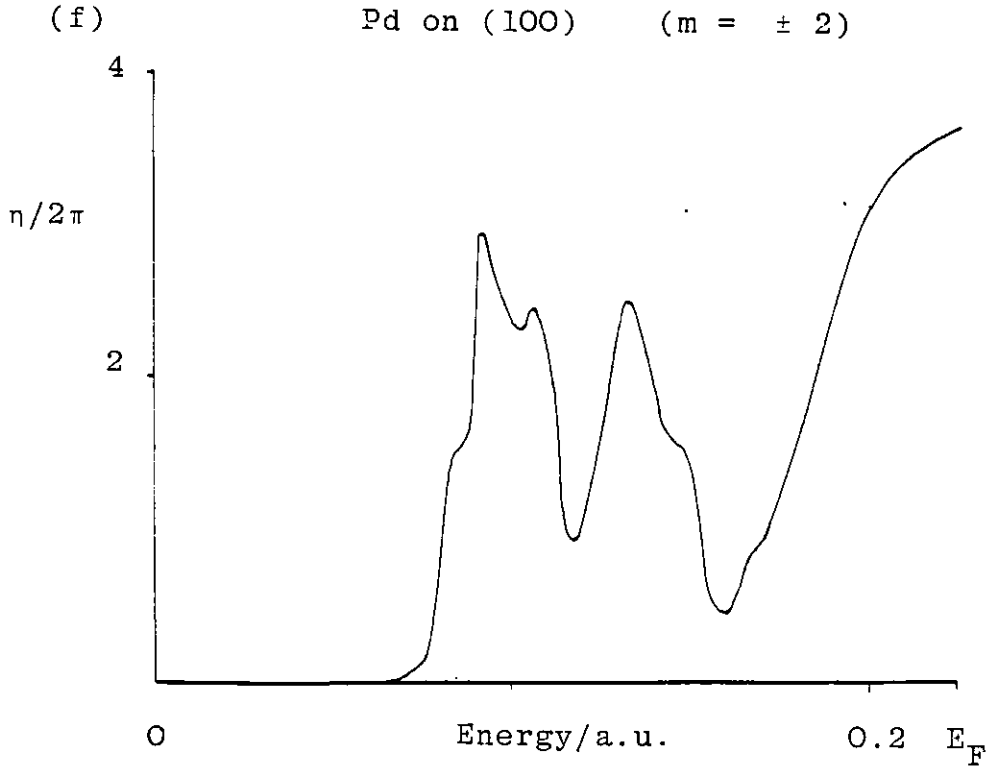


Figure 3.9 Phase shifts for Pd in bulk Pd and at the (100) Pd surface.

the Ag impurity is observed.

b) Energy of segregation.

Having obtained the phase shifts, the energy of segregation given by equation 3.1 can be calculated. In order to do that equation 3.2 must be expressed in terms of the phase shifts.

Equation 3.2 can be written as

$$\sigma = \int_0^{E_F} [n^s(E) - n_o(E)]\, E dE - \int_0^{E_F} [n^b(E) - n_o(E)]\, E dE \qquad 3.24$$

where $n_o(E)$ is the density of states of the electron gas without any scatterer.

The densities of states in equation 3.24 can be expressed in terms of the phase shifts, using Lloyd's formula, equation 3.15

$$n(E) - n_o(E) = (2/\pi)\ d\eta(E)/dE \qquad 3.25$$

so one can write

$$\int_0^{E_F} [n(E) - n_o(E)]\, E dE = (2/\pi) \int_0^{E_F} [\, d\eta(E)/dE\,]\, E dE =$$
$$= (2/\pi) \left[\, \eta(E) dE \Big|_0^{E_F} - \int_0^{E_F} \eta(E) dE \,\right] = (2/\pi) \left[E_F\, \eta(E_F) - \int_0^{E_F} \eta(E) dE'\,\right] \qquad 3.26$$

In this way σ can be expressed as

$$\sigma = \frac{2}{\pi} \int_0^{E_F} \eta^b(E) dE - \frac{2}{\pi} \int_0^{E_F} \eta^s(E) dE \qquad 3.27$$

The quantities $\frac{2}{\pi}\ \eta\ (E)$ which appear as integrands in equation 3.27 are the calculated phase shifts given in figures 3.6 and 3.7, which can be integrated numerically. For the (100) face one obtains

$$\sigma_{Ag}^{(100)} = (2/\pi)\left[\int_{o}^{E_F} \eta_{Ag}^{b}\ (E)dE - \int_{o}^{E_F} \eta_{Ag}^{(100)}\ (E)\ dE\right]$$

and

$$\sigma_{Pd}^{(100)} = (2/\pi)\left[\int_{o}^{E_F} \eta_{Pd}^{b}\ (E)dE - \int_{o}^{E_F} \eta_{Pd}^{(100)}\ (E)dE\right]$$

The change in internal energy when a silver atom located in the bulk of a palladium host exchanges position with a palladium atom at the (100) surface is given, within the approximations of the present model, by

$$\Delta E_s^{(100)} = \sigma_{Ag}^{(100)} - \sigma_{Pd}^{(100)}$$

This model was also applied to calculate the energy of segregation to the (111) and (110) surfaces. The results obtained for the three low index surfaces are given below

$$\Delta E_s(111) = -0.7\ eV$$
$$\Delta E_s(100) = -0.9\ eV$$
$$\Delta E_s(110) = -1.0\ eV.$$

The values of ΔE_s obtained are negative, indicating that the Ag impurity in Pd has a marked preference for the surface sites. The relative values show that the energy of segregation is largest for the more open (110) surface and decreases in going to the (100) surface and to the close-packed (111) surface, in agreement with the predictions of

the broken-bond model.

The absolute values of the energies of segregation calculated in this model are rather high in comparison with the values obtained using the models described in chapter 2. Better values could be obtained by the inclusion of second nearest neighbours, increasing the value of l_{max} used in the description of the vacuum MTs and relaxing the vacuum MT positions.

This electronic model succeeds in identifying the d resonances as playing a central role in the driving force responsible for Ag surface enrichment in AgPd alloys.

The vacuum MTs are also a very important part of the model. In his original work using the embedded cluster calculations for studying Cu surface segregation in CuNi, J.P. Muscat[3] tests the relative importance of the hosts and vacuum MTs.

He considers a cluster in which all the vacuum MTs are removed, so the "surface" is represented by the absence of Ni MTs on one side of the Cu impurity site. A calculation of ΔE_S showed no preference for either the bulk site or this kind of "surface" site.

In a second test he removes all the Ni MTs surrounding the Cu impurity and considers only the vacuum MTs. A calculation of ΔE_S showed in this case a marked preference

for the Cu impurity to exchange positions with a Ni surface atom, as in the case of the full cluster, showing that the surface potential is fundamental for the segregation phenomenon.

3.4 Surface core level energy shifts

The binding energy of a core level orbital is the difference in total energy between the final and initial states of a system in which one electron has been removed from that orbital.

The core level binding energies in an atom depend on its chemical environment, so there is a core-level binding energy shift between the free atom and when the atom is forming part of a molecule. This is the so called "chemical shift", extensively used in X-ray photoelectron spectroscopy (XPS) to characterize molecular states[7]. The simple model to explain the chemical shifts is that the chemical environment of the atom modifies the distribution of its valence electrons, which produces a change in the potential felt by the core electrons.

There is a core electron binding energy shift between the free atom and the condensed atom in its metallic state[8]. Even in this metallic state one expects a somewhat different core level binding energy for the surface atoms as compared with the bulk atoms. This difference corresponds to the so called surface core-level shift (SCLS).

The SCLS can be determined in a XPS experiment by comparing the core level binding energies of surface and bulk atoms. In such an experiment the initial state corresponds to the perfect metal and the final state corresponds to a core ionized atom totally screened by the conduction electrons. These core-level binding energies are usually measured relative to the Fermi level and are denoted here by $E_{c,F}$.

An expression for the SCLS of each component in a binary alloy AB has been given by K. Kumar et.al.[8] using the procedure of Johanson and Martensson[9]. The core level binding energy of, say, component A, $E_{c,F}(A, A_x B_{1-x})$, can be obtained assuming that the transition from the initial to the final state is carried out through the following steps:

a) First, one atom A is removed from the alloy. In order to obtain the free atom A, the cohesive energy $E_{coh}(A, A_xB_{1-x})$ is supplied

b) then, this atom A is ionized in a core level c and neutralized by accepting one electron in the lowest valence shell. The result is an A^* atom with a hole in the core level c. This process involves the energy $E_{c \rightarrow v}$, the excitation energy of the core electron c into the valence shell v.

c) Finally, this core-ionized A^* atom is taken into the alloy, releasing the cohesive energy $E_{coh}(A^*, A_xB_{1-x})$.

The completed sequence obeys the following relation:

$$-E_{c,F}(A,A_xB_{1-x}) = E_{coh}(A,A_xB_{1-x}) + E_{c\to v}(A) - E_{coh}(A^*,A_xB_{1-x}) \qquad 3.28$$

If the bulk and surface are denoted by the superscripts b and s, respectively, the SCLS of component A can be written as

$$\Delta E_c^s(A) = E_{c,F}^s(A,A_{x_s}B_{1-x_s}) - E_{c,F}^b(A,A_xB_{1-x}) =$$

$$[E_{coh}^s(A^*,A_xB_{1-x}) - E_{coh}^b(A^*,A_{x_s}B_{1-x_s})] - [E_{coh}^s(A,A_xB_{1-x}) -$$

$$E_{coh}^b(A,A_{x_s}B_{1-x_s})]$$

$$\equiv E^s(A^*,A_xB_{1-x}) - E^s(A,A_xB_{1-x}) \qquad 3.29$$

where $E^s(A,A_xB_{1-x})$ is the surface energy of A in the alloy, i.e. the work done in taking the atom A from the bulk and putting it at the surface.

For the SCLS of component B a similar expression is obtained:

$$\Delta E_c^s(B) = E^s(B^*,A_xB_{1-x}) - E^s(B,A_xB_{1-x}) \qquad 3.30$$

As can be seen in equation 3.29 the SCLS depends only on the cohesive energies E_{coh}^s, E_{coh}^b. It is the number and character of the valence electrons which largely determines these cohesive energies; in the case studied here these are

the conduction d electrons.

Moreover, as regards the conduction electrons, a core ionized atom of atomic number Z can be replaced by a normal atom of atomic number Z + 1, i.e. the screening charge distribution around the core ionized atom of atomic number Z can be approximated by that of an atom of atomic number Z + 1. This is known as the Z + 1 approximation.

If A and B are neighbouring elements in the periodic table (Eg, AgPd, A=Ag, B=Pd) then, within the Z + 1 approximation, $B^* = A$. Therefore equation 3.30 becomes

$$\Delta E_c^S(B) = E^S(A,A_xB_{1-x}) - E^S(B,A_xB_{1-x}) = \qquad 3.31$$

$$= [E_{coh}^s(A) - E_{coh}^b(A)] - [E_{coh}^s(B) - E_{coh}^b(B)]$$

The first term in this equation represents the work done in transferring one atom A from the bulk to the surface, whereas the second term represents the energy gain in transferring one atom B from the surface to the bulk. Comparing equation 3.31 with equation 3.1, one can see that the SCLS of atom B, $\Delta E_c^S(B)$, corresponds to the energy of segregation of component A in the alloy:

$$\Delta E_c^S(B) = \sigma_A - \sigma_B \qquad 3.32$$

so the energy of segregation of component A can be determined by measuring the surface core level shift of component B.

The experimental measurements of SCLS are, however, not easy to perform. The main difficulty being that the shift is a small fraction of one eV. A high resolution energy analyser, monochromatic radiation and the ability to distinguish signals originating in the bulk and at the surface, are clearly needed. A further difficulty is that core level shifts due to alloying effects could also be present.

References (Chapter 3)

1. Friedel J. 1969, in: "The Physics of Metals" ed. J.M . Ziman, London, Cambridge University Press.

2. Ph. Lambin, J.P. Gaspard. J. Phys. F. 10 (1980) 2413.

3. J.P. Muscat, J. Phys. C (GB) 15 (1982) 867.

4. J.S. Faulkner, J. Phys. C. 10 (1977) 4661.

5. J.P. Muscat (private communication).

6. V.L. Moruzzi, J.F. Janak and A.R. Williams, "Calculated Electronic Properties of Metals," 1978, Pergamon Press Inc.

7. T.A. Carlson, "Photoelectron and Auger Spectroscopy", Plenum Press, 1975.

8. K. Kumar, D. Tomanek and K.H. Bennemann, Solid State Comm. 39 (1981) 987.

9. B. Johansson and N. Martensson, Phys. Rev. B 21 (1980) 4427.

CHAPTER 4

QUANTITATIVE AUGER ELECTRON SPECTROSCOPY

4.1 Auger Electron Spectroscopy

Auger Electron Spectroscopy (AES) is a technique currently used for the compositional analysis of solid surfaces. Many good reviews describing in detail this spectroscopy have been published[1,2]; here a brief account is given.

When an neutral atom is ionized in an inner level "j", it is left in an excited state and tends to decay to a state of lower energy with an electron from a higher level "k" falling into the initial hole. The energy released in this process may appear in the form of a photon as in X-Ray fluorescence or may be transferred to another electron in a level "l" which is emitted from the atom, leaving it double ionized in its final state. This second, radiationless alternative is known as the Auger process, and according to the energy levels involved is described as the "jkl" Auger transition. In a solid, Auger transitions involving the valence band V are possible and "jkV" and "jVV" transitions are commonly found.

The kinetic energy of the emitted Auger electron depends on the energy levels involved and these levels are characteristic of each chemical element. In AES, Auger transitions are produced in a sample and the energy and

number of Auger electrons is measured in order to identify and quantify the elements present. A schematic diagram of an AES experiment is given in figure 4.1.

Ionizing radiation, usually an electron beam, impinges on the sample creating the initial holes. Electrons resulting from Auger transitions escape from the sample and are energy analysed producing the Auger spectrum. The Auger electrons are superimposed on a large and smooth background of secondary electrons. Differentiation of the electron distribution N(E) emitted from the sample sharply enhances the Auger features, so Auger spectra are typically presented in the dN(E)/dE mode; this is customarily achieved by electronic differentiation.

The kinetic energy E_{jkl} of a jkl Auger electron emitted from a free atom of atomic number Z can be approximated by

$$E_{jkl}(Z) = E_j(Z) - E_k(Z) - E_l(Z + \Delta Z) \qquad 4.1$$

where E_i is the one-electron binding energy of level i and the parameter ΔZ is included in order to take account of the fact that the atom is in a charged state when the Auger electron is emitted. The value of E_{jkl} is independent of the energy of the primary electron beam.

Chung and Jenkins[3] developed an empirical expression for E_{jkl} in which the effective binding energy of a level in a doubly ionized atom is given by the average binding

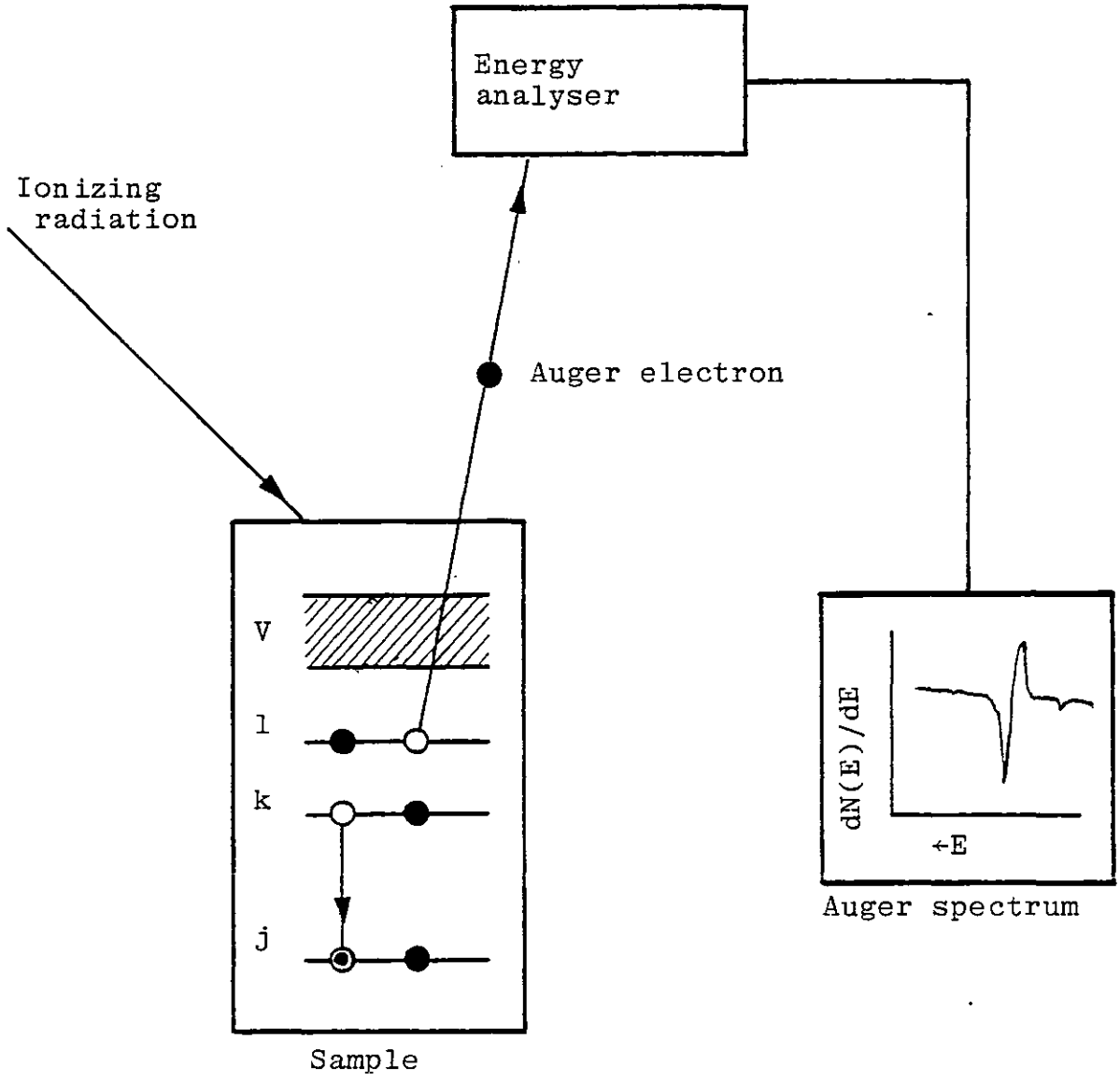


Figure 4.1 Schematic diagram of an experimental arrangement for AES and of a "jkl" Auger transition.

energies corresponding to the atomic numbers Z and Z + 1. The expression obtained is

$$E_{jkl}(Z)=E_j(Z)-\tfrac{1}{2}\left[E_k(Z)+E_k(Z+1)+E_l(Z)+E_l(Z+1)\right] \qquad 4.2$$

This equation was used by Coghlan and Clausing to calculate the possible Auger transitions between 10 and 3000 eV. for the elements from atomic numbers 3 through 92, listed in their Auger catalog[4].

Commonly, AES experiments are carried out on solid samples. In this case the ejected electrons have to overcome the sample work function ϕ_s in order to escape into the vacuum,so their kinetic energy is reduced by the value ϕ_s in comparison with the value given in equation 4.2. The energy of the electrons detected in the analyser is, however, measured relative to the Fermi level of the analyser material. This introduces the term $-(\phi_a - \phi_s)$, the contact potential between analyser and sample, where ϕ_a is the work function of the analyser. The measured kinetic energy is then given by

$$E_{jkl}(Z)=E_j(Z)-\tfrac{1}{2}\left[E_k(Z)+E_k(Z+1)+E_l(Z)+E_l(Z+1)\right] - \phi_a \qquad 4.3$$

Each chemical element has a series of Auger transitions well defined both in energy and relative intensity through which it can be identified. Catalogs of experimentally recorded Auger spectra are also available[5,6].

AES is a very surface sensitive technique. Only the Auger electrons coming from the few outermost layers of the solid are usually detected. Auger electrons generated in deeper layers lose energy through interaction with electrons in the solid and are inelastically scattered into the background of secondary electrons.

For light elements ($Z < 40$), Auger transitions occur with higher probability than the competing X-Ray emission. This makes AES particularly useful for the detection of typical impurities in solid surfaces.

4.2 Quasiatomic versus band-like Auger spectra.

Equation 4.1 implicitly assumes that there is only one possible final state for a free atom Auger transition. Usually, however, there are several possible final state configurations and therefore several peaks appear in the Auger spectrum of a given "jkl" transition. Denoting by Y the spectral term of the corresponding final state configuration, the Auger electron energy is better expressed[7] as

$$E^{at}(jkl,Y) = (E_j^{at} - E_k^{at} - E_l^{at}) - \Delta E^{at}(kl,Y) \qquad 4.4$$

where E_i^{at} is the one-electron binding energy of level i in the free atom and ΔE^{at} is given by

$$\Delta E^{at}(kl,Y) = \mathcal{F}(kl,Y) - R_a(kl) \qquad 4.5$$

The term $\mathcal{F}$ expresses the interaction between the two holes in the final state. The interaction between the 'k' and 'l' holes is partially reduced because the outer atomic levels relax around the 'k' hole partially screening it. This reduction is taken into account by the intra-atomic relaxation term R_a.

The Auger spectra of solids can broadly be classified into two categories, quasiatomic and band-like.

Quasiatomic spectra show a structure very similar to the one described for free atoms, i.e. spectral terms associated to the final state configurations in the corresponding atom or ion, shifted relative to the unperturbed value $(E_j - E_k - E_l)$. The energy of these quasiatomic peaks is given by

$$E(j\ k\ l,Y) = (E_j - E_k - E_l) - \Delta E(k\ l,Y) \qquad 4.6$$

where ΔE is now given by

$$\Delta E(k\ l,Y) = \mathcal{F}(k\ l,Y) - R_a(k\ l) - R_e(k\ l) \qquad 4.7$$

and the new term R_e, called the extra-atomic relaxation energy, accounts for the partial screening of one of the two final holes by the Fermi electron gas. The peak widths in quasiatomic spectra are comparable to the peak widths in spectra from free atoms. Quasiatomic spectra are typically found in Auger transitions involving only core levels.

Band-like Auger spectra are those involving the V valence band in which the band structure is apparent. For instance, in band-like Auger transitions of the jVV type the Auger electron distribution N(E) is proportional to the self-convolution of the valence-band density of states and there is no energy shift equivalent to ΔE in equation 4.6. This band like behaviour is found in free-electron metals and semiconductors.

The quasiatomic and band-like limits seems to be related to the localization and delocalization of the final holes respectively. Delocalized holes in a band can be efficiently screened and the term ΔE, characteristic of atomic spectra disappears. In this respect it is not immediately obvious which kind of behaviour is shown by Auger spectra involving 'd' bands due to the intermediate nature (extended - localized) of the d electrons in transition metals.

It is now generally accepted that the L_3VV Auger transition spectra of the first elements of the 3d transition series are of band-like nature , copper shows a clear quasiatomic character and nickel is a borderline case[8]. The same behaviour is found in the MVV Auger spectra of the 4d series, silver showing a well defined quasiatomic spectra and palladium being a borderline case[9].

The jVV Auger spectra of Cu, Ni Ag and Pd can then be considered as quasiatomic. It is expected that the same

quasiatomic character is present independently for each component in Cu Ni and AgPd alloys, specially since both systems show the split-band behaviour referred to in chapter 1. As far as the main features of the Auger spectra are concerned this has been found to be the case in AgPd alloys[10]. This situation can be thought as if on average the initial hole is de-excited before the electron in the d band can tunnel into another atom.

The quasiatomic nature of the Auger spectra in Cu Ni and AgPd alloys simplifies quantitative analysis since in this case the Auger signals can safely be assumed to be proportional to the number of atoms in which the transition is localized.

4.3 Quantitative Auger Electron Spectroscopy of Binary Alloys.

The quantitative analysis of the surface segregation phenomenon is Cu Ni and AgPd alloys will be carried out in this work fundamentally through the use of AES. The model used for transforming the measured Auger signals into quantitative information about the surface composition of a binary alloy AB is developed below.

The system considered is a substitutional alloy AB in which the enrichment takes place as shown schematically in figure 2.1, i.e. the atoms considered are always distributed on the sites of a periodic lattice.

The detected Auger electron current I_A associated with element A in the alloy matrix AB can be expressed[11] as

$$I_A = I_o \sigma_A \left[1 + r_{AB}(E_A)\right] T(E_A) D(E_A) R_{AB} \int_0^\infty N_A(z) A(z) dz \qquad 4.8$$

where

I_o is the primary electron beam current,

σ_A includes the cross section for the creation of the initial hole and the probability to eject the appropriate Auger electron per atom of component A.

$r_{AB}(E_A)$ is the backscattering factor,

$T(E_A)$ is the analyser transmission efficiency,

$D(E_A)$ is the electron detector efficiency

R_{AB} is the sample roughness factor

$N_A(z)$ is the atom density of A atoms at depth z, i.e. the composition profile,

$A(z)$ is the attenuation function, and the coordinate z is taken to be zero at the surface.

An expression equivalent to equation 4.8 can be written for the Auger current I_B associated with component B.

4.3.1. The attenuation function.

The attenuation function A describes the signal attenuation as a function of the depth z from which the signal is emitted and the relative orientation of sample

and analyser. It is given[12] by the expression

$$A(z/\lambda,\theta) = \left[\int_{\Omega} \varepsilon(\theta) e^{-z \sec \theta/\lambda_{AB}(E_A)} d\Omega \right] / \int_{\Omega} \varepsilon(\theta) d\Omega \qquad 4.9$$

where θ is the angle of emission of the Auger electron with respect to the surface normal. This expression assumes that inside the solid the number of Auger electrons is attenuated according to $\lambda_{AB}(E_A)$, the inelastic mean free path (i.m.f.p.) of the electron in the matrix AB.

$\varepsilon(\theta)$ describes the angular distribution of the emission from the source and Ω is the angular range of the analyser aperture.

The attenuation function depends on the particular analyser in use and on its orientation relative to the sample surface. For the RFA used in this work the geometrical configuration is as shown in figure 4.2a.

In a majority of cases the attenuation function approximates to a simple exponential

$$A(z) = e^{-z/d(E)} \qquad 4.10$$

where d(E) represents the "mean escape depth" related to the i.m.f.p. λ by

$$d(E) = K \lambda(E) \qquad 4.11$$

and K is a proportionality constant to be determined for each experimental arrangement.

Assuming an isotropic Auger emission ($\varepsilon(\theta) = 1$) and for the set up of figure 4.2a the attenuation function has been calculated and is shown in figure 4.2b. A distribution $\varepsilon(\theta) = \cos\theta$ gives basically the same straight line. From the line slope the relation

$$d = 0.8\ \lambda$$

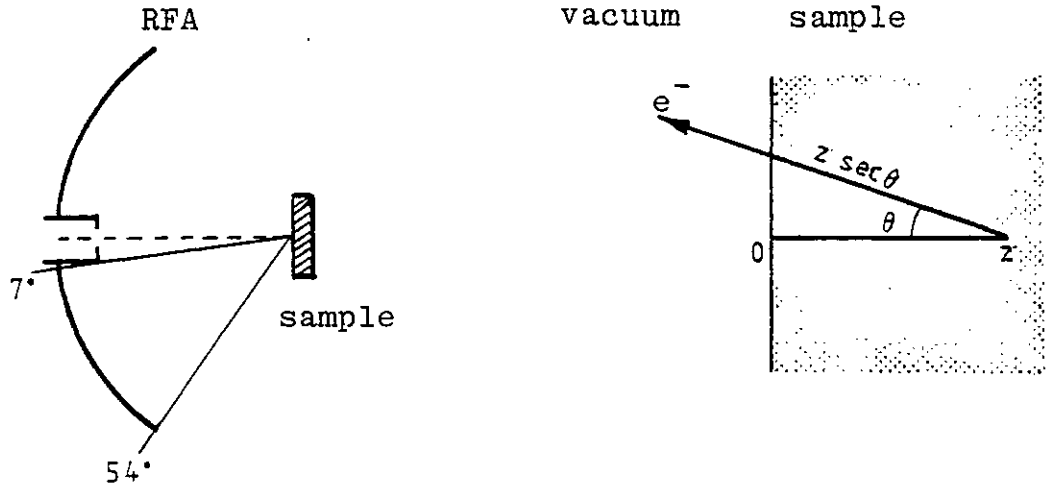
has been obtained.

In single crystal samples the Auger electrons are expected to be diffracted in their way out of the solid. These effects might be important in angle resolved measurements, but in angle integrated measurements like the ones performed here using the RFA they can be neglected.

4.3.2 Electron inelastic mean free paths.

The inelastic mean free paths of electrons in solids can be calculated from the recent compilation presented by Seah and Dench[13], shown in figure 4.3 for pure elements. It can be observed that the i.m.f.p. experimental values as a function of energy are distributed around an "universal curve". An i.m.f.p. of $\sim$6 monolayers is observed for electrons of 10 eV. energy, which decreases to $\sim$2 monolayers at 80 eV. and then increases to $\sim$10 monolayers at 2000 eV.

a)



b)

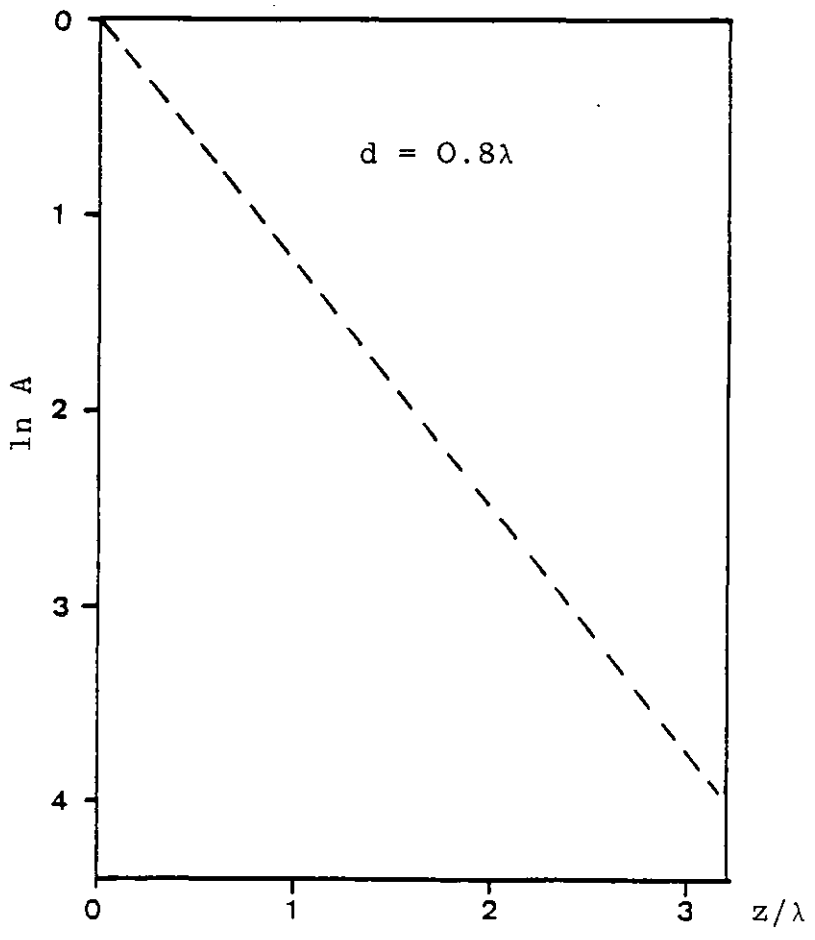


Figure 4.2 (a) Geometrical configuration sample-analyser used for calculating the attenuation function.

b) Logarithm of the attenuation function vs. z/λ.

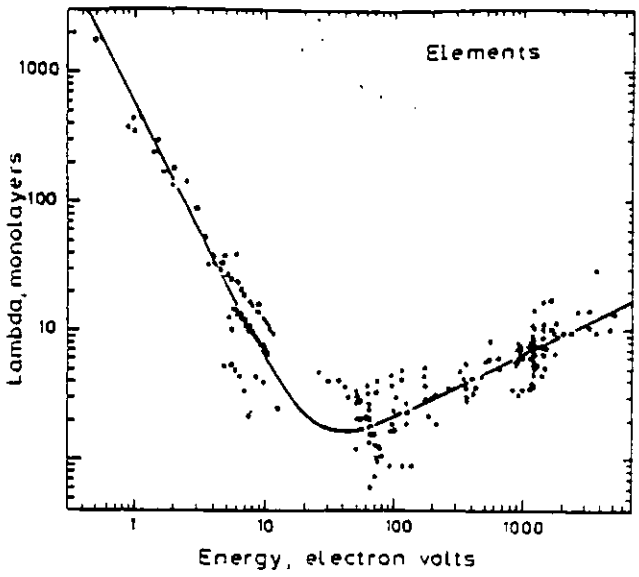


Figure 4.3 Electron mean free paths in pure elements. (After Seah and Dench[13]).

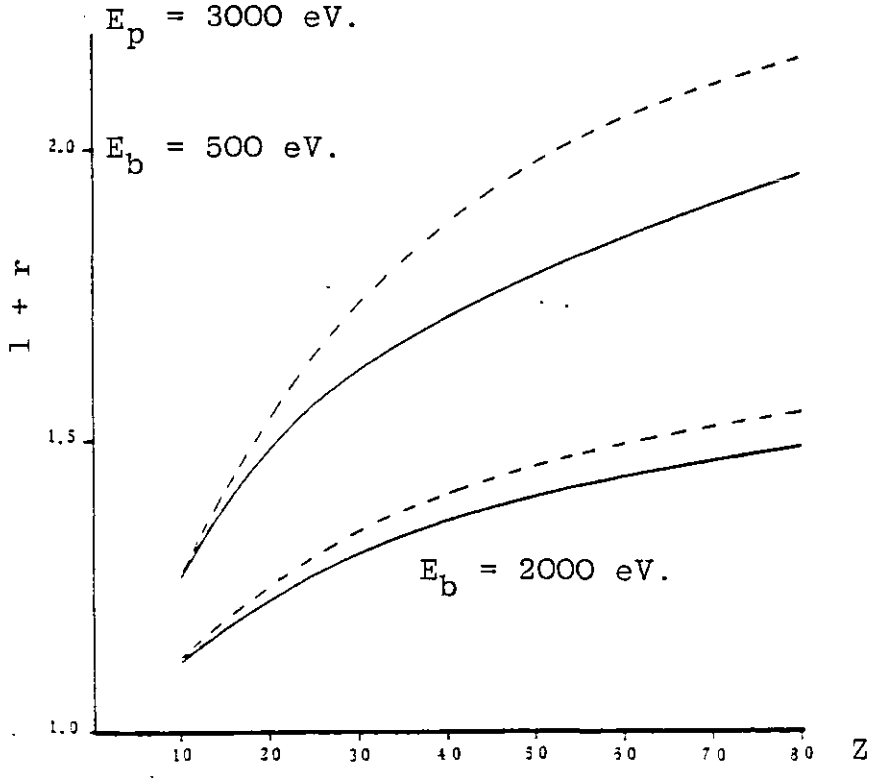


Figure 4.4 Backscattering factor as a function of atomic number. Dashed curves, Reuter's equation. Solid curves, equation of Ichimura and Shimizu.

The most accurate relation found for this curve is given by

$$\lambda = 538/E^2 + 0.41(a\,E)^{\frac{1}{2}} \qquad 4.12$$

with λ expressed in monolayers, the equivalent monolayer thickness "a" in nm. and the energy E in eV.

4.3.3. The Backscattering factor.

The backscattering factor is the ratio of Auger electrons produced by the backscattered electrons in the solid devided by those produced directly by the primary beam. It depends, in principle, on the Auger transition, composition of the solid and energy and incidence angle of the primary beam.

An empirical relation proposed by Reuter[14] expresses this factor as

$$1+r=1+2.8(1-0.9E_b/E_p)(-0.0254+0.016Z+0.000186Z^2+8.3\times10^{-7}Z^3) \qquad 4.13$$

where E_b is the ionization energy necessary to create the initial hole state (given in references 15,16), E_p is the primary beam energy and Z is the atomic number of the matrix element, which for a binary alloy can be taken as the weighted average of the atomic numbers of the two components. Since this equation was derived from experimental results in electron microprobe analysis with a 20 KeV. primary

beam at normal incidence, its extension to Auger analysis might not be accurate.

More recently, Ichimura and Shimizu[17] proposed an expression for the backscattering factor obtained by Monte Carlo calculations. They use the same parameters of Reuter's equation and for normal incidence obtain the expression

$$1+r=1+(4.35-3.93Z^{0.1})(E_b/E_p)^{0.25}+4.85Z^{0.1}-5.45 \quad 4.14$$

Values of the backscattering factor calculated from Reuter's equation are larger than those obtained from equation 4.14, specially for high atomic number materials. This is shown graphically in figure 4.4.

The dependence of the backscattering factor on the primary beam incidence angle has been investigated by Jablonski[18] also using a Monte Carlo algorithm. He finds important variations for angles of incidence relative to the surface normal in the range $45^{o} < \theta < 90^{o}$, where (1+r) goes through a maximum and then rapidly decreases to zero as shown in figure 4.5. This angular variation is important in experiments using a grazing incident electron beam.

In the experiments on Cu Ni and AgPd carried out in the present work a grazing incidence electron gun was used and a well defined maximum in the Auger signal was detected for an incidence angle of $\sim 75^{o}$. The position of this

maximum correlates well with the one shown in figure 4.5, so it is attributed to this angular variation of the backscattering factor.

Values of the backscattering factor obtained from Reuter's equation and from Monte Carlo calculations show a similar variation with atomic number, so the discrepancy between them is reduced when the ratio of backscattering factor of two samples is used.

4.3.4. Homogeneous binary alloy.

In the case of a binary alloy AB of homogeneous atomic composition C_A, C_B ($C_A + C_B = 1$) the Auger current I_A given in equation 4.8 reduces to

$$I_A = I_o \sigma_A \left[1 + r_{AB}(E_A) \right] T(E_A) D(E_A) R_{AB} N_A d_{AB}(E_A) \qquad 4.15$$

and an analogous expression can be written for I_B.

One commonly used method of quantifying Auger signals is to use samples of the pure components A and B as reference standards, measured with the same spectrometer and under similar experimental conditions as the AB alloy sample. The Auger signals of pure A and pure B will be denoted as I_A^∞ and I_B^∞ respectively.

By taking the ratios I_A/I_A^∞ and I_B/I_B^∞ one can get expressions in which the factors I_o, σ , T and D do not

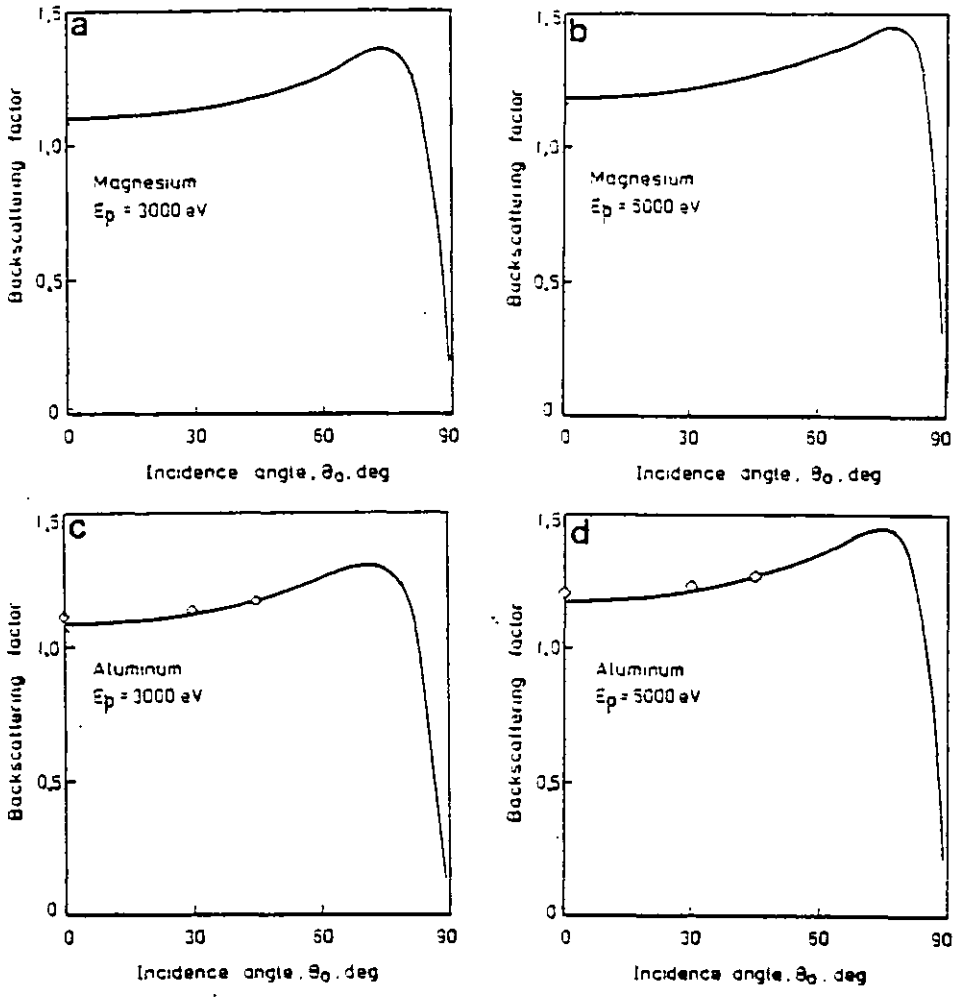


Figure 4.5 Backscattering factor as a function of primary beam incidence angle for Mg and Al. (After Jablonski[18]).

appear. If one makes the further asumption that the samples have the same roughness factor (same polishing treatment) then this factor does not appear either.

On can then write the following expressions

$$\frac{I_A}{I_A^{\infty}} = \frac{\left[1+r_{AB}(E_A)\right] N_A d_{AB}(E_A)}{\left[1+r_A(E_A)\right] N_A^{\infty} d_A(E_A)} \qquad 4.16$$

$$\frac{I_B}{I_B^{\infty}} = \frac{\left[1+r_{AB}(E_B)\right] N_B d_{AB}(E_B)}{\left[1+r_B(E_B)\right] N_B^{\infty} d_B(E_B)} \qquad 4.17$$

N_A^{∞} and N_B^{∞} are given by a_A^{-3} and a_B^{-3} respectively, where a_A and a_B are the atomic sizes (or "equivalent monolayer" thickness) in pure A and pure B. N_A and N_B are $C_A\ a_{AB}^{-3}$ and $C_B\ a_{AB}^{-3}$ respectively, where a_{AB} is the monolayer thickness of the alloy.

The atomic sizes (in nm.) can be derived from the relation

$$\rho\ N_o\ a^3 = 10^{21} \times (\text{atomic weight}) \qquad 4.18$$

where ρ is the density (in gm/cm^3) and N_o is the Avogadro's number.

The Auger signals can be taken as any quantity proportional to the Auger intensity. M. Seah[19] recommends

the use of the differential spectrum, taking the height of the negative peak from the background (high energy side) as the measure of the Auger signal, removing in this way the effects of peak shape changes, associated with changes in the energy loss structure.

In the present experiments on Cu Ni and AgPd no noticeable difference was found between the results using this value or the more conventional peak to peak height in the differential spectrum, so this later value was used since it is easier to measure.

Taking the ratio of equation 4.16 to equation 4.17 one obtains the expression

$$\frac{I_A/I_A^{\infty}}{I_B/I_B^{\infty}} = \left[\frac{1 + r_{AB}(E_A)}{1 + r_{AB}(E_B)}\right] \frac{d_{AB}(E_A)}{d_{AB}(E_B)} \left[\frac{1 + r_B(E_B)}{1 + r_A(E_A)}\right] \frac{d_B(E_B)}{d_A(E_A)} \frac{a_A^3 C_A}{a_B^3 C_B} \qquad 4.19$$

in which one can include the relation $C_A + C_B = 1$ in order to get an expression for the composition C_A in the alloy in terms of the measured Auger signals. This expression is

$$C_A = \frac{I_A}{I_A + I_B/P_{rel}(B,A)} \qquad 4.20$$

where $P_{rel}(B,A)$, the relative elemental sensitivity factor, is given by

$$P_{rel}(B,A) = \frac{I_B^{\infty}}{I_A^{\infty}} F(B,A) \qquad 4.21$$

and F(B,A) is the so called "matrix correction factor"[20], that takes into account matrix effects like backscattering, density and escape depths. It is given by

$$F(B,A) = \left[\frac{1 + r_{AB}(E_B)}{1 + r_{AB}(E_A)}\right] \frac{d_{AB}(E_B)}{d_{AB}(E_A)} \left[\frac{1 + r_A(E_A)}{1 + r_B(E_B)}\right] \frac{d_A(E_A)}{d_B(E_B)} \frac{a_B^3}{a_A^3} \qquad 4.22$$

F(B,A) depends implicitly on the alloy composition and this complicates the calculation of C_A using equation 4.20.

Hall and Morabito[20] have evaluated F(B,A) in the limit of dilute alloys and have tabulated it for 4860 AB pairs showing that its mean value is unity but the standard deviation from this mean is 50%. This means that neglecting the matrix effects, i.e. taking $P_{rel}(B,A) = I_B^{\infty}/I_A^{\infty}$, F(B,A)= 1 as is commonly done, can lead to large errors in the quantification. This is specially important in studies of surface segregation where neglecting the importance of F(B,A) can easily produce an apparent surface enrichment in one of the alloy components.

However, F_{BA} is not in general a strong function of composition; in fact it has been found that it has nearly the same value at both ends of an alloy series ($C_A \to 0$ and $C_A \to 1$) even though its value can be far from unity. This

can be explained as the result of a mutual cancellation of some of the terms in equation 4.22 as the composition changes. F(B,A) is often taken as a constant for all compositions, under the assumption that $\left[1+r_{AB}(E)\right] d_{AB}(E)$ is independent of concentration.

That approximation can be improved assuming that the function $\left[1 + r_{AB}(E)\right] d_{AB}(E)$ is a linear function of the concentration C_A. So one can write

$$\left[1 + r_{AB}(E_A)\right] d_{AB}(E_A) = a + b\ C_A \qquad 4.23$$

$$\left[1 + r_{AB}(E_B)\right] d_{AB}(E_B) = c + d\ C_A \qquad 4.24$$

and evaluate the constants a,b,c,d going to the limits $C_A = 0$ and $C_A = 1$. In this way one obtains

$$a = \left[1+r_B(E_A)\right] d_B(E_A)$$
$$b = \left[1+r_A(E_A)\right] d_A(E_A) - \left[1+r_B(E_A)\right] d_B(E_A)$$
$$c = \left[1+r_B(E_B)\right] d_B(E_B)$$
$$d = \left[1+r_A(E_B)\right] d_A(E_B) - \left[1+r_B(E_B)\right] d_B(E_B)$$

and

$$F(B,A) = \frac{a_B^{\,3}\ d_A(E_A)\left[1+r_A(E_A)\right]}{a_A^{\,3}\ d_B(E_B)\left[1+r_B(E_B)\right]} \quad \frac{\left[a+b\ C_A\right]}{\left[c+d\ C_A\right]} \qquad 4.25$$

In binary alloy systems in which surface enrichment takes place, the alloy composition is obviously inhomogeneous so the expressions derived above are not in principle

applicable. By choosing Auger electrons with small escape depth one can, however, estimate the average composition in the near surface region, i.e. the composition that would correspond to a homogeneous distribution of the alloy components within the sampled escape depth. It is clear that the smaller this escape depth, the closer will be this average value to the composition at the topmost layer.

Most theoretical and experimental studies of surface segregation show that at equilibrium the enrichment is limited to a few atomic layers, being more pronounced at the topmost one. The average composition of the segregating component obtained using equation 4.20 will then correspond to a lower limit of its composition at the first monolayer.

4.3.5 Enrichment restricted to the first monolayer.

An upper limit to the composition at the topmost layer can be obtained assuming that the enrichment is restricted to this layer and the rest of the sample has a known bulk composition.

Let us then consider a system that consists of an alloy substrate of a given homogeneous bulk composition C_A, C_B on which there is a surface layer of a different composition X_A, X_B.

If there were no overlayer the situation would correspond to the homogeneous case studied above and the Auger signals I_A, I_B would be given by equations 4.16 and 4.17. Let us call these signals I_A^m and I_B^m respectively. If one includes now the overlayer of composition X_A, X_B, the Auger signals would correspond to the bulk signals I_A^m, I_B^m attenuated on passing through the overlayer, plus some additional signals originating in the overlayer.

The detected Auger signals I_A, I_B are then given by

$$\frac{I_A}{I_A^\infty} = \frac{I_A^m}{I_A^\infty} e^{-1/d(E_A)} + X_A(1 - e^{-1/d(E_A)}) \left[\frac{1 + r_{AB}(E_A)}{1 + r_A(E_A)} \right] \qquad 4.26$$

$$\frac{I_B}{I_B^\infty} = \frac{I_B^m}{I_B^\infty} e^{-1/d(E_B)} + (1 - X_A)(1 - e^{-1/d(E_B)}) \left[\frac{1 + r_{AB}(E_B)}{1 + r_B(E_B)} \right] \qquad 4.27$$

where d(E) is the escape depth of electrons with energy E in a medium of the same composition of that of the overlayer, and $\left[1+r_{AB}(E)\right]$ is the backscatering factor in the bulk matrix.

Taking the ratio of equations 4.26 and 4.27 and using equations 4.16 and 4.17 for I_A^m/I_A^∞ and I_B^m/I_A^∞ one gets an expression from which the surface composition X_A is obtained as

$$X_A = \frac{I_A c_1 - (I_B/S)\, c_2}{I_A c_3 + (I_B/S) c_4} \qquad 4.28$$

where

$$S = I_B^\infty / I_A^\infty$$

$$c_1 = \left[1 + r_{AB}(E_B)\right]\left[1 + r_A(E_A)\right] d_A(E_A)\left[C_B d_{AB}(E_B) a^3 e^{-1/d(E_B)} + d_B(E_B)\, a_{AB}^3\,(1 - e^{-1/d(E_B)})\right]$$

$$c_2 = C_A\left[1 + r_{AB}(E_A)\right]\left[1 + r_B(E_B)\right] d_{AB}(E_A) d_B(E_B)\, a^3{}_A\, e^{-1/d(E_A)}$$

$$c_3 = \left[1 + r_{AB}(E_B)\right]\left[1 + r_A(E_A)\right] d_B(E_B) d_A(E_A)\, a_{AB}^3\,(1 - e^{-1/d(EB)})$$

$$c_4 = \left[1 + r_{AB}(E_A)\right]\left[1 + r_B(E_B)\right] d_A(E_A) d_B(E_B)\, a_{AB}^3\,(1 - e^{-1/d(E_A)})$$

The bulk matrix monolayer thickness a_{AB} can be taken as the weighted average of the monolayer thickness of the pure components

$$a_{AB} = C_A\, a_A + C_B\, a_B \qquad 4.29$$

The overlayer thickness is in general different from a_{AB} and will be taken as

$$a = X_A\, a_A + X_B\, a_B \qquad 4.30$$

It is needed for the evaluation of d(E).

A computer programme has been developed that calculates the "surface composition" of substitutional binary alloys from the measured Auger electron signals using both equation 4.20 and equation 4.28.

Details of this programme are given in the Appendix.

References (Chapter 4)

1. T.A. Carlson, "Photoelectron and Auger Spectroscopy", N.Y. Plenum (1975).

2. D. Chattarji, "The Theory of Auger Transitions", Academic Press (1976).

3. M.F. Chung and L.H. Jenkins, Surf. Sci. 22 (1970) 479.

4. W.A. Coghlan and R.E. Clausing, Atomic Data 5 (1970) 317.

5. P. Palmberg, G. Riach, R. Weber, N. MacDonald, "Handbook of Auger Spectroscopy", Physical Electronics Industries, Inc. (1972).

6. G.E. Mc. Guire, "Auger Electron Spectroscopy Reference Manual", Plenum Press, N.Y. (1979).

7. M. Salmeron, A.M. Baro and J.M. Rojo, Phys. Rev. B 13 (1976) 4348.

8. L.I. Ying, T. Tsang and I. Adler, Phys Rev. B 15 (1977) 2974.

9. J. Onsgaard, Physica Scripta 25 (1982) 896.

10. J.M. Mariot, C.F. Hague and J. Dufour, Phys. Rev. B 23 (1981) 3164.

11. M.P. Seah, Analusis 9(1981) 171.

12. J.C. Shelton, J. Electron Spectrosc. 3 (1974) 417

13. M.P. Seah and W.A. Dench, Surf. and Interf. Anal. 1 (1979) 2.

14. W. Reuter, in Proc. 6th Intern. Conf. on X-Ray Optics and Microanalysis, Eds. G. Shinoda, K. Kohra and T. Ichinokawa (Univ. of Tokyo Press, Tokyo, 1972) p. 121.

15. J.A. Bearden and A.F. Burr, Rev. of Modern Phys. 39 (1967) 125.

16. K.D. Sevier, Atomic and Nuclear Data Tables, 24 (1979) 323.

17. S. Ichimura and R. Shimizu, Surf. Sci. 124 (1983) L49 .

18. A. Jablonski Surf. Sci. 124 (1983) 39.

19. M.P. Seah, Surf. and Interface Analysis 1 (1979) 86.

20. P.M. Hall and J.M. Morabito, Surf. Sci. 83 (1979) 391.

CHAPTER 5

EXPERIMENTAL EQUIPMENT AND SAMPLE PREPARATION

Experimental measurements of the surface composition in CuNi and AgPd alloys were performed using Auger Electron Spectroscopy (AES) and Low Energy Electron Diffraction (LEED) in an ultra high vacuum (UHV) system. The equipment and methods that were used are described below.

5.1 Ultra high vacuum system and ancillary equipment

Most of the experiments presented in this work were performed in a LEED/AES, stainless steel ultra high vacuum system. The experimental chamber, gas handling manifold and pumping system were arranged as shown schematically in figure 5.1.

The experimental chamber, with a volume of approximately 20 l. is rough pumped with two sorption pumps and UHV is obtained by using a 140 l/sec. diode ion pump (Ferranti FJD145)

Pressure in the chamber is measured with a Bayard Alpertionization gauge. After a 12 hour bakeout at 200^{o}C, pressure was typically in the 10^{-10} torr range.

The gas handling line was fitted with two gas bottles (research grade CO and O_2, BOC, 11, 760 torr). It is

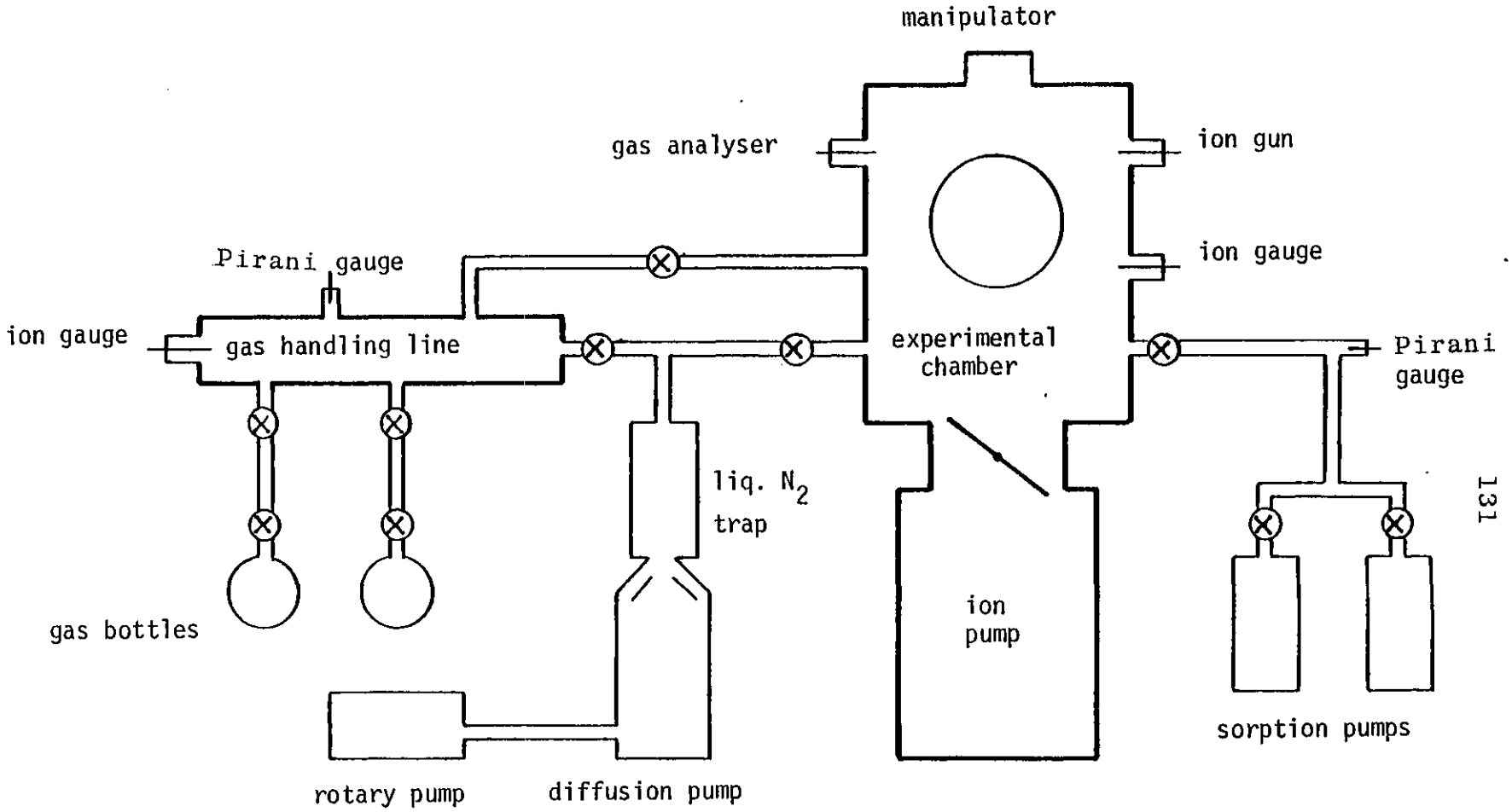


Figure 5.1 Schematic diagram of the ultra high vacuum system.

connected to the experimental chamber by a leak valve (VG., MD6) and is pumped by a liquid nitrogen trapped diffusion pump (Edwards, E02). Pressure in this line could be measured either with an ionization gauge or with a Pirani gauge.

The diffusion pump could also be connected to the experimental chamber in order to pump argon during ion sputtering of the sample or to speed up the pumping of gases in adsorption experiments.

A quadrupole residual gas analyser (Centronic, Q806), fitted to one of the ports in the experimental chamber, was used to monitor residual gas partial pressures and for routine leak testing. For thermal desorption experiments a VG Micromass QX200 gas analyser was used.

An ion gun (VG, AGS2), fitted to the experimental chamber, was used for argon ion bombardment of the sample. An Ar bottle (research grade, BOC, 11. 760 torr) was connected to the gun through a leak valve.

A simple specimen manipulator was positioned on top of the experimental chamber on a 150 mm flange fitted with electrical feedthroughs. This manipulator allowed a specimen translation of $\sim$ 20 mm in the vertical direction, translation of $\sim$ 10 mm in the horizontal plane, 360^{o} rotation about the manipulator axis and a very limited degree of tilt.

5.2 Sample preparation

a) CuNi

CuNi samples were prepared from $Cu_{0.05}$ $Ni_{0.95}$ and $Cu_{0.5}$ $Ni_{0.5}$ random oriented alloy single crystals (Metals Research). The crystals were fixed to a goniometer and using the Laue X-Ray back reflection method[1,2] were oriented within one degree of the desired surface planes. The goniometer was then transferred to a spark erosion machine (Servomet, Metals Research) and the surface was spark planed to a smooth finish and a thin slab was spark cut. Typically the slabs were 1.5 mm thick and presented an area of 40 - 50 mm^2 of the desired surface.

The oriented sample was then mounted in plastic and mechanically polished to mirror finish on rotating pads containing different grades of diamond paste (from 16μm down to 0.25μm). The plastic mounting was dissolved in chloroform and the sample ultrasonically cleaned with Decon 75 decontaminant, distilled water, acetone and ethanol. The samples were then ready for insertion into the UHV chamber.

Pure Cu(111) and Ni(111) samples, for use as standards were prepared in the same manner.

The bulk alloy composition was determined for each sample using electron microprobe analysis. It was found to be

uniform within 0.5% of the total composition. After being cleaned in the UHV system and studied with AES and LEED, the Cu, Ni and some CUNi samples were taken out of the vacuum chamber and electropolished in a mixture of 80% ethanol and 20% perchloric acid[3]. Subsequent analysis by LEED and AES did not show any difference with the results obtained when the samples were polished only mechanically.

b) AgPd

$Ag_{0.01}$ $Pd_{0.99}$ and $Ag_{0.07}$ $Pd_{0.93}$ random oriented single were obtained from Metal Crystals Ltd.

The bulk composition of the $Ag_{0.01}$ $Pd_{0.99}$ sample was determined by atomic absorption spectroscopy since the electron microprobe analysis gave unreliable results due to the superposition of the Ag and Pd signals and to the low Ag content. The composition of the $Ag_{0.07}$ $Pd_{0.93}$ was determined by electron microprobe analysis.

Polycrystalline samples of pure Ag and Pd to be used as standards were prepared by cold rolling 1mm thick high purity metal wires.

Samples with the desired surfaces were prepared following the procedure described above for CuNi. Polishing with 0.25μm diamond paste produced surface damage ("orange peel" effect). However, polishing with a paste formed from magnesium oxide and distilled water

gave a good mirror finish. These samples were not electropolished.

c) PdS

In order to calibrate Auger signals of sulphur on AgPd, a powder sample of PdS was prepared. H_2S gas, obtained by mixing hydrochloric acid with iron sulphide, FeS, was made to circulate through a solution of K_2PdCl_4 in destilled water at room temperature. The palladium sulphide, PdS, which precipitated as a dark brown powder was filtered, washed and dried, and finally pressed onto a polished aluminium sheet. This sample was then transferred to the UHV chamber for analysis.

5.3 Sample holder

For the work on CuNi the sample holder shown in figure 5.2a was made. Up to three samples could be mounted (typically Cu, Ni and CuNi). The samples were spot welded to the "U" shape stainless steel support and radiatively heated from behind by 0.1 mm W heating filaments. The temperature of the CuNi sample was monitored through a chromel/alumel thermocouple spot welded to its side.

A different kind of sample holder was made for the work on AgPd, as shown in figure 5.2b. The sample is spot welded between two 0.15 mm Ta wires which are themselves spot welded to 1 mm thick Ta wires embedded in Cu blocks. The Cu blocks were isolated from the stainless steel backing plate by

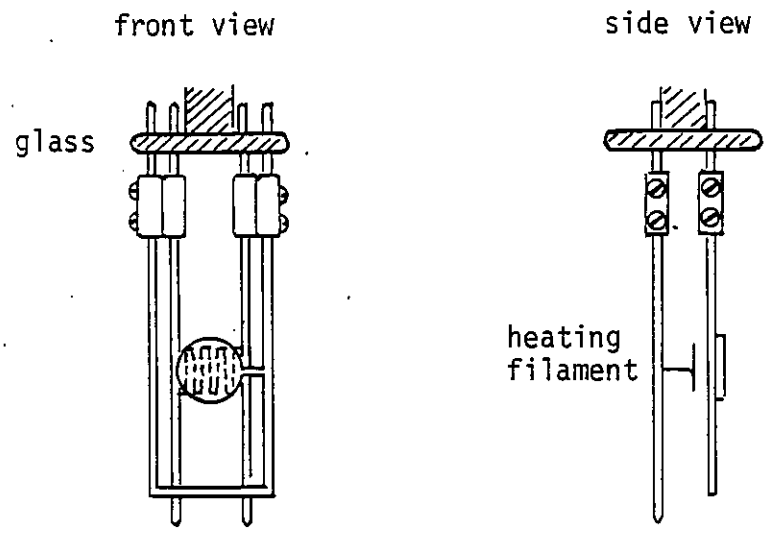


Figure 5.2a Sample holder used for work on CuNi

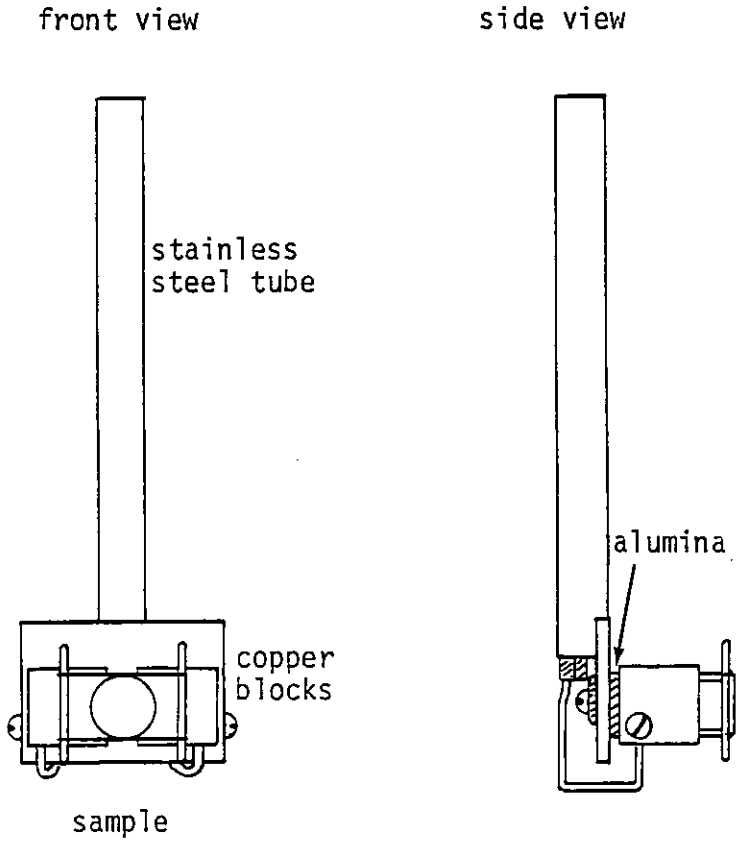


Figure 5.2b Sample holder used for work on AgPd.

alumina spacers. The sample could be resistively heated by passing current through the supporting wires. Temperature measurement is performed by a chromel/alumel thermocouple spot welded to the side of the sample. The thermocouple wires and the Cu wires used to take current to the heater, were isolated by alumina tubes and taken inside a stainless steel tube, fixed to the manipulator. Connections to the sample, heater and thermocouple were made via the electrical feedthroughs in the manipulator flange.

This mounting is very suitable for thermal desorption experiments and in general for controlled sample heating since the sample temperature responds very rapidly to the heating current. Although it was not tested here, sample temperatures of about 100K can be achieved by cooling the copper blocks with liquid nitrogen[4]. The robust finish of this holder and the dual function of the Ta wires as heaters and holders made it very easy to change samples.

5.4 Temperature controller

A temperature control circuit, based on the design of Herz et al.[4] was used for annealing and thermal desorption experiments on AgPd samples.

The heating current is provided by a programmable power supply. The e.m.f. generated by the thermocouple is fed into a programmer circuit which controls the power supply. By comparing the thermocouple e.m.f. with the voltage of a built

in ramp generator an error signal V_{error} is produced which controls the current flowing through the heater in order to produce a linearly varying thermocouple e.m.f.

Figure 5.3a shows a block diagram of the different parts of the circuit.

The preamplifier V_1 consists of a differential amplifier followed by an isolation amplifier (Analog Devices 284J). Amplification of this stage is 100x and isolation is up to 2500 V. A specimen temperature variation from 100K to 1500K, monitored with a chromel/alumel thermocouple with the reference junction at room temperature, will produce a voltage variation from -0.5V to 5V at the output of V_1.

C_1 is an amplifier which substracts an adjustable voltage V_{comp} from the output of the isolating preamplifier. Its output, termed V_{actual} represents the true temperature of the specimen, and is given by $V_{actual} = 2(100 \text{ e.m.f.} - V_{comp})$. By adjusting V_{comp}, V_{actual} is made positive.

RG generates a linear voltage ramp (termed $V_{nominal}$), varying between the values V_{start} and V_{stop}, which represents the target specimen temperature. V_{start}, V_{stop} and the rise time are adjustable over a wide range. This ramp generator comprises an integrator, a difference amplifier for fixing V_{start}, an adjustable clamp for fixing V_{stop} and a voltage follower.

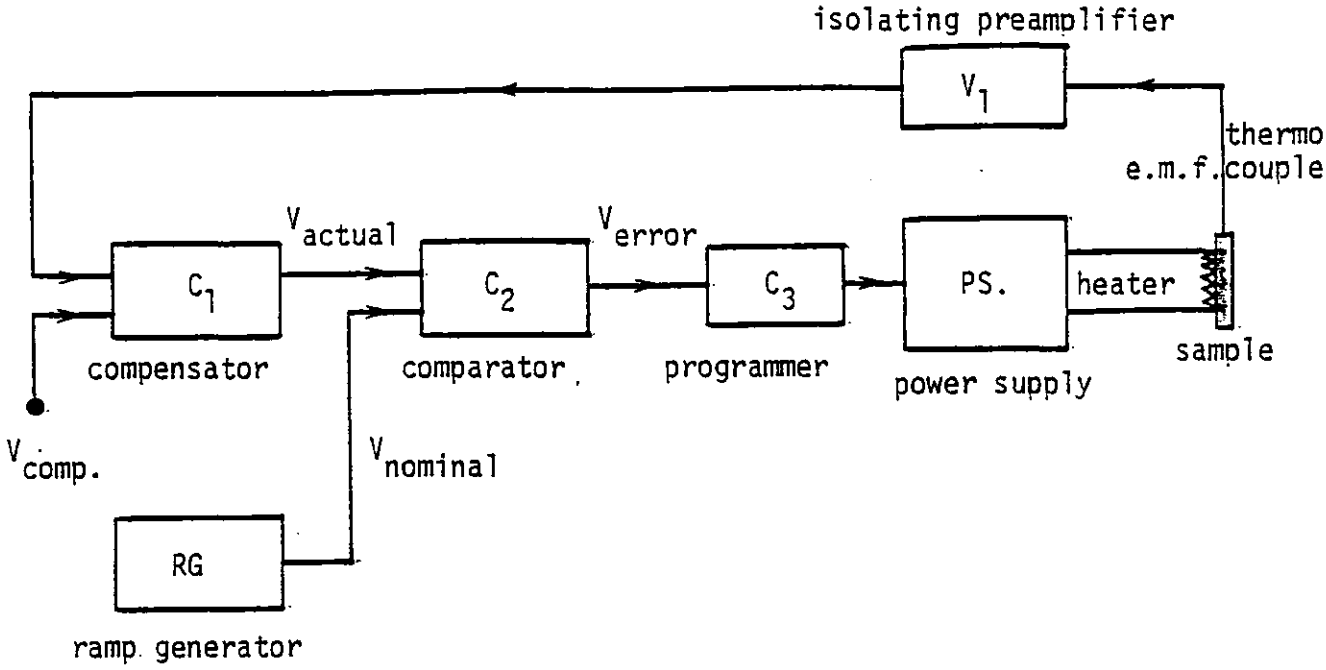


Figure 5.3a Schematic diagram of the temperature controller.

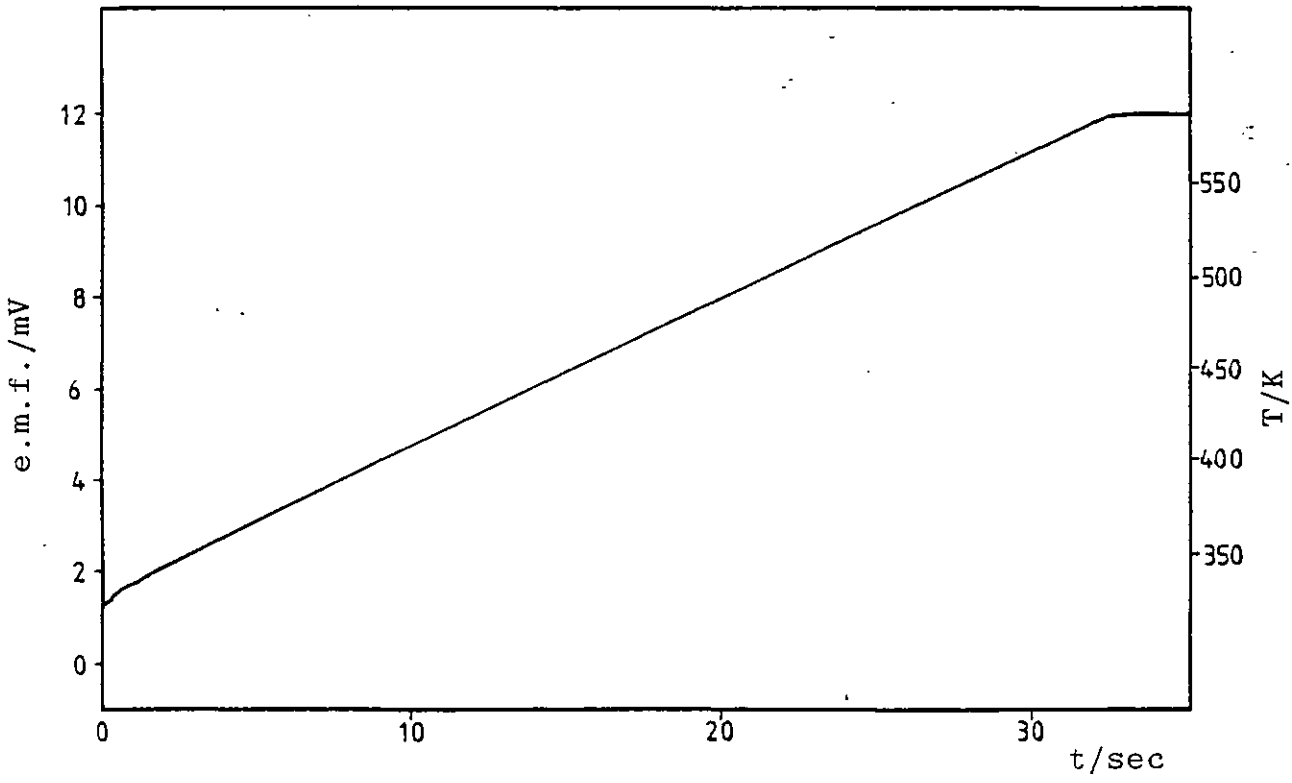


Figure 5.3b Heating curve T(t) of a AgPd specimen obtained using the temperature controller.

The voltage $V_{nominal}$ produced by the ramp is compared with V_{actual} in the comparator C_2. C_2 consists of a difference amplifier with a gain of 30x whose output $(V_{actual} - V_{nominal}) \times 30$ is fed to an amplifier with adjustable gain G and then fed via a voltage follower to the power supply controller C_3. The output of C_2 is an error signal $V_{error} = (V_{nominal} - V_{actual}) \times 30 \times G$. When the specimen temperature is lower than the target temperature, the positive voltage V_{error} is fed to C_3 which causes more current to flow through the heater. The amount of current necessary is controlled by the gain G and depends on the characteristics of the heater-specimen system.

The function of C_3 is to transform the error signal into the programming signal required by the particular power supply. In this case a Solartron AS 1412.2 was used.

Figure 5.3b displays a typical heating curve obtained by using this temperature controller in a TDS experiment.

5.5 LEED experimental arrangement

Low energy electron diffraction was used to identify the different crystalline surfaces, to study the structure formed by adsorbates and for a qualitative study of intensity variation with primary beam energy.

Figure 5.4 shows schematically the experimental arrangement used to record LEED patterns. A three grid LEED optics

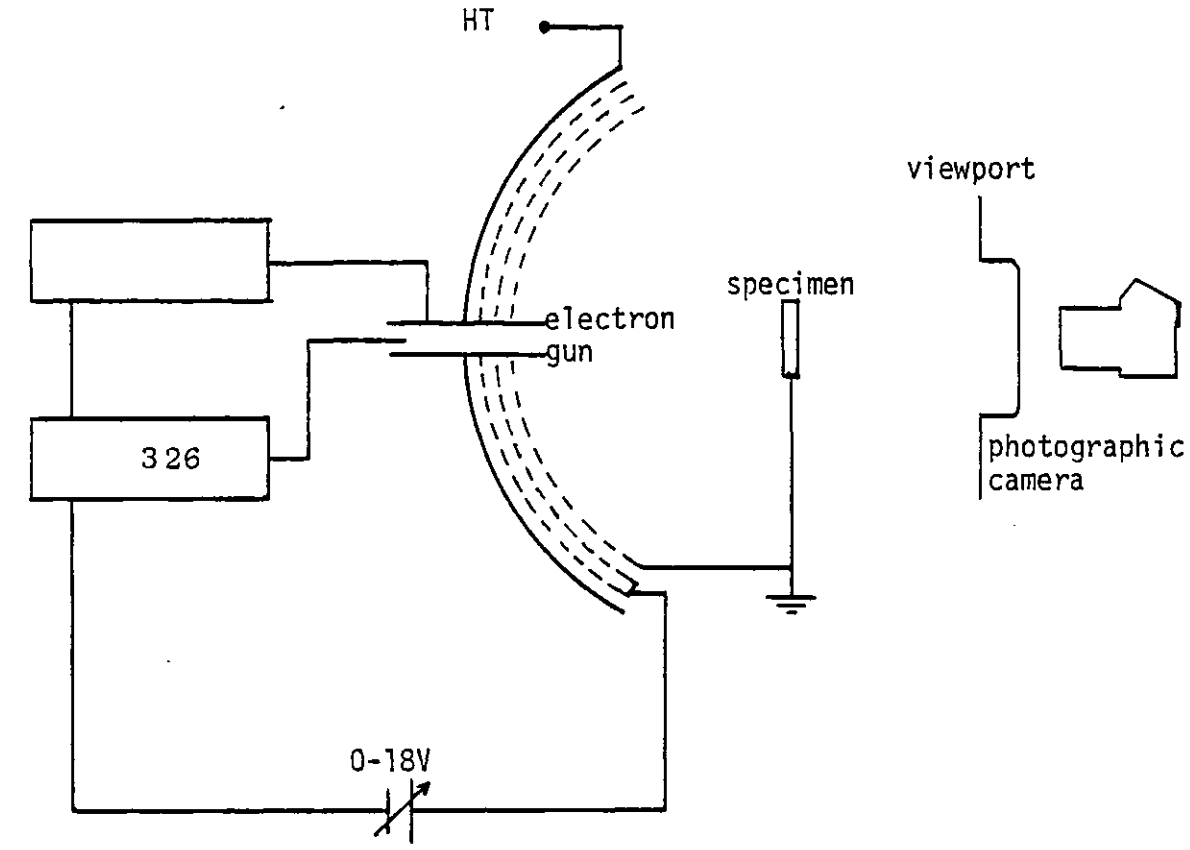


Figure 5.4 Experimental arrangement used for LEED.

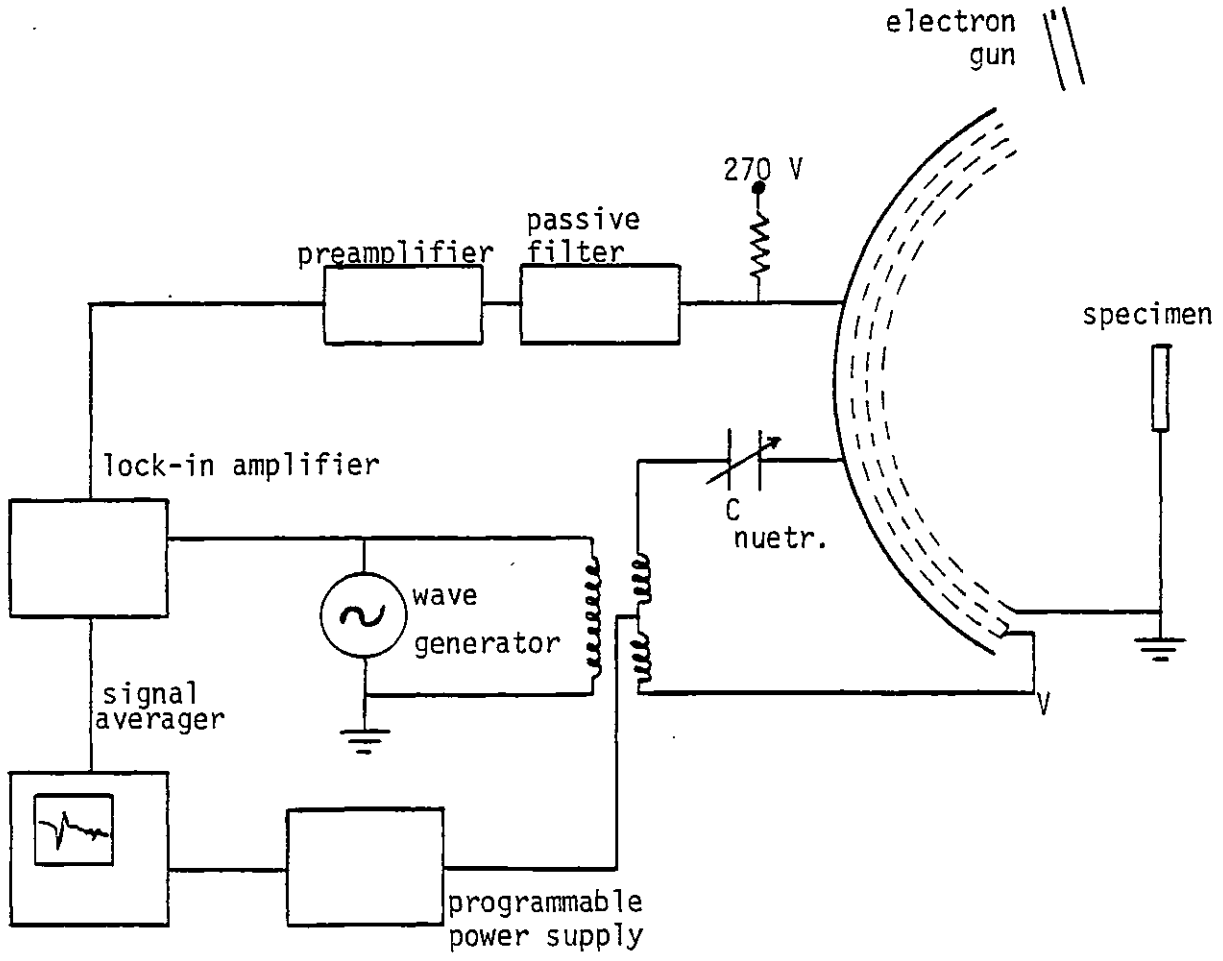


Figure 5.5 Experimental arrangement used for AES.

(Vacuum Generators) was used with the retard potential applied to the two inner grids. A VG 326 power supply controls the electron beam intensity and energy, and the retard potential. A separate power supply was used to bias the anodes of the electron gun.

The phosphor screen was held at a positive HT potential between 5 and 9 KV. LEED patterns were recorded with a 35 mm reflex camera using 400 ASA film. Exposure times varied between 1 and 10 seconds.

5.6 AES experimental arrangement

The same three grid optics was used as a retarding field analyser (RFA) for AES. The operation of the RFA for the energy analysis of the electron distribution N(E) has been reviewed by many authors[5,6].

The electrons collected in the RFA are those with enough kinetic energy to overcome the retarding potential V, so the output signal is proportional to the integral of the electron energy distribution N(E),

$$I(V) \propto \int_{E}^{E_{max}} N(E')dE' \qquad (E = eV) \qquad 5.1$$

In order to obtain the electron energy distribution curves N(E), the I(V) curve have to be differentiated with respect to the retard potential V. This can be efficiently done electronically by superposing a small AC modulation

voltage $\Delta V = K \sin \omega t$ on the retarding voltage V and detecting the collector signal with a lock-in amplifier.

It can be shown[6] that the collected current $I(V + \Delta V)$ can be expressed as

$$I(V+\Delta V) \approx I_o(V) + I'(V)k\sin \omega t - \frac{1}{4}I''(V)k^2 \cos 2\omega t \qquad 5.2$$

provided that the k^3 and higher order terms can be neglected. This expression shows that the amplitude of the fundamental harmonic frecuency term is proportional to I'(V) i.e. to the electron energy distribution N(E) and the amplitude of the second harmonic is proportional to its derivative dN(E)/dE.

The N(E) spectrum is obtained by tuning the reference channel of the lock-in amplifier to the modulating frequency ω, and the derivative spectrum dN(E)/dE by tuning it to the frequency 2ω.

For AES the derivative spectrum dN(E)/dE is recorded. Figure 5.5 shows the experimental arrangement that was used.

A grazing incidence electron gun operated by the VG 326 power supply produces an ionizing incident electron beam.

The built-in linear ramp of a signal averager (Nicolet, 1170) drives a programmable power supply (Oltronix, A2.5K-1OHR) which produces the negative potential applied to the retarding

grids. A waveform generator produces a sinusoidal voltage which is superposed on the retard voltage through a 1:1 transformer, and applied to the reference channel of the lock-in amplifier.

The collected current is fed to a double resonant current-to-voltage converter preamplifier[7] comprising a passive resonant filter and a RLC active resonant amplifier tuned to 3400 Hz. This RLC was later replaced by a Brookdeal 431 preamplifier.

The output of the preamplifier is connected to the signal channel of the lock-in amplifier (Brookdeal, 401) and the output of the lock-in is taken to the signal averager where the spectrum is recorded.

The stray capacitance existing between the retarding grid and the collector produces a coupling signal capable of saturating the amplifier or of masking the true electronic signal. In order to minimize this effect the neutralizing capacitors $C_{neutr.}$ was included in the circuit.

Typical operating conditions for the recording of Auger spectra were:

Primary beam energy: 2800 eV.

Electron beam current: 20 μA.

Modulation frequency: 1700 H_z

Modulation amplitude: 6V peak to peak for quantitative analysis and 2-3 V peak to peak

when looking for structure in the Auger signals.

Energy resolution: $\Delta E/E \sim 2\%$.

The noise level was reduced by signal averaging the Auger spectra. For 6V modulation 16 scans were typically taken for each spectrum and for 3V modulation 32 to 64 scans were necessary.

The signal averager has the possibility of performing a limited number of data manipulation techniques like addition and substraction of spectra and simple smoothing, integration and differentiation. Recorded spectra could also be stored on magnetic tape.

5.7 XPS system

Some X-Ray Photoemission Spectroscopy (XPS) measurements were carried out on a AgPd sample. The system used was a VG Escalab. This system comprises a preparation chamber with facilities for annealing (VG., P8 probe) and argon bombardment (VG., AGS2), and an analysis chamber with a Al/Mg twin anode X-Ray source and a hemispherical sector electron energy analyser. The specimen was mounted on a stainless steel stub which could be easily transferred between the two chambers. Specimen temperature was difficult to estimate accurately due to the impossibility of having a thermocouple attached to the sample and to the poor thermal contact between the specimen and the heating probe.

References (Chapter 5)

1. E.A. Wood, " Crystal Orientation Manual", Columbia University Press, New York (1963).

2. E. Preuss, B. Krahl-Urban and R. Butz, "Laue Atlas", John Wiley & Sons (1974).

3. A. Ozkok, "Secondary Electron Emission and Energy Losses from Metal Surfaces", Ph.D. Thesis, University of London (1983).

4. H. Herz, H. Conrad and J. Kuppers, J. Phys. E. Sci. Instrum. 12 (1979) 369.

5. N.J. Taylor, Rev. Sci. Instrum. 40 (1969) 792.

6. D. Chattarji, "The Theory of Auger Transitions", Academic Press (1976).

7. D.J. Pocker, Rev. Sci. Instrum. 12 (1979) 369.

CHAPTER 6

SURFACE SEGREGATION IN CuNi. EXPERIMENTAL RESULTS.

Recent studies of surface segregation have confirmed that Cu enriches the surface of annealed CuNi alloys[1]. Most of these studies have been performed on polycrystalline materials or on single crystals with Cu bulk composition larger than 10%.

Here, experimental results and quantitative analysis of surface segregation in a $Cu_{0.05}$ $Ni_{0.95}$ single crystal alloy are presented. In order to study possible differences in surface enrichment as a function of atomic surface roughness, experiments were performed on samples exposing the low index (100) (110) and (111) faces and on samples cut 5^{o} off the (100) face along the [001] and [011] directions to show a high density of steps and steps combined with kink sites.

A $Cu_{0.5}$ $Ni_{0.5}$ (111) sample was also prepared for comparison, and Cu (111) and Ni (111) were prepared to be used as reference standards.

6.1 Experimental procedure

Specimens were cleaned in the UHV chamber by repeated cycles of argon ion bombardment followed by heat treatment. The sample was sputtered for $\sim$ 5 minutes by a 3KV , 10-20μA ion beam and then heated to about 800K in 5 minutes.

Typically 8-10 of these cycles were necessary to produce a clean surface. Some of the samples were heated and ion bombarded simultaneously.

Sample cleanliness was monitored by AES using 10V peak to peak modulation in order to increase the sensitivity. The main contaminants that have been detected were carbon and sulphur. After annealing, the sample contamination was monitored again and if the sample was clean within the limits of AES, its composition was estimated from the Cu and Ni Auger signals. Figure 6.1 shows an Auger spectrum of a contaminated CuNi sample before the cleaning procedure and after it has been cleaned and annealed for 1 hour at $\sim$ 850K.

6.2 AES evidence for Cu surface segregation.

The strong $M_{23}VV$ Auger transitions of Ni and Cu occurring at 62 and 63 eV respectively (figure 6.1) are very surface sensitive but are too close in energy to be resolved by the present experimental system and therefore can not be used to evaluate the alloy surface composition. This signal was used only for optimizing the AES set up and as a reference signal to asess the levels of contamination.

6.2.1 High energy Auger transitions.

Figure 6.2 shows 700-950 eV Auger spectra obtained from the pure Ni and Cu standards. As can be seen the 920 eV Cu (L_3VV) and the 713 eV Ni ($L_3\ M_{23}\ M_{23}$) Auger signals are

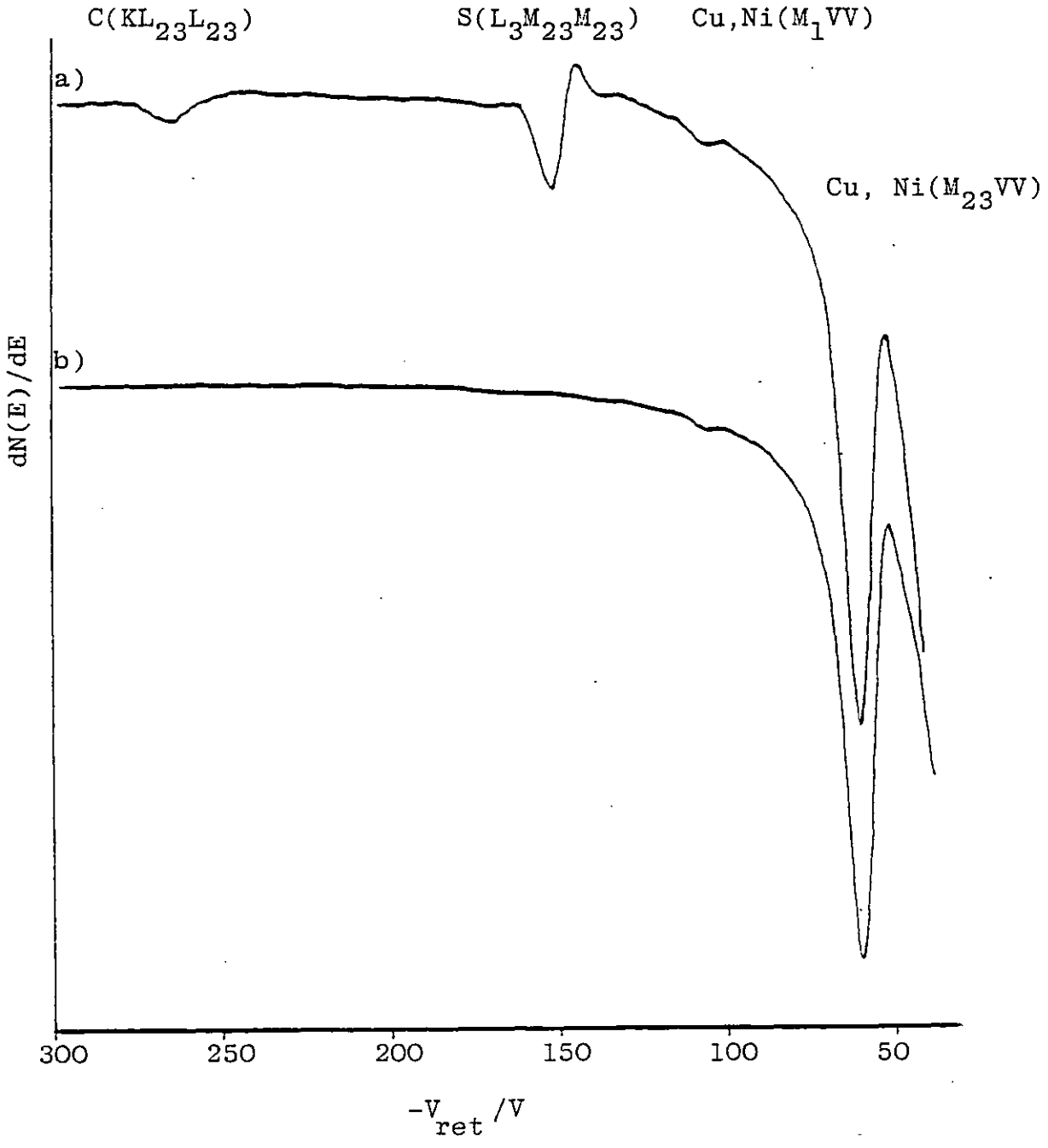


Figure 6.1 Auger spectra of a) contaminated $Cu_{0.05}Ni_{0.95}(100)$ sample; b) same sample after being cleaned and annealed for 2 hours at T = 800K.

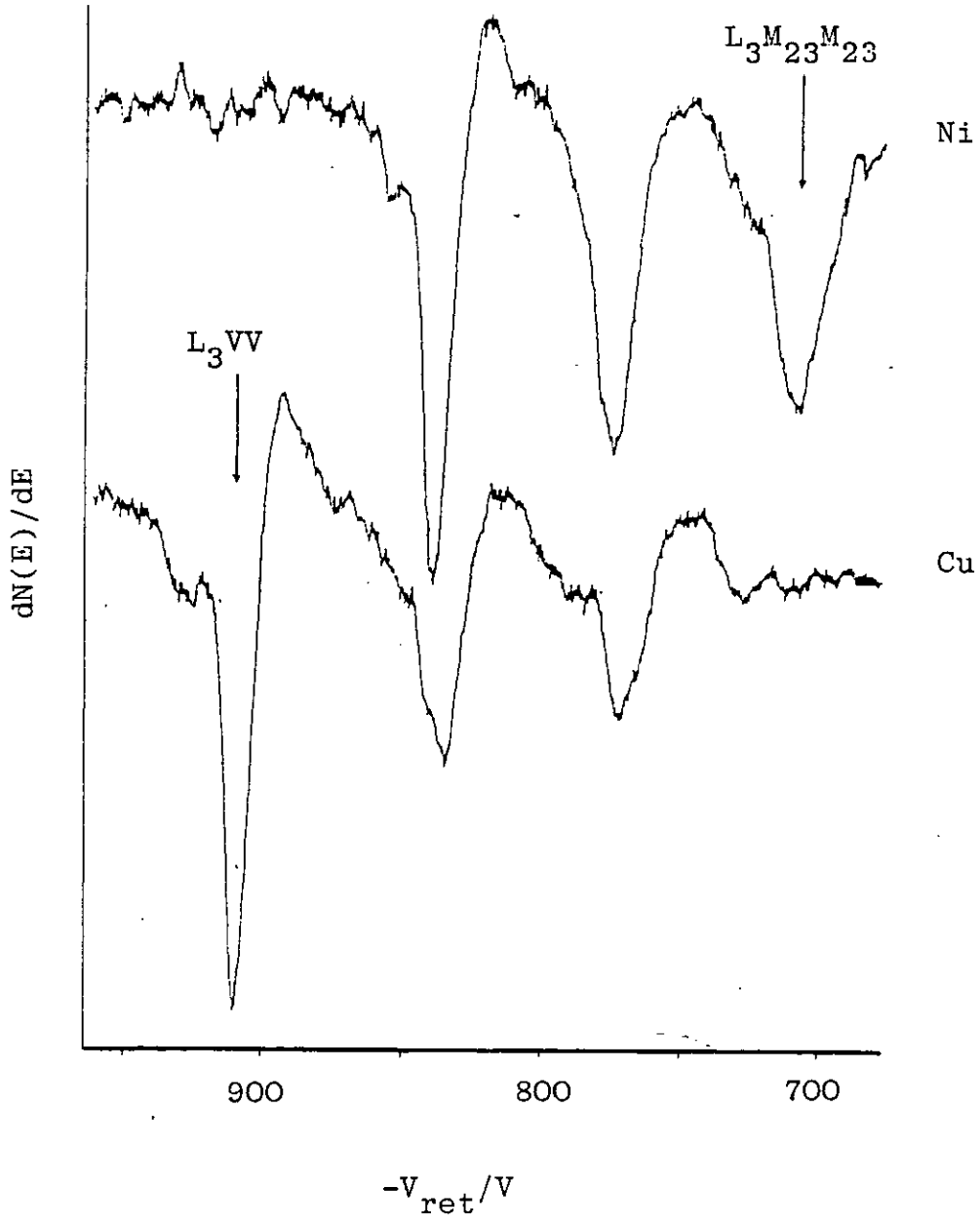


Figure 6.2 High energy Auger spectra of Ni and Cu

well resolved and can be used, together with the computing programme given in the Appendix, to calculate the CuNi surface composition. The sensitivity factor $S = I_{Ni}/I_{Cu}$ was calculated from these spectra as S = 0.43. The matrix correction factor of these transitions in the alloy was found to be fairly independent of composition, with the value F = 1.187. These Auger signals are however not very surface sensitive since their average escape depth is about 10 Å or 5 equivalent monolayers.

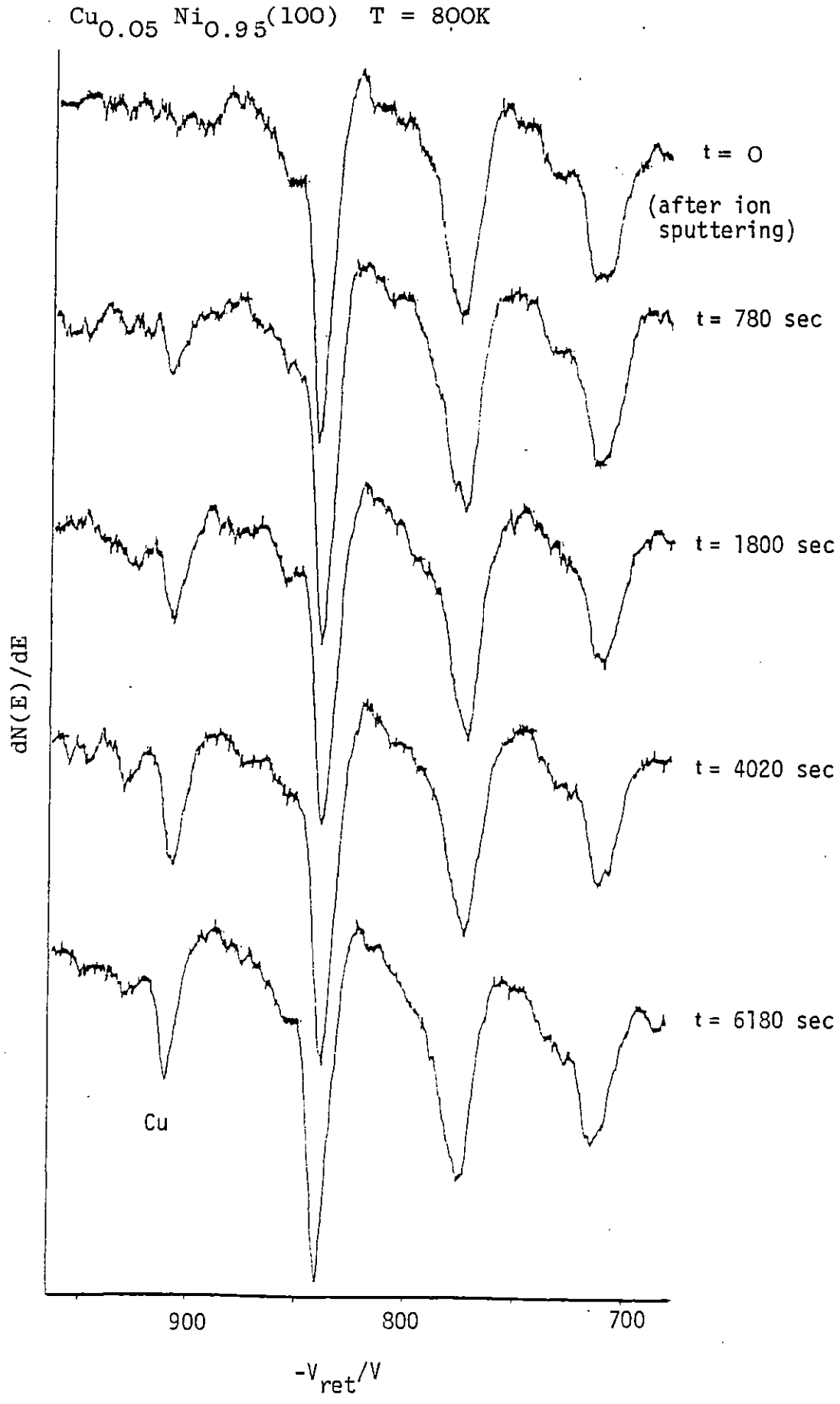
Figure 6.3 displays a series of high energy Auger spectra corresponding to a $Cu_{0.05}$ $Ni_{0.95}$ (100) specimen at 800K. The spectra were obtained while annealing the sample and the sequence corresponds to the various annealing times quoted in the figure. Note the appearance and gradual enhancement of the Cu (L_3VV) Auger feature providing direct evidence that Cu is enriching the surface region.

6.2.2 Low energy (M_1VV) Auger transitions.

The M_1VV Auger transitions of Cu and Ni at $\sim$ 100 eV are very surface sensitive since their escape depth is $\sim$ 4Å or 2 equivalent monolayers. They show, however, considerable overlap and could not be completely resolved in the alloy spectra.

Figure 6.4 displays the time evolution of the M_1VV Auger spectra for the same $Cu_{0.05}$ $Ni_{0.95}$ (100) sample at 800K. These spectra and those in figure 6.3 were obtained in the

Figure 6.3 Evidence for Cu surface segregation. High energy Auger spectra.



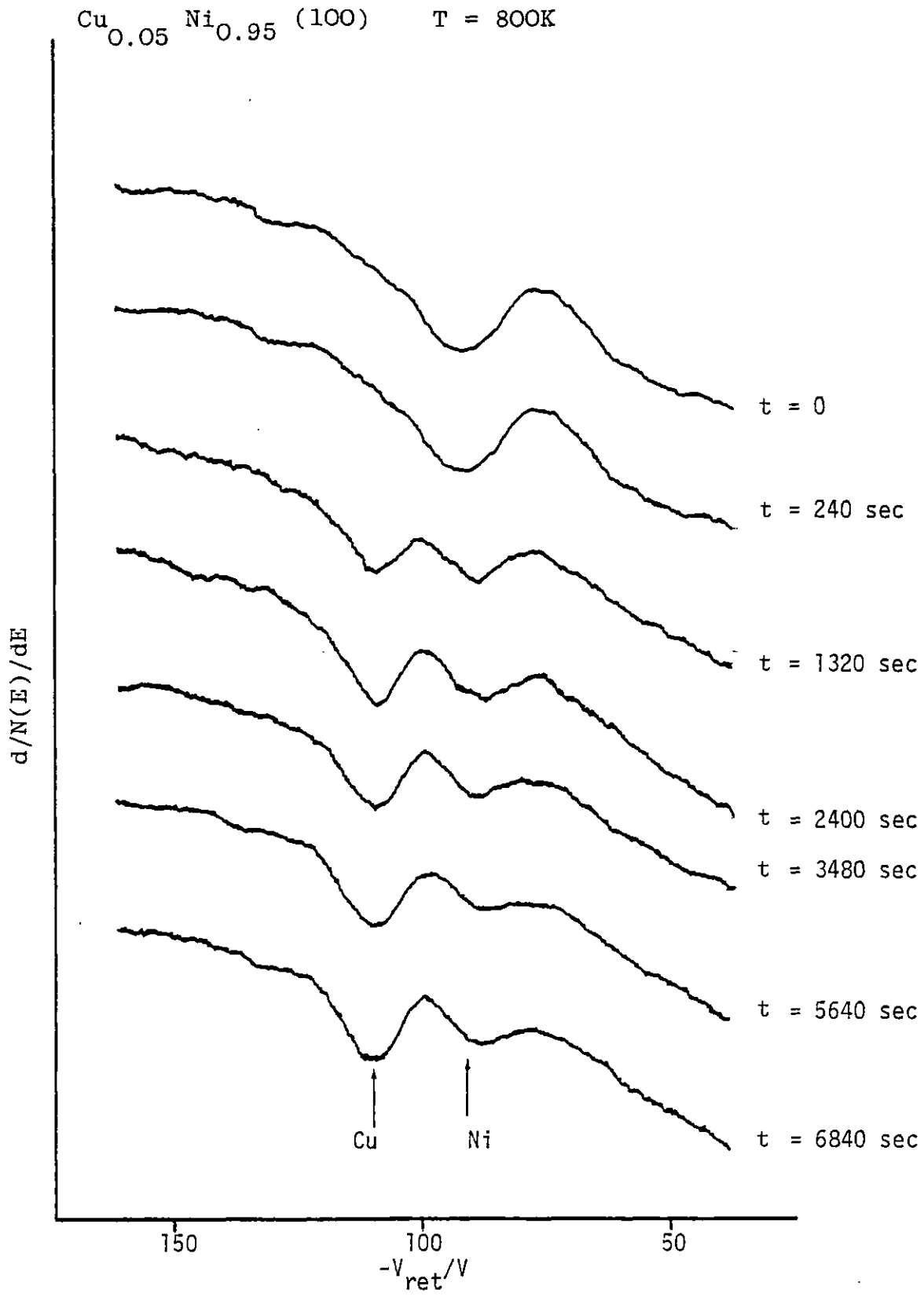


Figure 6.4 Evidence for Cu surface enrichment. Low energy spectra. (The arrows correspond to the minima incursions of the spectra for the pure elements).

same experiment.

Initially, after ion sputtering, the Auger spectrum shows a single feature, corresponding to Ni and gradually, as the annealing proceeds, the Cu signal emerges while the Ni signal diminishes.

6.3 Quantitative analysis of the surface composition using the M_1VV Auger signals.

The overlap between the Cu and Ni M_1VV signals precludes the use of the computing programme given in the Appendix to perform the quantitative analysis. In order to determine the surface composition of CuNi samples using these signals, spectra from clean Cu and Ni standards were recorded, stored and then added in various proportions to produce a set of simulated spectra (interval concentration 5%). These simulated spectra can then be compared to the real ones in order to estimate the alloy composition.

Figure 6.5 shows a set of simulated M_1VV spectra. The top curve (A) corresponds to the experimentally recorded spectrum of pure Ni and the bottom curve (B) that of pure Cu. The curves in between are the simulated spectra.

Comparison of figures 6.5 and 6.4 shows that the CuNi Auger spectra can be well represented by the simulated ones. This is further illustrated in figure 6.6 where the Auger spectra of a $Cu_{0.5}$ $Ni_{0.5}$ (111) sample after argon bombardment

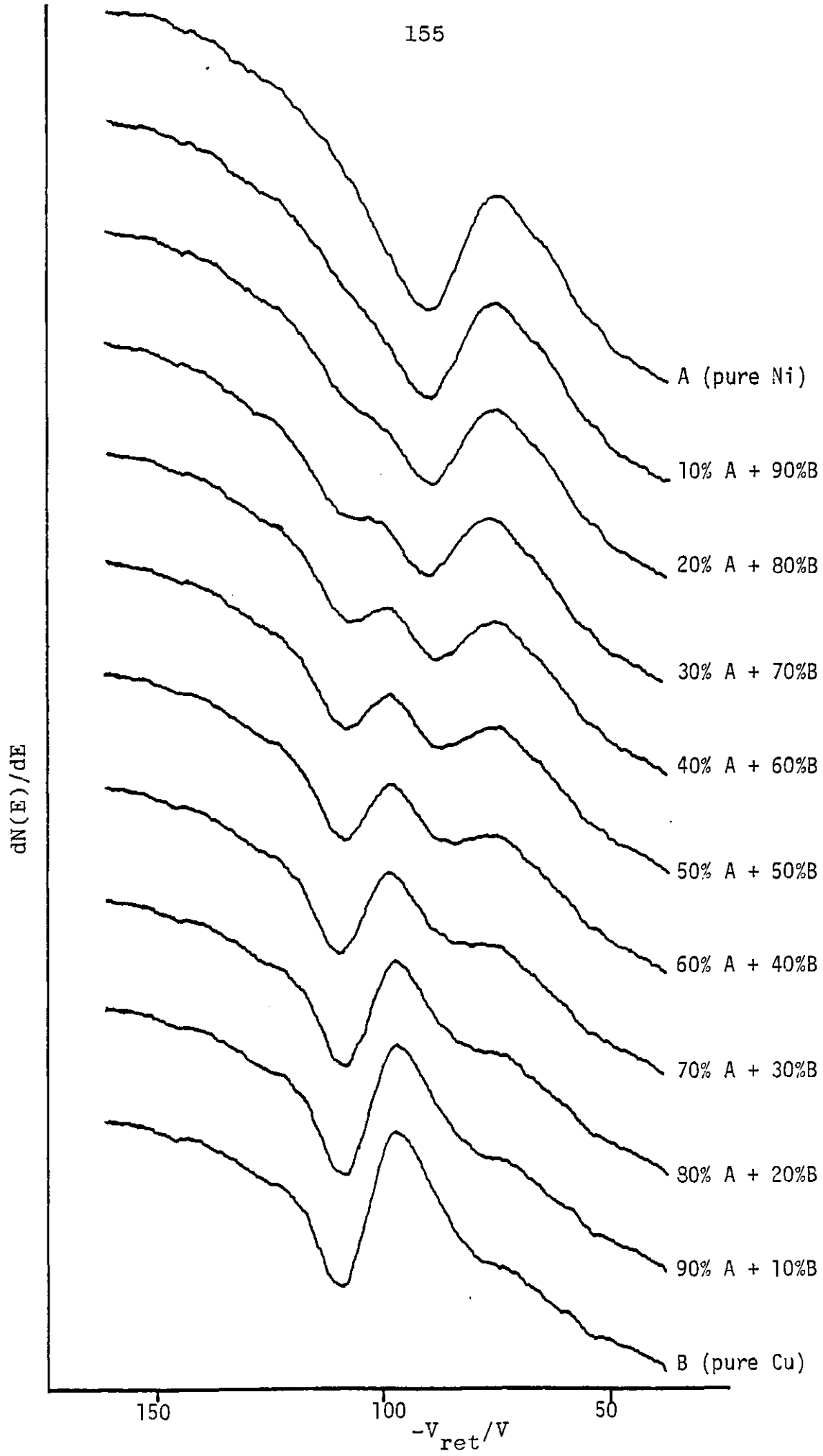


Figure 6.5 Simulated CUNi (M_1VV) Auger spectra.

and after 1 hour annealing at 723K are compared with simulated spectra.

For quantitative analysis a linear background was substracted from the simulated spectra and after measuring the peak heights h_A, h_B (fig. 6.6) the calibration curve of figure 6.7 was traced. A linear background is also substracted from the real spectra and after measuring h_A and h_B the composition is calculated using the calibration curve. For spectra in which the two peaks could not be resolved a direct comparison of the spectra was performed.

The sensitivity factor $S = I_{Ni}/I_{Cu}$ was found to be $S = 0.71$. No matrix effects are included in this method of quantitative analysis, but the matrix correction factor was calculated for a $Cu_{0.5}\ Ni_{0.5}$ sample as $F = 0.961$, so matrix effects can be neglected.

6.4 Approach to equilibrium

Annealing of the $Cu_{0.05}\ Ni_{0.95}$ (100) sample at T = 673K for approximately 4 hours failed to produce any observable Cu enrichment. Experiments performed on samples cut from the same single crystal[2] show that annealing at temperatures higher than 923K leads to irreversible Cu loss by evaporation. Annealing temperatures between 723K and 923K were then chosen for the surface segregation experiments presented here.

Figure 6.8 presents the calculated surface composition

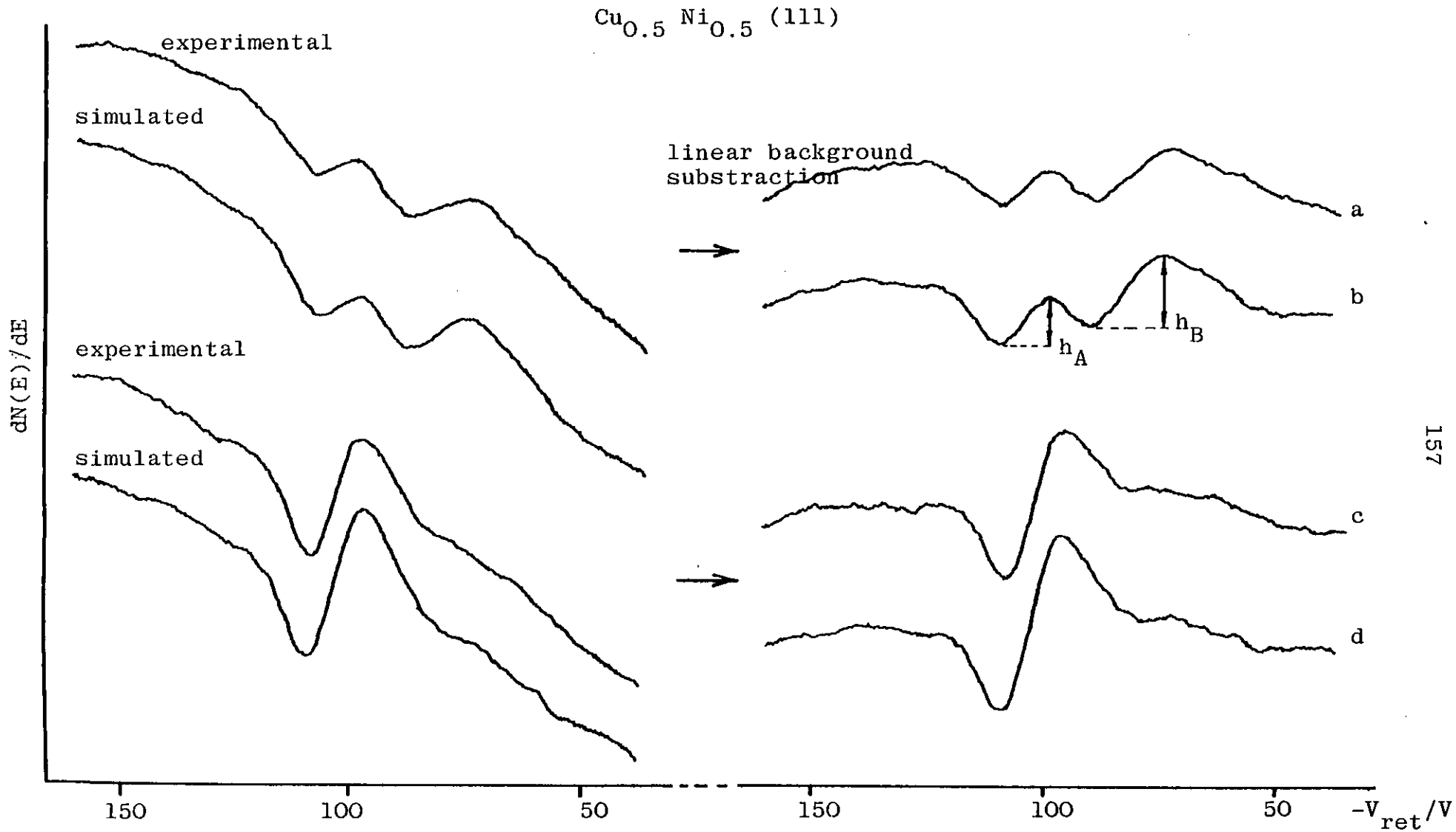


Figure 6.6 Comparison of experimental and simulated Auger spectra in $Cu_{0.5}$ $Ni_{0.5}$ (111). a) after argon bombardment. b) Simulated $Cu_{0.45}$ $Ni_{0.55}$. c) After 1 hour annealing at 723K. d) Simulated $Cu_{0.95}$ $Ni_{0.05}$

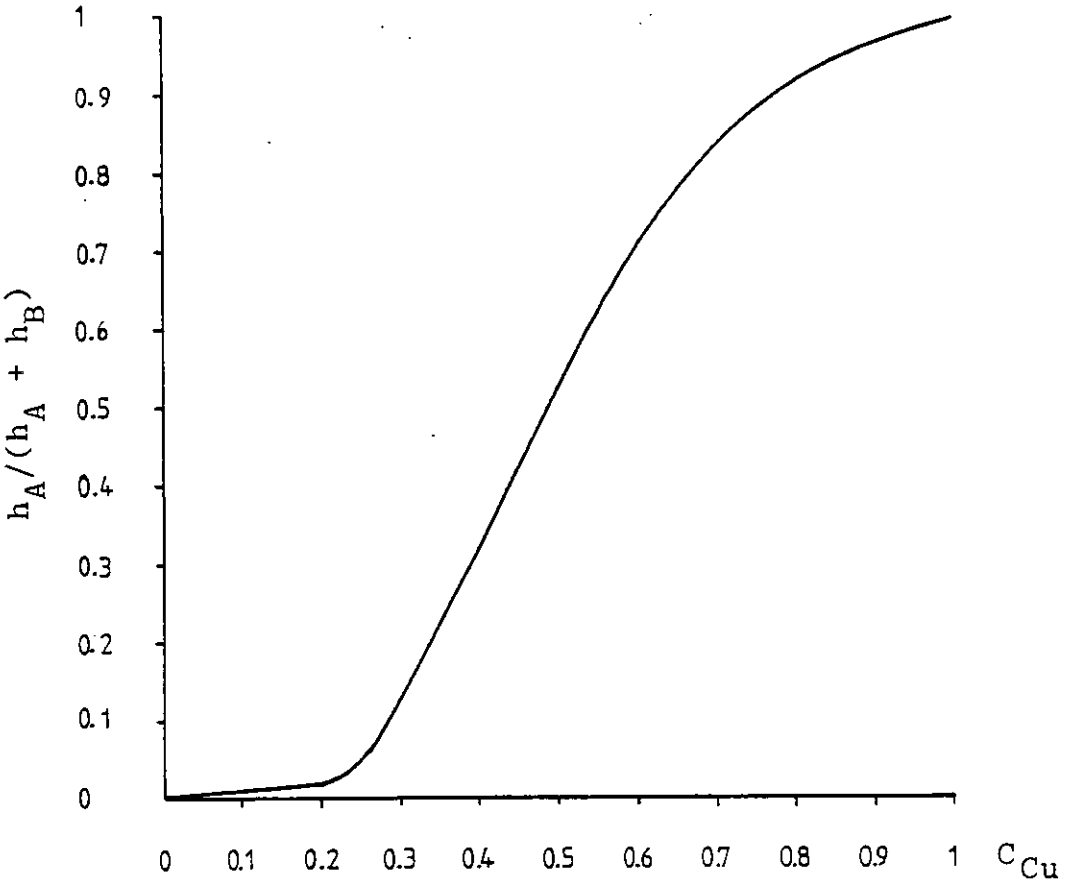


Figure 6.7 Calibration curve for CuNi (M_1VV) Auger spectra

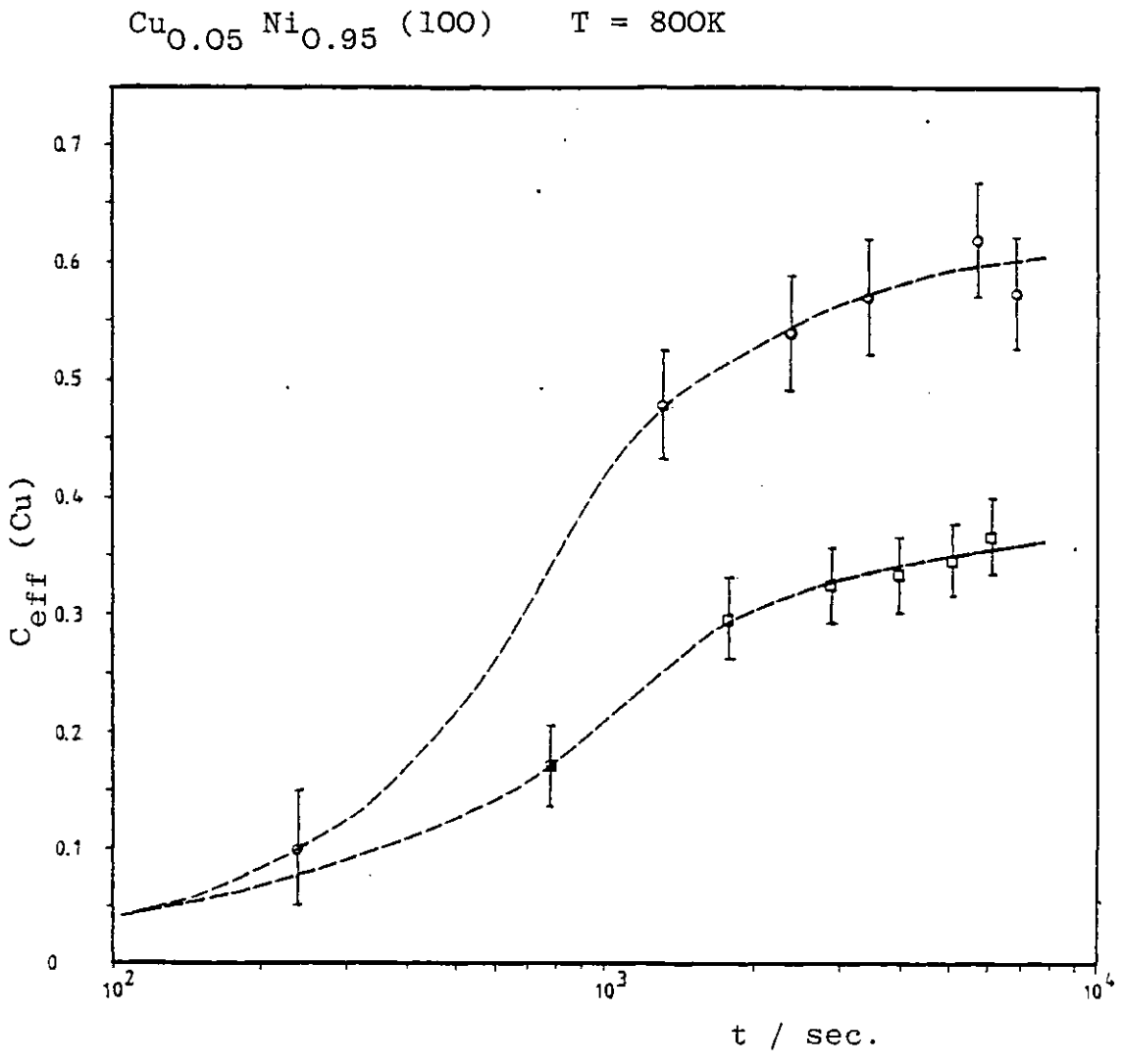


Figure 6.8 Cu "effective surface composition" as a function of time for $Cu_{0.05}$ $Ni_{0.95}$ (100) at T = 800K.

o: low energy (M_1VV) Auger signals
□: high energy (LMM) Auger signals.

Note logarithmic time scale.

as a function of time for a $Cu_{0.05}$ $Ni_{0.95}$ (100) at T = 800K, assuming uniform composition within the sampled depth. The low and high energy Auger signals used for the calculation were shown in figure 6.3 and 6.4.

As can be observed, the more surface sensitive low energy Auger transitions give a larger value of Cu enrichment than the high energy Auger transitions. After $\sim$ 2 hours annealing the low energy signals give $\sim$ 60% Cu surface composition while the high energy signals give $\sim$ 35% Cu. Note that the time scale is logarithmic. There is a fast increase in the Cu surface composition during the initial 30 minutes of annealing, after which the process slows down.

In this and in other experiments, Auger spectra were obtained while the sample was annealed and after allowing it to cool down to room temperature. No significant changes in the low or high energy Auger features were observed, even if the final equilibrium situation had not been achieved. Segregation curves like the ones in figure 6.8 could be obtained by interrupting the annealing at any time during the segregation process and then proceeding with the annealing after the room temperature Auger spectra were obtained.

Typically, specimens took less than one minute to cool down from 873K to 673K, a temperature at which no surface segregation could be observed.

6.5 Determination of the composition profile.

In the mathematical expressions relating the measured AES or XPS signals from atom A to its concentration in the alloy AB (e.g. equation 4.8), the composition profile $C_A(z)$ appears within the integral

$$\int_o^\infty C_A(z)e^{-z/d}\,dz \qquad 6.1$$

where $C_A(z)$ gives the concentration of atoms A a depth z and d is the escape depth of the characteristic electrons used in the analysis.

If the alloy AB is homogeneous ($C_A(z)$ = constant C_A)

$$\int_o^\infty C_A(z)e^{-z/d}\,dz = C_A d \qquad 6.2$$

and it becomes easy to calculate C_A from the AES or XPS measured signals.

If $C_A(z)$ is not constant but one still uses equation 6.2 to calculate the composition from the measured signals, what one obtains is an effective average composition C^A_{eff} related to the actual composition profile $C_A(z)$ according to

$$C_{eff}{}^A(d) = \left(\int_o^\infty C_A(z)e^{-z/d}\,dz\right)/d \qquad 6.3$$

Note that C^A_{eff} is not only a function of the composition profile but also of the escape depth d of the electrons used

in the analysis. Signals corresponding to different escape depth will, in general, give different values of the effective composition C^A_{eff} for the same composition profile, as was illustrated by figure 6.8.

If one can measure $C^A_{eff}(d)$ for different escape depths, one can then try to estimate the actual composition profile giving rise to the measured signals.

Figure 6.9a shows an arbitrary composition profile in which the atomic layers are denoted by the index n, 1 is the interlayer distance and C_n is the atomic fraction of atoms A within the n^{th} layer. C_n is equal to the bulk A composition C_b for $n > N$.

For this arbitrary profile the integral of equation 6.3 can be evaluated as

$$C_{eff}{}^A(d) = C_1 + \sum_{n=1}^{n} (C_{n+1} - C_n)e^{-n/d} \qquad 6.4$$

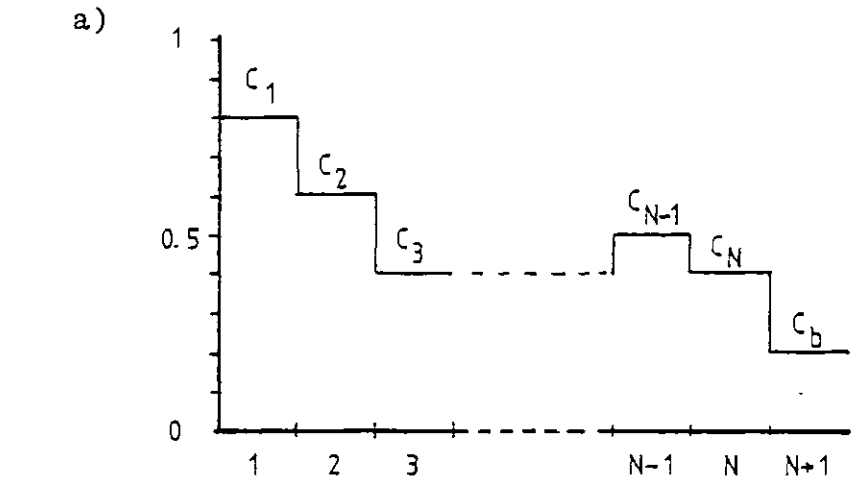
with d expressed in units of the interlayers distance 1.

For an homogeneous alloy, equation 6.4 reduces to

$$C^A_{eff}(d) = C_1 = C_b$$

as expected.

For enrichment restricted only to the first atomic layer,



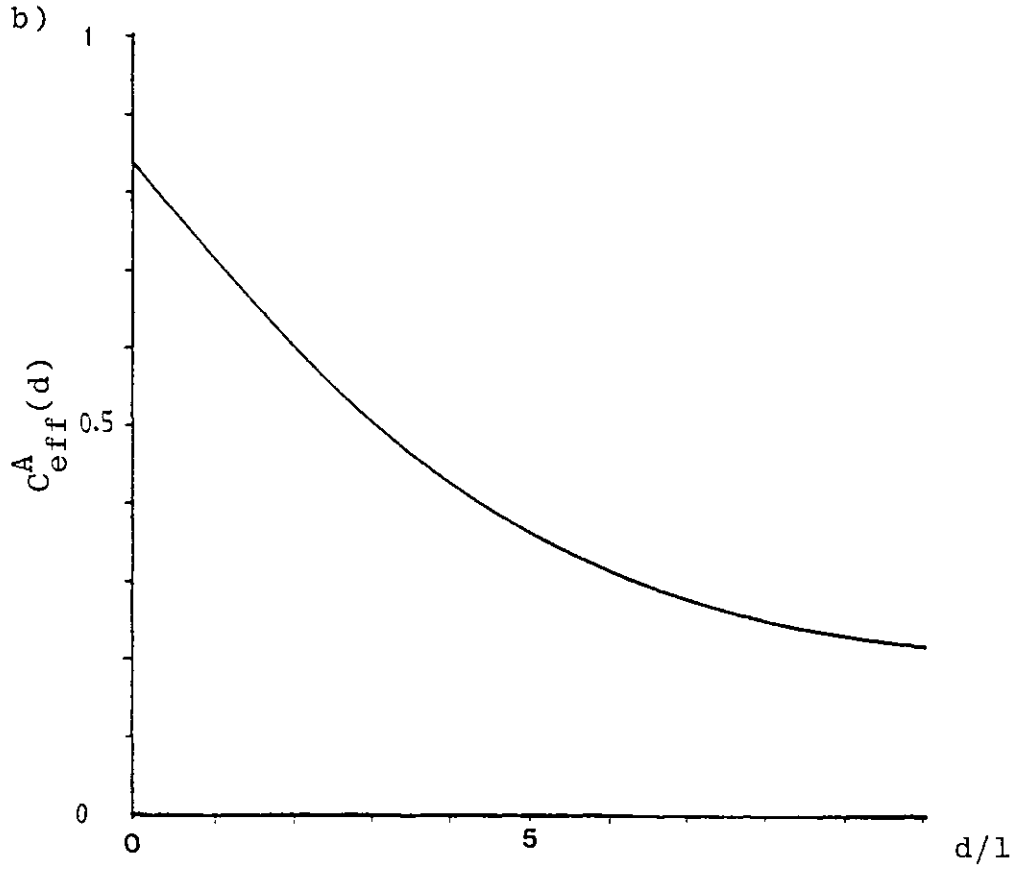


Figure 6.9 a) Schematic representation of an arbitrary composition profile. b) Function C^A_{eff} (d) corresponding to a strong A surface enrichment.

$$C^{A}_{eff}(d) = C_1 + (C_b - C_1)e^{-1/d}$$

Due to the exponential factor $e^{-n/d}$, the effective composition $C^{A}_{eff}(d)$ is a smoothly varying function of the escape depth d, as shown schematically in figure 6.9b. This function can be determined experimentally by using signals with different escape depths; the more data points one uses the better this function can be determined.

Having determined experimentally the function $C^{A}_{eff}(d)$ one can propose different composition profiles and using equation 6.4 calculate $C^{A}_{eff}(d)$ choosing the profiles that give a good fit to the experimental curve.

6.6 Composition profile of $Cu_{0.05}$ $Ni_{0.95}$ at T = 873K.

The effective Cu concentration of a $Cu_{0.05}$ $Ni_{0.95}$(100) sample at various depths has been determined using experimental data from a combination of AES and XPS techniques.

The Cu and Ni signals used, fall in pairs narrowly separated in kinetic energy and distributed over the range 100 - 1200 eV. These signals are the low (106/109 eV) and high (713/920 eV) energy Auger transitions and the Cu and Ni photoemission peaks corresponding to Mg Kα excited 2s, 2p, 3s core levels and Aℓ Kα excited 2s and 2p core levels.

Table 6.1 presents the appropriate mean free paths and

escape depths for these signals.

Table 6.1 Calculated electron escape depths.

AES or XPS signal		Kinetic energy/eV.	i.m.f.p/Å	Mean escape depth d/Å
M_1VV		106/109	4.5	3.7
Ni/Cu				
Mg Kα	Cu 2s	158	5.5	4.3
	Ni 2s	246	6.9	
Mg Kα	Cu 2p	313	7.9	5.8
	Ni 2p	390	8.7	
Aℓ Kα	Cu 2s	391	8.7	6.4
	Ni 2s	479	9.6	
Aℓ Kα	Cu 2p	546	10.0	7.4
	Ni 2p	616	11.0	
$L_3M_{23}M_{23}$	Ni	713	11.8	10.3
$L_3M_{45}M_{45}$	Cu	920	13.2	
Mg Kα	Cu 3s	1134	14.8	10.4
	Ni 3s	1142	14.9	

The AES measurements were obtained in the LEED/AES system that has been described. The XPS measurements were performed on the same samples by Dr. P. Webber[3] of this group in a VG - ESCA 3 spectrometer under UHV conditions. The ESCA 3 hemispherical analyser was set with a pass energy of 100 eV and 2 mm slits in the XPS mode. Photoelectrons were collected over a narrow band of angles about 45° relative to the sample normal. The effective escape depth is approx-

imated by $d = \lambda \cos 45^{o}$. Signal intensities were obtained from the Cu and Ni peak areas after a linear background substraction. Relative elemental sensitivity factors $k = I_{Cu}/I_{Ni}$ were determined from measurements on pure Cu and Ni samples and were found to be k = 1.1 for the 2p peaks and k = 1.05 for the 2s and 3s peaks. The effective surface composition was then calculated using the expression

$$C(Cu) = I_{Cu}/(I_{Cu} + kI_{Ni}) \qquad 6.5$$

The specimen was cleaned and annealed at T = 873K for 40 minutes, then it was allowed to cool to room temperature and the AES or XPS data collected. The cleaning and annealing procedures were the same in both systems.

Figure 6.10 presents the effective Cu surface composition, plotted against the mean escape depth for each pair of signals. The broken line represents the experimentally determined $C_{eff}(d)$ function. As can be observed, all the signals indicate copper enrichment with respect to the 0.05 bulk value composition; the detected enrichment increases as the escape depth decreases.

Figure 6.11 presents a set of possible composition profiles used to fit the experimental curve of figure 6.10. Seven layers were used to calculate $C_{eff}(d)$, the first six representing the "surface region" and the seventh with a fixed Cu composition equal to the bulk value.

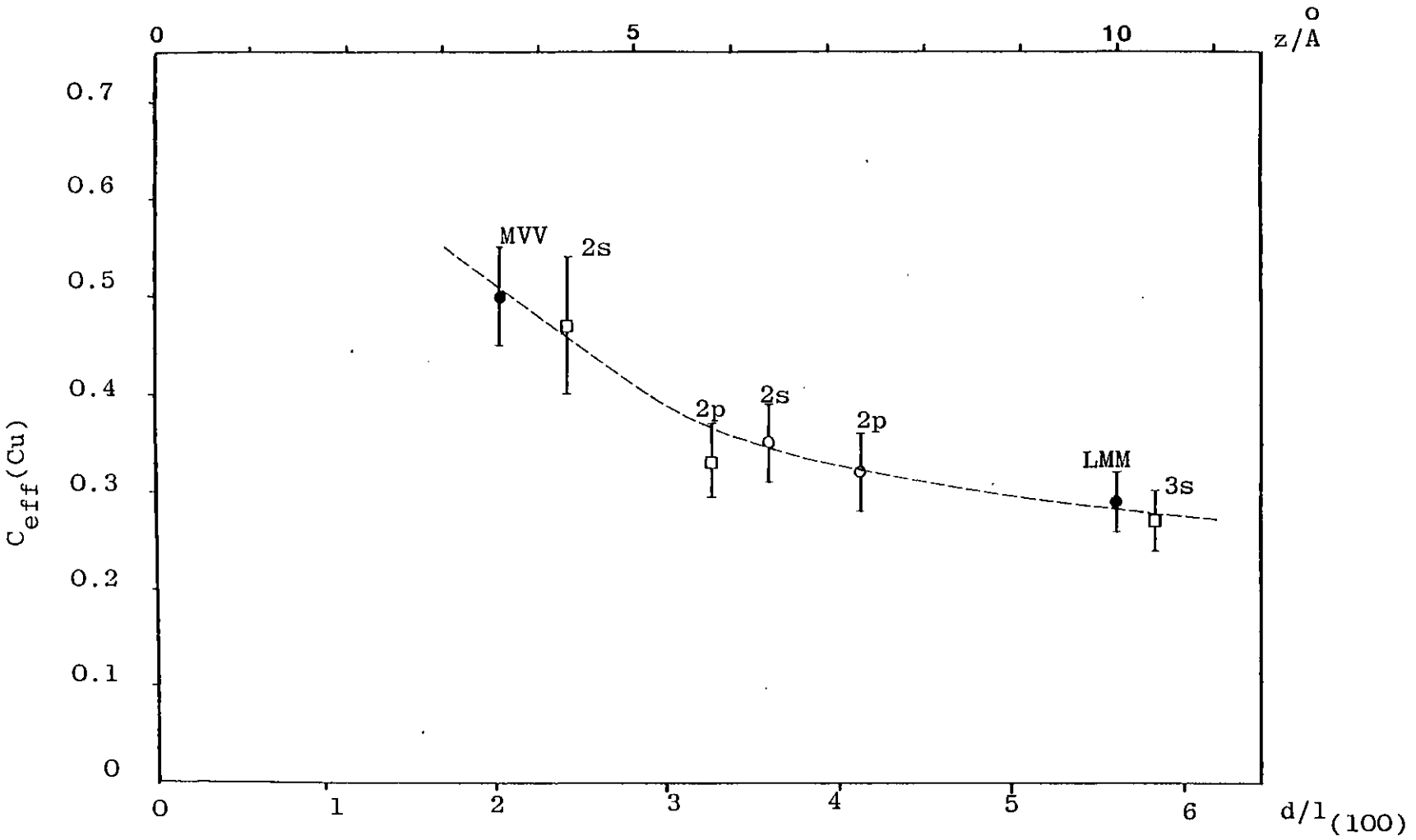


Figure 6.10 Surface somposition of $Cu_{0.05}$ $Ni_{0.95}$ (100) by AES and XPS as a function of electron escape depth. T = 873K. • Auger, □ MgKα excited XPS, ○ AlKα excited XPS.

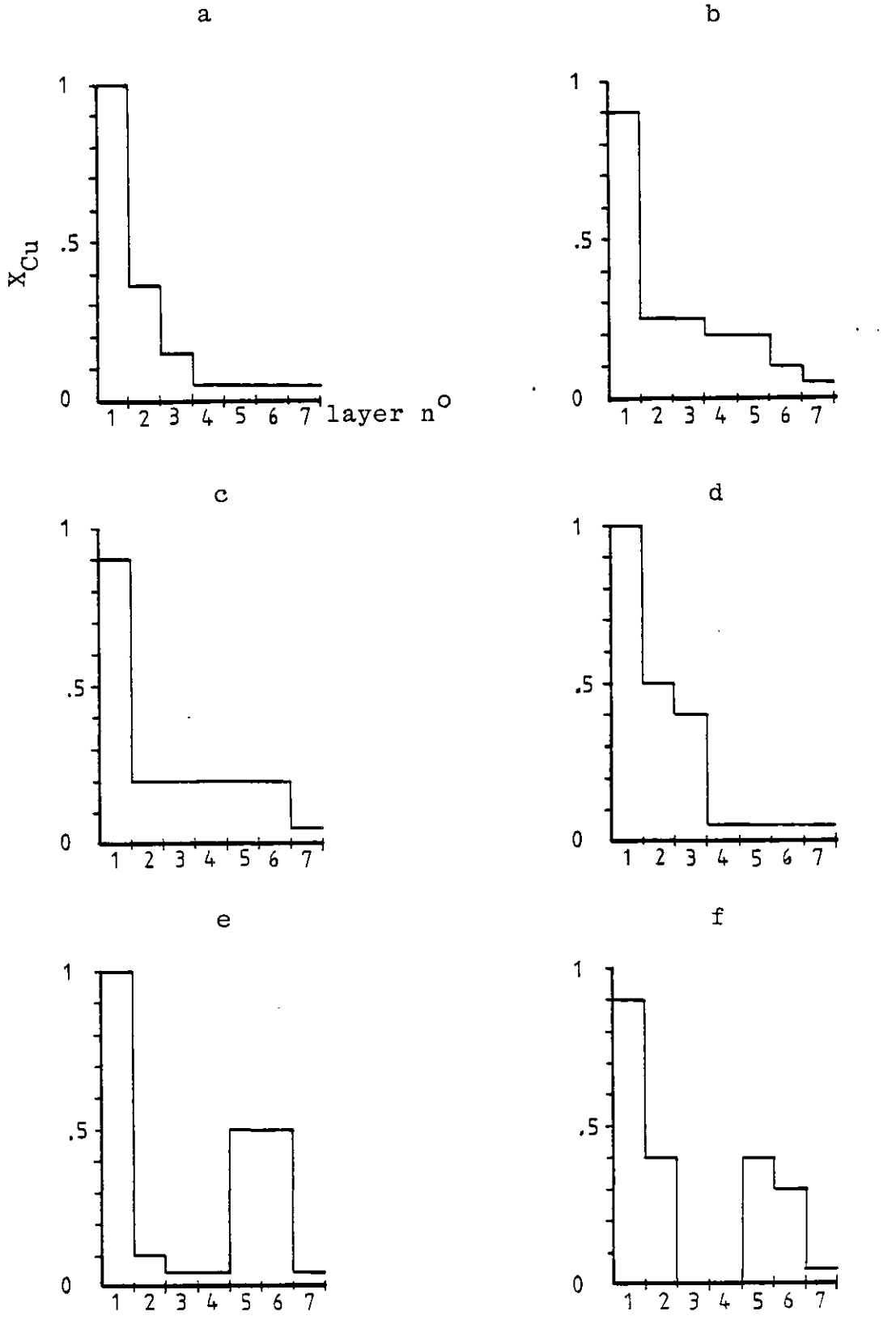


Figure 6.11 Composition profiles for $Cu_{0.05}$ $Ni_{0.95}$ (100) at T = 873K used to fit data in figure 6.10.

Profiles a - d show monotonic decreasing Cu distributions. Profiles a - c give good fits to the experimental curve, i.e. they produce a monotonic decreasing curve passing through all the error bars. Profile d is a limit case, producing a curve that does not go through all the error bars, because of its high Cu composition in the second layer.

Profiles e and f, presenting a composition oscillation with a minimum in the 3rd and 4th layers also give a good fit to the experimental curve.

As can be seen, the profiles producing good fits involve extensive Cu segregation in the first layer.

The same type of measurements of surface segregation described for the $Cu_{0.05}$ $Ni_{0.95}$ (100) face were carried out for the (111) and (110) faces and for the vicinal (100) surfaces presenting steps and step and kink sites, annealed at 873K . No difference was found in the levels of Cu enrichment in these samples compared with enrichment found in the (100) face[3].

6.7 Composition profile of $Cu_{0.5}$ $Ni_{0.5}$ (111) at T = 873K.

Data was also obtained for a $Cu_{0.5}$ $Ni_{0.5}$ (111) specimen annealed for $\sim$ 40 min. at $\sim$ 873K. The measured effective surface compositions are presented in figure 6.12. Three possible composition profiles giving a good fit to the experimental curve are given in figure 6.13. Again, top

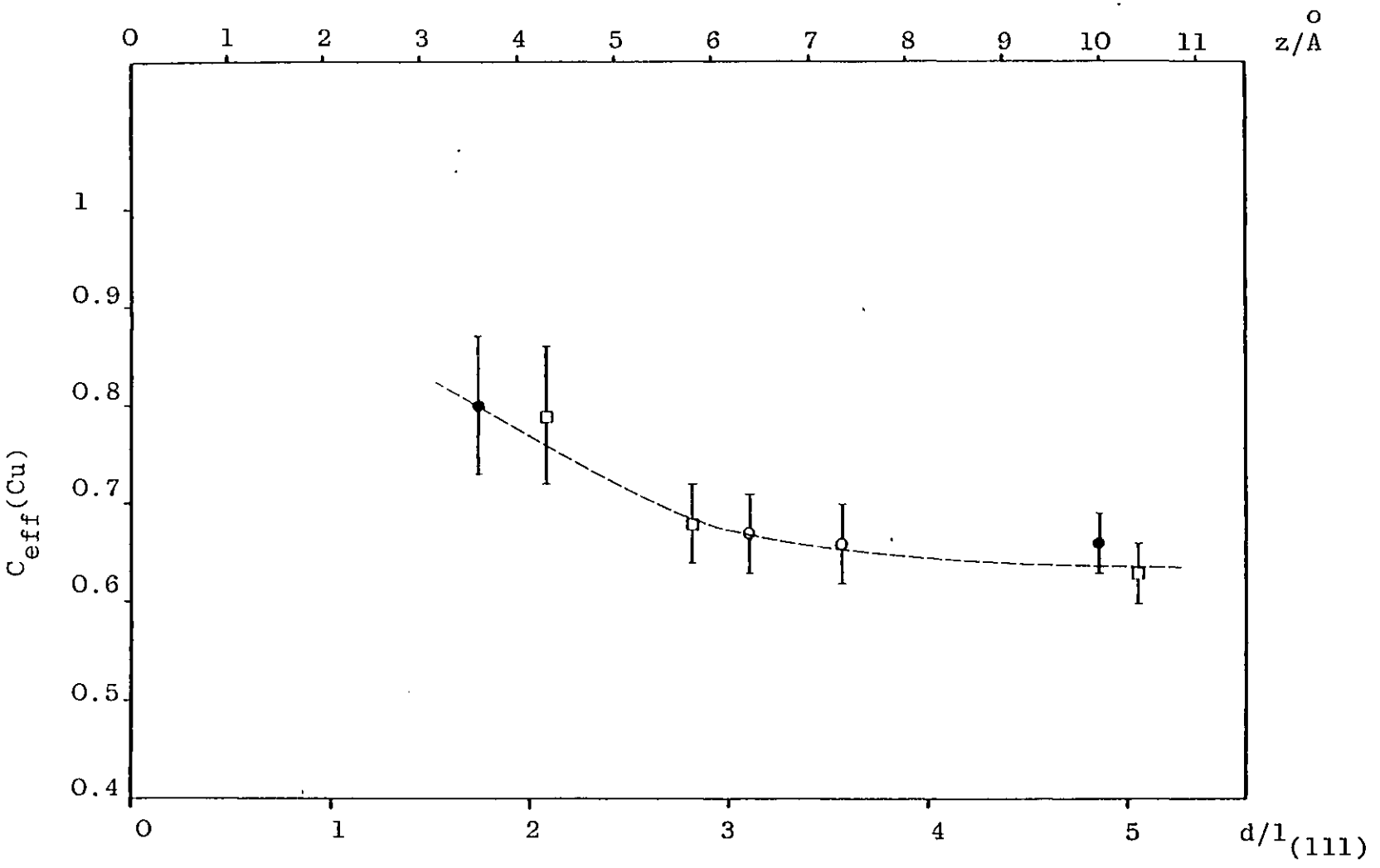


Figure 6.12 Surface composition of $Cu_{0.5}$ $Ni_{0.5}$ (111) by AES and XPS as a function of electron escape depth. T = 873K. Symbols as in Figure 6.10.

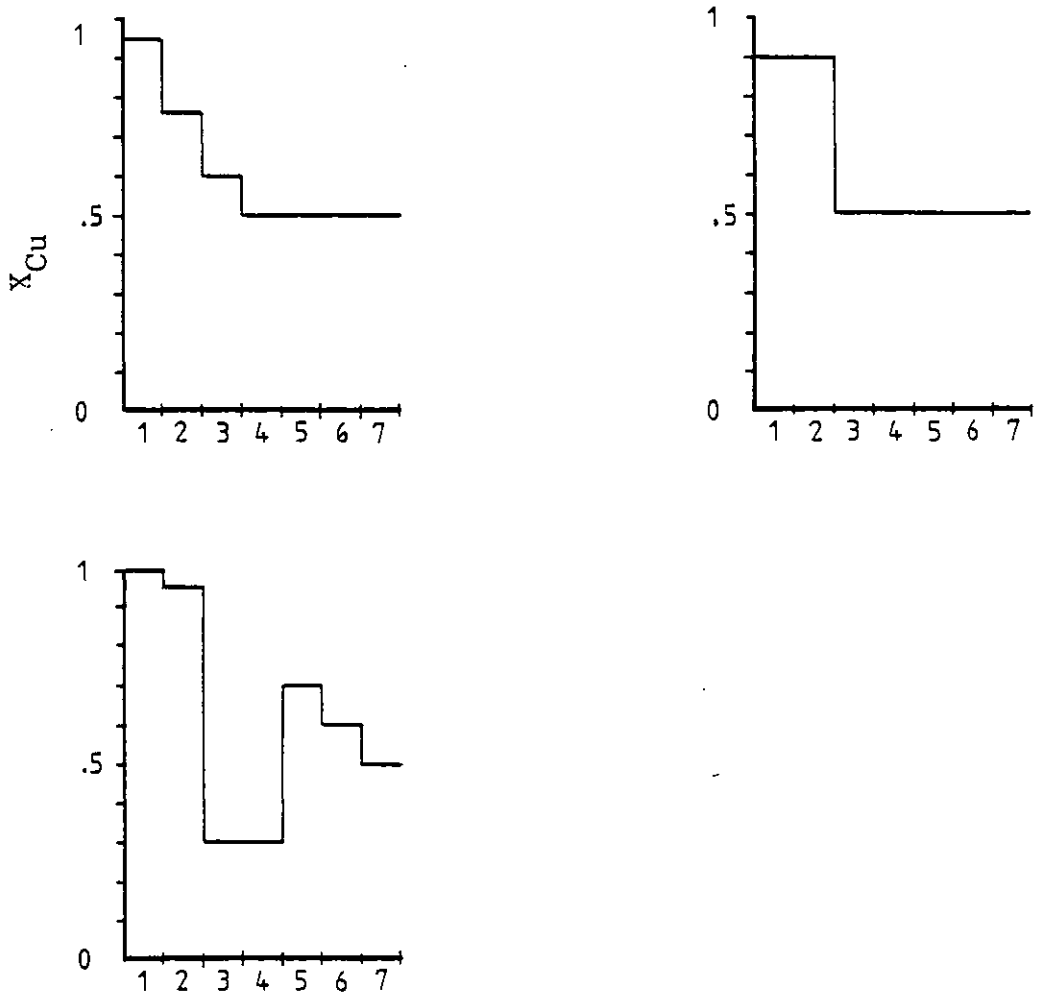


Figure 6.13 Possible composition profiles for $Cu_{0.5}$ $Ni_{0.5}$ (111) at T = 873K.

layer compositions of ∿ 100% are found. An oscillatory composition profile with a minimum in the 3rd and 4th layer is also possible.

6.8 Diffraction patterns

Low energy electron diffraction of the clean and annealed CuNi samples showed slightly diffuse patterns. Figure 6.14 compares the diffraction patterns observed for a Cu enriched $Cu_{0.05}$ $Ni_{0.95}$ (111) surface with those corresponding to Cu (111) and (111) at the same primary energy.

6.9 Discussion

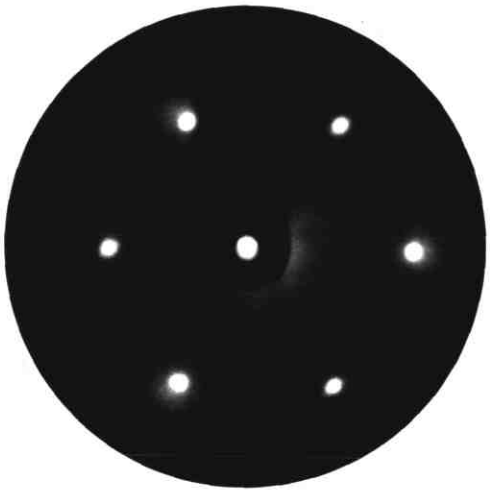
The similarity of the CuNi M_1VV simulated spectra with the real ones (figure 6.6) confirms that these transitions retain in the alloy the quasiatomic character found in the pure components. It also gives support to the quantitative analysis presented here. Due to their small escape depth these transitions have been fundamental in the determination of the high levels of Cu enrichment presented in this work.

The failure in detecting Cu segregation in earlier work on Cu Ni alloys[4,5] has been often attributed to the use of the not very surface sensitive high energy Auger transitions[6]. Here it is clearly shown (figure 6.8) that these transitions are useful in monitoring surface segregation.

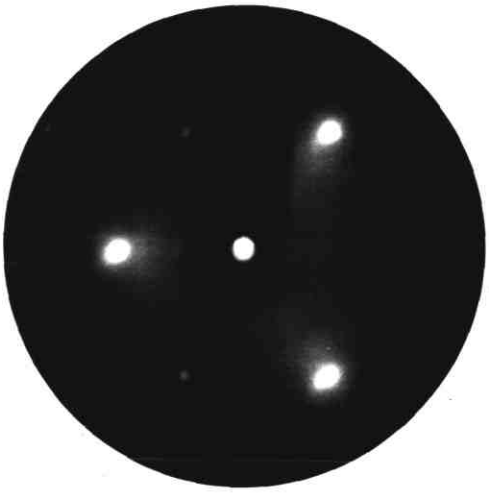
The determination of the $C_{eff}(d)$ function through the

E_p = 140 eV

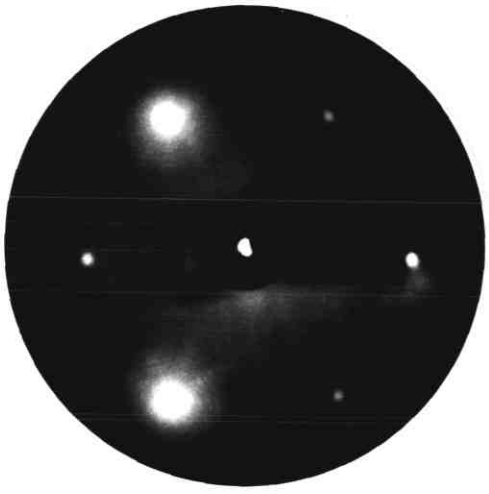
E_p = 160 eV



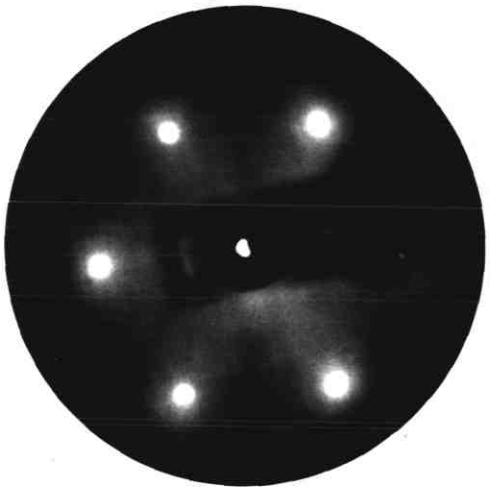
a) Cu (111)



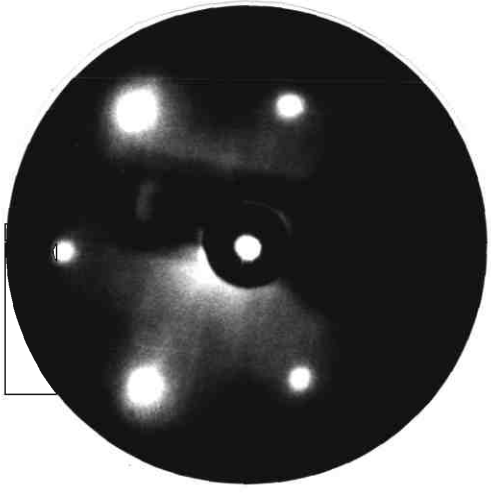
d) Cu (111)



b) Ni (111)



e) Ni (111)



c) CuNi (111)



f) CuNi (111)

Figure 6.14 Comparison of LEED patterns of Cu, Ni and CuNi.

combination of AES and XPS signals has permitted a better determination of the composition in the topmost layer and an estimation of the possible composition profiles.

For both the $Cu_{0.05}Ni_{0.95}$ (100) and the $Cu_{0.5}Ni_{0.5}$ (111) samples two kinds of possible composition profiles were found to explain the experimental data: a monotonic decreasing Cu profile and a profile showing an oscillation in the Cu composition.

Oscillations in the equilibrium composition profile are not expected on theoretical grounds for the CuNi system since it presents a tendency to clustering ($\omega > 0$). The profiles a - c in figure 6.11 and a - b in figure 6.13 would then represent our best estimates for the equilibrium composition in $Cu_{0.05}Ni_{0.95}$ and $Cu_{0.5}Ni_{0.5}$ respectively.

Oscillations in the composition profile can, however, arise if complete equilibrium between surface and bulk has not yet been achieved. A recent model of the kinetics of surface segregation[7] shows that an oscillation can be obtained because the surface layer approaches to its final composition more swiftly than the layers beneath it. For large values of the energy of segregation there can be situations in which no "real" equilibrium is present even if the maximum segregation level in the surface layer has already been achieved. The underlying layers are depleted in the segregating atoms and this produces a minimum in the composition profile which gradually smooths out as the "real"

equilibrium is attained. Since in the present experiments the approach to equilibrium was monitored only with the very surface sensitive M_1VV Auger transitions and the annealing times were not very long the possibility that complete equilibrium was not attained can not be ruled out.

All the profiles which give a good fit to the experimental data have a very high Cu enrichment in the topmost layer (80 - 100%). Theoretical models predict differences in the level of enrichment depending on the atomic roughness of the surface. Such differences were not observed in the present work. This can be explained in terms of the high levels of Cu enrichment obtained since any small difference which may exist in the 80 - 100% level of segregation would be lost within the experimental error.

6.10 Conclusions

The M_1VV Auger spectra of CuNi alloys consist of a simple compositionally weighted superposition of the spectra from pure Cu and pure Ni. This is a consequence of the split-band behaviour of the alloy band structure and of the quasiatomic character of these Auger transitions. A spectra simulation permits then the use of these transitions for quantitative analysis even if they can not be completely resolved.

The combination of data obtained from AES and XPS enables a better determination of the topmost layer composition of CuNi alloys and an estimation of the possible composition

profiles.

Composition variations within the first six atomic layers was found to be sufficient to give a good account of the experimental data. Two kinds of possible composition profiles were determined for both $Cu_{0.05}Ni_{0.95}$ (100) and $Cu_{0.5}Ni_{0.5}$ (111) at 873K: a) a monotonic decreasing profile with $\sim$ 90% Cu in the topmost layer and a sharp decrease to bulk composition levels, or b) an oscillatory profile with the same high level of Cu in the topmost layer and a minimum in composition in the third and fourth layers.

Due to the high levels of Cu enrichment that were obtained, no difference in surface composition as a function of atomic surface roughness could be detected for $Cu_{0.05}Ni_{0.95}$ samples at 873K.

References (Chapter 6)

1. M.J. Kelley and V. Ponec, Prog. in Surf. Sci. 11 (1981) 139.

2. P.R. Webber and D. Chadwick, Surf. Sci. 94 (1980) L151.

3. P.R. Webber, C.E. Rojas, P.J. Dobson and D. Chadwick, Surf. Sci. 105 (1981) 20.

4. G. Ertl and J. Kuppers, Surf. Sci. 24 (1971) 104.

5. D.T. Quinto, V.S. Sundaram and W.D. Robertson, Surf. Sci. 28 (1971) 504.

6. V. Ponec, NBS Special Publ. 475 (1977) 71.

7. S. Hofmann and J. Erlewein, Surf. Sci. 77 (1978) 591.

CHAPTER 7

Surface Segregation in AgPd. Experimental Results.

The equilibrium surface of AgPd alloys is expected to be enriched in silver in comparison with the bulk. This has been confirmed experimentally in a number of works on polycrystalline systems[1,2]. In this chapter the surface segregation of silver in well defined single crystalline specimens is studied.

Samples exposing the low index (100)(110)(111) faces were prepared from a $Ag_{0.01}$ $Pd_{0.99}$ single crystal. A $Ag_{0.07}$ $Pd_{0.93}$ sample exposing both the open (012) face and the close packed (111) face on the same single crystal piece was also prepared.

Polycrystalline $Ag_{0.05}$ $Pd_{0.95}$ and $Ag_{0.95}$ $Pd_{0.05}$ samples were used for comparison with other work and polycrystalline samples of pure Ag and Pd were used as standards for the quantitative analysis.

7.1 Experimental procedure.

As in the case of CuNi, specimens were cleaned by repeated cycles of argon ion sputtering followed by a fast heat treatment. Surface cleanliness was monitored by AES and LEED. The main contaminants that have been observed were carbon and sulphur. Sulphur could also be eliminated

by a 10^{-6}torr O_2 exposure for 5 minutes with the sample at $T \geq 773K$.

Figure 7.1 shows the Auger spectra of a $Ag_{0.01}Pd_{0.99}(100)$ sample before cleaning and after cleaning and annealing for 6 h. at T = 773K. The presence of carbon was difficult to detect because its main Auger signal is superimposed on some Ag and Pd signals.

Care was taken to monitor the approach to equilibrium. Most of the spectra were obtained while the sample was annealed , but they did not show any significant difference with spectra obtained using the interrupted annealing technique.

7.2 AES evidence for Ag surface segregation

The surface composition was calculated from the $M_{4,5}VV$ Auger transitions of Ag and Pd occurring at 353 and 329 eV respectively, shown for the pure standards in figure 7.2. The escape depth of these signals corresponds to $\sim$3 equivalent monolayers. The surface composition is calculated with the programme given in the Appendix and corresponds to the effective average composition over this depth.

Figure 7.3 displays a time sequence of Auger spectra corresponding to the $Ag_{0.01}$ $Pd_{0.99}(110)$ sample while being annealed at 773K. The appearance of the Ag Auger signal clearly shows that Ag enriches the annealed surface of this

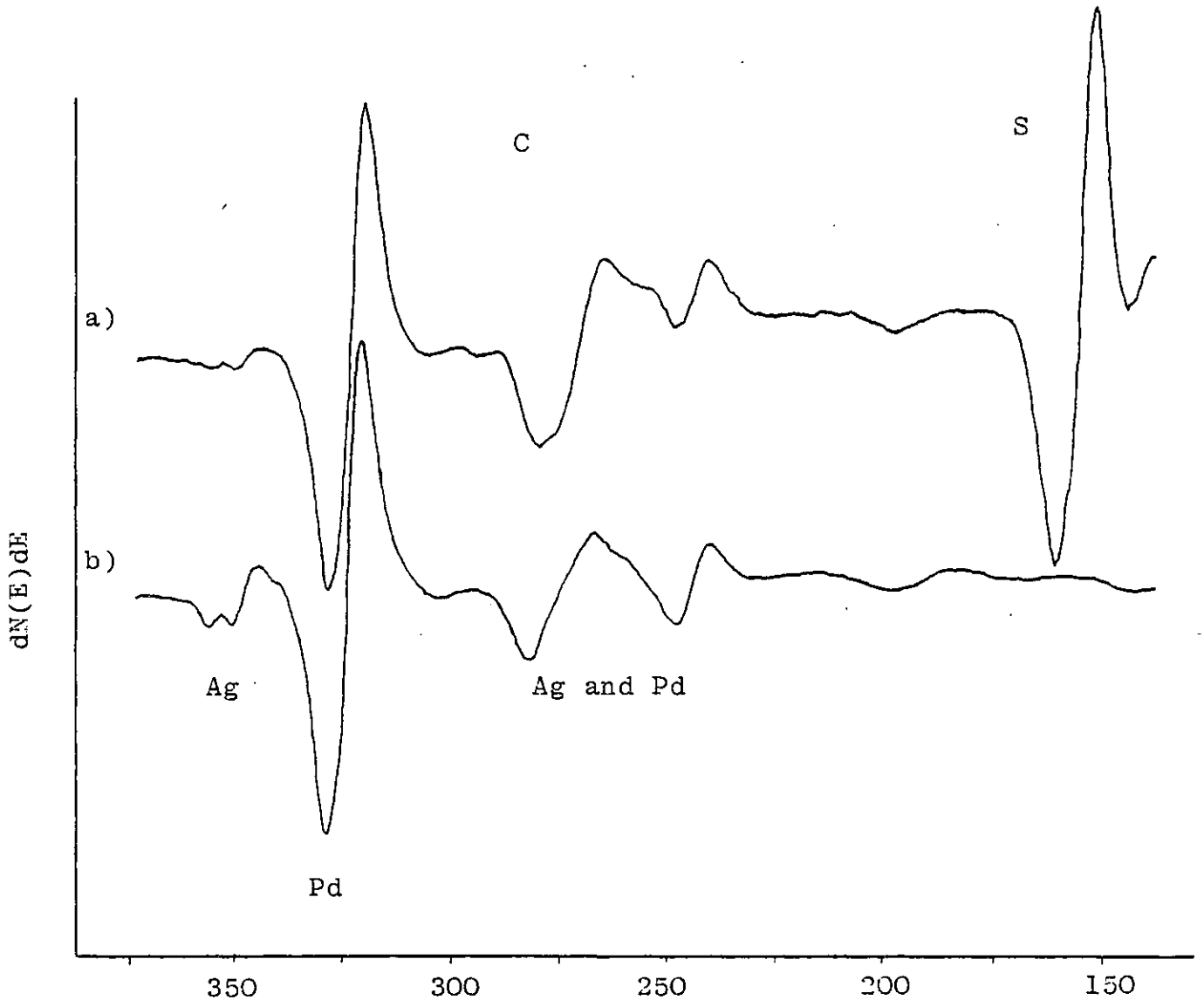


Figure 7.1 Auger spectra of a) contaminated AgPd sample, b) clean annealed sample. 6 V_{pp} modulation.

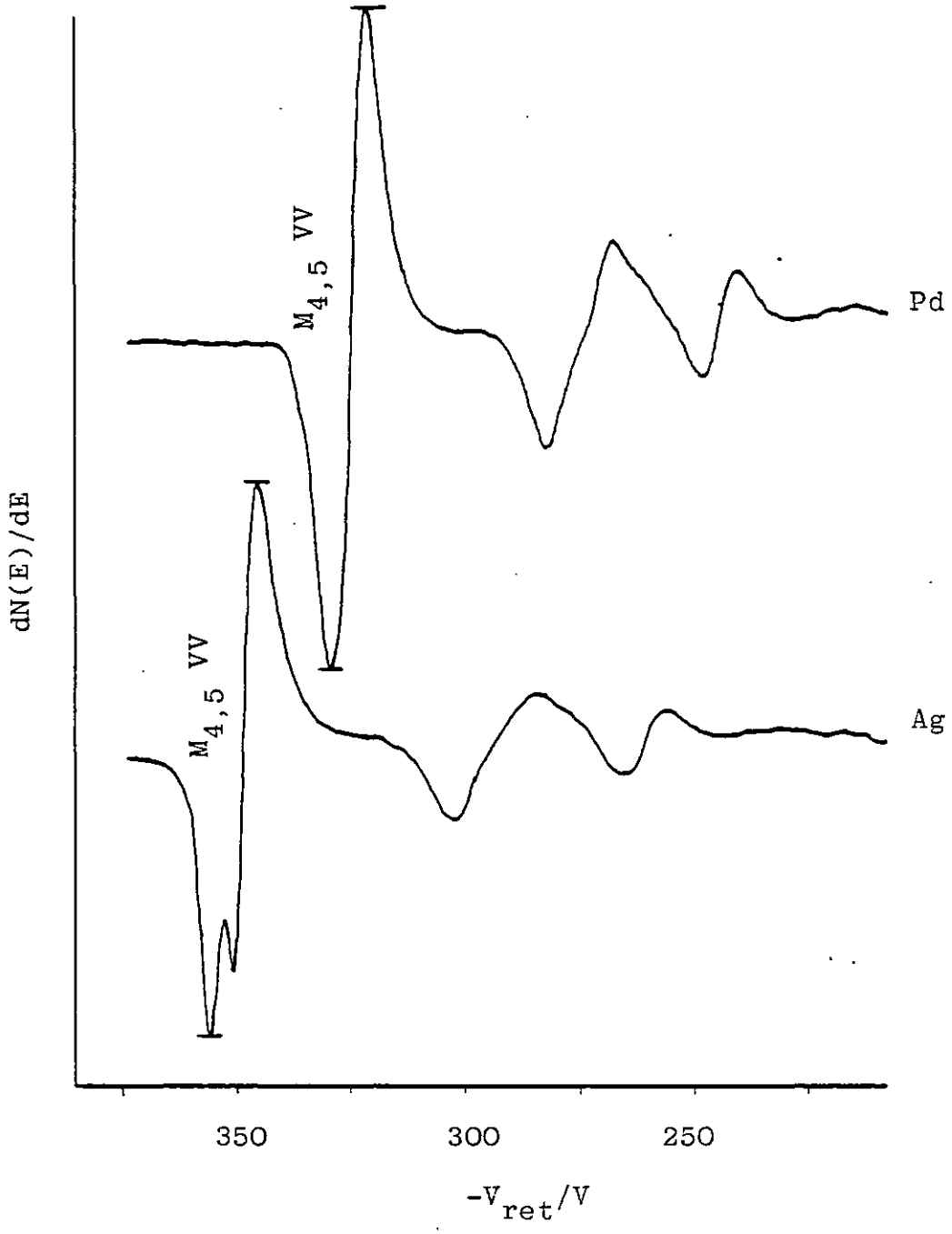


Figure 7.2 $M_{4,5}$ VV Auger signals of pure Pd and Ag used as reference standards. 6 V_{pp} modulation.

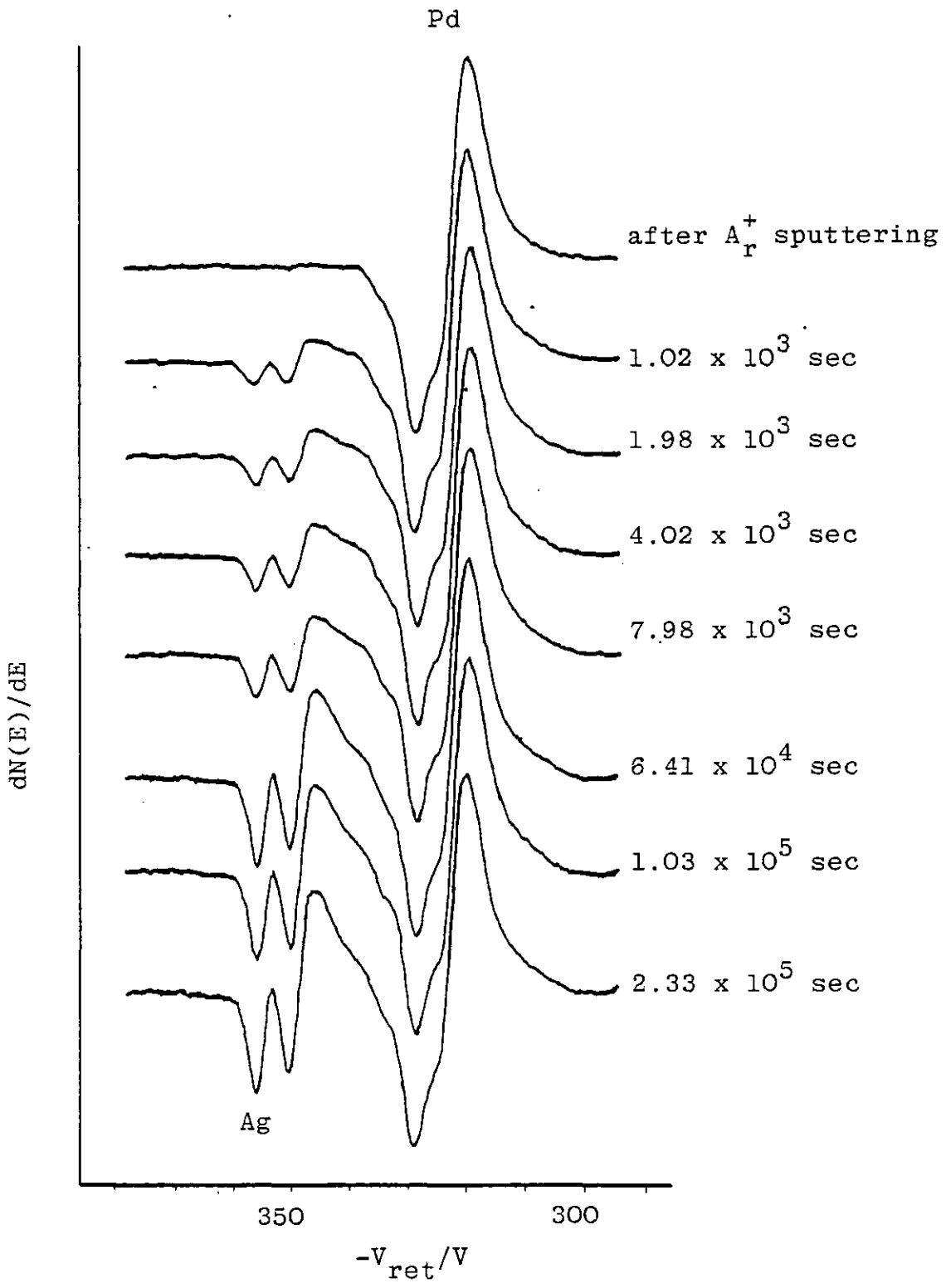


Figure 7.3 Auger evidence for Ag surface enrichment. $Ag_{0.01}$ $Pd_{0.99}$ (110) T = 773K. 4 V_{pp} modulation. Pd signals have been normalized to the same height.

alloy.

For quantitative analysis the spectra were recorded using 6V peak to peak modulation. In this case the relative sensitivity is $S = I_{Pd}/I_{Ag} = 1.18$. The matrix correction factor was found to be fairly independent of the alloy composition, with the value F = 1.109.

7.3 XPS evidence for Ag surface enrichment

Further evidence for Ag surface enrichment in AgPd alloys was obtained using X-Ray Photoelectron Spectroscopy on the $Ag_{0.01}$ $Pd_{0.99}$(111) sample, annealed for 35 hours at a temperature between 723K and 823K.

Figure 7.4 compares the XPS spectra of this annealed sample corresponding to normal emission and to a grazing emission of 5^{o} relative to the surface. The peaks displayed correspond to emission from the $Pd_{5/2,3/2}$ and Ag $3d_{5/2,3/2}$ core levels. The more surface sensitive grazing emission data shows a larger Ag signal indicating that the surface is enriched in this component.

It is interesting to note that the surface enrichment in Ag is also revealed in the photoemission spectrum of the alloy conduction band. Figure 7.5 displays the XPS spectra of this region, obtained at normal and grazing emission. Independent features corresponding to the Pd and Ag "d" density of states are observed, the silver

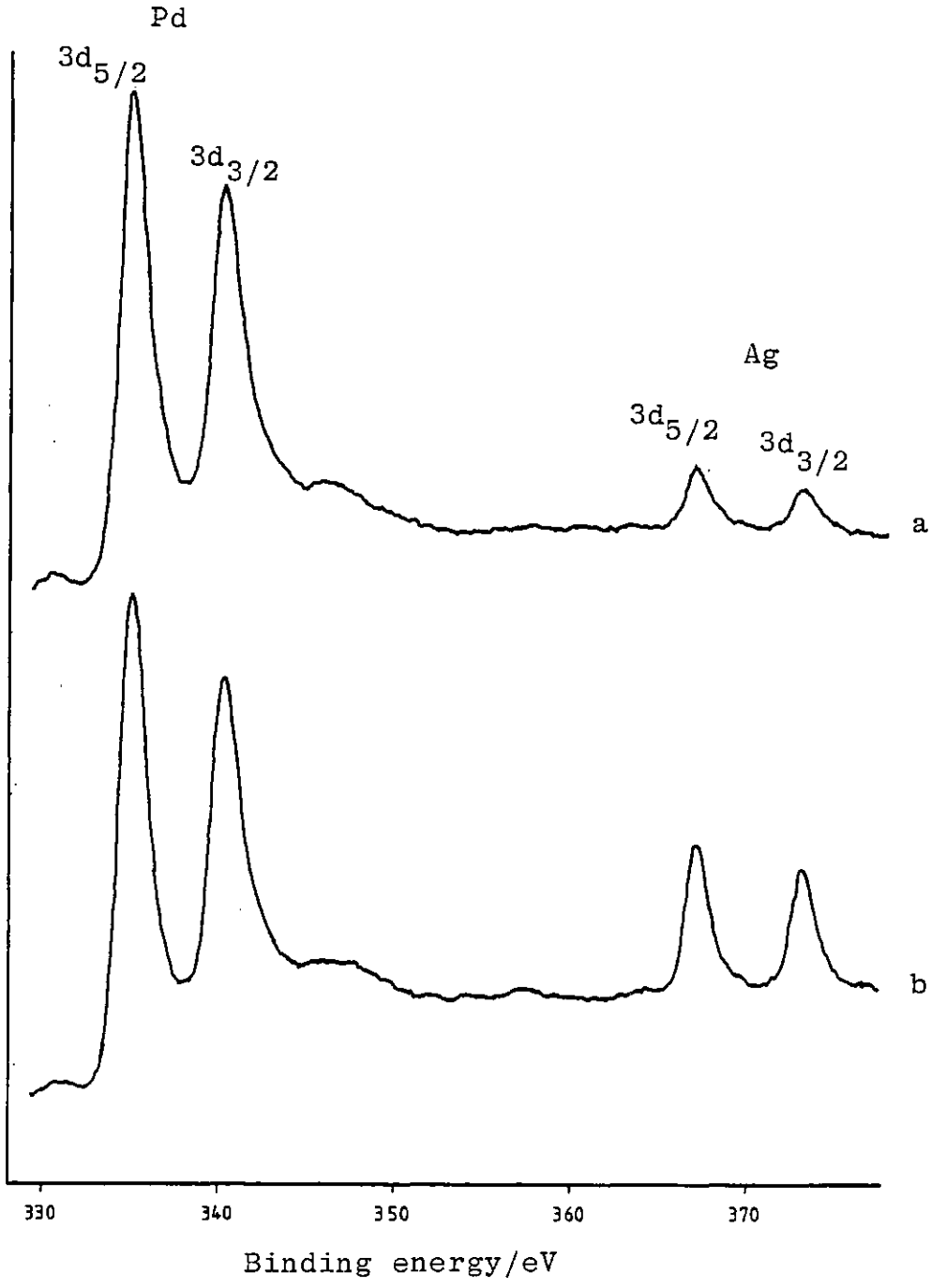


Figure 7.4. 3d XPS spectra of $Ag_{0.01}$ $Pd_{0.99}$ (111)
a) Normal emission. b) Grazing emission.

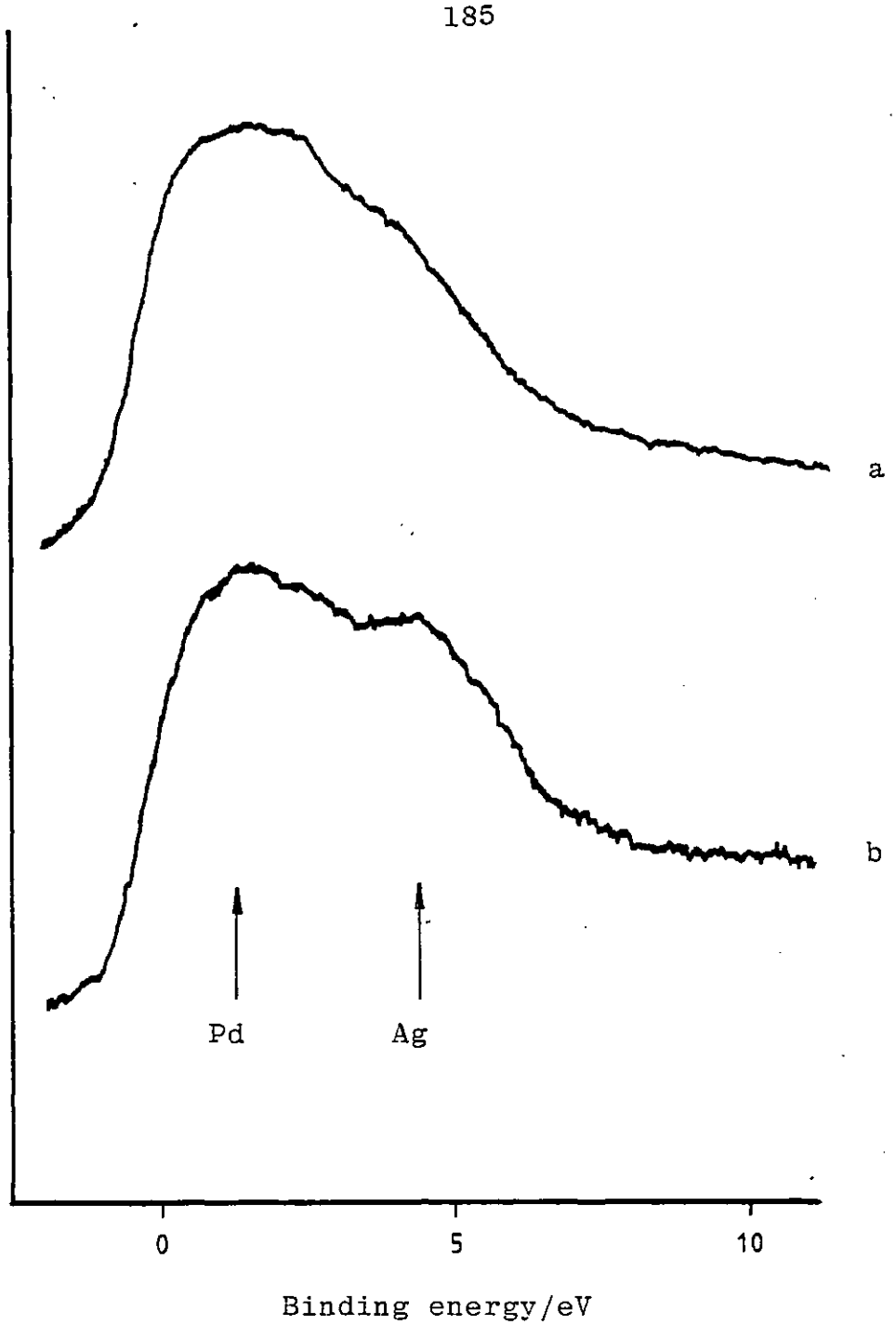


Figure 7.5 Conduction band XPS spectrum of $Ag_{0.01}$ $Pd_{0.99}$ (111) a) Normal emission. b) Grazing emission.

feature being more pronounced in the grazing emission spectrum.

7.4 Calibration of the sulphur Auger signal.

Sulphur impurity from the bulk could not be completely eliminated from the alloy samples and after long annealing times it segregated to the surface causing depletion of silver. In order to study this effect it is necessary to quantify the amount of sulphur. A calibration of the S Auger signal was carried out using Auger signals from PdS and LEED patterns of ordered layers formed by S on the (111) face of the $Ag_{0.07}$ $Pd_{0.93}$ specimen.

The amount of sulphur absorbed on the surface of a pure metal is usually a linear function of the ratio I_s/I_m where I_s is the height of the 150 eV S Auger signal and I_m is an Auger signal of the metal substrate[3]. In the case of sulphur absorbed on a substitutional alloy AB it is expected that this linearity is obtained between the amount of sulphur and the ratio $I_s/(I_A + I_B)$ where I_A and I_B are Auger signals of components A and B of similar escape depth.

The amount of S on AgPd was calculated from the measured Auger peak to peak heights I_S, I_{Ag}, I_{Pd} assuming a model in which an alloy of uniform composition C_{Ag}, C_{Pd} is covered by a fractional monolayer X_s of sulphur. X_s is defined in terms of a close packing of S atoms and not in relation to the substrate sites. The monolayer is considered

to be filled when the number of S atoms per unit area is a_s^{-2}, where a_s is the S atomic size, calculated from equation 4.18 as $a_s = 2.95$ Å.

The Ag and Pd Auger signals from the alloy substrate, attenuated on passing through the S fractional monolayer are given by[4]

$$I_{Ag} = C_{Ag} I_{Ag}^{\infty} \left[1 - X_s + X_s \exp\left(-1/d_s(E_{Ag})\right)\right] \qquad 7.1$$

$$I_{Pd} = (1 - C_{Ag})\, I_{Pd}^{\infty} \left[1 - X_s + X_s \exp\left(-1/d_s(E_{Pd})\right)\right] \qquad 7.2$$

The S Auger signal is related to I_s^{∞}, the signal in pure sulphur by

$$I_s = X_s\, I_s^{\infty} \frac{\left[1 + r_{AgPd}(E_s)\right]}{\left[1 + r_s(E_s)\right]} \left(1 - \exp\left(-1/d_s(E_s)\right)\right) \qquad 7.3$$

The ratio $I_s^{\infty}/I_{Pd}^{\infty}$ was calculated from the expression

$$\frac{I_s^{\infty}}{I_{Pd}^{\infty}} = \frac{I_s^{*}}{I_{Pd}^{*}} \frac{\left[1 + r_s(E_s)\right]}{\left[1 + r_{Pd}(E_{Pd})\right]} \qquad 7.4$$

where I_s^{*} and I_{Pd}^{*} are the heights of the S and Pd signals obtained from the Auger spectrum of PdS. Figure 7.6 shows the Auger spectrum from which the value $I_s^{*}/I_{Pd}^{*} = 4.82$ was obtained.

From the above expressions, X_s can be calculated in terms of the ratio $Is/(I_{Ag} + I_{Pd})$. Figure 7.7 shows the results of this calculation for signals obtained from various

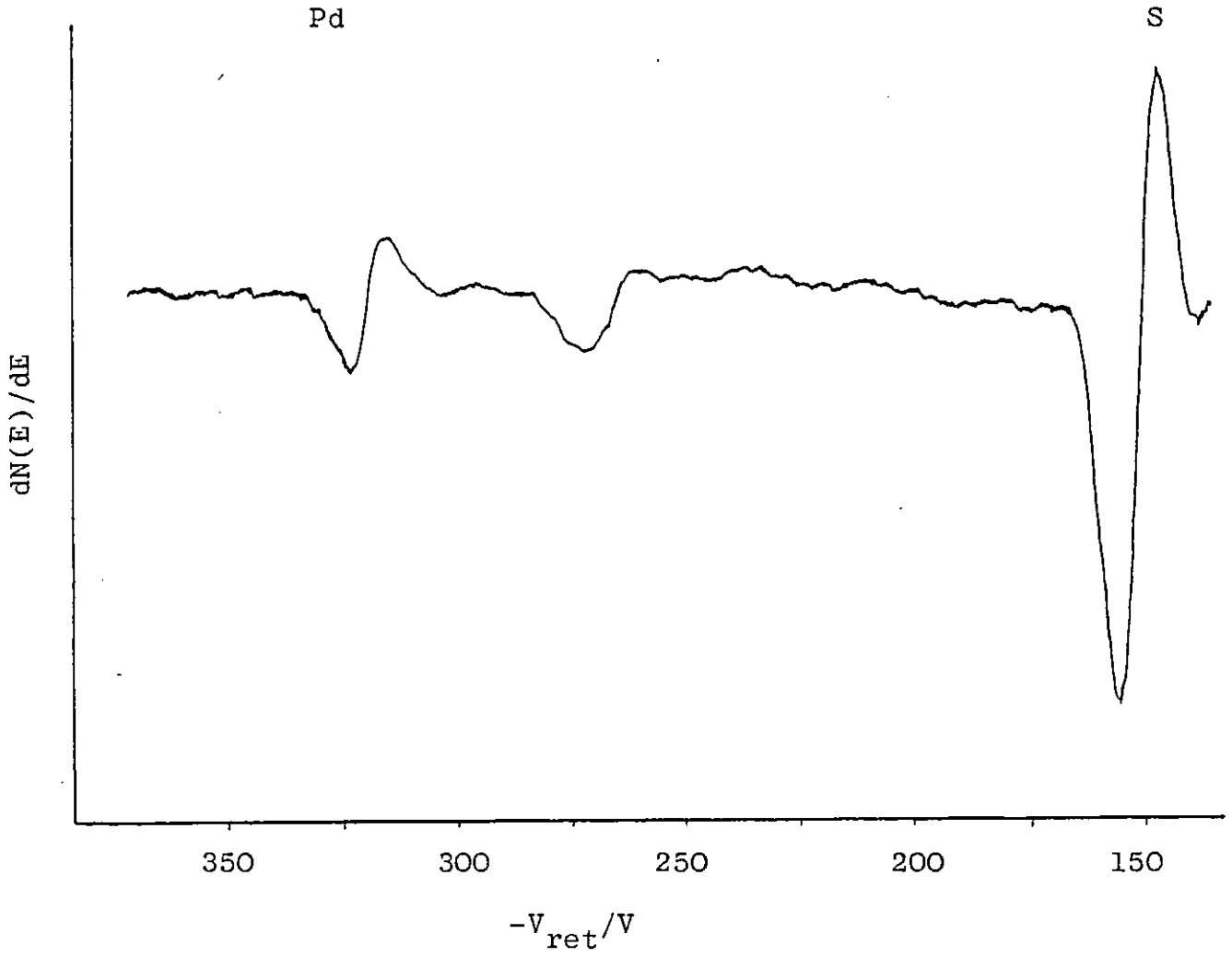


Figure 7.6 Auger spectrum of PdS. 6 V_{pp} modulation

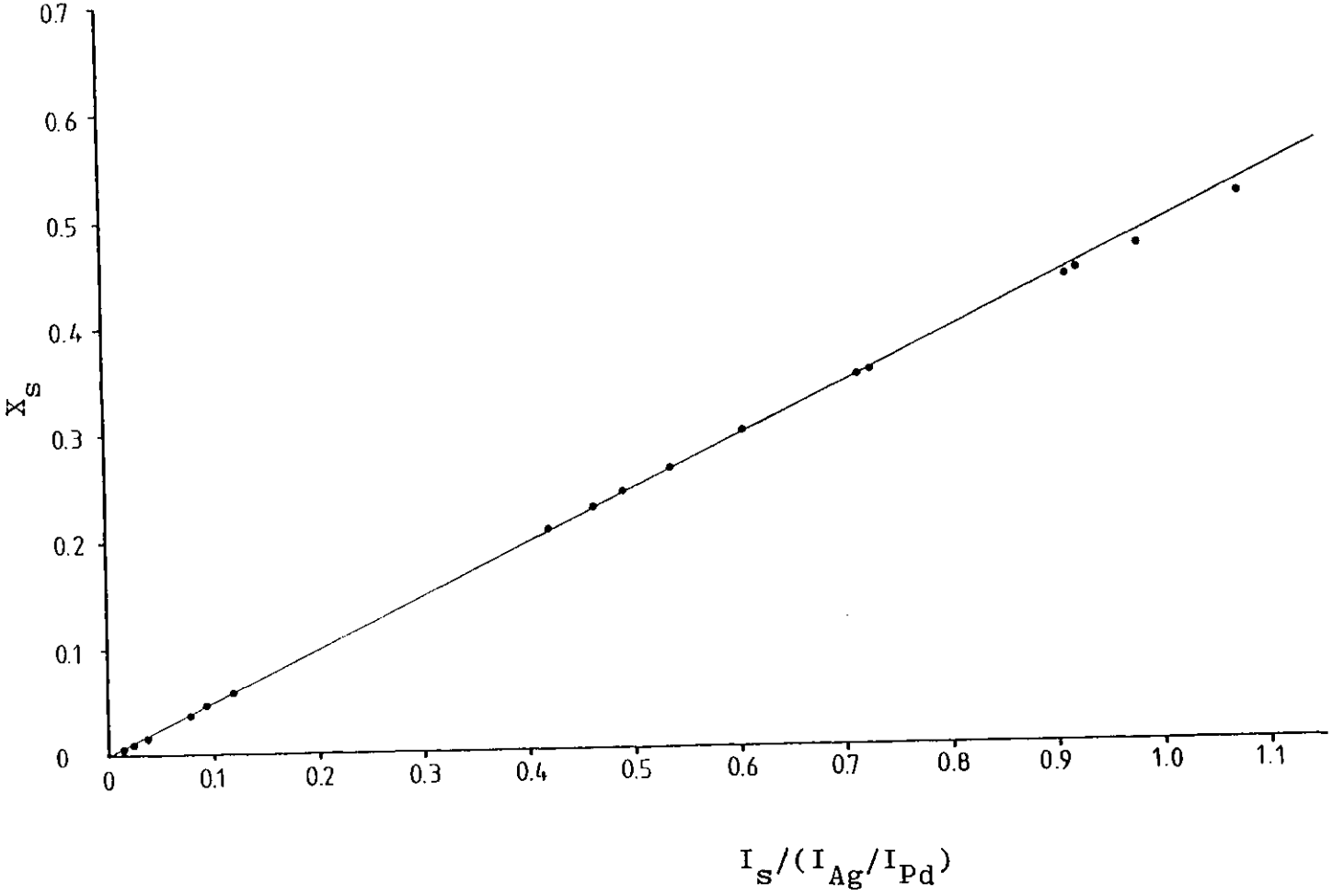


Figure 7.7 Calibration curve for S on AgPd obtained using PdS Auger spectrum.

samples displaying a wide range of S, Ag and Pd compositions. The "calibration curve" can be approximated by a straight line of slope 0.485.

The fractional monolayer X_s is related to the fractional coverage $\theta_s(h\ k\ \ell)$ of the $(h\ k\ \ell)$ surface by the expression

$$X_s = \theta_s\ (h\ k\ \ell)\ x\ \frac{a_s^2}{A_{h\ k\ \ell}} \qquad 7.5$$

where $A_{h\ k\ \ell}$ is the area associated with the two-dimensional primitive cell of the $(h\ k\ \ell)$ surface.

An independent calibration of the S signal was carried out using the two well defined LEED patterns shown in figure 7.8 which accurred when S segregated to the (111) surface of the $Ag_{0.07}\ Pd_{0.93}$ specimen.

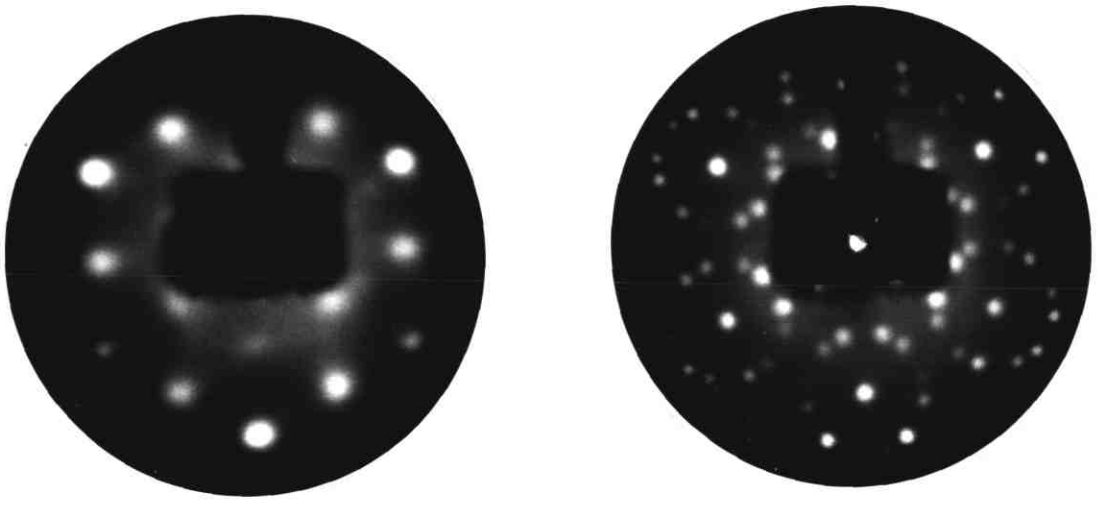
The first pattern corresponds to a p(2 x 2) S overlayer given a fractional coverage θ_s (111) = 1/4.

The interpretation of the second pattern is similar to the one given by J. L. Domange and J. Oudar[5] for S absorbed on Cu (111): Two equivalent domains rotated by 30^o as shown in figure 7.8c. The corresponding fractional coverage is θ_s (111) = 3/7, considered to be the saturation level.

These two fractional coverages are plotted in figure 7.9 as a function of the corresponding values of $I_s/(I_{Ag} + I_{Pd})$

a) Ep = 83 eV

b) Ep = 110 eV



c)

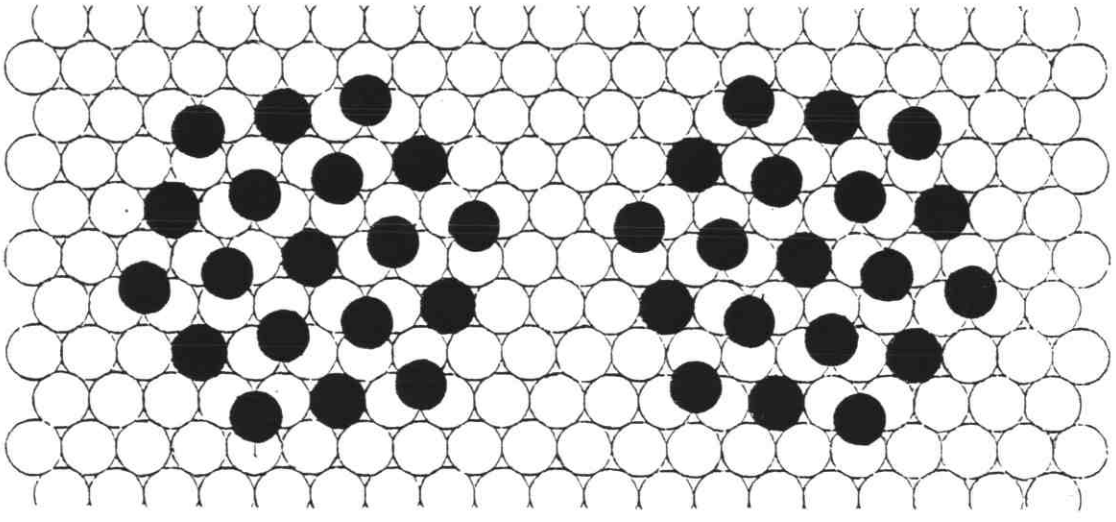


Figure 7.8 S/AgPd (111) LEED patterns used for the calibration of the Auger sulphur signal. a) p (2 x 2) b) Superposition corresponding to the two equivalent coincidence structures proposed in c)

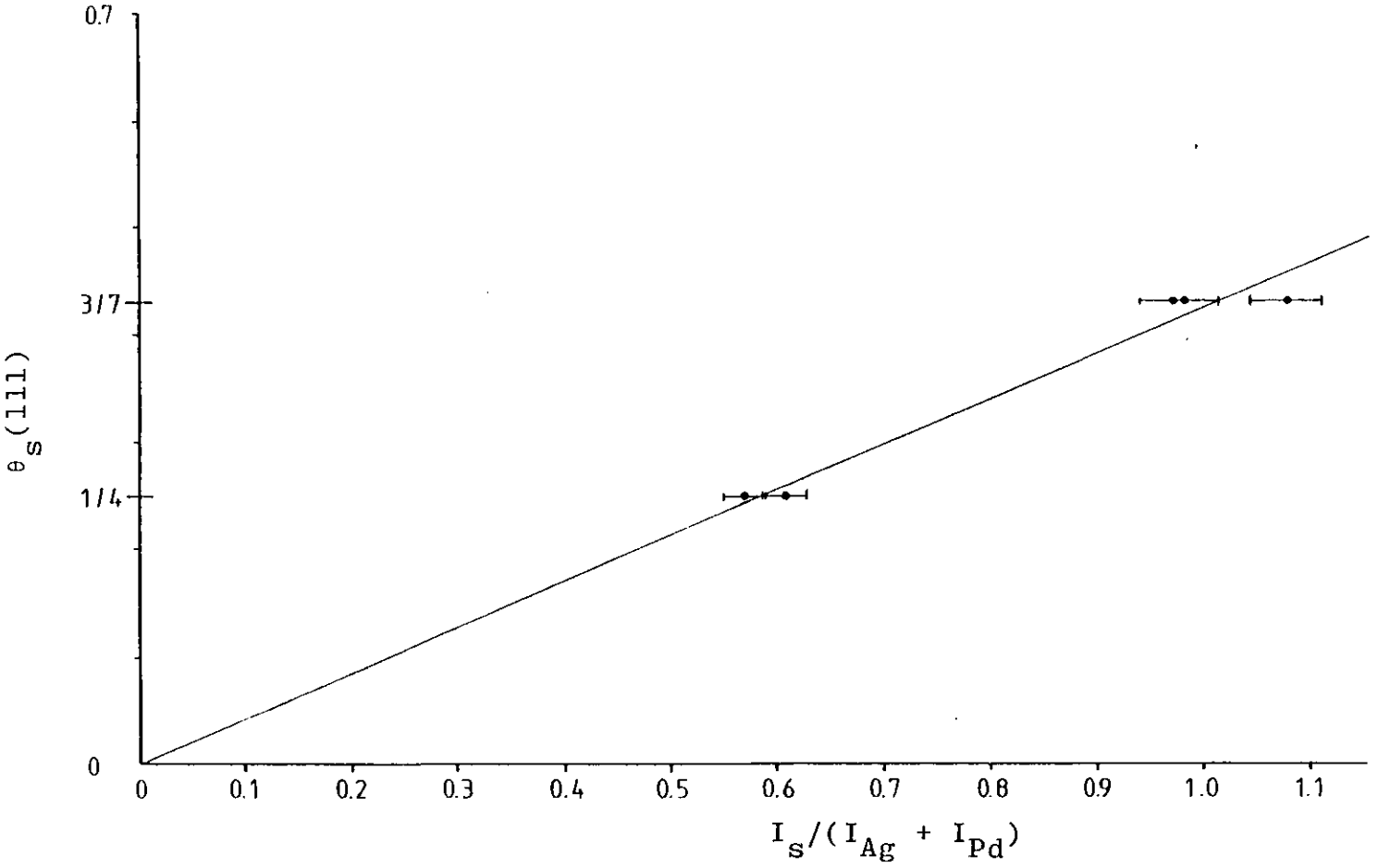


Figure 7.9 Calibration curve for S on AgPd (111) obtained from the combination of LEED and AES data.

obtained from AES. The data points are joined by a straight line of slope 0.42, or 0.53 if expressed in terms of the fractional monolayer X_s. The average slope between both curves was chosen and the calibration given by

$$X_s = 0.50\ I_s/(I_{Ag} + I_{Pd})$$

or

$$\theta_s(111) = 0.40\ H$$
$$\theta_s(100) = 0.46\ H$$
$$\theta_s(110) = 0.65\ H$$
$$\theta_s(012) = 1.02\ H$$
$$\theta_s(\text{polyc.}) = 0.50\ H$$

where $H = I_s/(I_{Ag} + I_{Pd})$.

7.5 Ag segregation in $Ag_{0.01}\ Pd_{0.99}$(100)(110)(111) at 773K.

Measurements of the Ag and Pd Auger signals as a function of time were obtained for the three low index faces of $Ag_{0.01}\ Pd_{0.99}$ while the specimen was annealed at 773K. The alloy effective composition over the escape depth of the $M_{4,5}$ VV Auger signals was calculated using the programme given in the Appendix. Cosegregation of sulphur was also monitored and quantified in terms of fractional coverage.

Figure 7.10 shows the segregation curve detained for the (100) surface. Note that the time scale is logarithmic; equilibrium is approached rather slowly and is achieved only after $\sim$ 2 days annealing.

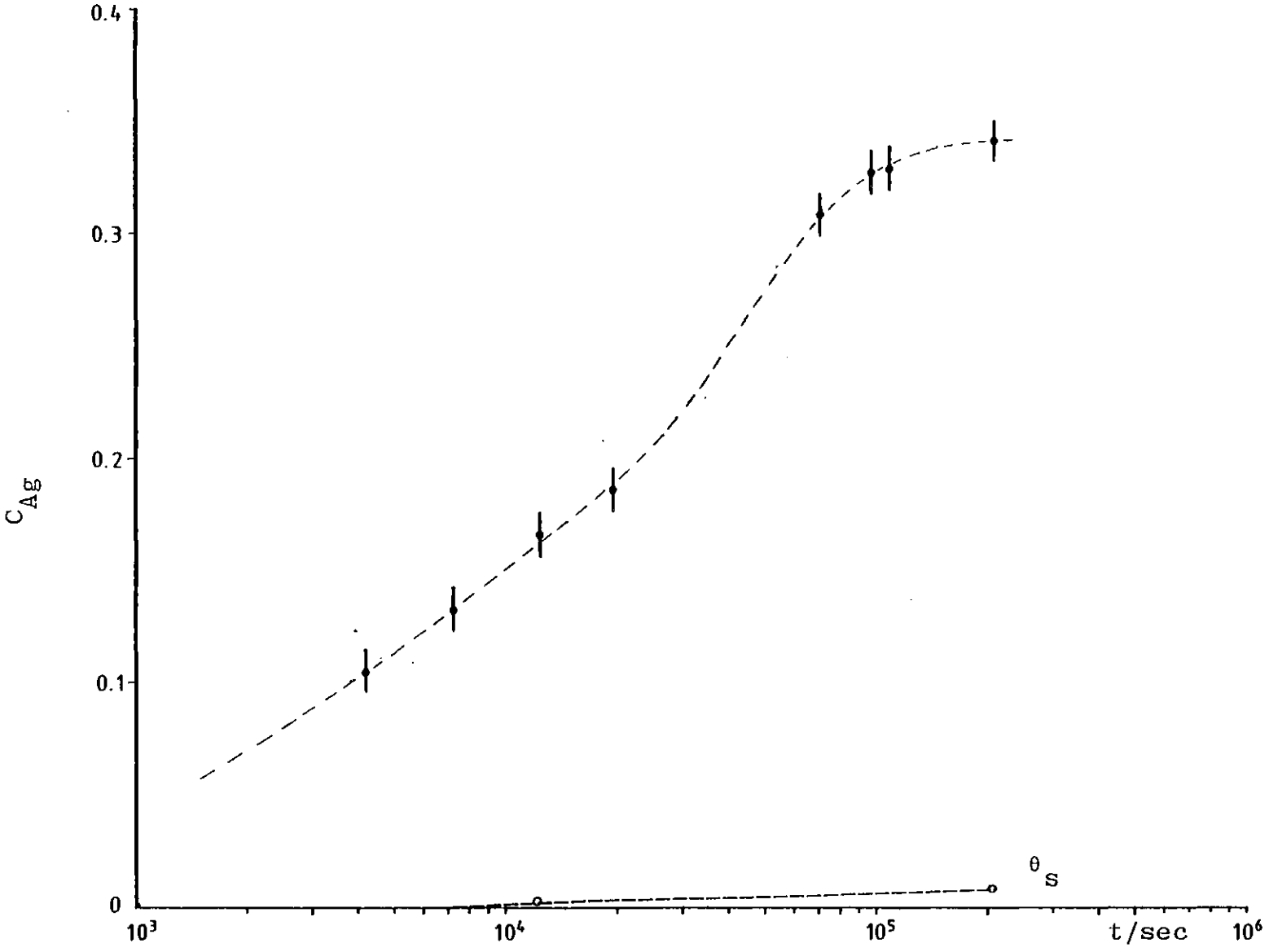


Figure 7.10 Segregation curve for $Ag_{0.01}$ $Pd_{0.99}$ (100) at 773K.

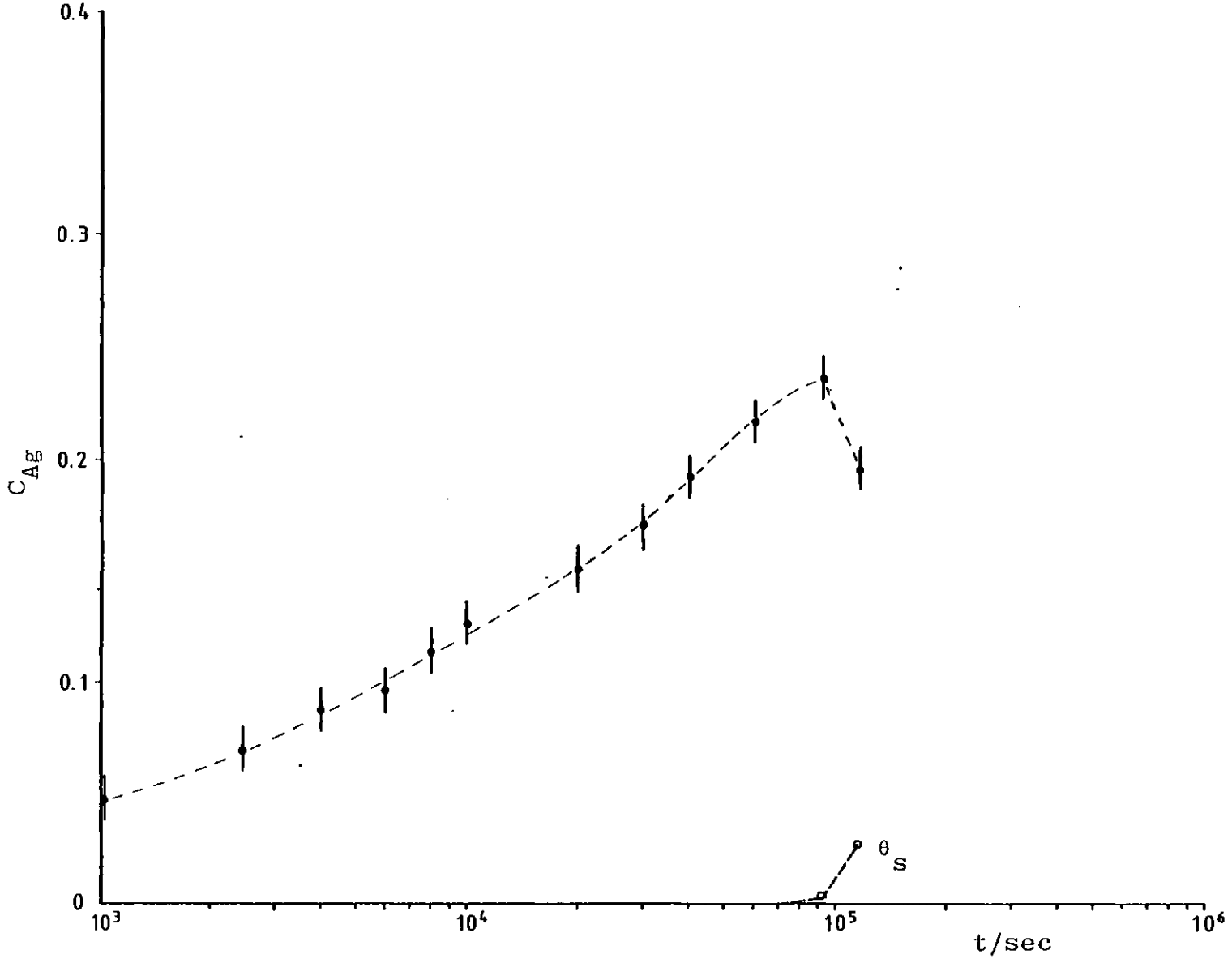


Figure 7.11 Segregation curve for $Ag_{0.01}$ $Pd_{0.99}$ (111) at 773K

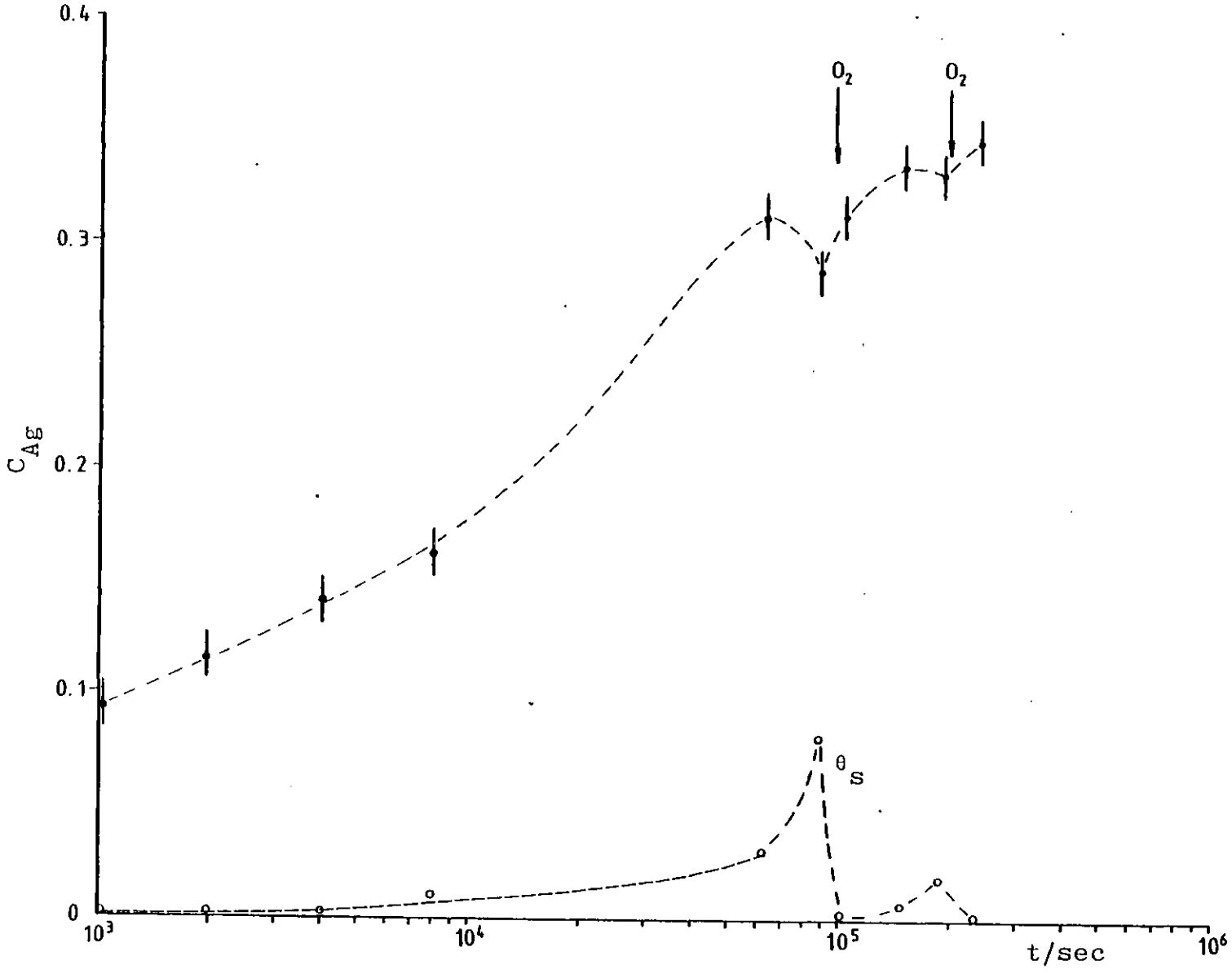


Figure 7.12 Segregation curve for $Ag_{0.01}$ $Pd_{0.99}$ (110) at 773K

Figure 7.11 presents the corresponding segregation curve for the (111) surface. The Ag surface composition is always smaller than for the (100) face. At the end there is a reduction in the surface Ag composition, associated with a marked increase in the S coverage.

The segregation curve for the (110) face is presented in figure 7.12. In the absence of sulphur the Ag surface composition obtained for this surface are higher than the compositions obtained for the other two. Note that the marked increase in S coverage is associated with a decrease in the silver surface composition. Sulphur was eliminated twice from the surface by exposing the sample to 10^{-5} torr of oxygen for 5 minutes (indicated by arrows in the graph). When S dissapears the Ag composition increases again. No oxygen could be detected by AES. This clearly shows that S surface segregation causes Ag desegregation in AgPd.

7.6 Effect of temperature on Ag segregation

Segregation curves $C_{Ag}(t)$ for different temperatures were obtained for the $Ag_{0.01}\ Pd_{0.99}$ (110) sample. The segregation curve corresponding to T = 773K has already been shown in figure 7.12. Figure 7.13 presents the segregation curve obtained while the sample was annealed at T = 873K. Note that segregation now occurs faster and the Ag surface composition is lower than the one obtained at 773K. Equilibrium is attained after $\sim$ 3 hours. Ag

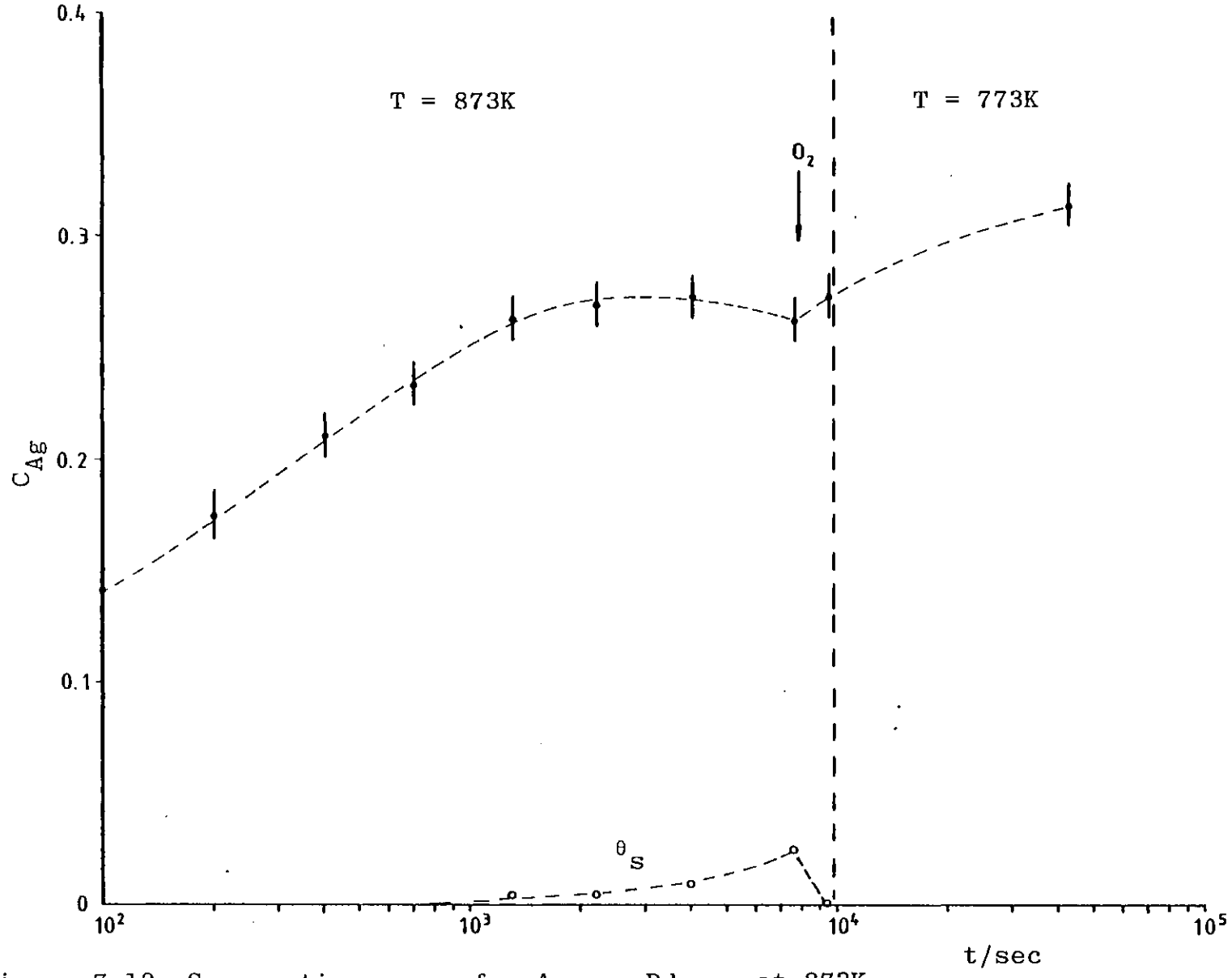


Figure 7.13 Segregation curve for $Ag_{0.01}$ $Pd_{0.99}$ at 873K

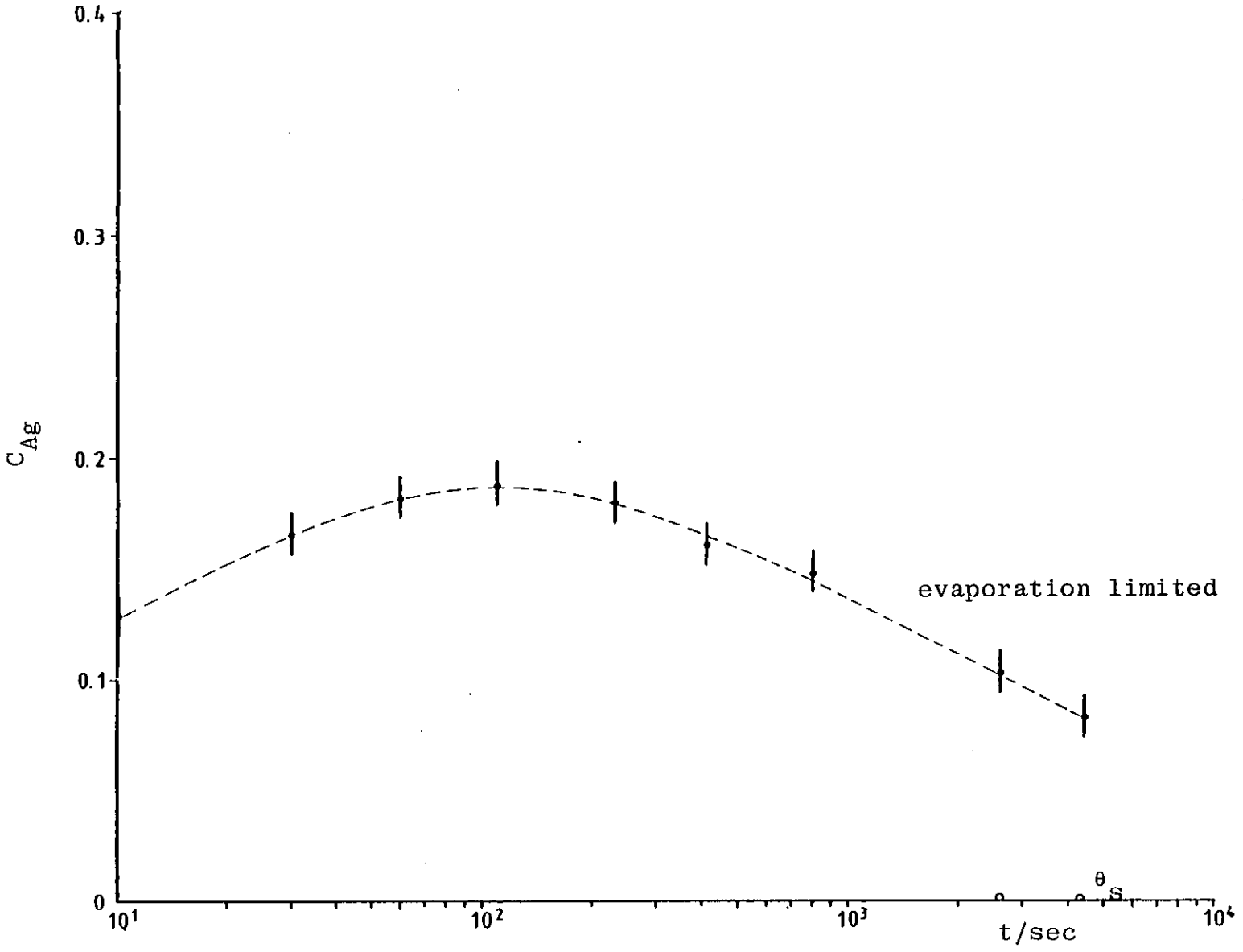


Figure 7.14 Segregation curve for $Ag_{0.01}$ $Pd_{0.99}$ at 973K.

desegregation caused by S segregation is also observed. After equilibrium was obtained, the temperature was reduced to 773K and the annealing continued for ∿ 9 hours. An increase in the Ag surface composition is observed, indicating that the Ag enrichment is reversible as a function of temperature.

Figure 7.14 shows the segregation curve for T = 973K. The observed levels of Ag enrichment are lower than the ones obtained at 773K and 873K. The Ag surface composition rapidly increases, reaches a maximum in ∿ 100 sec. and then decreases. The decrease in Ag composition is not a result of S segregation but of irreversible Ag loss by evaporation. At this temperature a true equilibrium surface composition can not be obtained.

7.7 Ag - S cosegregation in S contaminated $Ag_{0.07}$ $Pd_{0.93}$

The effect of sulphur on the silver segregation was further investigated in a $Ag_{0.07}$ $Pd_{0.93}$ single crystal sample which presented high levels of S segregation. This sample was prepared to expose both the "close packed" (111) surface and the "open" (012) surface. An interrupted annealing at T = 823K was carried out; Auger spectra and diffraction patterns were recorded at room temperature and then the annealing was continued.

Figure 7.15 presents the segregation curves obtained for the (012) and (111) surfaces. A strong S segregation

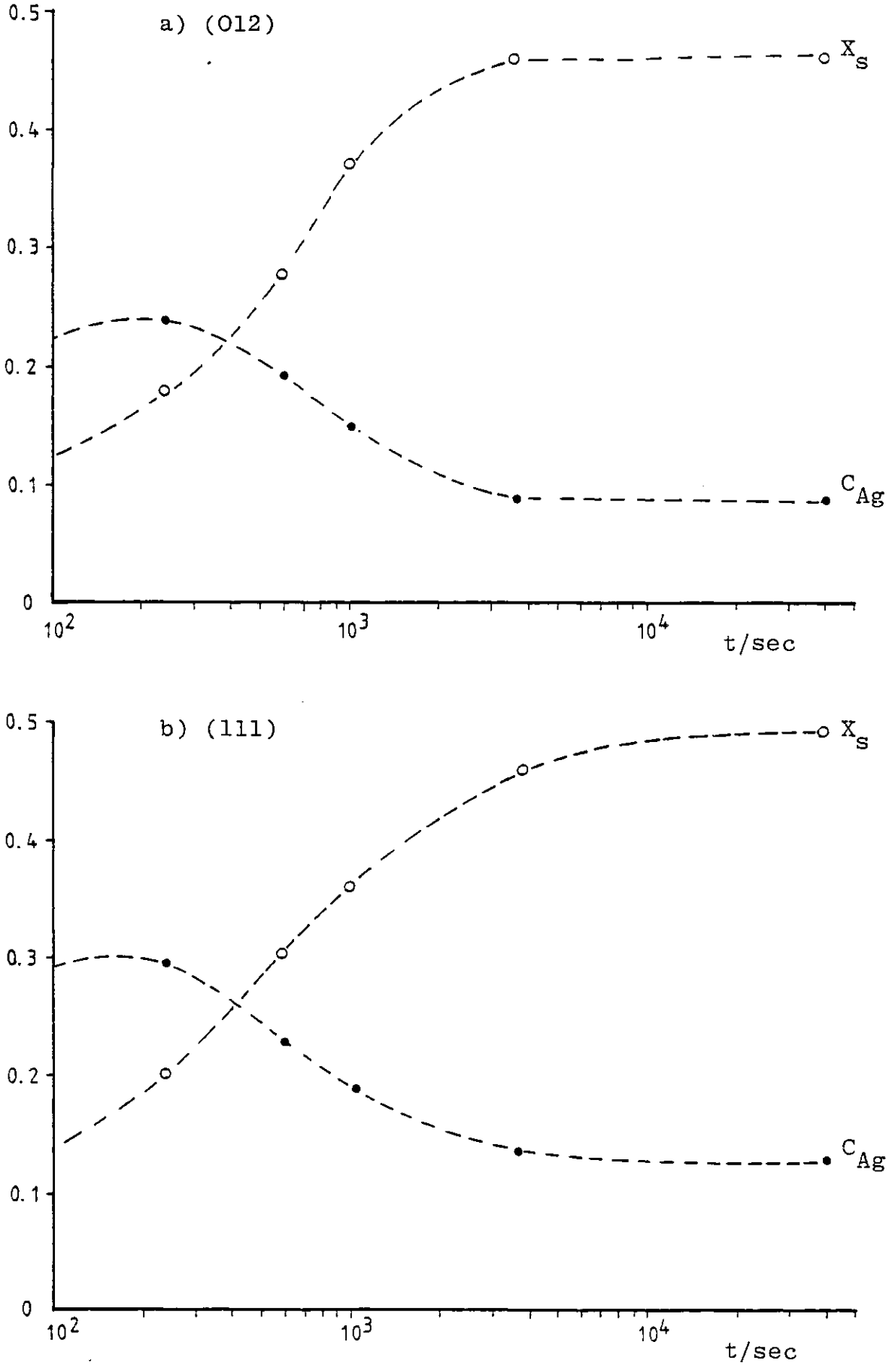


Figure 7.15 Segregation curve for $Ag_{0.07}$ $Pd_{0.93}$ at 823K. a) (012) surface; b) (111) surface.

is manifested. The Ag surface composition initially rises and then falls as S segregates. The Ag surface composition has been plotted in figure 7.16 as a function of the fractional S monolayer X_S. As can be observed, the reduction of silver as a function of the sulphur increase can be well approximated by a straight line. Such a linear relation has been observed for all the samples which presented Ag depletion as a consequence of S segregation, and permit us to make estimates of the levels of silver that would exist in the absence of sulphur.

LEED patterns corresponding to the different stages of S segregation are given in figures 7.17 and 7.18 for the (012) and (111) surfaces respectively.

The diffraction patterns corresponding to the (012) surface show initially a diffuse background that gradually diminishes giving a better defined 1 x 1 structure.

On the (111) surface the segregating sulphur gives rise to a sequence of ordered structures. The pattern of figure 7.17c corresponds to the p(2 x 2) structure shown in figure 7.8a and the pattern 7.17f corresponds to the saturation structure shown in figure 7.8b.

The shape of the S Auger peak at the different stages of segregation was monitored using a 3 V_{pp} modulation. Figure 7.19 shows the sequence corresponding to sulphur on the (012) surface; a triplet structure consisting of a main peak (labelled B) and two shoulders (labelled A and C) are

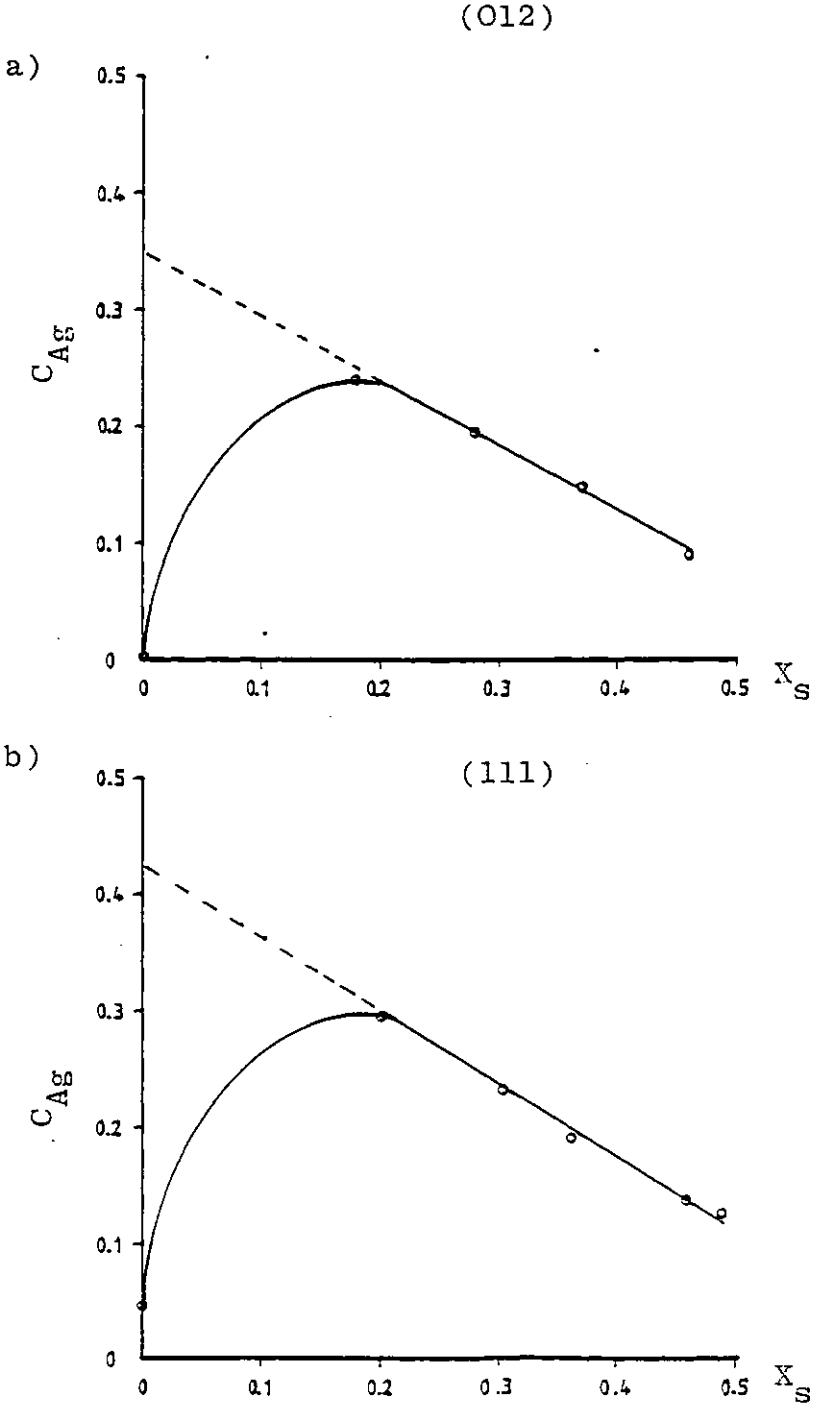
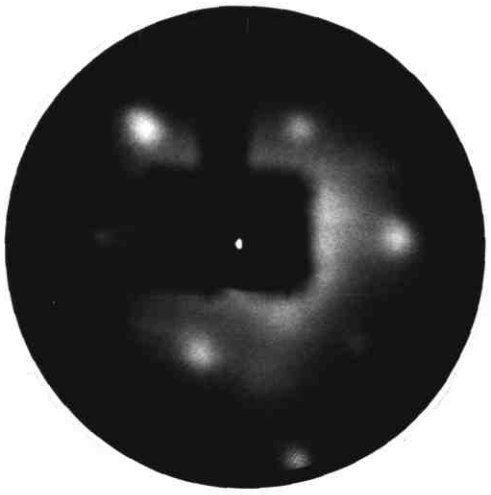
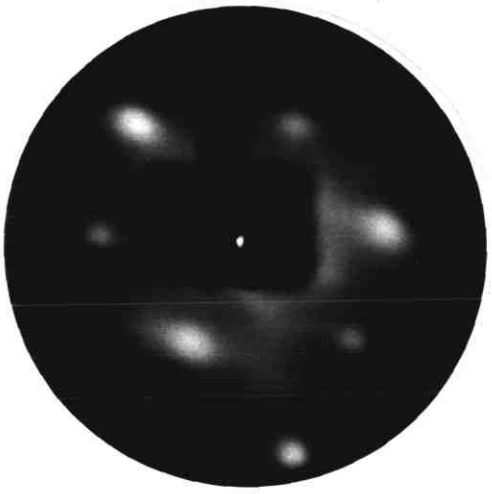


Figure 7.16 Ag surface composition as a function of S fractional monolayer for the $Ag_{0.07}$ $Pd_{0.93}$ (012) and (111) surfaces.

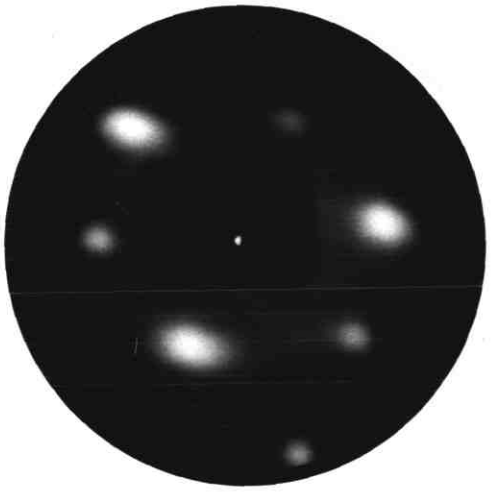
t = 240 sec



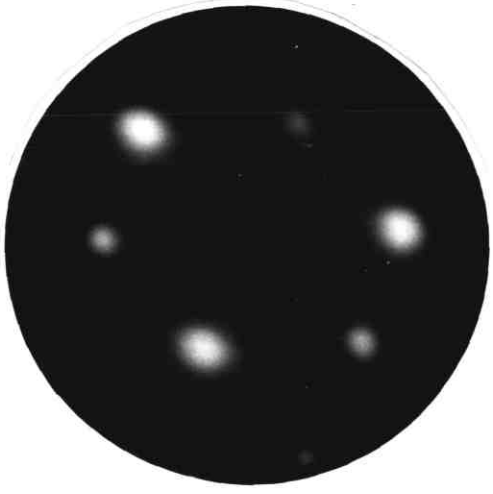
t = 600 sec



t = 1020 sec



t = 3660 sec



t = 40000 sec

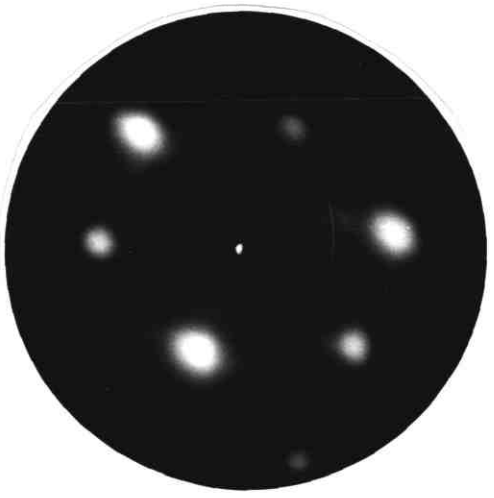
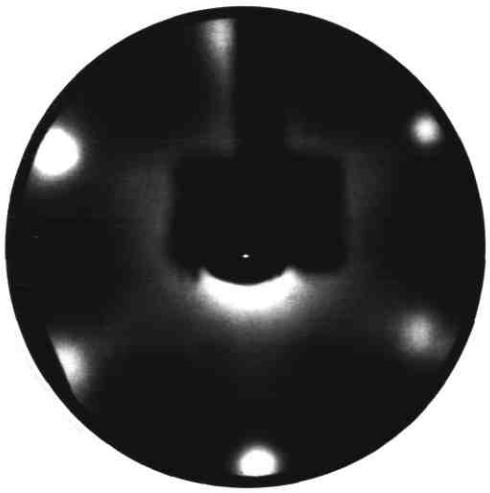
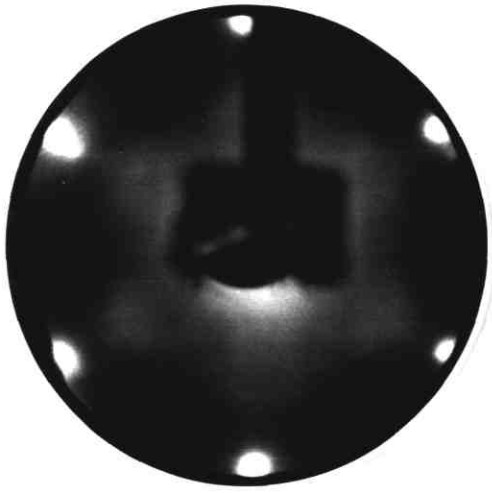


Figure 7.17 LEED patterns of sulphur segregating to the $Ag_{0.07}$ $Pd_{0.93}$ (012) surface. T = 823K. Ep = 50 eV.

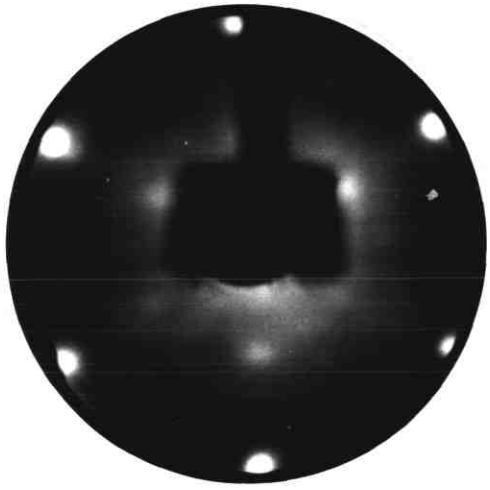
a) t = 0 sec



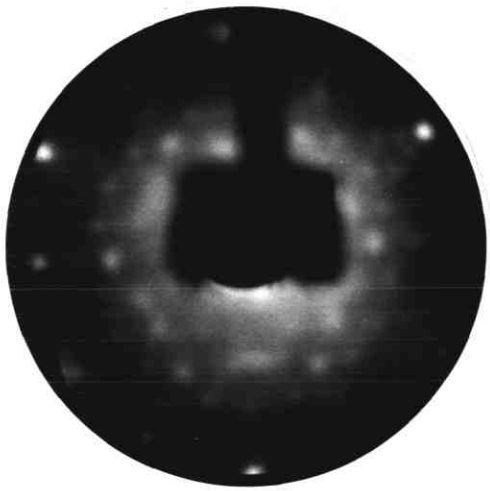
b) t = 240 sec



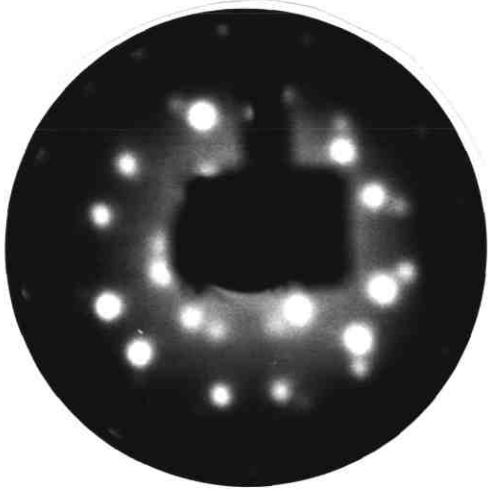
c) t = 600 sec



d) t = 1020 sec



e) t = 3660 sec



f) t = 40000 sec

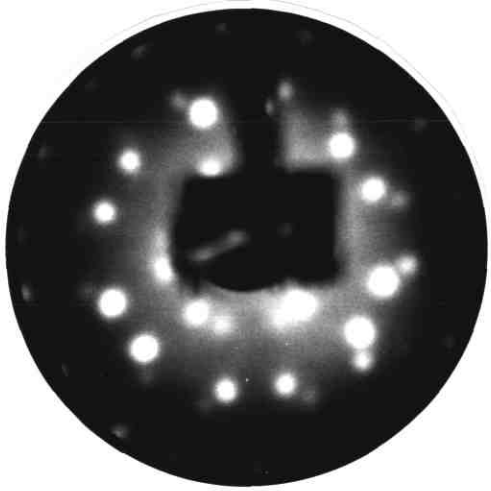


Figure 7.18 LEED patterns of sulphur segregating to the $Ag_{0.07}$ $Pd_{0.93}$ (111) surface. T = 823K Ep = 55 eV

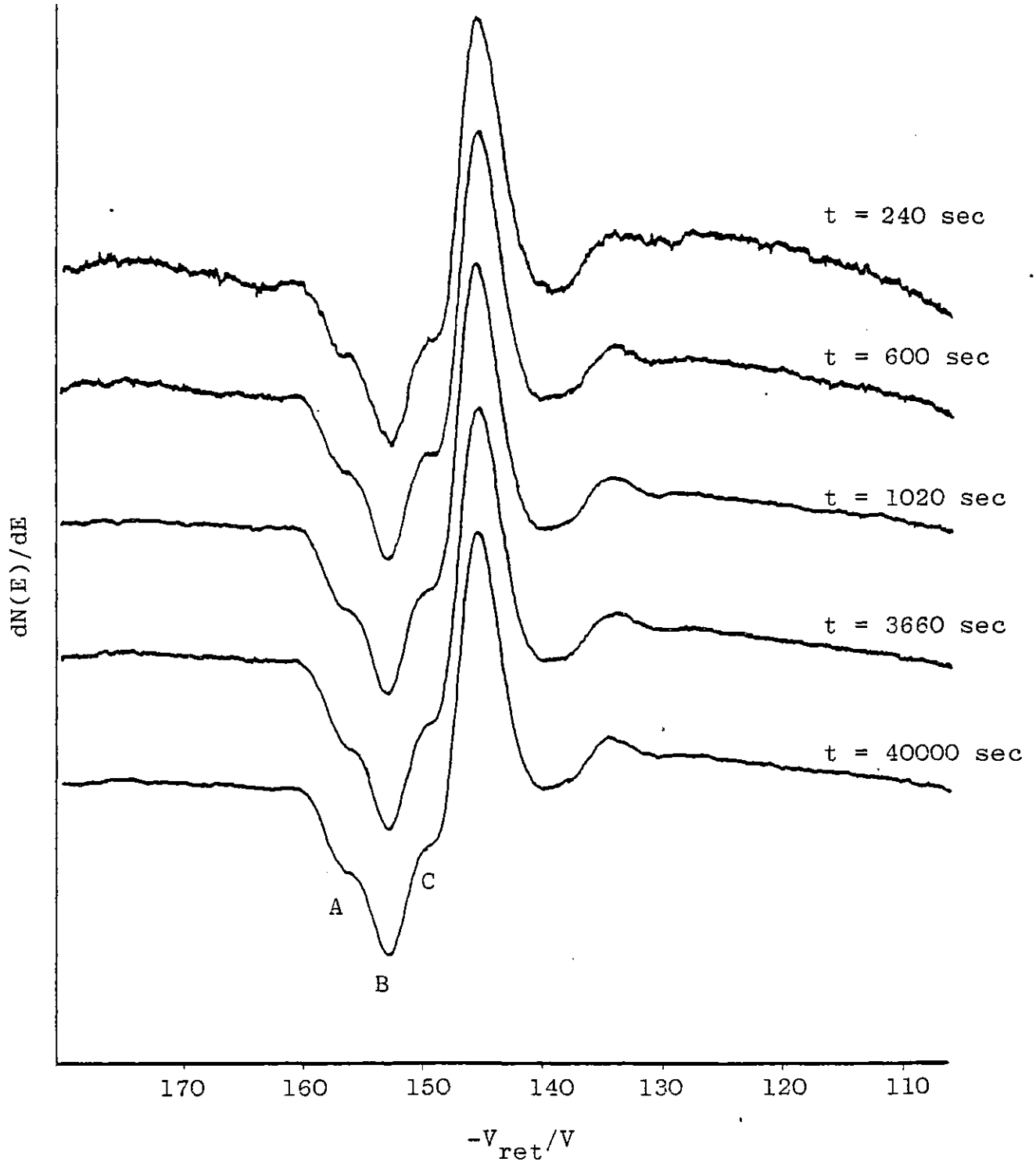


Figure 7.19 Auger S line shape for different segregation levels on $Ag_{0.07}$ $Pd_{0.93}$ (012). 3 V_{pp} modulation.

observed on the negative incursion of the S Auger peak. There is not much change of shape for the different coverages.

The sequence shown in figure 7.20 corresponds to sulphur on the (111) surface. As the S coverage increases, the shoulders A and C develop into well defined minima. Although the spectra presented here were obtained at room temperature, it was verified that this structure is also present at 750K.

It is known that the shape of the Auger peak of a given element may give information about its chemical environment. In a study of the S Auger line shape, W. Losch[6] reports line shapes for S segregated to the surface of a CuAu alloy which are very similar to the ones presented here, and he reaches the following conclusions:

a) Atomic S presents only the main peak B without the A, B fine structure.

b) S in the $S^{(2-)}$ oxidation state is characterized by the peak C, shifted to the low energy side of the main peak. Generally, a doublet from $S^{(2-)}$ (peak C) and S (peak B) is observed with varying peak intensities, depending on the amounts of S and $S^{(2-)}$.

c) S adsorbed on metallic substrates appears as a doublet: the main peak B and the peak A, shifted to the high energy side.

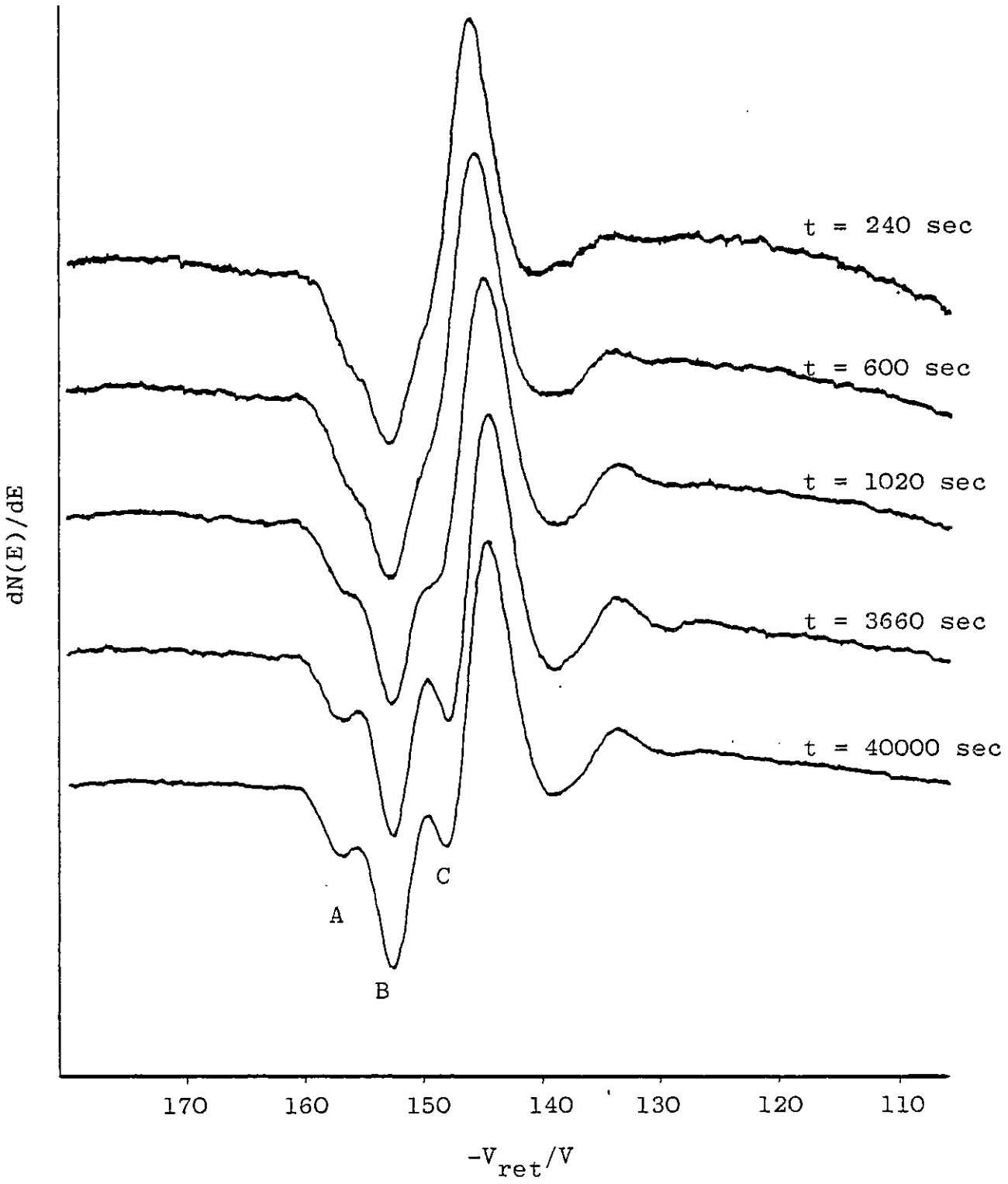


Figure 7.20 Auger S line shape variation on $Ag_{0.07}$ $Pd_{0.93}$ (111) due to increasing segregation levels. 3 V_{pp} modulation.

Peak A, has been observed for S absorbed on several metals. T. Miura[7] assigns it to an interatomic Auger process, the final holes of which are in states originating from the substrate metal atoms.

Figure 7.21 compares the final S Auger line shape obtained for S on the (012) and (111) surfaces with that of S in the PdS compound. Note that the feature A, associated with the interatomic Auger transition, is absent in the compound spectrum. Although it is not immediately obvious, the feature C could be associated to the sulphur peak in PdS, in agreement with Losch's conclusions.

A further test of the state of sulphur on AgPd was carried out by comparing the XPS spectra of PdS with that of sulphur segregated to the (111) face of the $Ag_{0.07}$ $Pd_{0.93}$ alloy. The level of sulphur on the surface was $X_S \approx 0.22$ monolayers and the Ag surface composition was $C_{Ag} \approx 0.18$ and was starting to diminish as a consequence of the sulphur presence.

Figure 7.22 compares the Pd 3d core level spectra in the alloy and in PdS. A chemical shift of $\sim$ 1 eV. is observed in the compound as compared with the metal. Figure 7.23 compares the corresponding S 2p signals. No noticeable shift is observed, indicating that the amount of charge per surface sulphur atom is comparable with that of sulphur in PdS.

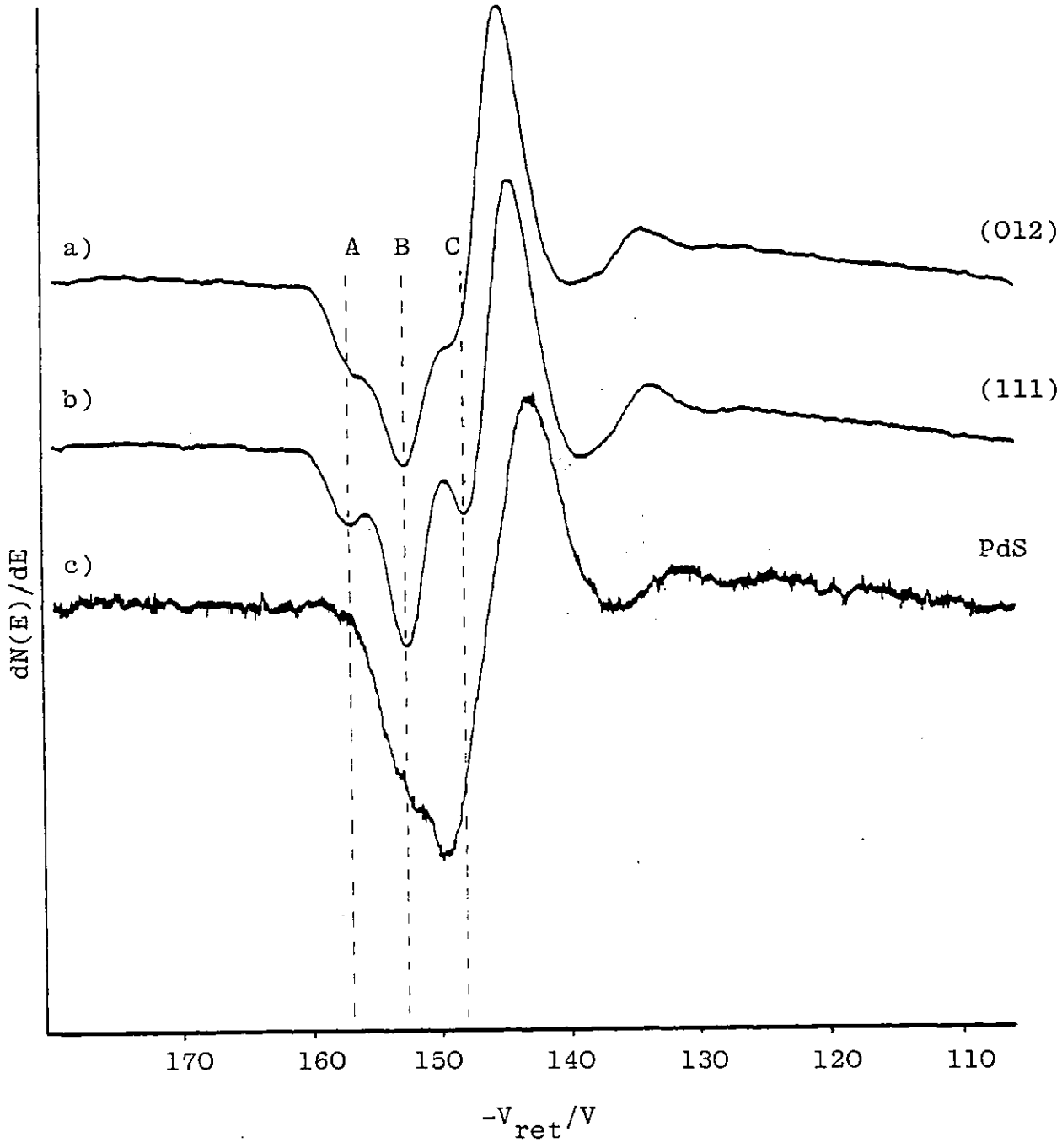
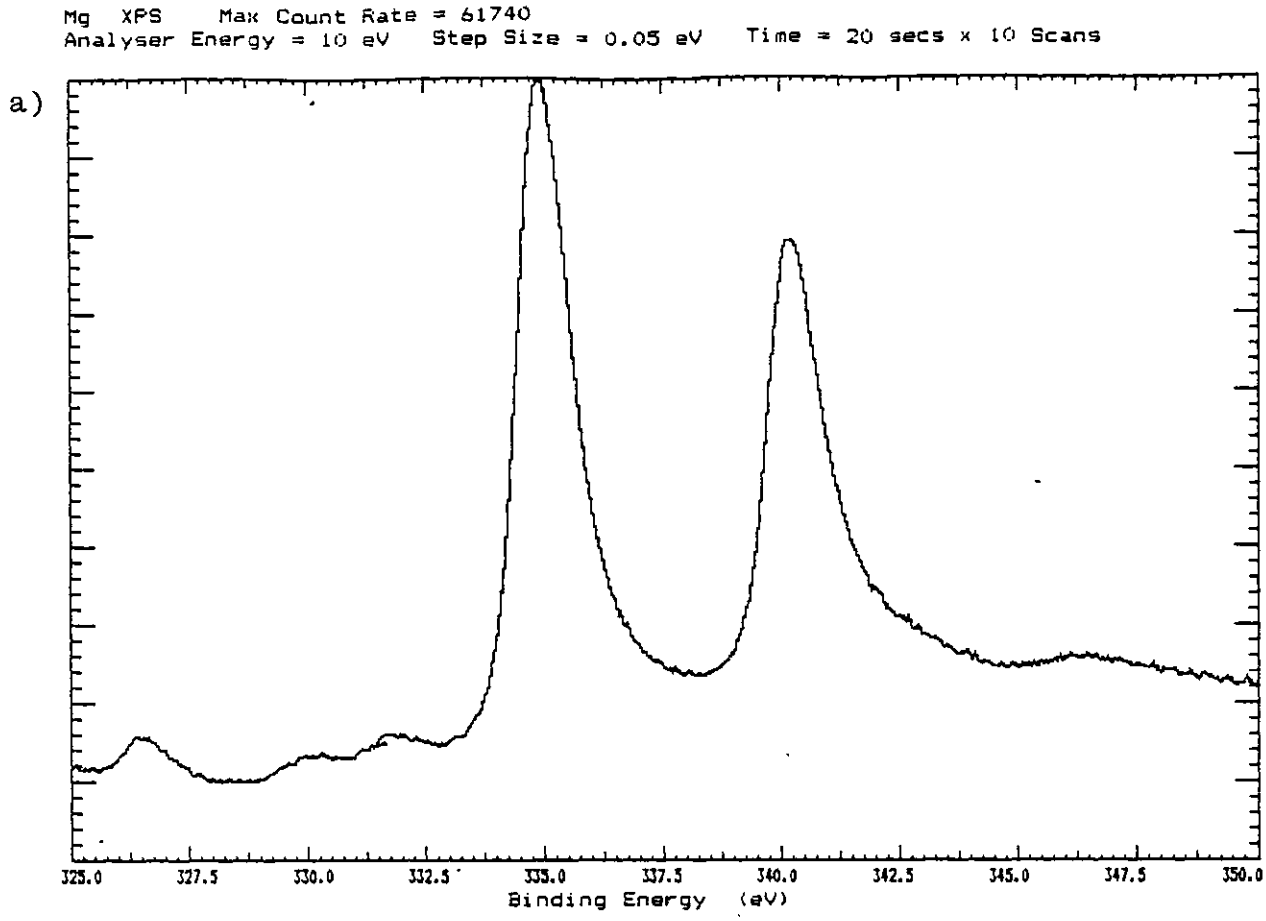


Figure 7.21 Comparison of Auger S line shapes.

a) S on $Ag_{0.07}$ $Pd_{0.93}$ (012)

b) S on $Ag_{0.07}$ $Pd_{0.93}$ (111)

c) S in PdS.



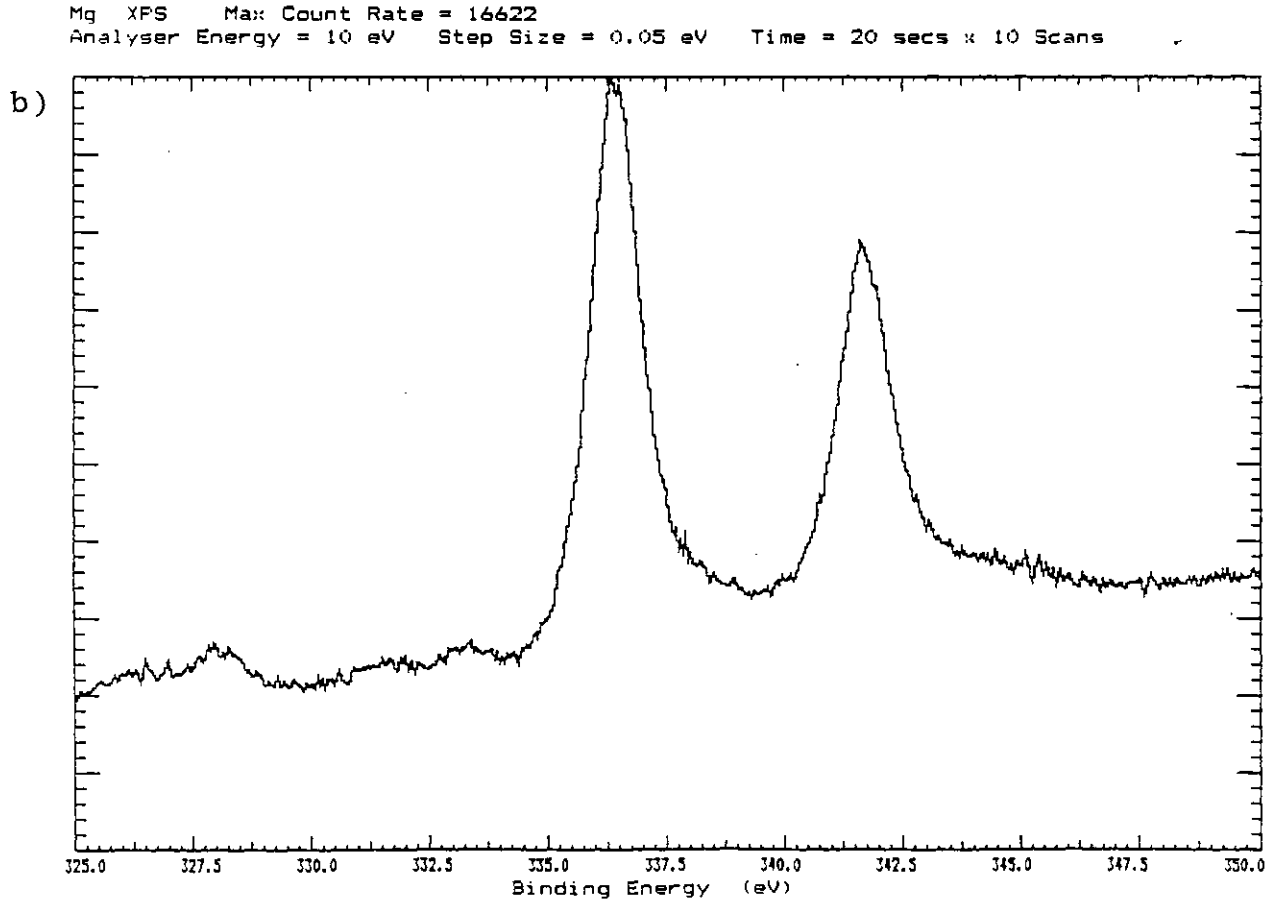
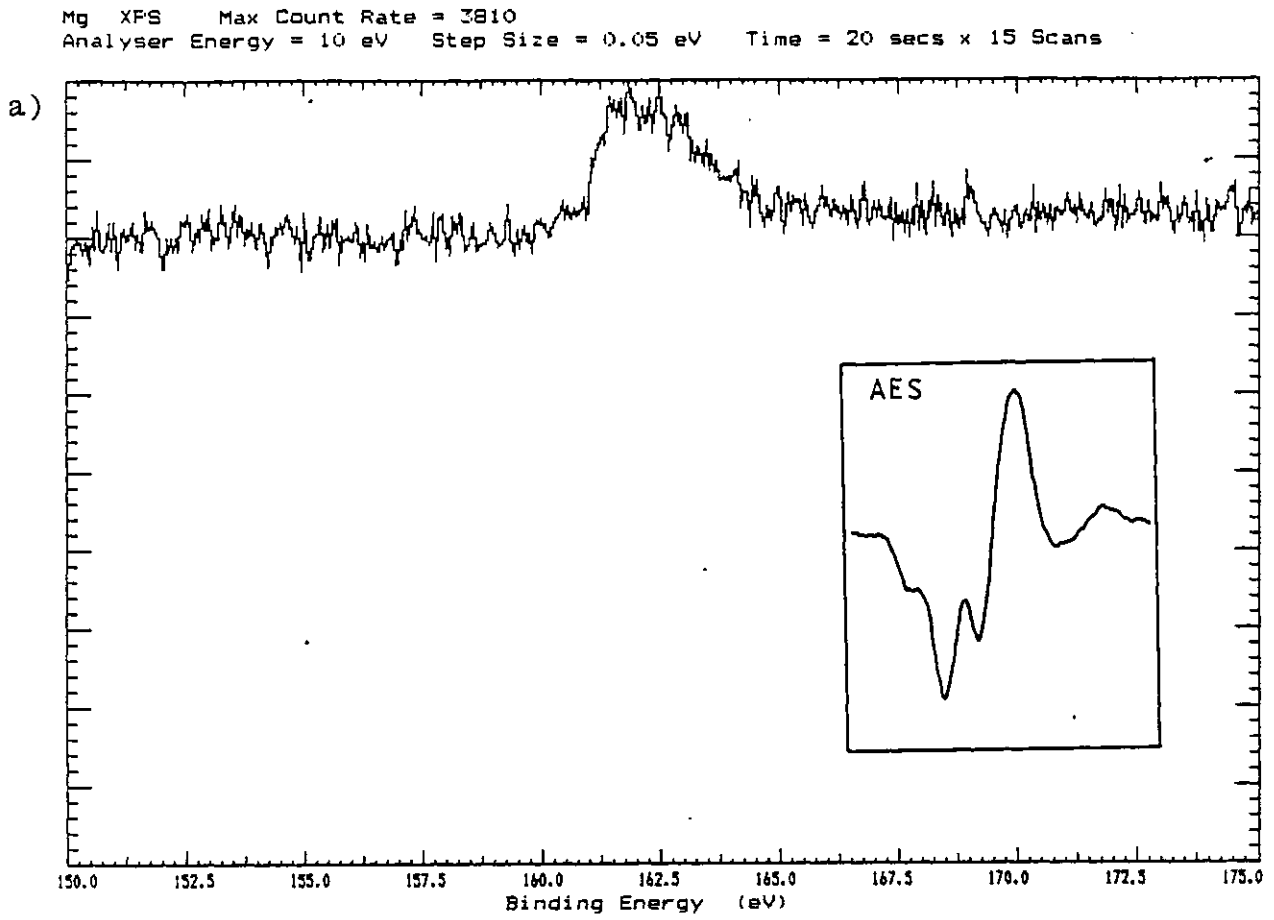


Figure 7.22 Palladium 3d XPS spectra. a) in AgPd.

b) in PdS.



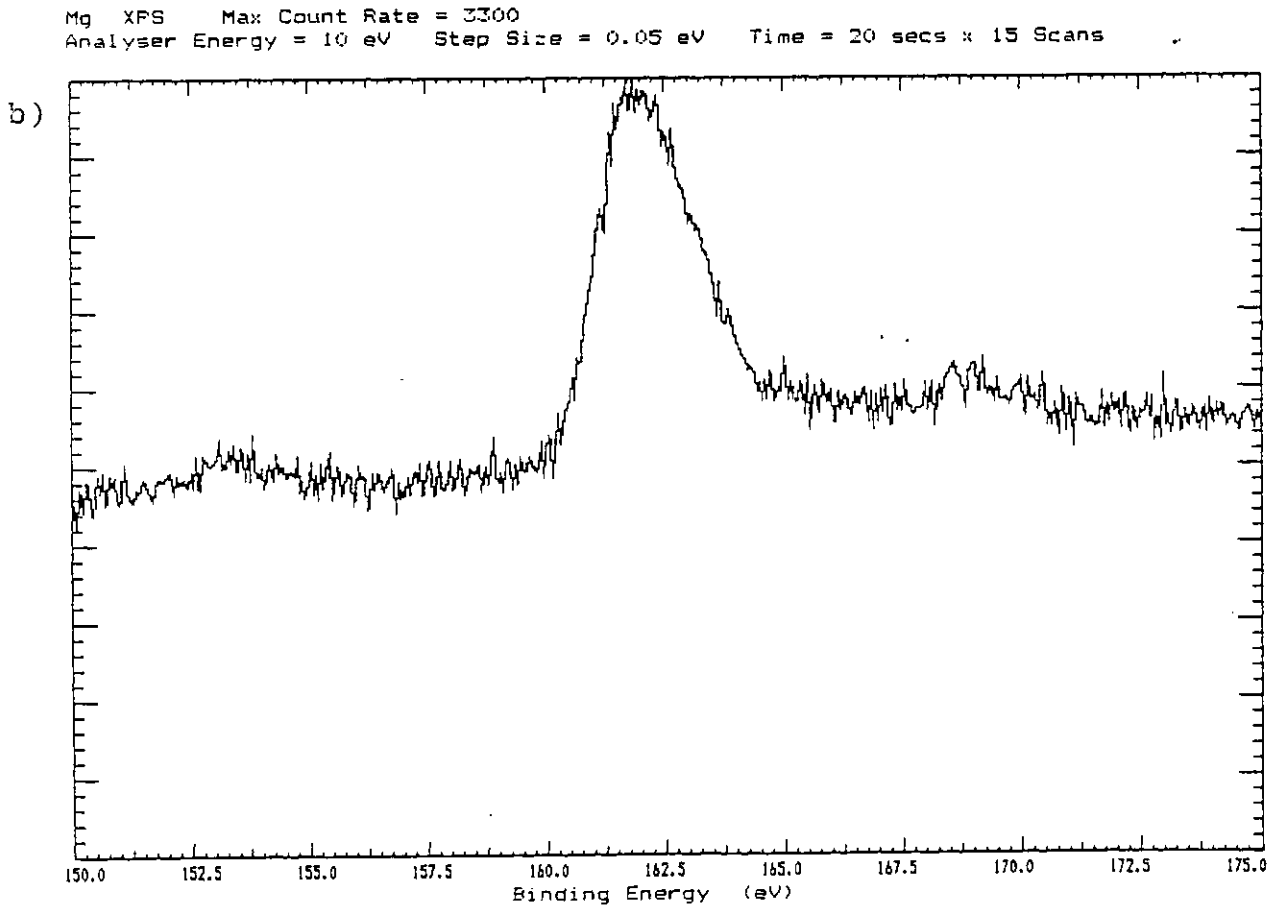


Figure 7.23. Sulphur 2p XPS spectra. a) S on AgPd (sulphur Auger line shape shown inset) b) S in PdS.

The sequence of Auger spectra given in figures 7.19 and 7.20 would then indicate that on the (012) face the relative amount of sulphur in the $S^{(-2)}$ like state is approximately constant for different converages while on the (012) it increases with coverage.

In a study of sulphur segregation in a polycrystalline Pd specimen, Matsumoto et. al.[8] have shown that sulphur on the Pd surface is negatively charged due to the strong interaction with the metal. The amount of negative charge on S being comparable with that on PdS when the sulphur coverage is low and decreasing as the coverage increases, approaching that of solid sulphur. The results presented here suggest that this behaviour can be dependent on the surface orientation.

7.8 Annealing of AgPd alloys in the presence of CO

In order to check for a possible CO chemisorption induced Pd Segregation in AgPd, measurements of the surface composition were made on polycrystalline $Ag_{0.95}\ Pd_{0.05}$ and $Ag_{0.05}\ Pd_{0.95}$ samples annealed in UHV and in the presence 10^{-4} torr of CO.

Annealing of these samples at 473K for 24 hours showed a very slight Ag increase. In presence of CO the sulphur coverage increased from $X_S = 0$ to $X_S \approx 0.03$ monolayers. At this temperature, carbon was clearly detected on the $Ag_{0.05}\ Pd_{0.95}$ sample.

The segregation curve for the $Ag_{0.05}$ $Pd_{0.95}$ specimen in UHV was obtained for T = 673K as shown in figure 7.24. At this temperature the segregation process is extremely slow and the observed maximum in the silver composition was reached in ∿ 7 days. Cosegregation of sulphur was also observed. After this period the ion pump was switched off and CO was admitted at a pressure of 10^{-4} torr, while pumping with the diffusion pump. As can be observed a large increase in sulphur was obtained with a correspondingly large decrease in silver. It could not be established whether sulphur segregated from the bulk or was absorbed from contaminants in the gas phase. Mass spectra of the residual gas with a CO partial pressure of 10^{-6} torr failed to show any S containing species.

Figure 7.25 shows a segregation curve for a similar experiment on the same sample at 773K.

7.9 Thermal desorption of CO from $Ag_{0.01}$ $Pd_{0.99}$ (100)

Thermal desorption experiments of CO from the $Ag_{0.01}$ $Pd_{0.99}$ (100) surface were performed in the 300 -550K temperature range using a linear heating rate β = 8K/sec. Gas exposures were carried out at room temperatue with 10^{-8} Torr CO partial pressure.

Due to preferential silver sputtering the surface did not show any Ag Auger signal after argon bombardment. A set of thermal desorption spectra corresponding to different

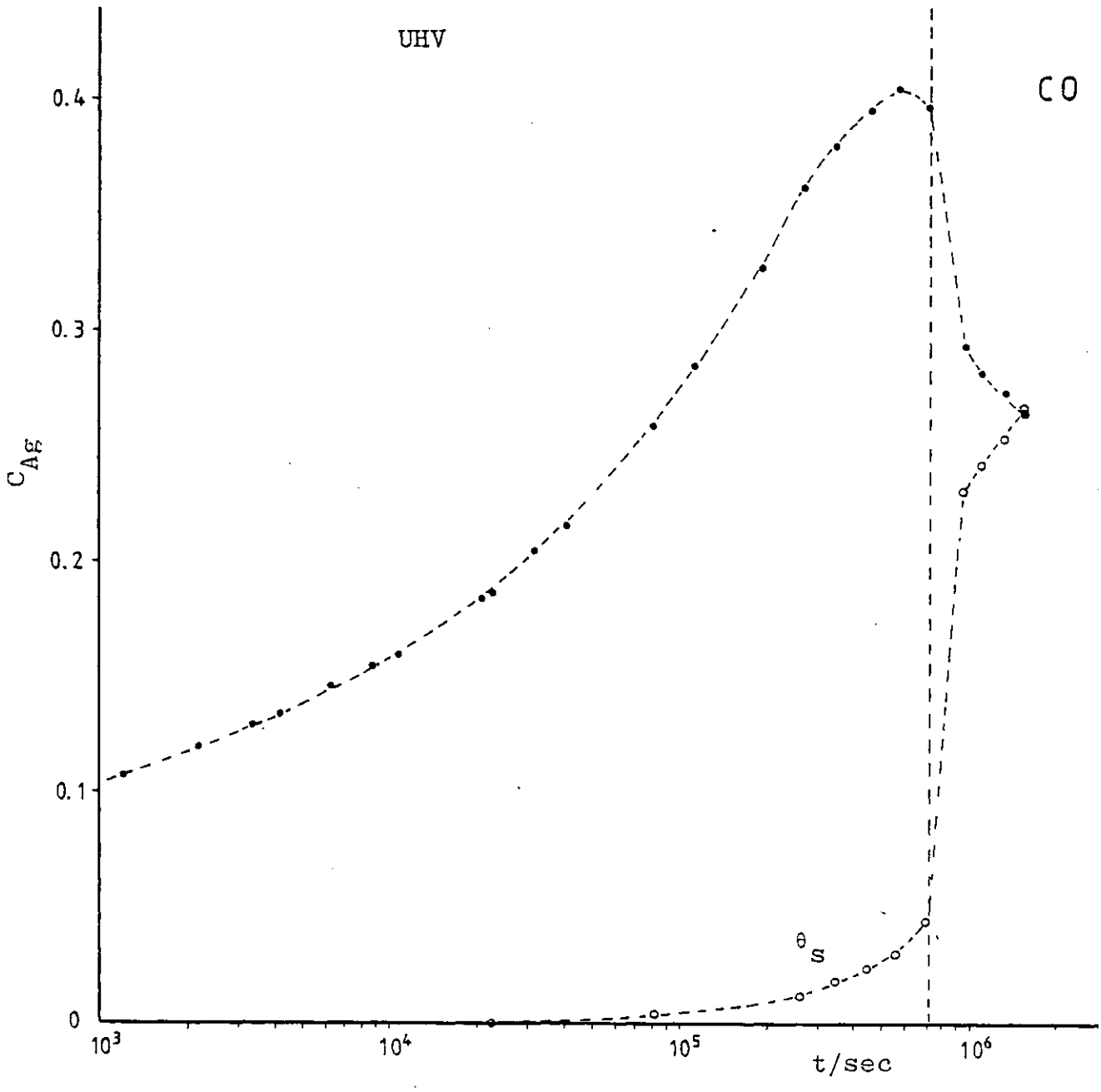


Figure 7.24 Segregation curve for polycrystalline $Ag_{0.05}$ $Pd_{0.95}$ atT = 673K.

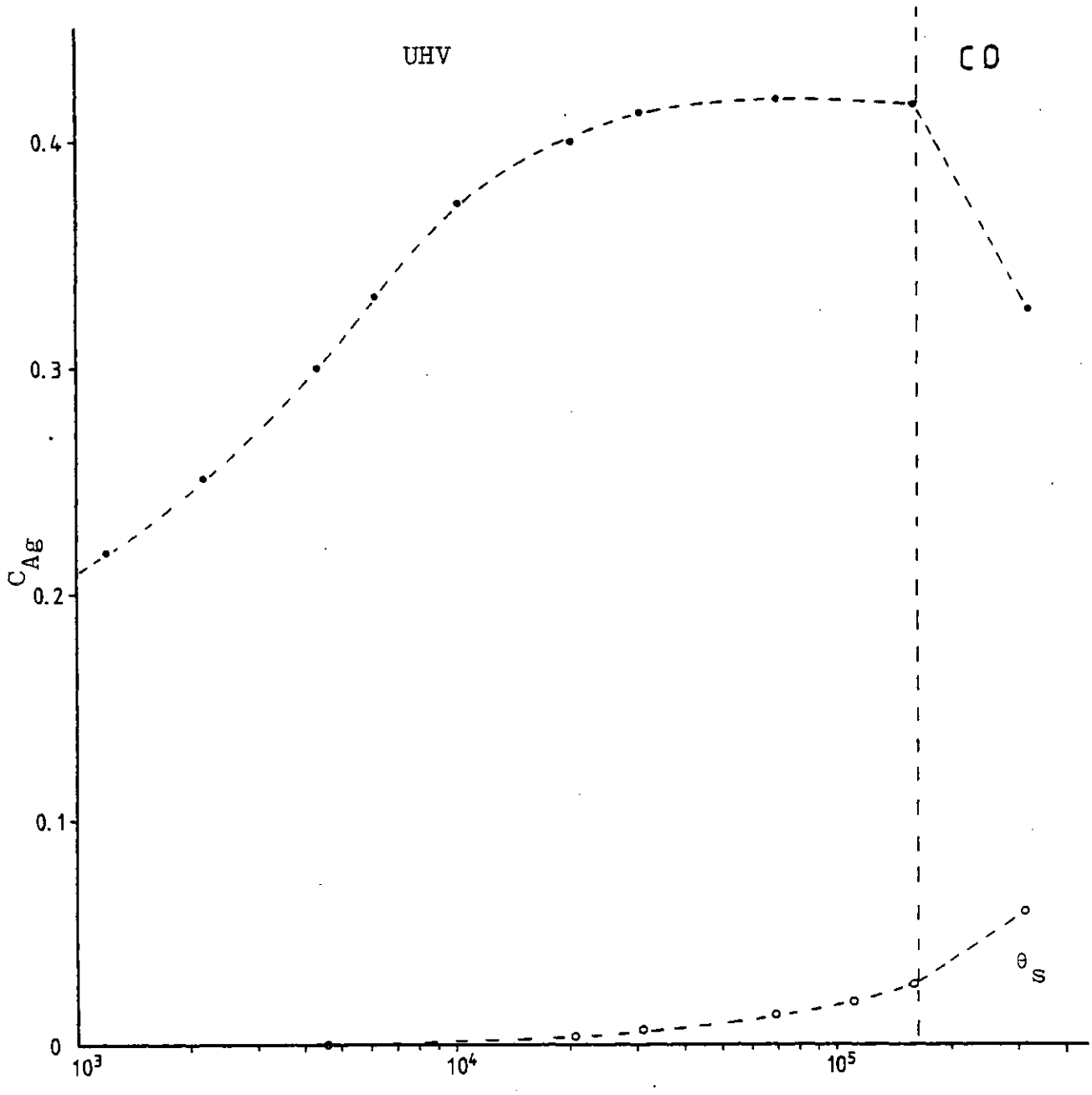


Figure 7.25 Segregation curve for polycrystalline $Ag_{0.05}$ $Pd_{0.95}$ at T = 773K.

CO exposures on this 100% Pd surface are presented in figure 7.26. At low coverages a single peak is observed, with its maximum at 476K. This peak shifts to lower temperatures as the CO exposure increases. At higher exposures a second lower temperature peak, centred at ∿ 430K appears. At 1L both peaks are of roughly the same intensity. No variation is the alloy surface composition was observed after the TDS experiments.

The high temperature peak in pure Pd has been attributed to a first order CO desorption process with coverage dependent activation energy[9].

Thermal desorption spectra were also recorded for 1L CO exposures on the same specimen with different Ag surface compositions. The alloy surface composition was carried in a controlled way by interrupted annealing at 773K andis given as the average effective composition calculted by AES.

Figure 7.27 presents a set of thermal desorption spectra corresponding to various Ag surface compositions. The two peaks present in the spectrum from the 100% Pd surface composition alloy sample gradually decrease with decreasing Pd surface content. The high temperature peak, however, suffers a more pronounced reduction than the low temperature one. The surface composition before and after each desorption spectrum was the same.

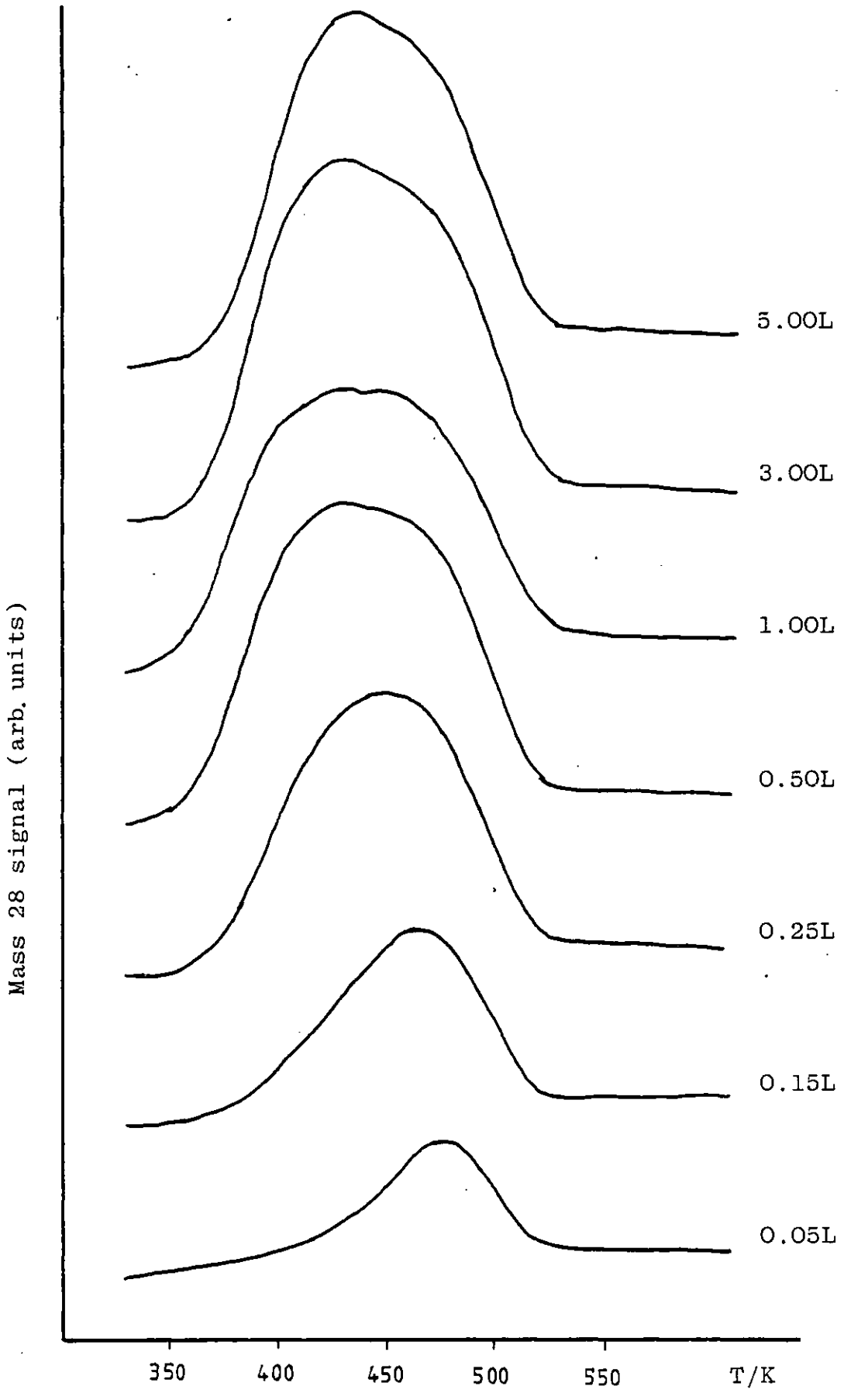


Figure 7.26 Thermal desorption spectra of CO on $Ag_{0.01}$ $Pd_{0.99}$ (100) after argon bombardment. Surface compostion = 100% Pd.

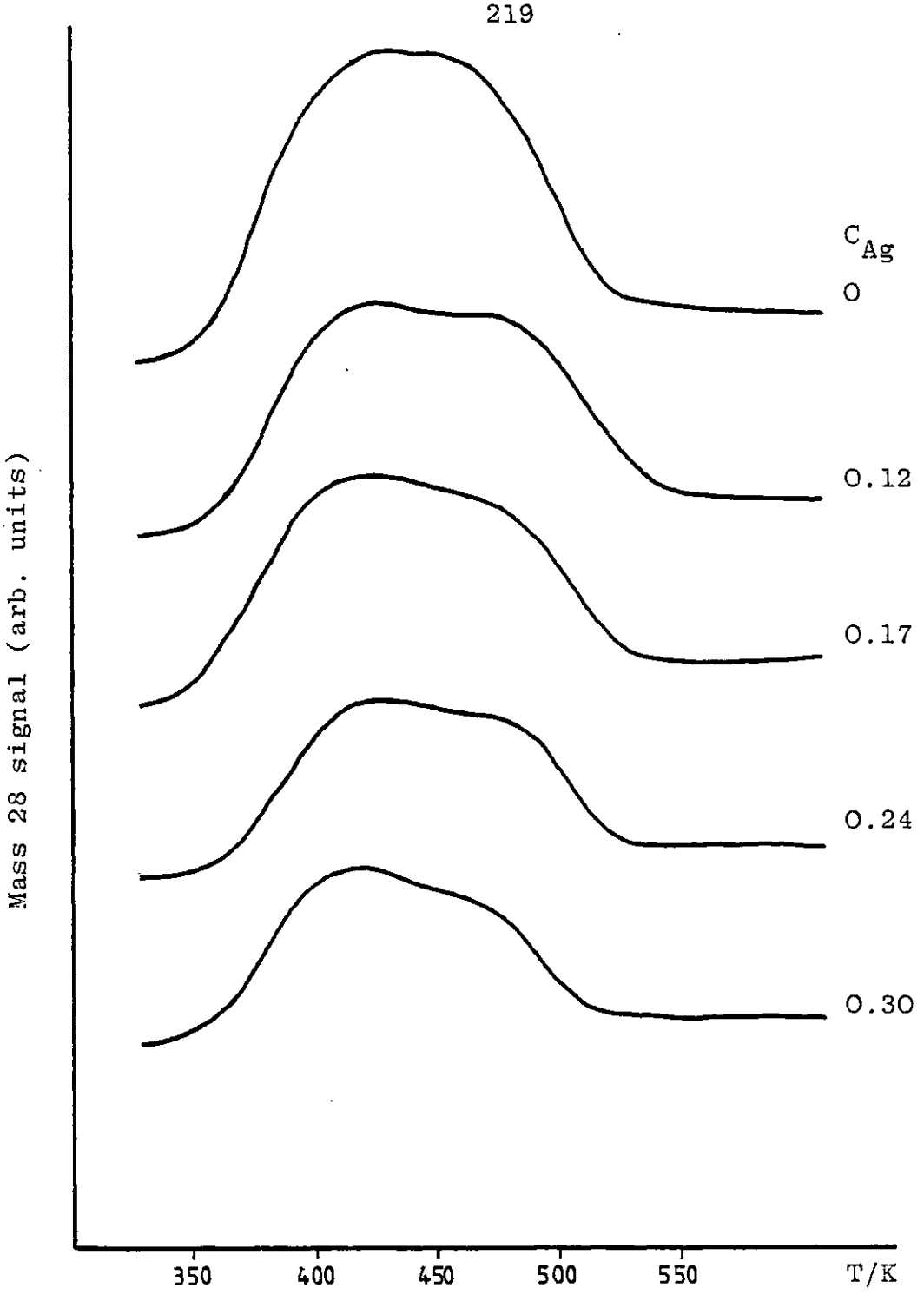


Figure 7.27 Thermal desorption spectra for 1L CO on $Ag_{0.01}$ $Pd_{0.99}$ (100) with different Ag effective surface compositions.

It is known[10] that CO does not adsorb on Ag at the temperatures used in the present experiments. The two peaks observed for the 100% Pd surface can be assigned to two different kinds of CO adsorption on Pd sites: the high temperature state is associated with the bonding of CO to a "large" number of Pd atoms and the low temperature state is associated with CO bonding to a smaller number of Pd atoms. The effect of silver is then to dilute the available Pd sites for the adsorption of CO; the number of "large" Pd ensembles, necessary for strong CO adsorption being more affected than the number of "small" ensembles corresponding to the weak CO adsorption.

7.10 Discussion.

Most theories of surface segregation in alloys describe systems in equilibrium. In practice, however, since the approach to equilibrium is controlled by diffussion from the bulk, the time to reach equilibrium can be very long at feasible temperatures.

As was shown in the segregation curves presented here, the annealing times necessary to reach equilibrium in AgPd alloys at 673K, 773K and 873K are of the order of 10^6, 10^5 and 10^4 seconds respectively. At lower temperatures the equilibration time becomes extremely long. At higher temperatures silver loss by evaporation becomes important and equilibrium can not be achieved.

The segregation curves obtained for the three low index faces of $Ag_{0.01}$ $Pd_{0.99}$ at 773K show that the (110) surface presents a slightly higher Ag enrichment than the (100) surface. Both of these faces presented a clearly larger Ag enrichment than the close packed (111) surface. This variation is attributed to the different atomic roughness of these surfaces. The estimated Ag equilibrium compositions are 0.35, 0.34 and 0.25 for the (110) (100) and (111) respectively. These values correspond to the effective composition over 3 monolayers approximately, so the Ag enrichment in the topmost layer is actually much more pronounced.

Pd surface segregation induced by CO chemisorption on the alloy surface was not observed. At a partial pressure of 10^{-4} torr CO is not expected to be adsorbed on the alloy surface for temperatures above 573K. For temperatures below 573K, segregation occurs so slowly that this effect can not be observed within a reasonable experimental observation time. The Ag desegregation that was observed in the $Ag_{0.05}$ $Pd_{0.95}$ polycrystalline sample after annealing in 10^{-4} torr CO at 673K and 773K was associated with an increase in sulphur on the surface so it can not be attributed directly to CO.

Indirect evidence for Pd segregation induced by CO chemisorption on AgPd thin films has been reported by Bouwman et. al.[11] using measurements of the work function and the electron emission constant on samples exposed to

$\sim 10^{-4}$ torr CO during several hours at temperatures as low as 293K. Comparison with the experiments performed in the present work would indicate that in their samples the metal atoms have a much higher mobility than in the polycrystalline samples used here. However, they do not give any data on the presence of contaminants so a direct comparison with our results is difficult.

The silver depletion caused by sulphur cosegregation as observed in the present work has also been observed by Schwartz in a $Ag_{0.4}$ $Pd_{0.6}$ polycrystalline alloy using AES. This phenomenon can be explained in a similar way to the chemisorption induced surface segregation in terms of the relative strength of the bonds formed by the segregating S impurity to each of the components of the alloy.

Investigations of the adsorption and segregation of sulphur to the surface of several transition and noble metals have determined that S is strongly bonded to the metal surface atoms and that at high coverages it can even form a true adsorbed two-dimensional sulphide[12]. Correlations of the heats of adsorption of sulphur on these metals indicate that the metal-sulphur surface bonds are markedly stronger that the metal-sulphur bonds in the bulk sulphides[13]. Figure 7.28 indicates a linear relation between the heat of adsorption of sulphur at a coverage $X_S = 1/2$ and the heats of formation of the respective bulk sulphides. This figure can be used to estimate the heat of adsorption of sulphur on the surface of Pd, for which

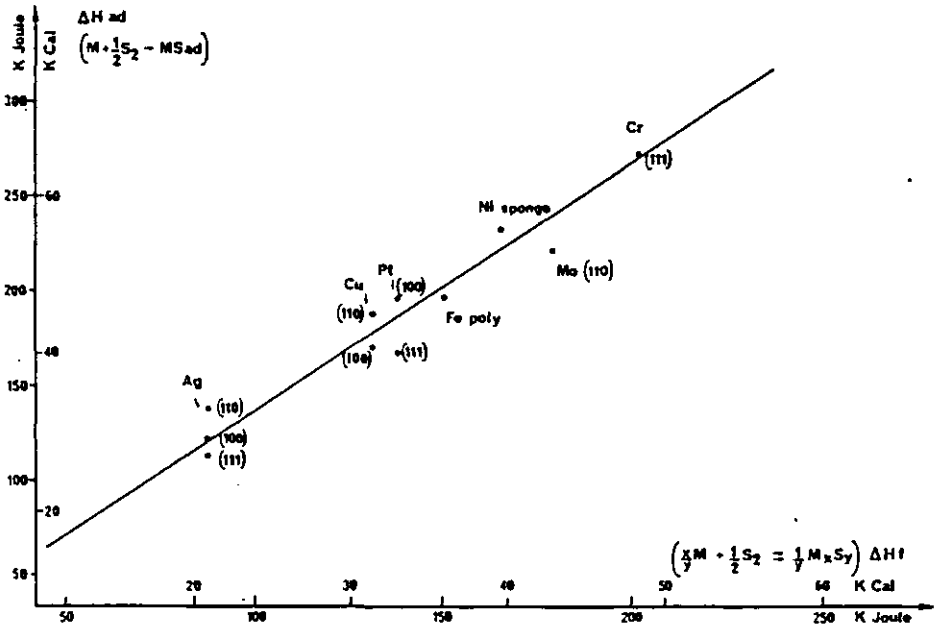


Figure 7.28 Heats of sulphur adsorption (X_S = 1/2) versus heats of bulk sulphide formation. The straight line is approximately given by $|\Delta H_{ad}|$ 1600 + 1.3$|\Delta H_f|$ in cal/mole. (After Bénard et.al.[13]).

there is not experimental data available. Using also the heat of adsorption of sulphur on silver and the heats of solution of sulphur in silver[14] and in palladium[15], the approximate energy diagram of figure 7.29 can be constructed. As can be seen the estimated heat of adsorption on Pd is higher than on Ag; the heat of segregation of S in Pd is much higher than the heat of segregation of Ag in Pd given in table 2.4

The effect of S cosegregation in AgPd alloys can be explained in terms of a segregation model for ternary alloys proposed by Gutman[16] and by Tyson[17].

The heat of segregation for Ag and S in Pd are approximated in this model by

$$\Delta H'_{Ag} = \Delta H_{Ag}^{S} + \alpha' X_S$$

$$\Delta H'_{S} = \Delta H_{S}^{S} + \alpha' X^{S}_{Ag} \qquad 7.6$$

where ΔH_i^S is the heat of segregation of solute i in the absence of solute j and α' represents an extra interaction energy of solute i per surface monolayer of solute j.

For segregation of S and Ag into separate sets of surface sites, the equilibrium surface composition is given by the simultaneous solution of the system of equations

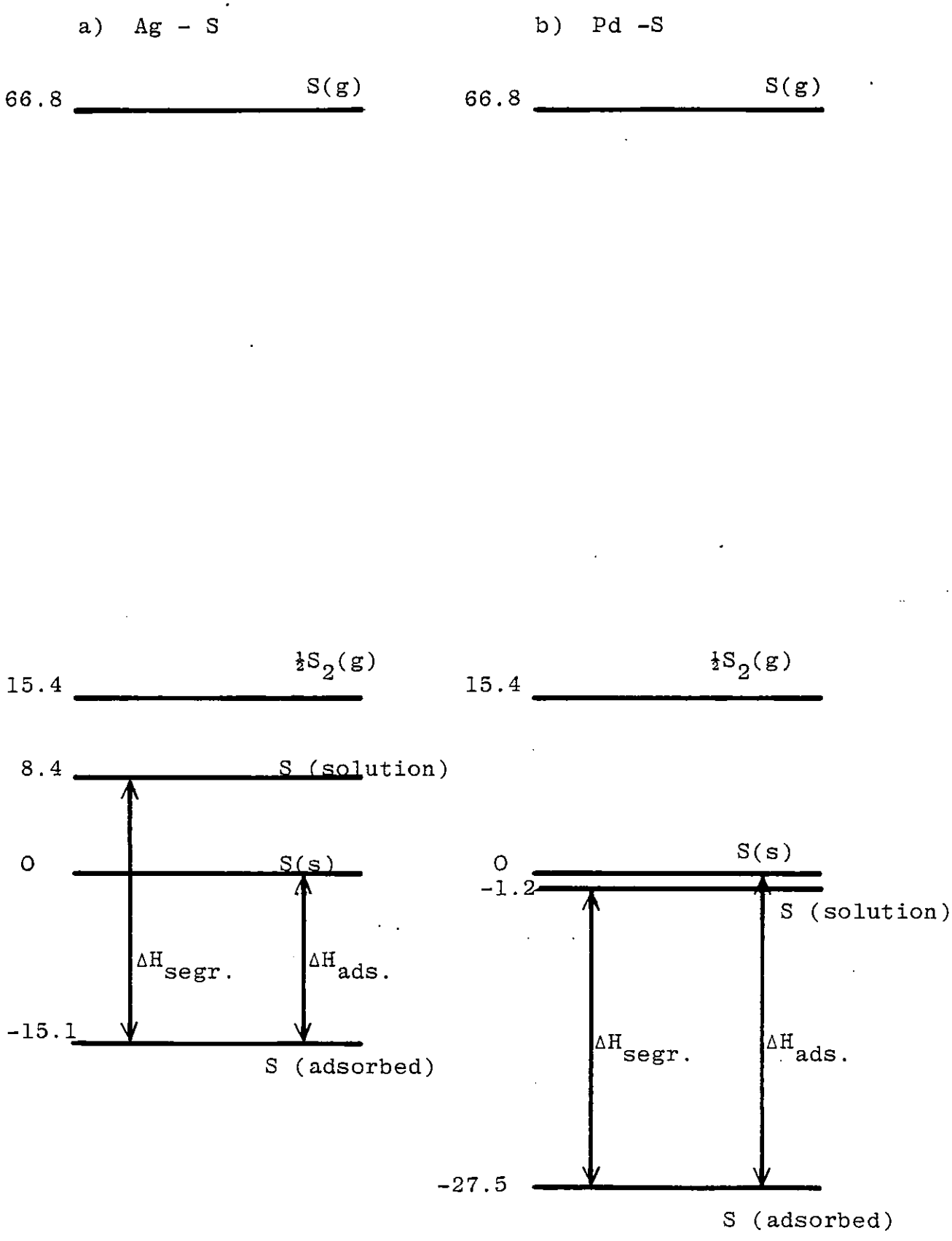


Figure 7.29 Approximate energy diagram for the adsorption and solution of a) S in Ag and b) S in Pd: Energy values in Kcal/mole.

$$\frac{X^{s}_{Ag}}{1-X_{Ag}{}^{s}} = \frac{X^{b}_{Ag}}{1-X_{Ag}{}^{b}} \exp\left(-\Delta H'_{Ag}/RT\right) \qquad 7.7$$

$$\frac{X_s}{1-X_s} = X_s{}^{b} \exp(-\Delta H'_s/RT)$$

The factor α' contains the relative interaction of the solutes S and Ag with respect to the solvent Pd and is given by

$$\alpha' = \alpha_{Ag-S} - \alpha_{Pd-S} - \alpha_{Ag-Pd} \qquad 7.8$$

where the different α_{ij} terms represent the surface bond strength between atoms i and j.

A rough estimate of the $\alpha_{metal-S}$ terms can be made using the adsorption energies given in figure 7.29 and assuming that the adsorbed half layer of sulphur behaves like a regular solution. Using for $\Delta H_{Ag}{}^{s}$ a value of -8400 cal/mole (table 2.4), the heat of surface segregation of silver is given approximately by

$$\Delta H'_{Ag} = (-8400 + 71000X_s) \text{ cal/mole}$$

so it has a strong dependence with the sulphur coverage X_s; it can change its sign for sulphur coverages of the order of 0.1 monolayers.

7.11 Conclusions

Segregation curves $C_{Ag}(t)$ show that the annealing times necessary to attain an equilibrium surface composition in AgPd alloys are of the order of 10^6, 10^5 and 10^4 seconds at T = 673K, 773K and 873K respectively.

Strong Ag enrichment was observed on the clean low index surfaces of a $Ag_{0.01}$ $Pd_{0.99}$ alloy single crystal, the level of enrichment reversibly diminishing with increasing temperature. At T = 973K silver depletion caused by evaporation becomes important.

Evidence for surface specificity in Ag segregation was found; the close packed (111) surface clearly showing a lower level of enrichment than the more open (100) and (110) surfaces.

Strong, reversible Ag desegregation was observed when S segregates to the alloy surface. This can be explained in terms of the stronger bonding existing between S and Pd at the surface in comparison with the bonding between S and Ag.

TDS spectra of CO adsorbed on the $Ag_{0.01}$ $Pd_{0.99}$ (100) surface with different levels of Ag surface enrichment suggest that the effect of Ag is to dilute the Pd sites available for CO adsorption. The number of adsorption sites associated with large Pd ensembles are reduced more than

the number of sites associated with small Pd ensembles.

References (Chapter 7)

1. G.P. Schwartz, Surf. Sci. 76 (1978) 113.

2. F.J. Kuijers and V. Ponec, J. Catalysis 60 (1979) 100.

3. M. Perderau, Surf. Sci. 24 (1971) 239.

4. M.P. Seah and W.A. Dench, Surf. Interf. Analysis 1 (1979) 2.

5. J.L. Domange and J. Oudar, Surf. Sci. 11 (1968) 124.

6. W. Losch, J. Vac. Sci. Technol. 18 (1979) 865.

7. T. Miura, Jpn. J. Appl. Phys. 20 (1981) 1987.

8. Y. Matsumoto, M. Soma, T. Onishi and K. Tamaru, J.C.S. Faraday I, 76 (1980) 1122.

9. V.S. Sundaram, S.P. Da Cunha and R. Landers, Surf. Sci. 119 (1982) L383.

10. J.J. Stephan, P.L. Franke and V. Ponec, J. Catal. 44 (1976) 359.

11. R. Bouwman, G. Lippits and W. Sachtler, J. Catal. 25 (1972) 350.

12. C.H. Bartholomew, P.K. Agraval and J.R. Katzer, Adv. Catal. 31 (1982) 139.

13. J. Benard, J. Oudar, N. Barbouth, E. Margot and Y. Berthier, Surf. Sci. 88 (1979) L35.

14. J. Oudar and N. Barbouth, C.R. Acad. Sc. Paris - C 267 (1968) 644.

15. M. Assefi. and Y. Berthier, C.R. Acad. Sc. Paris - C 286 (1978) 643.

16. M. Gutmann, Surf. Sci. 53 (1975) 213.

17. W.R. Tyson, Acta Metall. 26 (1978) 1471.

Appendix

Computer programme for quantitative AES of binary alloys.

This programme calculates the "surface composition" of a binary substitutional alloy from measured Auger signals using equations 4.20 and 4.28.

The necessary input data consist of:

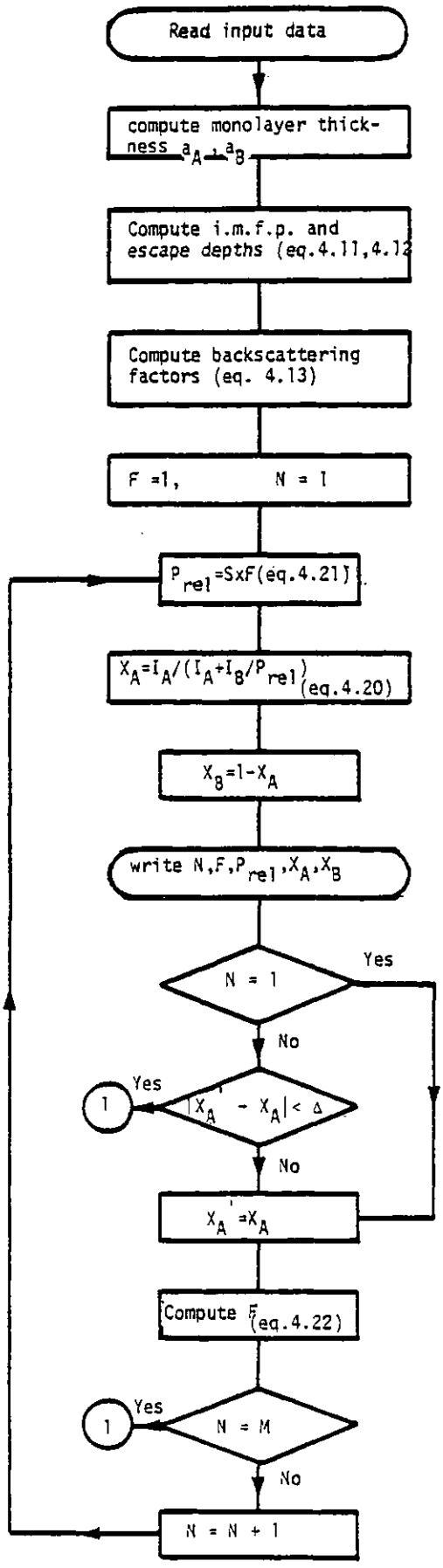
1. Atomic numbers of the alloy components Z_A, Z_B.
2. Bulk composition C_A of component A. It is necessary only for equation 4.28
3. Atomic weights of the alloy components.
4. Densities of the alloy components (in gr/cm^3)
5. Energies of the Auger transitions used (in eV.)
6. Ionization energies of the hole core levels, associated with the Auger transitions (in eV.)
7. Primary beam energy (in eV.)
8. Proportionality constant K relating the escape depth with the i.m.f.p.
9. Ratio of Auger signals of pure B to pure A.
10. Auger signals I_A, I_B.
11. Convergence parameter, Δ.
12. Integer M given the maximum number of iterations.

The programme works as shown in the flow chart. The left hand side of the diagram corresponds to the homogeneous composition case. X_A is computed iteratively, initially taken a unity matrix correction factor. The composition so obtained is used to compute a new value of F(B,A) and the

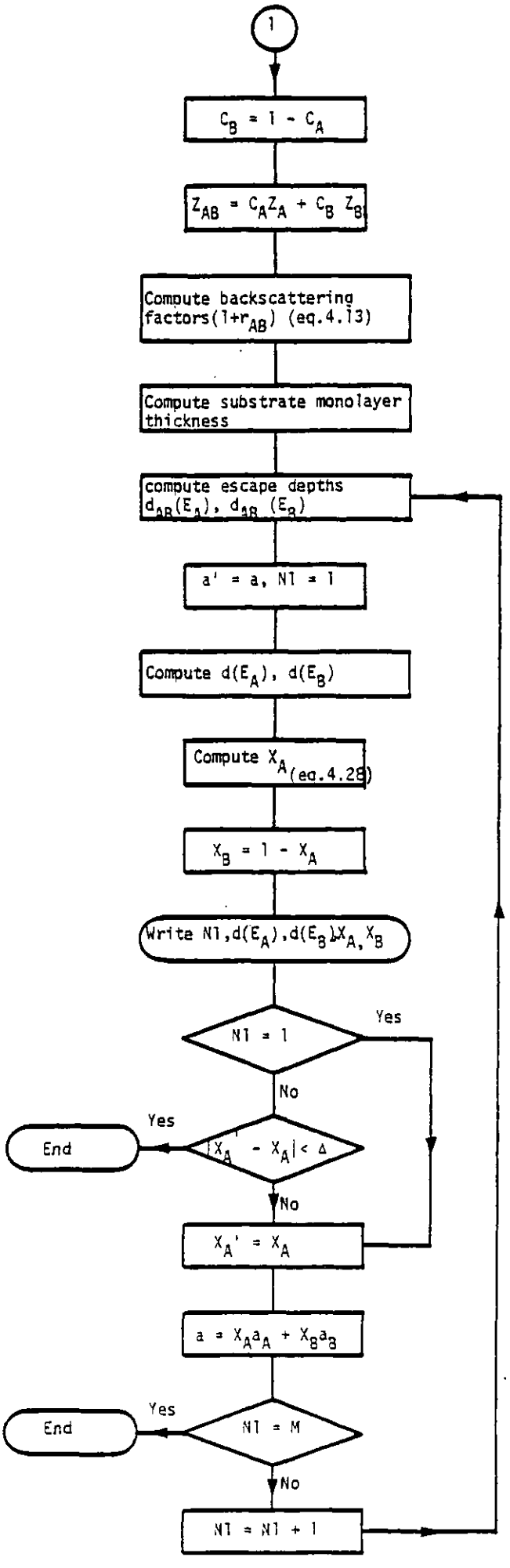
iteration is continued until the difference between two successive values of the composition differ in less than the convergence parameter Δ, or until a maximum number of iterations M is reached. The programme provides values of monolayer thickness, escape depths, matrix correction factors and alloy compositions within the escape depth.

The right hand side of the diagram corresponds to the case of enrichment restricted to the first monolayer. The backscattering factors associated with the bulk matrix are calculated assuming a weighted average atomic number Z_{AB}, using the known bulk composition. The surface composition depends implicitly on the overlayer thickness "a" through the escape depth d(E). The overlayer thickness is taken initially as the bulk monolayer thickness and this value used to compute X_A. The value X_A so obtained is used in equation 4.30 to get a new value of "a" and this procedure is continued iteratively. This part of the programme provides values of matrix monolayer thickness, overlayer thickness, escape depths and surface compositions X_A, X_B.

Homogeneous composition



Enrichment in the first layer



```
00100 PROGRAM AESAB(DATAES,OUTPUT,TAPE5=DATAES,TAPE6=OUTPUT)
00110C *
00120C *******QUANTITATIVE AUGER ANALYSIS OF BINARY ALLOYS*******
00130C *
00140C *      IT IS ASSUMED FIRST THAT THE ALLOY IS HOMOGENEOUS
00150C *      WITHIN THE SAMPLED DEPTH. THEN IT IS ASSUMED THAT
00160C *      THE ENRICHMENT IS RESTRICTED TO THE FIRST LAYER
00170C *
00180 REAL IA(20),IB(20),K,IBA,MONA,MONB
00190 INTEGER NV
00200C *
00210C *   (ZA,ZB) ATOMIC NUMBERS OF BINARY ALLOY COMPONENTS
00220 READ(5,*  )ZA,ZB
00230 WRITE(6,110)ZA
00240C *
00250 110 FORMAT(///,1X,'ATOMIC NUMBER OF COMPONENT A=',F4.1,/)
00260 WRITE(6,120)ZB
00270 120 FORMAT(1X,'ATOMIC NUMBER OF COMPONENT B=',F4.1,/)
00280C *    CA IS THE BULK 'A' COMPOSITION (ASSUMED KNOWN)
00290 READ(5,*  )CA
00300C *
00310 WRITE(6,128)CA
00320 128 FORMAT(1X,'BULK COMPOSITION CA =',F5.3,/)
00330C *      (AWA,AWB) ATOMIC WEIGHT OF ALLOY COMPONENTS
00340 READ(5,*  )AWA,AWB
00350C *
00360 WRITE(6,140)AWA
00370 140 FORMAT(1X,'ATOMIC WEIGHT OF COMPONENT A =',F6.2,/)
00380 WRITE(6,150)AWB
00390 150 FORMAT(1X,'ATOMIC WEIGHT OF COMPONENT B =',F6.2,/)
00400C *        (DA,DB) DENSITIES OF ALLOY COMPONENTS (GRAM/CC)
00410 READ(5,*  )DA,DB
00420 WRITE(6,160)DA
00430 160 FORMAT(1X,'DENSITY OF COMPONENT A=',F6.2,' GRAM/CC',/)
00440 WRITE(6,170)DB
00450 170 FORMAT(1X,'DENSITY OF COMPONENT B=',F6.2,' GRAM/CC',/)
00460C *        (EA,EB) AUGER TRANSITION ENERGIES
00470 READ(5,*  )EA,EB
00480 WRITE(6,180)EA
00490 180 FORMAT(1X,'ENERGY OF AUGER TRANSITION A =',F7.2,' EV.',/)
00500 WRITE(6,190)EB
00510 190 FORMAT(1X,'ENERGY OF AUGER TRANSITION B =',F7.2,' EV.',/)
00520C *        (ECA,ECB) IONIZATION ENERGY TO CREATE INITIAL HOLE
00530C *        STATE FOR AUGER TRANSITIONS A AND B (IN EV.)
00540C *
00550 READ(5,*  )ECA,ECB
00560 WRITE(6,200)ECA
00570 200 FORMAT(1X,'IONIZATION ENERGY HOLE AUGER TRANSITION A ='
00580+ ,F7.2,' EV.',/)
00590 WRITE(6,210)ECB
00600 210 FORMAT(1X,'IONIZATION ENERGY HOLE AUGER TRANSITION B ='
00610+ ,F7.2,' EV.',/)
00620C *             EP, PRIMARY BEAM ENERGY (IN EV.)
00630 READ(5,*  )EP
00640C *
00650 WRITE(6,230)EP
00660 230 FORMAT(1X,'PRIMARY BEAM ENERGY =',F7.2,' EV.',/)
00670C *        DELTA IS A CONVERGENCE PARAMETER
00680C *
00690 READ(5,*  )DELTA
00700 WRITE(6,240)DELTA
00710 240 FORMAT(1X,'CONVERGENCE PARAMETER =',F5.2,/)
00720C *        M IS THE MAXIMUM NUMBER OF ITERATIONS
00730 READ(5,*  )M
00740C *
00750 WRITE(6,250)M
00760 250 FORMAT(1X,'MAXIMUM NUMBER OF ITERATIONS =',I3,//)
00770C *        K IS A CORRECTION FACTOR FOR THE IMFP THAT TAKES
00780C *        INTO ACCOUNT THE ATTENUATION FUNCTION OF THE ANALYZER
00790 READ(5,*  )K
00800C *
00810 WRITE(6,270)K
00820 270 FORMAT(1X,'K =',F7.3,/)
00830C *        IBA IS THE RATIO OF AUGER SIGNALS OF PURE B TO PURE A
00840 READ(5,*  )IBA
00850 WRITE(6,280)IBA
00860 280 FORMAT(1X,'(I PURE B)/(I PURE A) =',F7.3,/)
00870C *        NV IS THE NUMBER OF PAIRS OF VALUES (IA,IB)
00880C *
00890 READ(5,*  )NV
00900 WRITE(6,290)NV
00910 290 FORMAT(1X,'NUMBER OF PAIRS (IA,IB) =',I3,/)
00920C *
00930C *
```

```
00940C *       (IA,IB) AUGER SIGNALS OF COMPONENTS
00950C *       A AND B IN THE ALLOY (ARBITRARY UNITS)
00960C *
00970 DO 300 I=1,NV
00980 300 READ(5,*  )IA(I),IB(I)
00990 WRITE(6,310)
01000 310 FORMAT(1X,'   IA      IB  ',//)
01010 WRITE(6,130)(IA(I),IB(I),I=1,NV)
01020 130 FORMAT(2F7.2)
01030C *           MONOLAYER THICKNESS (IN NM.)
01040 VOLA=(AWA/(DA*602.3))
01050 MONA=(VOLA)**(1./3.)
01060 VOLB=(AWB/(DB*602.3))
01070 MONB=(VOLB)**(1./3.)
01080 WRITE(6,320)MONA
01090 320 FORMAT(1X,'MONOLAYER THICKNESS OF COMPONENT A ='
01100+ ,F6.3,' NM.',/)
01110 WRITE(6,330)MONB
01120 330 FORMAT(1X,'MONOLAYER THICKNESS OF COMPONENT B ='
01130+ ,F6.3,' NM.',/)
01140 ABA=(AWB*DA)/(AWA*DB)
01150C *
01160C *           CALCULATION OF INELASTIC MEAN FREE PATHS
01170C *
01180 DAA=FMFP(MONA,EA)
01190 DAB=FMFP(MONA,EB)
01200 DBA=FMFP(MONB,EA)
01210 DBB=FMFP(MONB,EB)
01220C *      IMFP IS MULTIPLIED BY K TO GIVE EFFECTIVE ESCAPE DEPTH
01230 DAA=K*DAA
01240 DAB=K*DAB
01250 DBA=K*DBA
01260 DBB=K*DBB
01270 WRITE(6,340)
01280 340 FORMAT(1X,'    DAA       DAB       DBA       DBB (MONOLAYERS)'
01290+ ,/)
01300 WRITE(6,350)DAA,DAB,DBA,DBB
01310 350 FORMAT(1X,4F9.3,///)
01320C *        CALCULATION OF BACKSCATTERING FACTOR (1+R)
01330 RAA=BACK(ECA,EP,ZA)
01340 RAB=BACK(ECB,EP,ZA)
01350 RBA=BACK(ECA,EP,ZB)
01360 RBB=BACK(ECB,EP,ZB)
01370C *
01380 AA=DAA*RAA
01390 AB=DAB*RAB
01400 BA=DBA*RBA
01410 BB=DBB*RBB
01420C *
01430C *
01440 CB=1.0-CA
01450 Z=(CA*ZA+CB*ZB)
01460 RMA=BACK(ECA,EP,Z)
01470 RMB=BACK(ECB,EP,Z)
01480 A=(CA*MONA+CB*MONB)
01490 VOLM=A*A*A
01500 DMA=FMFP(A,EA)
01510 DMB=FMFP(A,EB)
01520 DMA=K*DMA
01530 DMB=K*DMB
01540 WRITE(6,530)A
01550 530 FORMAT(1X,'MATRIX MONOLAYER THICKNESS =',F7.3,' NM.',/)
01560 WRITE(6,540)DMA
01570 540 FORMAT(1X,'DMA=',F7.3,' ML.',/)
01580 WRITE(6,550)DMB
01590 550 FORMAT(1X,'DMB=',F7.3,' ML.',/)
01600C *
01610C *       START OF LOOP FOR DIFFERENT PAIRS (IA,IB)
01620C *
01630 DO 600 I=1,NV
01640 WRITE(6,360)IA(I)
01650 360 FORMAT(1X,'AUGER INTENSITY COMPONENT A =',F7.2,/)
01660 WRITE(6,370)IB(I)
01670 370 FORMAT(1X,'AUGER INTENSITY COMPONENT B =',F7.2,//)
01680 WRITE(6,380)
01690 380 FORMAT(1X,'   N    F      PR      XA      XB  ',/)
01700 F=1.0
01710 N=1
01720 400 PR=IBA*F
01730 XA=IA(I)/(IA(I)+(IB(I)/PR))
01740 XB=1.0-XA
01750C *
01760 WRITE(6,410)N,F,PR,XA,XB
01770 410 FORMAT(1X,I4,4F7.3,/)
01780 IF(N.EQ.1)GO TO 420
01790 IF(ABS(XA-XAN).LE.DELTA) GO TO 510
01800 420 XAN=XA
01810 F=FBA(XA,ABA,AA,AB,BA,BB)
01820C *
01830 IF(N.EQ.M)GO TO 510
01840 N=N+1
01850 GO TO 400
```

```
01870C *         CALCULATION OF SURFACE COMPOSITION ASSUMING
01880C *         ENRICHMENT RESTRICTED TO FIRST LAYER AND KNOWN
01890C **        UNDERLYING BULK COMPOSITION CA,CB
01900C *
01910C *
01920 510 CONTINUE
01930 WRITE(6,520)
01940 520 FORMAT(1X,'SURFACE COMPOSITION ASSUMING ENRICHMENT ONLY IN THE
01950+FIRST MONOLAYER',//)
01960 AS=A
01970 N1=1
01980 WRITE(6,560)
01990 560 FORMAT(1X,'   N    DSA(ML.)  DSB(ML.)     XA         XB',//)
02000 570 CONTINUE
02010 DSA=FMFP(AS,EA)
02020 DSB=FMFP(AS,EB)
02030 DSA=K*DSA
02040 DSB=K*DSB
02050 EDA=EXP(-1.0/DSA)
02060 EDB=EXP(-1.0/DSB)
02070 C1=RMB*RAA*DAA*(CB*OMB*VOLB*EDB+DBB*VOLM*(1.0-EDB))
02080 C2=CA*RMA*RBB*OMA*DBB*VOLA*EDA
02090 C3=RMB*RAA*DAA*DBB*VOLM*(1.0-EDB)
02100 C4=RMA*RBB*DAA*DBB*VOLM*(1.0-EDA)
02110 XA1ST=(IA(I)*C1-(IB(I)/IBA)*C2)/(IA(I)*C3+(IB(I)/IBA)*C4)
02120 XB1ST=1.0-XA1ST
02130 WRITE(6,580)N1,DSA,DSB,XA1ST,XB1ST
02140 580 FORMAT(1X,I4,4F10.3,/)
02150 IF(N1.EQ.1)GO TO 590
02160 IF(ABS(XA1ST-XA1N).LE.DELTA)GO TO 600
02170 590 XA1N=XA1ST
02180 AS=(XA1ST*MONA+XB1ST*MONB)
02190 IF(N1.EQ.M)GO TO 600
02200 N1=N1+1
02210 GO TO 570
02220 600 CONTINUE
02230 END
02240C *
02250C *       FUNCTION FMFP CALCULATES INELASTIC MEAN FREE PATH
02260C *       USING SEAH'S FORMULA
02270C *
02280 FUNCTION FMFP(A,E)
02290 B=538.0/(E*E)
02300 C=0.41*SQRT(A*E)
02310 FMFP=B+C
02320 RETURN
02330 END
02340C *
02350C *        FUNCTION BACK CALCULATES THE BACKSCATTERING FACTOR
02360C *        (1+R) USING REUTER'S FORMULA
02370C *
02380 FUNCTION BACK(EC,EP,Z)
02390 REAL NU
02400 A=EC/EP
02410 B=2.3*(1.0-0.9*A)
02420 NU=0.0254+0.016*Z-0.000186*(Z*Z)+(8.3E -7)*(Z*Z*Z)
02430 R=B*NU
02440 BACK=1.0+R
02450 RETURN
02460 END
02470C *
02480C *
02490C *        FUNCTION FBA CALCULATES THE MATRIX CORRECTION FACTOR F
02500C *
02510 FUNCTION FBA(XA,ABA,AA,AB,BA,BB)
02520 A=(AA-BA)
02530 B=(AB-BB)
02540 C=AA/BB
02550 D=BA+A*XA
02560 E=BB+B*XA
02570 G=D/E
02580 FBA=ABA*C*G
02590 RETURN
02600 END
```

Acknowledgements

I would like to express my gratitude to my supervisor, Dr. P.J. Dobson, for the proposal of the subject and to Dr. P.R. Webber for his assistance in the experimental work.

I would also like to extend my thanks to Dr. J.P. Muscat for allowing me to use his computer programme of surface segregation, to Dr. A.E. Hughes for his help in the use of the XPS system, to N. Norton for his help in the construction of the temperature controller and to Fiona Scroggs for the typing of this thesis.

The financial support provided by the "Consejo de Desarrollo Científico y Humanístico de la Universidad Central de Venezuela" is gratefully acknowledged.